OPTICAL TRAPPING: OPTICAL INTERFEROMETRIC METROLOGY AND NANOPHOTONICS

Woei Ming Lee

A Thesis Submitted for the Degree of PhD
at the
University of St. Andrews

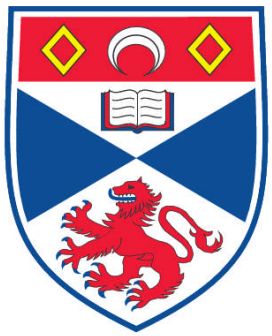

2010

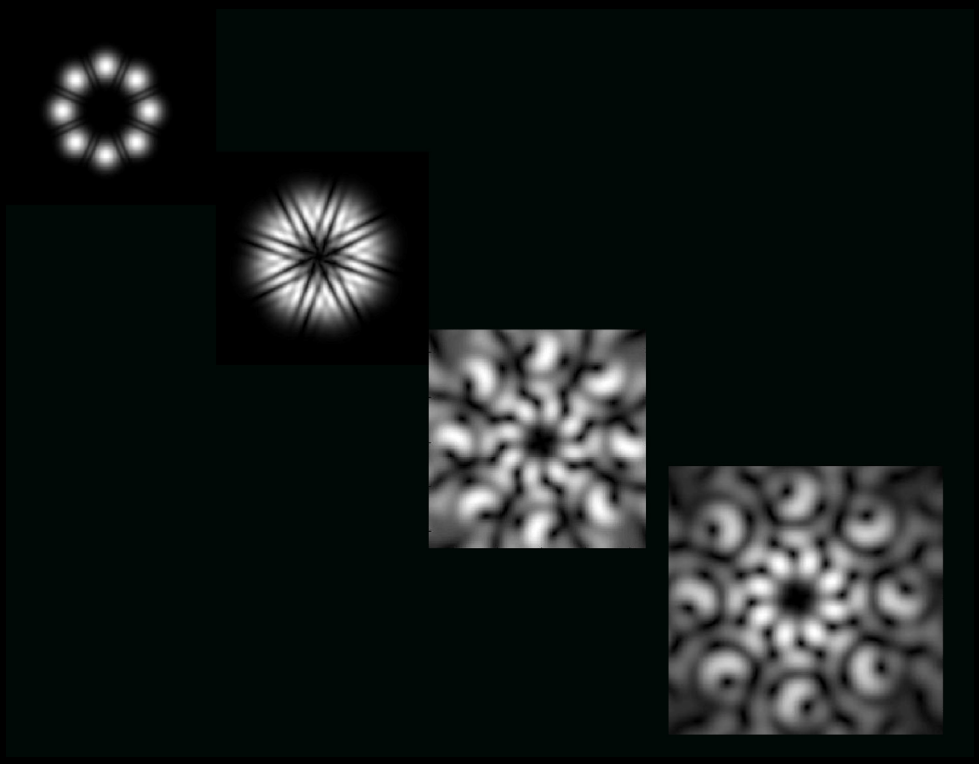

UNIVERSITY OF ST ANDREWS

OPTICAL TRAPPING: OPTICAL INTERFEROMETRIC METROLOGY AND NANOPHOTONICS

2009

Tuning light for the microscopic world | WOEI MING LEE

Optical trapping: optical interferometric metrology and nanophotonics

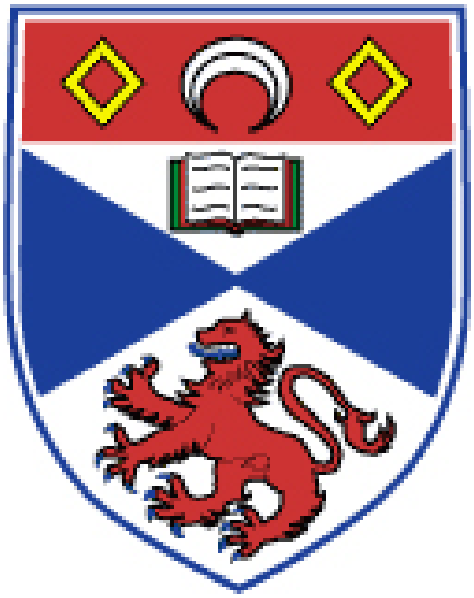

WOEI MING LEE

A thesis submitted to the University of St Andrews

in fulfillment of the requirement for the degree of

Doctor of Philosophy

October 2009

Declarations

I, Woei Ming Lee, hereby certify that this thesis, which is approximately 60000 words in length, has been written by me, that it is the record of work carried out by me and that it has not been submitted in any previous application for a higher degree.

I was admitted as a research student in February 2006 and as a candidate for the degree of Doctor of Philosophy in February 2006; the higher study for which this is a record was carried out in the University of St Andrews between 2006 and 2009.

Date ……...Signature of candidate ……

I hereby certify that the candidate has fulfilled the conditions of the Resolution and Regulations appropriate for the degree of Doctor of Philosophy in the University of St Andrews and that the candidate is qualified to submit this thesis in application for that degree.

Date …… Signature of supervisor ……

In submitting this thesis to the University of St Andrews we understand that we are giving permission for it to be made available for use in accordance with the regulations of the University Library for the time being in force, subject to any copyright vested in the work not being affected thereby. We also understand that the title and the abstract will be published, and that a copy of the work may be made and supplied to any bona fide library or research worker, that my thesis will be electronically accessible for personal or research use unless exempt by award of an embargo as requested below, and that the library has the right to migrate my thesis into new electronic forms as required to ensure continued access to the thesis. We have obtained any third-party copyright permissions that may be required in order to allow such access and migration, or have requested the appropriate embargo below. The following is an agreed request by candidate and supervisor regarding the electronic publication of this thesis:

Access to Printed copy and electronic publication of thesis through the University of St Andrews.

Date ……..

Signature of candidate …….

Signature of supervisor …….

Dedication

This thesis is dedicated to …

my dearest wife Ally who has endured with me, through all my trials and tributes.

our precious daughter Iona who is the love of my life, and a constant joy to wake up to every morning.

my family: my sister, my mother and my father, all of whom have selflessly given me all the support to carry me through this arduous journey.

Kishan who gave me a wonderful opportunity to pursue my passion in science

To all my friends that gave me their wisdom of advice when most needed.

"Science is a way of trying not to fool yourself.
The first principle is that you must not fool yourself,
and you are the easiest person to fool",

Dr. Richard P. Feynman

Acknowledgments

Kishan D: *For all your brilliant ideas and being a great supervisor through the whole PhD.*

Ewan W: *For your clarity, patience and perseverance in your teachings on nonlinear physics.*

Peter R: *Glad to work alongside with you to complete the QPD program and of course the TVR!!*

Demetri C, Ramy El: *Provided me with an excellent theoretical support and a wonderful time at Baltimore.*

Ivan.F, Luis and Irais: *Thanks for working with me during your visit to St Andrews…*

Pascal A, Chen S: *Thanks for all the support and teaching of nanoparticles and quantum dots*

Tomas C: *Enjoyed all our discussions and collaborations, and we will have a paper together soon!!*

Rob M: *Enjoyed all the afternoon microfludics sorting experiments and thanks for improving my Labview trap stiffness post-processing program.*

Yoshi A: *Working with me on nanosecond and femtosecond ablations experiments!!*

Mackej A: *Enjoyed working with you on the DHM!!*

Yoshi A , Mackej A*: Enjoyed countless lunch discussions.*

Vene G.C: *Guiding and helping me when I first arrive in St Andrews.*

Janelle. S: *Working together on femtosecond trapping and thanks for motivating me to improve my Labview programming skills.*

Susan S: *For motivating me to improve my BPM code.*

Eddie T: *Bring our first OCT project to a paper and a good friend…*

Weelee T: *Your immense generosity, selfless support !!!*

John L, David G, Graham M, Philip J, Klaus M, Michael S, David C, Xanthi T: *Best bunch of office mates and friends that I could ever ask for.*

Lani T, Patience M*: For finishing the difficult cell experiments and being patience with me.*

Kishan D, Tzu Hao C, Huimin L: *For proof reading the thesis.*

Mark N, Carlos P : *For their critical and valuable comments on the thesis.*

All the support staff of St Andrews: *For all the technical and administrative support that helped realise my research.*

Abstract

The two main themes in this thesis are the implementation of interference methods with optically trapped particles for measurements of position and optical phase (optical interferometric metrology) and the optical manipulation of nanoparticles for studies in the assembly of nanostructures, nanoscale heating and nonlinear optics (nanophotonics).

The first part of the thesis (chapter 1, 2) provides an introductory overview to optical trapping and describes the basic experimental instrument used in the thesis respectively. The second part of the thesis (chapters 3 to 5) investigates the use of optical interferometric patterns of the diffracting light fields from optically trapped microparticles for three types of measurements: calibrating particle positions in an optical trap, determining the stiffness of an optical trap and measuring the change in phase or coherence of a given light field. The third part of the thesis (chapters 6 to 8) studies the interactions between optical traps and nanoparticles in three separate experiments: the optical manipulation of dielectric enhanced semiconductor nanoparticles, heating of optically trapped gold nanoparticles and collective optical response from an ensemble of optically trapped dielectric nanoparticles.

Overview of thesis

Chapter 1 provides a brief overview of the optical trapping techniques and the related applications in a number of interdisciplinary sciences. Chapter 2 outlines the experimental implementation of an optical trapping system that is used in the majority of the thesis (chapter 3-7).

Chapter 3 describes the use of back focal plane (BFP) interference with a quadrant photodiode (QPD) for the calibration of an optical trapping system. The intensity variations of the interference pattern from the diffracted light field of the optically trapped particle captured by the QPD are used to measure both the particle position and stiffness of an optical trap.

Non-zero order laser modes (Laguerre-Gaussian) can be generated from Gaussian beam using beam shaping techniques. Chapter 4 investigates two techniques of generating a Laguerre-Gaussian (LG) beam from a Gaussian beam. Using the BFP interferometry and a calibrated QPD, I show the direct observation of the position shift along the axial direction of an optically trapped microsphere due to the low axial scattering in a focused LG beam, when comparing with a focused Gaussian beam.

The interference pattern from a Young's double slits (or pinholes) elucidates any changes to the phase or spatial coherence of a sampled light field. In the BFP interferometry, a microsphere is

considered to be a diffracting aperture. A microscopic Young's slits type interference experiment can be performed using the diffracting light fields from two microspheres. Chapter 5 demonstrates two sets of experiments that use optically trapped microparticles as diffracting apertures for phase and spatial coherence measurements. The first set of experiments employs the sampling beam (LG beam) itself to trap the microspheres. Two or more optically trapped spheres are used to controllably map out the phase (wavefront) of the LG beam in an in-situ manner. The second set of experiments uses two independent optical traps (dual Gaussian beam optical traps) to manipulate two individual microparticles for studies of spatial coherence on a separate sampling light field (LG beam). The independent optical traps, which are separated from the sampling light field, offer more controllability over the positions in which the microparticles are positioned.

The optical manipulation of semiconductor nanoparticles can have an important role in optical construction of photonics devices. Chapter 6 demonstrates the trapping of dielectric enhanced semiconductor nanosheets and nanotubes. The efficiencies in the optical manipulation of the nanoparticles are measured by the BFP interferometry and brightfield video microscopy.

Nanoparticles do offer new phenomena to explore such as localised heating. Controlled in-vitro cell hyperthermia with gold nanoparticle has numerous therapeutic purposes, especially in the controlled destruction of cancerous cells. Chapter 7 investigates the heating effects of a single trapped gold nanoparticle on a biological cell. In this chapter, a confocal laser scanning fluorescence imaging system is incorporated with the optical trapping system (chapter 2) and position detection setup (chapter 3). The integrated manipulation and imaging apparatus carries out time-lapse fluorescence imaging and tracking of trapped gold nanoparticle-cell adhesion. The collected fluorescence signals measure the effects of a cell during and after being exposed to a single heated gold nanoparticle.

Techniques in building nanostructures from an ensemble of nanoparticles form an important platform for nanophotonics. In the presence of an optical field, a large density of nanoparticles (nanosuspension) experience an optical gradient force that attracts them into the spatial regions of high intensity, thereby increasing the local density and subsequently the refractive-index. Hence, the nanosuspension can serve as a nonlinear (photorefractive) medium, where the local refractive index change is intensity dependent. In chapter 8, I measure the nonlinearity (Kerr-like or exponential) of a nanosuspension with a novel fiber based Z-scan variant setup, and compare the experimental data with the theoretical predictions.

Publication list

Peer-Review Journal

1. Y. Arita, M.L.Torres-Mapa, W.M.Lee, T Čižmár, F J. Gunn-Moore, K Dholakia, "laser-induced breakdown (LIB) of optically trapped nanoparticles for gene transfection", Nature Methods in submission (2010)
2. J.C.Shane, M.Mazilu, W.M.Lee, K Dholakia "Effect of pulse temporal shape on optical trapping using ultrashort pulsed lasers" Opt Express in submission (2010)
3. P. Mthunzi, W.M.Lee, C.T.A. Brown, F Gunn-Moore,A. C. Riches, K Dholakia, "Intracellular dielectric tagging for improved optical mammalian cell manipulation" IEEE JQST Biophotonics, In Press (2009)
4. R. El-Ganainy and D. N. Christodoulides, E. M. Wright, W. M. Lee and K. Dholakia Phys Rev A , In Press (2009)
5. W. M. Lee, R. El-Ganainy, D. N. Christodoulides K. Dholakia and E. M. Wright , "Nonlinear optical response of colloidal suspensions," Opt. Express **17**, 10277-10289 (2009)
6. K. M. Tan, M. Mazilu, T. H. Chow, W. M. Lee, K. Taguichi, B. K. Ng, W. Sibbett, C. S. Herrington, C.T. A. Brown, and K. Dholakia, "In-fiber common-path optical coherence tomography using a conical-tip fiber," Opt. Express **17**, 2375-2384 (2009)
7. J. L. Hernandez-Pozos, W. M. Lee, V.-R. L. Irais, A. Campero, and K. Dholakia, "Controlled three-dimensional manipulation of vanadium oxide nanotubes with optical tweezers," Applied Physics Letters **93**, 243107 (2008).
8. W. M. Lee, P. J. Reece, R. F. Marchington, N. K. Metzger, and K. Dholakia, "Construction and calibration of an optical trap on a fluorescence optical microscope," Nature Protocols **2**, 3226-3238 (2007).
9. W. M. Lee, and K. Dholakia, "Optically trapped and controlled microapertures for studies of spatial coherence in an arbitrary light field," Applied Physics Letters **90**, 261101 (2007).
10. W. M. Lee, V. Garces-Chavez, and K. Dholakia, "Interference from multiple trapped colloids in an optical vortex beam," Optics Express **14**, 7436-7446 (2006).

Book Chapter and Reviews

11. K. Dholakia, and W. M. Lee, "Optical trapping takes shape: the use of structured light fields," in Advances in Atomic, Molecular and Optical Physics **56** 261-337. (2008)
12. K. Dholakia, W. M. Lee, L. Paterson, M. P. MacDonald, R. McDonald, I. Andreev, P. Mthunzi, C. T. A. Brown, R. F. Marchington, and A. C. Riches, "Optical separation of cells on potential

energy landscapes: Enhancement with dielectric tagging," IEEE Journal of Selected Topics in Quantum Electronics **13**, 1646-1654 (2007).

Conference presentations

13. Y. Arita, M.L.Torres-Mapa, W.M.Lee, T Čižmár, F J. Gunn-Moore, K Dholakia, "laser-induced breakdown (LIB) of optically trapped nanoparticles for gene transfection", BioMed, OSA, in submission (2009)
14. W. M. Lee, J. L. Hernandez-Pozos, V.-R. L. Irais, A. Campero, P. Andre, Chen S and K. Dholakia, "Manipulating vanadium oxide nanotube with optical tweezers" Optical Trapping and Optical Micromanipulation VI, K. Dholakia and G. C. Spalding, Eds., In Press, SPIE, San Diego, CA, USA (2009)
15. E. M. Wright, W. M. Lee, K. Dholakia, R. El-Ganainy and D. N. Christodoulides "Optical nonlinearity of liquid nanosuspensions: Kerr versus exponential model" Optical Trapping and Optical Micromanipulation VI, K. Dholakia and G. C. Spalding, Eds., In Press, SPIE, San Diego, CA, USA (2009)
16. W. M. Lee, K. Dholakia, E. M. Wright, R. El-Ganainy and D. N. Christodoulides "Probing the nonlinear optical response of nanosuspensions," in Conference on Lasers and Electro-Optics/International Quantum Electronics Conference, p. IWE3, Optical Society of America (2009)
17. E. M. Wright, W. M. Lee, P. L. Giscard and K. Dholakia, "Long distance beam propagation in colloidal suspensions: comparison between theory and experiment," in Optical Trapping and Optical Micromanipulation V K. Dholakia and G. C. Spalding,Eds., pp. 70380-70389, SPIE, San Diego, CA, USA (2008).
18. W. M. Lee, A. E. Carruthers, V. Garces-Chavez and K. Dholakia, "Far field interference measurements of vortex light fields in optical trapping - art. no. 64830N," in Conference on Complex Light and Optical Forces D. L. Andrews, E. J. Galvez and G. Nienhuis, Eds., pp. N4830-N4830, SPIE, San Jose, CA (2007).
19. W. M. Lee and K. Dholakia, "Optical coherence measurements of vortex light fields using optically manipulated micro-apertures - art. no. 66440Y," in Conference on Optical Trapping and Optical Micromanipulation IV K. Dholakia and G. C. Spalding, Eds., pp. Y6440-Y6440, SPIE, San Diego, CA (2007).

CONTENT

Appendix E

Additional position and trap stiffness measurements

i. Mechanical vibration from EMCCD
ii. Position measurement in an LG beam
iii. Trapping 48nm nanospheres
iv. Trapping CdSe nanosheets without silica coat

Appendix F

Additional interference from multiple trapped spheres

Appendix G

Digital holography microscopy

List of acronyms

LG	Laguerre Gaussian
BFP	Back focal plane
AOD	Acousto Optic Deflector
CCD	Charge Coupled Device
CGH	Computer Generated Holograms
EOD	Electro-Optic Deflector
NA	Numerical Aperture
OAM	Orbital Angular Momentum
QPD	Quadrant Photodiode

List of units

m	metre
cm	centimetre (10^{-2}m)
mm	millimetre (10^{-3}m)
µm	micrometre (10^{-6}m)
nm	nanometre (10^{-9}m)
N	Newton
g	grams
pN	pico-Newton (10^{-12}N)
nN	nano-Newton (10^{-9}N)
Hz	Hertz
V	voltage
mW	milliwatt
s	second

Chapter 1 –

Optical trapping

1. Optical trapping

1.1. Overview

Optical trapping is a powerful and versatile technique based upon the interaction of light and matter. Whilst the forces exerted by optical traps are naturally very small (in the order of piconewton, 10^{-12} N), they are sufficient to realise non-invasive mechanical controls over mesoscopic particles within atomic, biological and colloidal systems. This chapter introduces the development of optical trapping, the related physical concepts and the associated applications.

In this section, I provide an overview of the topics that are discuss in this chapter. First, I shall briefly introduce the development of optical trapping since its early inception by Arthur Ashkin [1, 2].

Secondly, I move onto the explanation of the optical forces exerted by a focused Gaussian laser beam (optical tweezers) on a selection of particle sizes and types. The optical forces are sufficient to manipulate particles sizes that are much larger (Mie regime) or smaller (Rayleigh regime) than the wavelength of the trapping beam. The optical forces are decoupled into two main components: scattering and gradient forces. In general, the scattering forces are dependent on the intensity of light field, while the gradient forces are dependent on the gradient of the intensity of the light field. Both components of the optical forces do scale with particle sizes. It is critical to understand that the optical forces at work, so as to efficiently use the optical trapping technique. In the Mie regime, the optical forces can be understood through simple ray optics i.e. treating the particles as lens. At the Rayleigh regime, the optical forces are better described by dipole approximations i.e. treating particles as single dipoles. Typically transparent microspheres are being used in optical trapping experiments. However, optical traps can also manipulate birefringent and metallic particles. Micrometer birefringent particles (i.e. calcite) can be rotated by an optical trap. The double refractive indices of the birefringent crystal impart different phase shifts to an input light field. The output light field contains two components: ordinary and extraordinary. The differences in the phase shifts of the light field exiting the crystal create an angular momentum, which in turn creates an optical torque upon the birefringent microparticle. Metallic microparticles, like a micro-mirror, can be optically trapped by a focused Gaussian beam. The strong axial scattering forces along the propagation axis of the Gaussian beam act to push the metallic microparticle upon a surface and the transverse gradient forces confine it in two dimensions. However, for metallic nanoparticle (diameter < 200 nm), the axial scattering force is greatly reduced due to a smaller scattering cross-section. While the polarisability of the metallic

nanoparticle has shown to enhance the axial gradient forces, this permits three dimensional optical trapping [3].

Thirdly, a trapped particle tends to reside at its equilibrium position (minimum energy) within the trapping beam. Once the particle is perturbed from the centre of the optical potential energy well in any dimensions, it will experience a restoring force that is linearly (to a certain degree) proportional to the distance away from centre of the optical potential energy well (the equilibrium position). This linear restoring force is akin to a miniscule spring that obeys Hooke's law i.e. harmonic oscillator. The modelling of the optically trapped particle as a harmonic oscillator with a spring constant is crucial to the conversion of an optical trap into an effective force transducer. Here, I shall describe the modelling of the motion of an optical trapped particle using the Langevin equation of motion in one dimension.

Lastly, I will briefly discuss the applications of optical traps in a number of interdisciplinary sciences. The first part of this section covers an overview of the applications of optical trapping in biophysical systems and colloidal systems. The second part of this section considers two photonics areas namely, optical interferometric metrology and nanophotonics, that are associated with optical trapping. These two photonics areas motivate the main research works that are carried out in this thesis. I begin by introducing the interferometric measurement schemes that are used to calibrate the particle position within the optical trap and to measure the spring constant of the optical trap. Next, I discuss the conventional aperture-based interferometric methods for measuring wavefront of a sampling light field, whilst highlighting on optically trapped microapertures. Finally, I provide an overview of the current interests in nanoparticle and light interaction, starting with the optical manipulation of semiconductor nanoparticles for construction of nanostructures [4-6], the use of optically induced heated gold nanoparticles [7] for nanoscale cell hyperthermia [8] and ending with the nonlinear optical interactions of an ensemble of dielectric nanoparticles [9-12].

1.2. Brief introduction to optical trapping

Light-matter interaction has a profound impact over a spread of interdisciplinary sciences [13]. The mechanical forces arising from light-matter interactions have been used to draw a deeper understanding in field of photonics, atomic and molecular systems. The minuscule forces (piconewton (pN) to femtonewton (fN)) of light have made a large impact on the size scales ranging from an atom (angstrom) to molecule (nanometre), and to biological cells (micrometre). For atomic ensemble, light forces paved way for the methods of laser cooling [14-16], ultra cold

quantum gases and Bose-Einstein condensate [17-19]. On the other hand, the precise calibration of the optical forces exerted upon micron-sized spheres has enabled us to measure the conversion of chemical energy into discrete mechanical motion in macromolecules [20] and how cells can ingest foreign objects with their filopodia [21, 22].

First we must ask ourselves, how can light exert any force on matter even though it possesses almost negligible mass ($\approx 10^{-51}$ g) [23]. How do such light forces arise? From Einstein's explanation of the photoelectric effect and Planck's theory of radiation, it is known that each photon (elementary light particle) may be considered as a quanta of energy that possesses a well-defined momentum. With this in mind, one can consider: a stream of photons (from a laser beam) coming into contact with an object and spark a momentum exchange. Over a given period of time, this exchange of momentum results in a given amount of force: Newton's second law of motion. Light may move, hold, and exert controllable linear and angular forces on an object, depending on the object's physical properties (i.e. refractive index, absorption and size). This form of optical momentum transfer and the subsequent force is at the heart of the area of optical trapping [24].

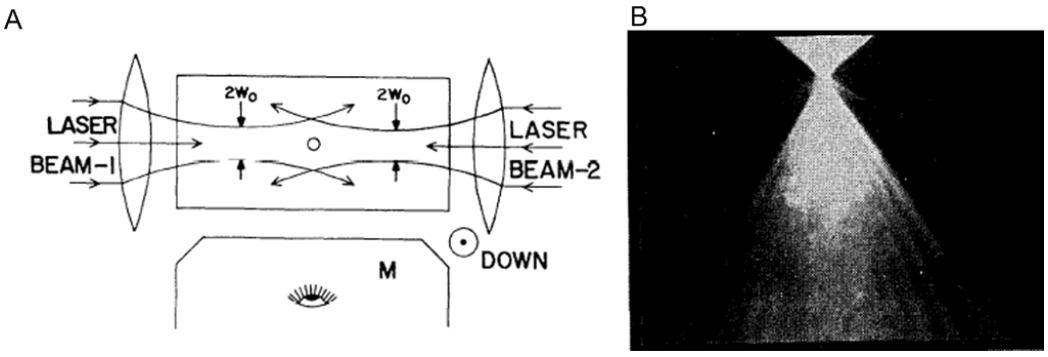

Figure 1.1: Dual beam optical trapping geometry and a single 10μm sphere trapped in three dimensions, both invented by A. Ashkin [1, 2]. (A) Two counter-propagating laser of the same beam waist (wo) is shown to stably confine a microsphere at the centre of the chamber [1]. (B) Red fluorescent signal (white in this image) of the focused argon ion laser beam as it trapped a 10μm sphere just below the beam focus in three dimension [2].

In 1970, Ashkin [1] performed experiments with a visible argon ion laser and microspheres with higher refractive index than the surrounding aqueous medium. In a single horizontally propagating beam, microspheres were seen to be drawn and aligned along the highest intensity region of the beam. Upon entry into the beam, they were seen to be propelled or guided along the propagation direction of the beam. This is because the particles are optically trapped in the transverse plane but not along the beam propagation. He then added a second beam (of equivalent optical power) in the counter-propagating geometry that halted the motion of a single sphere along

the longitudinal axis of the first beam, thus forming the first stable optical trap, see figure 1.1(A). Equal scattering forces from the two counter-propagating beam are balanced, thereby achieving a stable trapping position along the two beams' propagation axis. This counter-propagating beams optical trapping geometry [1] has now been realized with optical fibers [25]. In subsequent studies, Ashkin and Dziedzic [26] also investigated the stable optical trapping of large microspheres (20μm) with a single laser beam coming in from underneath the microsphere. The microspheres are optically trapped with the gradient forces on the transverse plane. In the axial plane, the particle is stably trapped along the propagation direction of the input beam by balancing the scattering forces and gravity (mass of the object). With a non-zero order laser beam (TEM^*_{01}), they were able to stably trap the hollow microspheres using the same trapping geometry. This is because the hollow particle (lower refractive index than the surrounding) tends to be repelled from the regions of high light intensity in a Gaussian trapping beam [26]. The non-zero order laser beam mode (an annular intensity pattern) was needed so as to optically "cage" the hollow particle.

Sixteen years after the dual beam trap, Ashkin *et al* [2] realised that a strongly focused laser beam (beam waist at focus to be about a few hundred nanometres) can create ***a single three dimensional optical trap (also known as optical tweezers),*** as shown in figure1.1B. Optical tweezers can be used to move micrometre and nanometre sized particles. It has been over thirty five years since the first optical trapping experiments and over twenty years since the inception of the popular "optical tweezers" based on a highly focused Gaussian beam [2]. Optical tweezers has now been well-recognised technique and have the largest impact within the field of optical micromanipulation. A series of extensive reviews have been written over the last few years [27-33] on this topical research area, while the original paper has until now received over 1,500 citations (average ≈ 65 citations per year). In comparison with other micromanipulation techniques, optical tweezers has the quality of an ideal non-invasive biological forces transducer. A main advantage in the optical tweezers technique is that one can easily pick and drop a desired object by simply switching the laser beam on and off. This is unlike other micromanipulation techniques (e.g. atomic force manipulator (AFM)) that can succumb to strong surface "sticky" forces (e.g. Van Der Waals). Unfortunately, the forces exerted by optical traps can only reach the range of hundreds of pN. They fall well short of force required to break covalent bonds (1 nN) [34] which is achievable using other techniques [35]. In the next section, I shall elaborate on the optical forces involved in trapping a transparent microsphere with an optical tweezers system.

1.3. Consideration of optical forces

The optical forces are decoupled into two main components: scattering and gradient forces. In the simplest terms, the optical forces can be understood by organizing particles sizes with respect to the wavelength of the trapping beam. Particles with radius, ***r***, larger or smaller than the wavelength, λ, can be classify into Mie regime or Rayleigh regime respectively [36]. In both cases, the scattering forces are dependent on the intensity of laser beam and the gradient forces are dependent on the gradient of the intensity. This section describes the optical forces pertaining to the Mie and Rayleigh regime respectively.

1.3.1. Particle size - Mie and Rayleigh regime

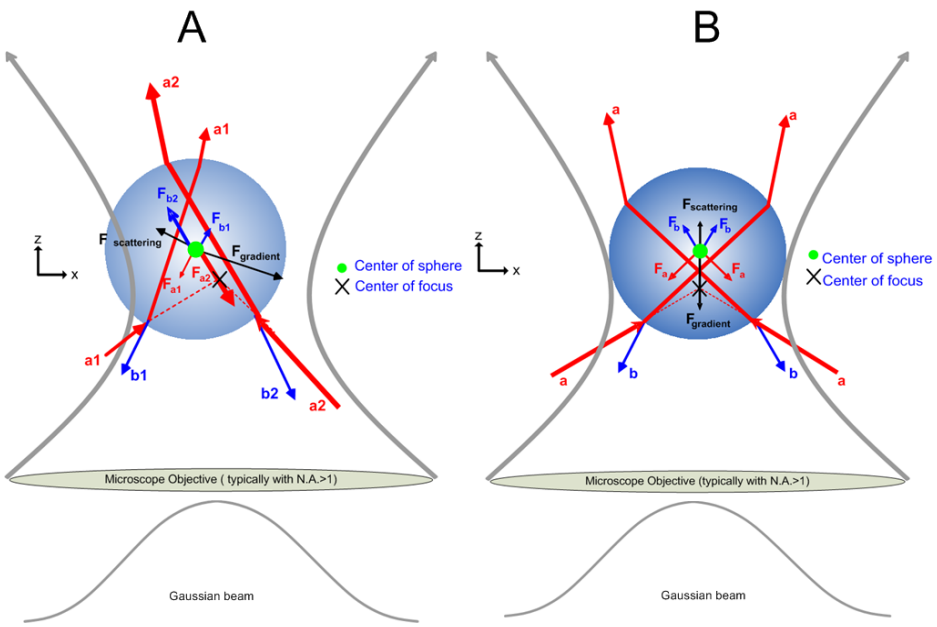

Figure 1.2: Force diagrams for Mie transparent sphere using ray tracing. The lateral and axial trapping forces involved in the three dimensional trapping of a single transparent dielectric microsphere (Mie regime) as illustrated with ray optics. (a) shows the microsphere positioned away from the centre of the focus beam, (b) shows the microsphere trapped slightly above the centre of the focus beam where the gradient and scattering forces are balanced. (The forces (gravity) due to the mass of the microsphere are not discussed in the diagram).

Here I consider the use of an optical tweezers (three dimensional optical trap) to illustrate the optical forces in the Mie regime. To consider an object in the Mie regime, the particle radius, ***r***, needs to be much larger than the laser wavelength, λ. One can then invoke the use of geometrical ray optics to picture the forces involved. Ashkin [36] showed a clear calculation of how to derive the forces present in this instance by ray tracing and use of the Fresnel equations at the sphere-

medium boundary. The scattering and gradient forces are considered to arise from the reflection and refraction of light. A trapped microsphere (if of higher refractive index than its surroundings and transparent to the incident light) acts as a microscopic lens that focuses the light field. This focusing effect in turn causes the particle to move to the position of the highest light intensity as may be seen in figure 1.2.

Figure 1.2 shows the visualisation of the optical forces in the Mie regime with a high numerical aperture (N.A) microscope objective [36]. Both lateral (figure 1.2 (a)) and axial trapping (figure 1.2 (b)) in the transverse plane **(x)** and axial direction **(z)** are considered. In this diagram, the gradients of light intensity in the lateral and axial direction are crucial to the operation of this technique. A Gaussian beam is being focused through a high numerical aperture (typical N.A. > 1) microscope objective and enters the microsphere from underneath to create the optical tweezers. In figure 1.2 (a), the refracted rays (solid lines arrows) from two input rays (**a1**, **a2**), enter a transparent sphere that is positioned off the centre of the focused Gaussian beam, with **a1** being the one of lower intensity. The dotted line indicates their unrefracted paths. Each ray produces a force **($\mathbf{F_{a1}}$ $\mathbf{F_{a2}}$)** upon the microsphere that draws it towards the direction of each ray. The net force ($\mathbf{F_{gradient}}$) from $\mathbf{F_{a1}}$ and $\mathbf{F_{a2}}$ would draw the microsphere towards the centre of the focus. On the other hand, each of the reflected light rays (**b1**, **b2**) would generate a force ($\mathbf{F_{b1}}$, $\mathbf{F_{b2}}$) upon the microsphere. The net force ($\mathbf{F_{scattering}}$) from $\mathbf{F_{b1}}$ and $\mathbf{F_{b2}}$ would push the particle away from the centre of the focus. The focused Gaussian beam will have a steep intensity gradient in the transverse (x) and axial (z) directions. Hence, the microsphere moves close to the focus of the beam (in x and z) due to the gradient force (steep intensity gradient). In figure1.2 (b), the microsphere is shown to be trapped stably at a position that is slightly above the upward propagating and focused Gaussian beam. At the trapping position, an equilibrium is established where the net forces $\mathbf{F_{gradient}}$ and $\mathbf{F_{scattering}}$ are balanced in both the transverse and axial plane (**x, z**). The typical NA needed to achieve enough intensity gradient in the transverse and axial plane is approximately more than or equivalent to 1. The forces (gravity) due to the mass of the microsphere are not discussed in the diagram.

In the Mie regime, the description of the optical forces can be understood in simpler terms i.e. any light reflected from the microsphere would result in a force opposing the direction of light propagation, and any refraction of the light from the microsphere would result in a force attracting the particle to the region of highest light intensity. However, such a rudimentary physical explanation cannot be use to explain optical forces exerted upon objects that are far smaller than

the wavelength: Rayleigh regime ($r \le \lambda / 20$). In the Rayleigh regime, it is more appropriate to consider the particle as a dipole. The dipole minimizes its energy in the field gradient (intensity gradient) created by the focused Gaussian beam [37]. Since the object is considered as a point dipole, the contributions of the time-averaged gradient force $F_{gradient}$ and scattering forces $F_{scattering}$ may be readily separated as follows:

$$F_{gradient} = \frac{2\pi\alpha}{cn_m^{\ 2}}\nabla I \tag{1.1}$$

$$F_{scattering} = \frac{I\sigma n_m}{c} \tag{1.2}$$

where α denotes the polarisability of the sphere which for a standard non-absorbing dielectric object is proportional to the volume of the particle is equal to $n_m^2 r^3 \left(m^2 - 1\right) / \left(m^2 + 2\right)$, σ is the scattering cross section of the sphere equal to $\left(128\pi^5 r^6 / 3\lambda^4\right)\left(\left(m^2 - 1\right) / \left(m^2 + 2\right)\right)^2$, r is the particle radius, I is the intensity, n_m is the refractive index of the surrounding medium, c denotes the speed of light, m refers to the ratio of the refractive indices (particle (n) to that of the surrounding medium (n_m)) and λ is the wavelength of the trapping laser used. As such, the scattering forces are directly proportional to the laser intensity and the gradient (or dipole) forces upon the object are due to the inhomogeneous field gradient created by focusing the Gaussian beam to its diffraction limited spot through a high N.A. (>1) objective lens [3, 24, 29]. In figure 1.3, I show a schematic to illustrate the intensity gradient ∇I (black arrows) of the focused Gaussian beam along the transverse plane (xy). A nanometre sized particle is shown to be drawn towards the highest intensity region of the beam, due to the transverse and axial gradient forces (blue arrow).

A full theoretical treatment of how an optical tweezers performs for a given object in a light field is a non-trivial question. In principle, the generalized Lorenz–Mie scattering theory (GLMT) can bridge the gap between the Rayleigh (dipole) and Mie regimes (ray optics). In other words, it can even be apply to cases where the particle size is equal to the wavelength of the trapping beam. GLMT describes the scattering of a plane wave by a sphere under a Gaussian beam illumination. The incident field is expanded in terms of constituent plane waves. This allows the apodization and aberration transformations (due to the high numerical aperture microscope objective) to be incorporated in the theoretical model so as to yield the resultant optical forces [38, 39]. The theory can be extended to particles of different geometrical shapes [40]. Barton and co-workers [41, 42] derived a fifth order correction to the focused Gaussian beam so as to compute the forces using a

Maxwell stress tensor approach. Rohrbach and Stelzer [43] extended the Rayleigh theory to make it valid for large particles by inclusion of second-order scattering terms (based on Mie scattering). The vast majority of optical trapping experiments are performed, where the particle diameter is comparable to the wavelength of the trapping laser beam. Rohrbach later [44] reported good quantitative agreement between the theoretical calculations and experimental measurements pertaining to the strength of the optical traps. His theoretical approach for trapping forces computed the Lorentz force density. He found that the optimal trapping performance is reached when the diameter of the particle d is comparable to the wavelength of light, λ (within the viscous medium of refractive index n_m), $d \approx \lambda / n_m$ [44]. Overall, it is important to note that the numerical and theoretical modelling of optical forces at these scales still presents many challenges. In this section, I have discussed the effects of optical forces in dielectric transparent microspheres and nanoparticles. Although the optical forces discussed in this section are based on an optical tweezers system, the forces still apply to other forms of optical traps. Next, I shall describe two other particles types that are often used in optical trapping, namely birefringent microparticles and gold nanoparticles.

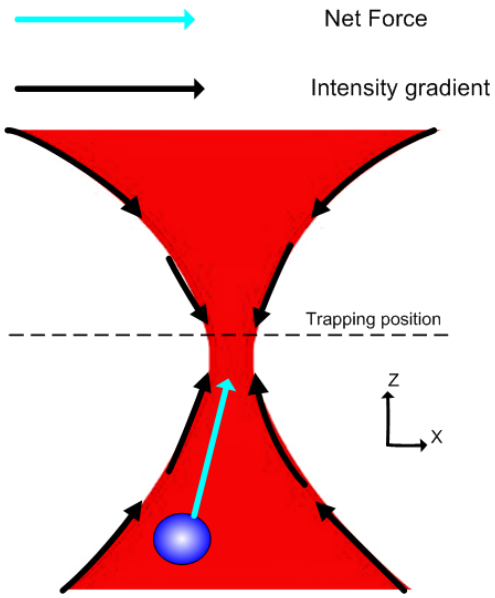

Figure 1.3: Intensity gradient for focused Gaussian beam. Black arrow points to the direction of the high intensity region in the beam in the transverse (x) and axial (z) plane. The blue arrow indicates the direction in which the Rayleigh particle is moving

1.3.2. Other types of particles

Transparent high refractive index dielectric spheres of diameter ≈ 0.2 - 10 μm (polymer or silica) are typically used in optical trapping. It is only possible to control the transverse and axial

position of a microsphere with an optical tweezers. Birefringent (based on shape or refractive index) particles can provide a way to control the optical torque within an optical trapping system, as first demonstrated by Friese *et al* [45]. In section 1.3.2.1, I will discuss the angular rotation due to double refractive indices in calcite microparticles. This applied optical angular torque has been used to study angular forces within macromolecules [46] and rotational microviscosity [47]. Svoboda and Block [3] first demonstrated the three dimensional optical trapping of gold nanoparticles (36 nm in diameter) with an optical tweezers system. They experimentally showed that the gold nanoparticles experience an enhanced trapping effect (stronger gradient forces) due to polarisability of gold (see section 1.3.2.2), as compared to the polymer sphere of the same size. This pioneering work spawns the possibility of using optical forces to manipulate nanoparticles. I will elaborate on the polarisability of the gold nanoparticles and the absorption of light that will led to possible residual heat.

1.3.2.1. Birefringent

Crystalline materials may have different indices of refraction that are associated with the different crystallographic directions. Calcite crystals have two distinct indices of refraction, and they are called birefringent particles. The two indices of refraction that characterise birefringent materials are: the ordinary (n_o) and the extraordinary (n_e). Calcite particles can be used as polarisation wave-plates due to their birefringent nature. On a micron scale, light passing through the calcite particle would undergo different phase shift due to the ordinary and extraordinary components. The phase shifts (depending on the input polarisation) would result in a change in the angular momentum carried by the light and a corresponding optical torque. The controlled optical rotation of a particle adds a new set of geometry for one to exert such angular torque [47, 48].

The total torque per unit area T from an incident elliptical polarised Gaussian beam on a birefringent particle trapped on the beam axis is given by [49]

$$T = -\frac{c\varepsilon}{2w} E_0^2 \sin(kd(n_0 - n_e)) \cos 2\phi \sin 2\theta + \frac{c\varepsilon}{2w} E_0^2 \left(1 - \cos(kd(n_0 - n_e))\right) \sin 2\phi \qquad (1.3)$$

where E_0 is the input electric field, c is the speed of light, k is the wave number, ε is the permittivity, ϕ is the degree of ellipticity of the input light (0, π/2, π/4), w is the angular frequency, θ is the angle between the fast axis of the waveplate producing the elliptically polarised light and the optic axis of the birefringent material, d is the thickness of the particle and n_0, n_e are

the extraordinary and ordinary refractive indices of the birefringent material. Rotational viscous drag force and/or the angular Brownian motion of a trapped birefringent microparticle have provided measurements of DNA (deoxyribonucleic acid) torsional elasticity as well as torque during DNA structural transitions [50]. In chapter 5 of the thesis, a trapped and rotated calcite particle is used as a micro-diffuser for studies in spatial coherence in a light field.

1.3.2.2. Metallic particles

Large metallic (gold) particles are like a micrometer sized mirror. By "pinning" the metallic microparticles [51, 52] with a optical trap upon a surface, it is possible to manipulate them in two dimensions. When the size of the metallic or gold particle is brought down to around 100 nm, the optical forces that act upon the particles radically change.

In principle, from equation 1.1, it is easy to infer that the gradient force in the Rayleigh regime is directly proportional to the polarisability (α) of an object. Gold nanoparticles possess a much larger polarisability than the dielectric particles of the same size (100 nm and below) [53]. The dielectric function of gold is a complex number ε_{gold} = -54 + i5.9 at λ=1.047um [3, 53] ($n = \sqrt{\varepsilon.\mu}, \varepsilon_r$ is the material's relative permittivity, μ is the relative permeability of the material at the optical frequency). At wavelengths further away from the resonance wavelength ($\lambda_{resonance}$≈0.5um), the scattering and absorption coefficient is greatly reduced while the polarisability may remain unchanged. The polarisability, α, in equation 1.1, given by the Claussius-Mossotti relation $\alpha_{gold} = \alpha' + i\alpha'' = V\left(\varepsilon_{gold} - \varepsilon_{water} / \varepsilon_{gold} + 2\varepsilon_{water}\right)$, where V is the volume of the particle and ε_{water} is the permittivity of water. The skin depth of gold is about 23 nm and for particles with radius smaller than the skin depth is considered uniformly polarised. Hence for particles with radius larger than the skin depth, the particle shape could influence the polarisability. From equation 1.1 and 1.2, it is likely that the strong reduction in the scattering forces and large enhancement of the polarisability of the gradient forces at such a size scale. This would therefore favour the stable trapping of gold nanoparticles in three dimensions. This effect is confirmed experimentally by Svoboda and Block [3] with an optical tweezers system. I shall experimentally evaluate this in chapter.6, section.6.3.

Recent studies [54] showed that it is important not to neglect the absorption at wavelength away from resonance i.e. λ=1070nm. The focused light field (high power density mW/μm^2) [54] can induce a relatively large thermal heating effect [54]. Seol *et al* [54] formalised the increase in

temperature (ΔT) of a gold nanoparticle based on its absorbed optical power as follows, $\Delta T(r) = P_{abs} / 4\pi rC$ where P_{abs} is the absorbed power, r is the radius of the sphere and C is the conductivity of the medium. With this formula, they calculated a 266 ^{o}C/W based on a 50nm (radius) gold nanoparticle with an illuminating near infrared beam (wavelength of 1064nm, beam waist of 427nm). A more recent work [7] also confirms this heating effect (linear temperature increase) from a single gold nanoparticles illuminated with a focused 1064nm laser. The heat measurement scheme makes use of lipid bilayers, which has a specific melting point at (33^{o}C). The dramatic increase in the temperature of an optically trapped metallic nanoparticle can be used for selective cell hyperthermia in an optical tweezers system, describe in detail in Chapter.7, section 7.4.

1.4. Langevin equation of motion: Harmonic oscillator

Converting an optical trap into a highly accurate force measurement system requires an understanding of the underlying physical principles of the relations between particle dynamics and Brownian motion. The crucial tenet is that the optically trapped particle may be modelled as a nearly ideal overdamped harmonic oscillator.

From the fluctuation-dissipation (Langevin) theorem, the equilibrium of a particle is brought about by a dissipation force ("friction") between the particle and the reservoir [55]. The dissipation process produces random, fluctuating forces on the particle. The processes are uniquely determined by the statistical nature of the microscopic forces (by "statistical nature", I mean that it refers to the application of probability distribution i.e. Boltzmann statistics). In essence with the Langevin theorem, it can derived the nature of the particle interactions using Newton's second law of momentum ($Force = m\left(\partial^2 x / \partial t^2\right)$), where m is mass, x is distance in one direction and t is time). If I consider an environment where a large particle is consistently "pushed around" by a sea of smaller particles, the total force imposed on the large particle (in one dimension) is given as in equation 1.4,

$$m\frac{\partial^2 x}{\partial t^2} = F_f(t) - \gamma\,\frac{\partial x}{\partial t} \tag{1.4}$$

where $F_f(t)$ is the sum of fluctuating microscopic forces (thermal) and $\gamma\left(\partial x / \partial t\right)$ is the viscous drag force imposed upon the particle suspended in water that is dissipative (γ is the drag

coefficient). Now if another force, F_{trap} , that acts to restrict the particle's path of motion is included into equation 1.4, I can obtain equation 1.5.

$$m\frac{\partial^2 x}{\partial t^2} = F_f(t) - \gamma\frac{\partial x}{\partial t} - F_{trap}$$
$$m\frac{\partial^2 x}{\partial t^2} + \gamma\frac{\partial x}{\partial t} + F_{trap} = F_f(t) \qquad (1.5)$$

Equation 1.5 is a modified Langevin equation for an optical trap along one dimension. In particular, the particle resides in a parabolic potential energy well that is created by the optical trap. When the particle is at equilibrium, it tends to rest at the centre of the potential well where the energy is at minimum. Once the particle is perturbed from the centre of the optical potential well, it will experience a restoring force ($F_{trap} = kx$) that is linearly (to a certain degree) proportional to the distance away from centre of the optical potential well (the equilibrium position). This linear restoring force is akin to a miniscule spring that obeys Hooke's law: this perhaps innocuous statement embodies some of the most powerful principles of optical trapping as illustrated in figure 1.4.

In the left-hand side of equation 1.5, the first term represents the inertial force component for a particle mass m, the second term is the velocity dependent viscous damping force, where γ is the drag coefficient, and the final term is the optical restoring force for the trap stiffness, *k*. The right hand side of the equation represents the fluctuating force, $F_f(t)$, due to the Brownian motion. This fluctuation force can be measured by the distribution of the particle position within the optical trap as described in chapter.3. Under typical trapping conditions (which is a low Reynolds number regime [56]), the viscous damping forces dominate and the inertial effects (i.e. $m\left(\partial^2 x/\partial t^2\right)$ in equation 1.5) may be neglected.

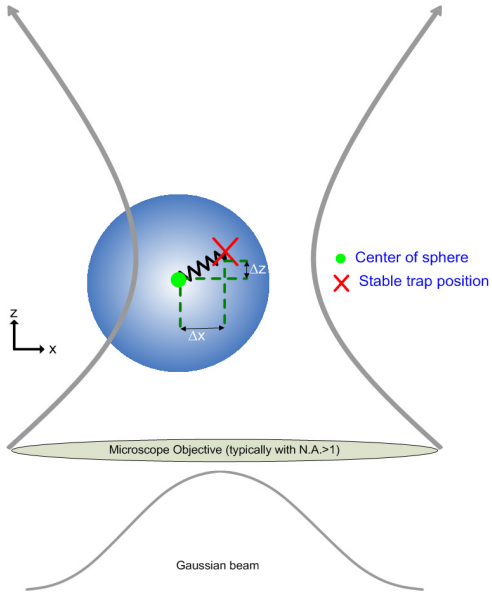

Figure 1.4: Stiffness of an optical tweezers. A basic diagram that illustrates a particle being perturbed (i.e. Brownian motion) where the restoring forces are proportional to the displacements (Δx & Δz) of the particle from the stable trapping position.

As illustrated in figure 1.4, the particle that is residing within an optical tweezers system essentially behaves like a spring drawn towards a fixed point (in each of the dimension). An optical trapped particle can obey the classical Hooke's law, where the force on the object is proportional to the displacement along one of the directions. Here, in figure 1.4, I illustrate two directions in which the particle is displaced Δx and Δz. The proportionality of the distance x, z from the centre of the trap proportional to force will be denoted as the trap stiffness, k_x *and* k_z. The particle positions over a given period of time in each direction may be recorded as a histogram. The position histogram can be used to define the shape of the potential energy well of an optical trap (Boltzmann distribution, section 3.73). The optical potential energy is only harmonic over the size range that is a fraction of the trapping wavelength [57, 58].

1.5. Overview of optical trapping and its applications

1.5.1. Biophysical and colloidal sciences

The quantification of the position and force for each optical trapped particle offers a direct measurement of translation motion and mechanical forces in biological or colloidal systems. Typically, optically transparent dielectric spheres (usually of size 0.5 - 3 μm in diameter) are used for optical trapping. Microspheres that have a high degree of optical transparency and low

absorption, with respect to the trapping laser, will not result in a significant change of the local temperature during an experiment.

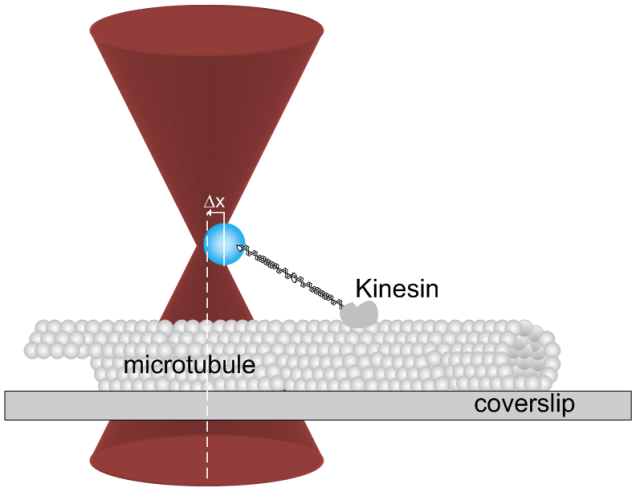

Figure 1.5 Operation of a surface based assay optical force measurement system. The diagram illustrates an optical force clamp recording displacements of single kinesin molecules while maintaining an average load [59].

Optical tweezers usually operate upon macromolecules (kinesin or deoxyribonucleic acid) in an indirect fashion; via dielectric handlers (i.e. microspheres). By labelling macromolecules with biotin and mixing them with polystyrene microspheres (coated with streptavidin that binds to biotin with high affinity [60]), one can obtain for example "molecular handles" with tethered microspheres. These spheres form the physical "handles" that is required to indirectly manipulate the molecular strands.

One of the first landmark biophysics experiments that made use of the optical tweezers is for single molecule studies. Researchers measured the individual steps taken by kinesin, a molecular porter. During its motion along a fixed microtubule track created upon a microscope slide, the kinesin molecule moves along in a "jerky" stride [61] with alternating step sizes. A microsphere was bound with appropriate surface chemistry to a single kinesin molecule, as described earlier, and then held close to its microtubule track [59] with an optical tweezers as shown in figure1.5. A buffered salt solution containing the chemical fuel adenosine triphosphate (ATP) constituted as the sample medium. The use of a single optical tweezers and a quadrant photodiode (QPD) permitted the detailed observations of the kinesin motor and microtubule track interaction. The trapped sphere was pulled along by the kinesin and the experiment was able to reveal approximately 8 nm steps taken by the kinesin molecule. The behaviour of the kinesin molecule was attributed to it pausing at a random interval, after taking each step as it waited for a

fresh ATP molecule to arrive. Another biophysics application is the use of a dual optical tweezers system [62] to study the actin-myosin system, which is the molecular motor associated with muscle action. This interaction was studied by Finer *et al.* [63] who used the dual optical tweezers system [62] to hold the two proteins, actin and myosin, in close proximity and directly recorded several interactions of a myosin molecule and an actin filament. This dual optical tweezers system [62] uses two Gaussian beams focused through a single microscope objective. This trapping system is different from the dual counter-propagating beam trapping geometry, as first proposed by Ashkin [1, 25], as it forms two optical traps instead of one. The studies on motor proteins are likely to be paradigms for future single molecule mechanical studies using optical tweezers system [20, 64].

DNA has also been studied extensively with optical tweezers. Knowledge of the mechanical properties of DNA gives us an understanding over its polymer mechanics [65]. One instance is the study of the DNA bend-persistence length (about 50 nm). It has been observed that if two pieces of the sequence are 20 nm apart then the intervening length of DNA is relatively stiff, but if they are 500 nm apart, then the linking region will be flexible enough to allow the two regions to come together. Later, researchers [66, 67] applied very large forces (>60 pN) to DNA and found that it suddenly overstretches and breaks the double-helical B-form to give a parallel ladder. Optical tweezers have produced some seminal studies within single molecule biophysics and allowed an insight into this field in a manner hitherto unforeseen [68].

Ashkin's early work dealt with the possibility of using optical tweezers to move and manipulate biological cells and its internal organelles [13]. The trapped microsphere can also be used to tether onto cell membranes, for example blood cells [69], which allows the measurements of its mechanical structures using a dual optical tweezers system. Guck *et al.* [70, 71] showed that the forces from two diverging beams (output from two optical fiber ends – fiber optics version of the first optical trap by Ashkin [1]) can steadily measure the mechanical deformation on red blood cells without the need for tethering. In this way, the elastic and viscoelastic properties of red blood cells (RBCs) are observed to change in correlations with the cell's structural and molecular alternation. These alterations can be due to the onset and progression of a disease (i.e. cancer) within the cell. Hence, the cell deformation in the presence of the exerted force can be used to calculate the mechanical properties (shear modulus).

More recently, Kress *et al.* [22, 72] were able to measure direct binding of beads to cell membranes of living cells during the process of phagocytosis. Kress and co workers were able to measure, with a calibrated optically trapped latex bead, the F-actin-dependent stepwise retraction of

filopodia. The filopodia acts as cellular tentacles, which pulls particles into the cells during cell ingestion as shown in figure1.6. The measured refraction forces can be as high as 19 pN and at a mean step size of 36 nm.

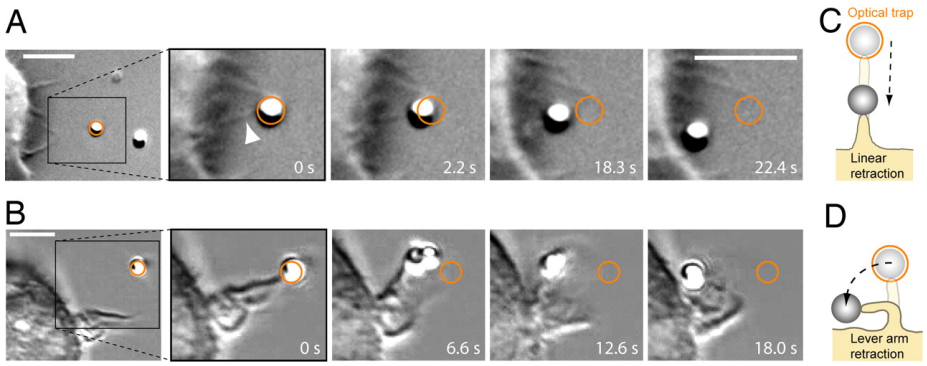

Figure 1.6. Filopodial and ruffle retraction preceding phagocytosis. (*A*) An IgG-coated bead in the optical trap (orange circle) is moved toward a filopodium of a J774 macrophage. Upon binding, the filopodium (arrowhead) retracts and pulls the bead toward the cell to initiate phagocytic uptake. (*B*) Two trapped beads are moved toward a membrane ruffle. Upon binding (second picture), the ruffle retracts in a lever arm manner and pulls the beads toward the cell. (*C* and *D*) Sketch of the linear and the lever arm retraction respectively (Scale bars: 5 μm.) [22].

On an additional note, optical scissors (pulse laser beams) can be used together with optical tweezers. Liang *et al* [73] used optical tweezers in combination with pulsed laser cutting (laser scissors) to manipulate and explore the behaviour of chromosomes during cell division in view of studying the complexities of mitosis. Seeger *et al.* [74] used the same type of technique for isolation of a microdissected gene. An excellent and thorough review of optical microbeams (laser scissors) may be found in the articles by Berns [75].

A calibrated optical tweezers system can have applications in areas of colloidal sciences, especially in the measurements of weak interaction forces between small particles suspended in a viscous medium. Meiners and Quake [76] made use of a dual beam tweezers system [62] and measured the hydrodynamic interaction between two trapped spheres. They recorded the position fluctuations of each bead and determined both the correlation and anti-correlation functions. They showed that these trapped spheres exhibit a pronounced, time-delayed dip in the cross-correlation. This time delay is linked to the relaxation time of the harmonic potential energy well created by the optical tweezers. A more detailed study by the authors showed that the anti-correlations can be well understood by using the Langevin equation of motion and a standard Oseen tensor hydrodynamic coupling [76]. A more recent paper by Brau *et al* [77] summarises the range of microrheology applications that optical tweezers can be employed in. The non-invasive nature of optical tweezers lends itself very well in exploring the local viscoelastic properties of solutions. The optical tweezers

may act in either an active or passive mode for microrheology applications. In the passive mode, one simply monitors the position of the particle and relates these observations with the predictions of the Stokes-Einstein equations. A more active role is that the trapped particle may be dragged through the sample, thus mechanically deforming the medium under study.

The applications of the optical tweezers primarily rely on the ability to accurately calibrate the optical tweezers. In the next section1.5.2, I provide an overview of the calibration of the optical tweezers using optical interferometric techniques. In addition, I will address the steps to achieve a calibrated optical tweezers in chapter.3.

1.5.2. Optical interferometric metrology and nanophotonics

Apart from biological and colloidal science, photonics applications also form a strong basis for the drive in the progress of optical trapping. In this section, I will provide an outline for the association of the two photonics applications, optical interferometric metrology and nanophotonics, with optical trapping. This section serves as an introductory overview of the work that will be carried out in rest of the thesis (Chapter.3-8).

Optical interferometry is widely accepted as a suitable metrology method for accomplishing precise measurement of position fluctuations and wavefront distortions [78]. Interferometric measurement schemes have been used in a number of ways for the calibration of an optical trap for precision position and forces measurements [79-85]. Particle position measurement with optical interferometry has emerged as one of the most sensitive and rapid approaches [29]. Webb and co-workers [83, 86-89] was the first to introduce the optical differential interferometer. They were able to measure small displacements and forces of optically trapped particle along a single dimension. This technique is extremely sensitive (accuracy of 10^{-12} m) [83]. It requires an extensive optical setup and additional polarisation optics and so reduces the flexibility of adaptation to commercially available microscope platforms. Few have successfully adopted this approach for high resolution position and force measurements of biological system [61, 84].

Gittes and Schmidt [80, 90] later proposed the back focal plane (BFP) interference technique for high resolution position mapping of the particle. The technique takes advantage of the first order far-field interference between the scattered and the non-scattered components of the light being diffracted from a trapped microsphere. The BFP technique is now a main stay in high resolution force spectroscopy and is used in a number of biophysical experiments as described in section 1.5.1 [29, 91]. The BFP interference combined with a quadrant photodiode (QPD) detection

scheme is widely used to calibrate the particle positions within the optical trap [92]. The variations in the particle positions over time are captured by a QPD. This data is then used to deduce the spring constant of the optical trap. In chapter 3, I will describe the implementation of the BFP interferometry with a QPD to carry out calibrated measurements in an optical tweezers system. To date, there have been a wide number of applications using the non-zero order laser beam mode LG beams [93-98] but none has calibrated a LG trapping beam using with BFP interferometry. In chapter 4, I introduce the use of BFP interference with QPD detection to calibrate an optical tweezers formed with a focused non-zero order laser beam mode (Laguerre-Gaussian).

In optical wavefront metrology, the use of multiple apertures, e.g. Young's slits interferometry or Shack-Hartmann wavefront sensor, are well-known techniques for measuring the wavefront of a light field. Traditionally, the Young's slits or Shack-Hartmann techniques comprises of pinholes or array of microlens of a given geometrical arrangements. With current microlithography techniques, the size of the slits or array of microlens often relies on good fabrication technique. In addition, the arrangements of the microlens and slits are fixed and cannot be changed at will.

Microspheres (polystyrene and silica) are widely available from a large number of companies and they come in a range of size selection (typically from 20nm to 20μm). In BFP interferometry, a microsphere is considered to be a diffracting aperture. Hence, microspheres could serve as the ideal pinholes (soft Gaussian type aperture). The interference pattern of the light diffracted from two microspheres forms a microscopic Young's slit type interferometry. This form of micro-interferometry can then be used to probe the properties (phase and coherence) of a sample light field. Using optical traps, the microsphere can be optically organized into different arrangements at will. In chapter 5 of this thesis, I initiate two sets of experiments that make use of optically trapped microparticles as diffracting apertures for phase and spatial coherence measurements. The first set of experiments employ the sampling beam (LG beam) itself to trap the microspheres. Two or more optically trapped spheres are used to controllably map out the wavefront of the LG beam in an in-situ manner. The second experiment uses two independent optical traps (dual beam optical traps) to manipulate microparticles for studies of spatial coherence on a separate sampling light field (LG beam). The independent optical traps offer more controllability over the position in which the microparticles can reside within the separate sampling field.

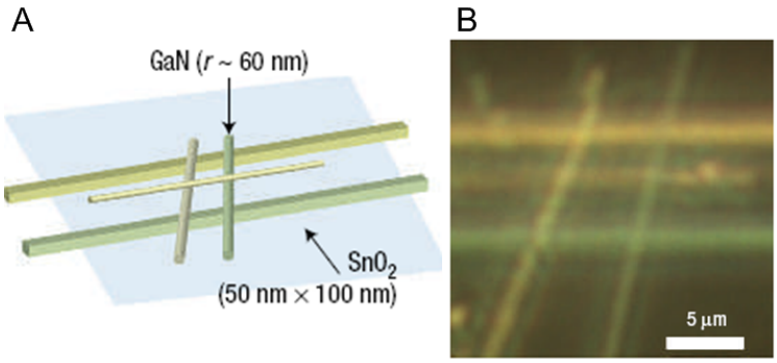

Figure 1.7 Demonstration of nanowire junctions and assemblies built using optical trapping. Schematic (A) and optical darkfield microscopic image (B) of a three-dimensional nanowire assembly consisting of tin oxide (SnO_2) nanoribbons and gallium nitride (GaN) nanowires [5].

Full three dimensional positional controls over a nanoparticle would naturally be beneficial in the construction of nanostructures as seen in figure 1.7 A and B. A number of groups [4-6, 99-102] have recently been using the optical trapping technique for direct manipulation of semiconductor nanostructures. In chapter 6, I shall discuss on the trapping of dielectric enhanced semiconductors nanosheets and nanotubes. Using optical traps, it is possible to perform direct trapping and patterning of semiconductor nanoparticles on a given substrate.

Nanoparticles do offer new phenomena to explore such as localised heating source. Controlled in vitro cell hyperthermia using heated nanoparticles has numerous therapeutic purposes especially in the controlled destruction of cancerous cells. Metallic nanoparticle, with relatively high absorption co-efficient at a given optical wavelength, can create highly localised thermal bath [103]. However, the current techniques rely on ingested (phagocytosis or endoscytosis) nanoparticles within a cell. These methods lack controllability. Since there is no control over the position of the nanoparticles, it will not be possible to study the quantitative effects of a biological cell when exposed to just one single metallic nanoparticle. A single optically trapped metallic gold nanoparticles can be used as a localised heating source [7]. This effect has been exploited to achieve nanoscale cell hyperthermia [8]. In chapter, 7, I make use of the optical tweezers technique to directly quantify the biological cell morphology during and after exposure to a single heated gold nanoparticle. The changes of the biological cell are monitored with time lapse confocal laser scanning fluorescence imaging.

The study of the interaction between light and an ensemble of nanoparticles can prove to be an important platform for nanophotonics i.e. building nanostructures from an ensemble of nanoparticles. The optical interactions of an ensemble of optically trapped dielectric nanoparticles

(nanosuspension) with a continuous-wave (cw) laser beam have been first characterised as a form of nonlinear response, by Ashkin and co-workers [9-12]. They demonstrated nonlinear effects (self-focusing, photorefractivity and filamentation) using aqueous suspensions of nanoparticles. Each dielectric nanoparticle possesses a discrete refractive index. With an increasing number of the nanoparticles entering into the optical field due to optical gradient force, the local particle density will increase and subsequently change the local refractive-index along the beam propagation axis. The formation of the chain of nanoparticles can act as a self-assembling waveguide. The localized refractive index change due to the gathering nanoparticles is dependent on the intensity of light. Such a refractive index change can then be characterized as a nonlinear response: photorefractivity. In chapter 8, I explore the nonlinear optical response using an aqueous suspension of nanoparticles. The experiment results (with a novel fiber based Z-scan variant setup) in chapter 8 are aim to reveal the exact nature of the nonlinearity of a nanosuspension and to match the theoretical predictions made with the non-ideal gas model.

1.6. Conclusion

In this chapter, I have first introduced the development of optical trapping by Ashkin [1, 2] on the counter propagating dual beam optical trap and the single beam optical tweezers. In the second section, I have discussed the effects of optical forces in transparent microspheres and nanoparticles. Although the optical forces discussed in this section are based on an optical tweezers system, the forces still apply to other forms of optical traps. A simple way to classify the two types of force regime is by comparing the particles sizes (diameter, d) with respect to the wavelength (λ) of the trapping beam. In the Mie regime ($d>>\lambda$), one can consider the scattering and gradient forces as arising from the reflection and refraction of light entering and exiting the microparticle over a given time. In the Rayleigh regime ($d<<\lambda$), it is more appropriate to consider the particle as a dipole that minimizes its energy in the field gradient created by the light [37, 104]. Since the object is considered as a point dipole, the contributions of the time-averaged gradient force and scattering forces may be readily separated. This fundamental optical force concept is important for the experiments carried out in this thesis namely microparticles (chapter 2-5) and nanoparticles (chapter 6-8). I also elucidate the mechanisms behind the rotational torque of micron-sized calcite crystals (chapter 5) and trapping of metallic nanoparticle (chapter 6, 7).

In the third section, I moved onto describing the modelling of an optically trapped particle as a harmonic oscillator (mechanical spring). The model uses the Langevin equation of motion to

describe the trapped particle. The linear restoring force (spring constant multiple by displacement) is crucial for using an optical trap as an effective force transducer. The calibration of particle displacement and measurement of the spring constant using an optical tweezers system will be described in chapter 3

In the final section, I briefly discussed the applications associated with optical trapping. Firstly, I mentioned the biophysical and colloidal applications that use a calibrated optical tweezers. Using microspheres as handles or probe, optical tweezers have ventured into pioneering studies of kinesin stepping, elasticity of DNA molecules and cellular mechanics (phagocytosis). A calibrated optical tweezers can also be used in the measurements of weak interaction forces (i.e. hydrodynamics) between small particles or surfaces in a viscous aqueous medium. Secondly, I outlined the experiments in the remainder of the thesis (chapter 3-8) and its relations with the field of optical interferometric metrology and nanophotonics. The first set of experiments is associated with optical interferometric metrology. The optical interferometric patterns are from the diffracting light field of optically trapped microparticles. They are then used for the calibration of particle positions in an optical trapping system (chapter 3, 4), measuring the optical spring constant of an optical tweezers (chapter 3, 4) and the phase or coherence of a sample light field (chapter 5). The second set of experiments relates to nanophotonics. They include the trapping characteristics of dielectric enhanced semiconductor nanoparticles (chapter 6), heating of optically trapped gold nanoparticles for cell hyperthermia (chapter 7) and nonlinear optical interactions between an ensemble of optically trapped nanoparticles and a Gaussian optical trap (chapter 8).

References

1. A. Ashkin, "Acceleration and trapping of particles by radiation pressure," Physical Review Letters **24**, 156-159 (1970).
2. A. Ashkin, J. M. Dziedzic, J. E. Bjorkholm, and S. Chu, "Observation of a single-beam gradient force optical trap for dielectric particles," Optics Letters **11**, 288-290 (1986).
3. K. Svoboda, and S. M. Block, "Optical Trapping of Metallic Rayleigh Particles," Optics Letters **19**, 930-932 (1994).
4. R. Agarwal, K. Ladavac, Y. Roichman, G. Yu, C. Lieber, and D. Grier, "Manipulation and assembly of nanowires with holographic optical traps," Opt. Express **13**, 8906-8912 (2005).
5. P. J. Pauzauskie, A. Radenovic, E. Trepagnier, H. Shroff, P. Yang, and J. Liphardt, "Optical trapping and integration of semiconductor nanowire assemblies in water," Nat Mater **5**, 97-101 (2006).
6. A. van der Horst, A. I. Campbell, L. K. van Vugt, D. A. Vanmaekelbergh, M. Dogterom, and A. van Blaaderen, "Manipulating metal-oxide nanowires using counter-propagating optical line tweezers," Opt. Express **15**, 11629-11639 (2007).
7. P. M. Bendix, and L. B. Oddershede, "Direct measurement of heating by optically trapped gold nanoparticles using molecular sorting in lipid bilayers," Submitted (2009).
8. G. S. Terentyuk, G. N. Maslyakova, L. V. Suleymanova, N. G. Khlebtsov, B. N. Khlebtsov, G. G. Akchurin, I. L. Maksimova, and V. V. Tuchin, "Laser-induced tissue hyperthermia mediated by gold nanoparticles: toward cancer phototherapy," Journal of Biomedical Optics **14**, 021016-021019 (2009).

9. A. Ashkin, J. M. Dziedzic, and P. W. Smith, "Continuous-wave self-focusing and self-trapping of light in artificial Kerr media," Opt. Lett **7**, 276-278 (1982).
10. P. W. Smith, P. J. Maloney, and A. Ashkin, "Use Of A Liquid Suspension Of Dielectric Spheres As An Artificial Kerr Medium," Optics Letters **7**, 347-349 (1982).
11. P. W. Smith, A. Ashkin, and W. J. Tomlinson, "4-Wave Mixing In An Artificial Kerr Medium," Optics Letters **6**, 284-286 (1981).
12. J. E. Bjorkholm, and A. A. Ashkin, "cw Self-Focusing and Self-Trapping of Light in Sodium Vapor," Physical Review Letters **32**, 129 (1974).
13. A. Ashkin, "Optical trapping and manipulation of neutral particles using lasers," Proceedings of the National Academy of Sciences of the United States of America **94**, 4853 - 4860 (1997).
14. S. Chu, "The manipulation of neutral particles," Reviews of Modern Physics **70**, 685-706 (1998).
15. C. N. Cohen-Tannoudji, "Manipulating atoms with photons," Reviews of Modern Physics **70**, 707-719 (1998).
16. W. D. Phillips, "Laser cooling and trapping of neutral atoms," Reviews of Modern Physics **70**, 721-741 (1998).
17. M. R. Andrews, C. G. Townsend, H. J. Miesner, D. S. Durfee, D. M. Kurn, and W. Ketterle, "Observation of interference between two Bose condensates," Science **275**, 637-641 (1997).
18. K. B. Davis, M. O. Mewes, M. R. Andrews, N. J. Vandruten, D. S. Durfee, D. M. Kurn, and W. Ketterle, "Bose-Einstein condensation in a gas of sodium atoms," Physical Review Letters **75**, 3969-3973 (1995).
19. K. M. O'Hara, M. E. Gehm, S. R. Granada, S. Bali, and J. E. Thomas, "Stable, strongly attractive, two-state mixture of lithium fermions in an optical trap," Physical Review Letters **85**, 2092-2095 (2000).
20. W. J. Greenleaf, M. T. Woodside, and S. M. Block, "High-resolution, single-molecule measurements of biomolecular motion," Annual Review of Biophysics and Biomolecular Structure **36**, 171-190 (2007).
21. H. Kress, E. H. K. Stelzer, G. Griffiths, and A. Rohrbach, "Control of relative radiation pressure in optical traps: Application to phagocytic membrane binding studies," Physical Review E **71** (2005).
22. H. Kress, E. H. K. Stelzer, D. Holzer, F. Buss, G. Griffiths, and A. Rohrbach, "Filopodia act as phagocytic tentacles and pull with discrete steps and a load-dependent velocity," Proceedings of the National Academy of Sciences **104**, 11633-11638 (2007).
23. J. Luo, L.-C. Tu, Z.-K. Hu, and E.-J. Luan, "New Experimental Limit on the Photon Rest Mass with a Rotating Torsion Balance," Physical Review Letters **90**, 081801 (2003).
24. A. Ashkin, "History of optical trapping and manipulation of small-neutral particle, atoms, and molecules," IEEE Journal of Selected Topics in Quantum Electronics **6**, 841-856 (2000).
25. A. Constable, J. Kim, J. Mervis, F. Zarinetchi, and M. Prentiss, "Demonstration Of A Fiberoptic Light-Force Trap," Optics Letters **18**, 1867-1869 (1993).
26. A. Ashkin, and J. M. Dziedzic, "Stability of optical levitation by radiation pressure," Applied Physics Letters **24**, 586-588 (1974).
27. J. E. Molloy, and M. J. Padgett, "Lights, action: optical tweezers," Contemporary Physics **43**, 241-258 (2002).
28. D. G. Grier, "A revolution in optical manipulation," Nature **424**, 810-816 (2003).
29. K. C. Neuman, and S. M. Block, "Optical trapping," Review of Scientific Instruments **75**, 2787-2809 (2004).
30. K. Dholakia, and P. Reece, "Optical micromanipulation takes hold," Nano Today **1**, 18-27 (2006).
31. D. McGloin, D. R. Burnham, M. D. Summers, D. Rudd, N. Dewar, and S. Anand, "Optical manipulation of airborne particles: techniques and applications," Faraday Discussions **137**, 335-350 (2008).
32. Dholakia. K, Reece. P, Gu. M,, "Optical micromanipulation," Chem. Soc. Rev **37**, 42 - 55 (2008).
33. K. Dholakia, and W. M. Lee, "Optical Trapping Takes Shape: The Use of Structured Light Fields," in *Advances in Atomic, Molecular and Optical Physics*(2008), pp. 261-337.
34. M. Grandbois, M. Beyer, M. Rief, H. Clausen-Schaumann, and H. E. Gaub, "How strong is a covalent bond?," Science **283**, 1727-1730 (1999).
35. K. C. Neuman, and A. Nagy, "Single-molecule force spectroscopy: optical tweezers, magnetic tweezers and atomic force microscopy," Nature Methods **5**, 491-505 (2008).

36. A. Ashkin, "Forces of a single-beam gradient laser trap on a dielectric sphere in the ray optics regime," Biophysical Journal **61**, 569-582 (1992).
37. Y. Harada, and T. Asakura, "Radiation forces on a dielectric sphere in the Rayleigh scattering regime," Optics Communications **124**, 529-541 (1996).
38. J. A. Lock, "Calculation of the Radiation Trapping Force for Laser Tweezers by Use of Generalized Lorenz-Mie Theory. I. Localized Model Description of an On-Axis Tightly Focused Laser Beam with Spherical Aberration," Appl. Opt. **43**, 2532-2544 (2004).
39. J. A. Lock, "Calculation of the Radiation Trapping Force for Laser Tweezers by Use of Generalized Lorenz-Mie Theory. II. On-Axis Trapping Force," Appl. Opt. **43**, 2545-2554 (2004).
40. A. A. R. Neves, A. Fontes, L. d. Y. Pozzo, A. A. de Thomaz, E. Chillce, E. Rodriguez, L. C. Barbosa, and C. L. Cesar, "Electromagnetic forces for an arbitrary optical trapping of a spherical dielectric," Opt. Express **14**, 13101-13106 (2006).
41. J. P. Barton, and D. R. Alexander, "Fifth-order corrected electromagnetic field components for a fundamental Gaussian beam," Journal of Applied Physics **66**, 2800-2802 (1989).
42. J. P. Barton, D. R. Alexander, and S. A. Schaub, "Theoretical Determination of Net-Radiation Force and Torque for a Spherical-Particle Illuminated by a Focused Laser-Beam," Journal of Applied Physics **66**, 4594-4602 (1989).
43. A. Rohrbach, and E. H. K. Stelzer, "Trapping forces, force constants, and potential depths for dielectric spheres in the presence of spherical aberrations," Applied Optics **41**, 2494-2507 (2002).
44. A. Rohrbach, "Stiffness of optical traps: Quantitative agreement between experiment and electromagnetic theory," Physical Review Letters **95**, 168102 (2005).
45. M. E. J. Friese, T. A. Nieminen, N. R. Heckenberg, and H. Rubinsztein-Dunlop, "Optical alignment and spinning of laser-trapped microscopic particles (vol 394, pg 348, 1998)," Nature **395**, 621-621 (1998).
46. C. Deufel, S. Forth, C. R. Simmons, S. Dejgosha, and M. D. Wang, "Nanofabricated quartz cylinders for angular trapping: DNA supercoiling torque detection," Nature Methods **4**, 223-225 (2007).
47. S. J. Parkin, G. Knoner, T. A. Nieminen, N. R. Heckenberg, and H. Rubinsztein-Dunlop, "Picoliter viscometry using optically rotated particles," Physical Review E **76** (2007).
48. M. E. J. Friese, T. A. Nieminen, N. R. Heckenberg, and H. Rubinsztein-Dunlop, "Optical alignment and spinning of laser-trapped microscopic particles," Nature **394**, 348-350 (1998).
49. H. Rubinsztein-Dunlop, T. A. Nieminen, M. E. J. Friese, and N. R. Heckenberg, "Optical trapping of absorbing particles," in *Advances in Quantum Chemistry, Vol 30*(1998), pp. 469-492.
50. C. Deufel, S. Forth, C. R. Simmons, S. Dejgosha, and M. D. Wang, "Nanofabricated quartz cylinders for angular trapping: DNA supercoiling torque detection," Nat Meth **4**, 223-225 (2007).
51. M. Gu, and D. Morrish, "Three-dimensional trapping of Mie metallic particles by the use of obstructed laser beams," Journal of Applied Physics **91**, 1606-1612 (2002).
52. H. Furukawa, and I. Yamaguchi, "Optical trapping of metallic particles by a fixed Gaussian beam," Optics Letters **23**, 216-218 (1998).
53. P. M. Hansen, V. K. Bhatia, N. Harrit, and L. Oddershede, "Expanding the optical trapping range of gold nanoparticles," Nano Letters **5**, 1937-1942 (2005).
54. Y. Seol, A. E. Carpenter, and T. T. Perkins, "Gold nanoparticles: enhanced optical trapping and sensitivity coupled with significant heating," Opt. Lett. **31**, 2429-2431 (2006).
55. P. Espanol, and P. Warren, "Statistical-mechanics of dissipative particle dynamics," Europhysics Letters **30**, 191-196 (1995).
56. T. M. Squires, and S. R. Quake, "Microfluidics: Fluid physics at the nanoliter scale," Reviews of Modern Physics **77**, 977-1026 (2005).
57. K. Berg-Sorensen, and H. Flyvbjerg, "Power spectrum analysis for optical tweezers," Review of Scientific Instruments **75**, 594-612 (2004).
58. K. Svoboda, and S. M. Block, "Biological Applications of Optical Forces," Annual Review of Biophysics and Biomolecular Structure **23**, 247-285 (1994).
59. K. Visscher, M. J. Schnitzer, and S. M. Block, "Single kinesin molecules studied with a molecular force clamp," Nature **400**, 184-189 (1999).
60. D. C. Appleyard, K. Y. Vandermeulen, H. Lee, and M. J. Lang, "Optical trapping for undergraduates," American Journal of Physics **75**, 5-14 (2007).

61. S. M. Block, L. S. B. Goldstein, and B. J. Schnapp, "Bead Movement by Single Kinesin Molecules Studied with Optical Tweezers," Nature **348**, 348-352 (1990).
62. E. Fallman, and O. Axner, "Design for fully steerable dual-trap optical tweezers," Applied Optics **36**, 2107-2113 (1997).
63. J. T. Finer, A. D. Mehta, and J. A. Spudich, "Characterization of Single Actin-Myosin Interactions," Biophysical Journal **68**, S291-S297 (1995).
64. A. D. Mehta, M. Rief, J. A. Spudich, D. A. Smith, and R. M. Simmons, "Single-molecule biomechanics with optical methods," Science **283**, 1689-1695 (1999).
65. T. T. Perkins, S. R. Quake, D. E. Smith, and S. Chu, "Relaxation of a Single DNA Molecule Observed by Optical Microscopy," Science **264**, 822-826 (1994).
66. S. B. Smith, Y. J. Cui, and C. Bustamante, "Optical-trap force transducer that operates by direct measurement of light momentum," in *Biophotonics, Pt B*(2003), pp. 134-162
67. C. Bustamante, Z. Bryant, and S. B. Smith, "Ten years of tension: single-molecule DNA mechanics," Nature **421**, 423-427 (2003).
68. S. M. Block, M. H. Larson, W. J. Greenleaf, K. M. Herbert, N. R. Guydosh, and P. C. Anthony, "Molecule by molecule, the physics and chemistry of life: SMB 2007," Nat Chem Biol **3**, 193-197 (2007).
69. M. Dao, C. T. Lim, and S. Suresh, "Mechanics of the human red blood cell deformed by optical tweezers," Journal of the Mechanics and Physics of Solids **53**, 493-494 (2005).
70. J. Guck, R. Ananthakrishnan, C. C. Cunningham, and J. Kas, "Stretching biological cells with light," Journal of Physics-Condensed Matter **14**, 4843-4856 (2002).
71. J. Guck, R. Ananthakrishnan, H. Mahmood, T. J. Moon, C. C. Cunningham, and J. Kas, "The optical stretcher: A novel laser tool to micromanipulate cells," Biophysical Journal **81**, 767-784 (2001).
72. H. Kress, E. H. K. Stelzer, G. Griffiths, and A. Rohrbach, "Control of relative radiation pressure in optical traps: Application to phagocytic membrane binding studies," Physical Review E (Statistical, Nonlinear, and Soft Matter Physics) **71**, 061927-061910 (2005).
73. H. Liang, W. H. Wright, S. Cheng, W. He, and M. W. Berns, "Micromanipulation of chromosomes in PTK2 cells using laser microsurgery (optical scalpel) in combination with laser induced optical forces (optical tweezers) " Experimental Cell Research **204**, 110-120 (1993).
74. S. Seeger, S. Monajembashi, K. J. Hutter, G. Futterman, J. Wolfrum, and K. O. Greulich, "Application of laser optical tweezers in Immunology and Molecular-Genetics," Cytometry **12**, 497-504 (1991).
75. M. W. Berns, Y. Tadir, H. Liang, and B. Tromberg, "Laser scissors and tweezers," in *Methods in Cell Biology, Vol 55*(1998), pp. 71-98.
76. J. C. Meiners, and S. R. Quake, "Direct measurement of hydrodynamic cross correlations between two particles in an external potential," Physical Review Letters **82**, 2211-2214 (1999).
77. R. R. Brau, J. M. Ferrer, H. Lee, C. E. Castro, B. K. Tam, P. B. Tarsa, P. Matsudaira, M. C. Boyce, R. D. Kamm, and M. J. Lang, "Passive and active microrheology with optical tweezers," Journal of Optics A: Pure and Applied Optics **9**, S103-S112 (2007).
78. N. K. Mohan, and P. K. Rastogi, "Recent developments in interferometry for microsystems metrology," Optics and Lasers in Engineering **47**, 199-202 (2009).
79. A. Rohrbach, H. Kress, and E. H. K. Stelzer, "Three-dimensional tracking of small spheres in focused laser beams: influence of the detection angular aperture," Opt. Lett. **28**, 411-413 (2003).
80. F. Gittes, and C. F. Schmidt, "Interference model for back-focal-plane displacement detection in optical tweezers," Opt. Lett. **23**, 7-9 (1998).
81. M. Capitanio, G. Romano, R. Ballerini, M. Giuntini, F. S. Pavone, D. Dunlap, and L. Finzi, "Calibration of optical tweezers with differential interference contrast signals," Review of Scientific Instruments **73**, 1687-1696 (2002).
82. L. P. Ghislain, and W. W. Webb, "Scanning-force microscope based on an optical trap," Opt. Lett. **18**, 1678 (1993).
83. W. Denk, and W. W. Webb, "Optical measurement of picometer displacements of transparent microscopic objects," Appl. Opt. **29**, 2382-2391 (1990).
84. R. M. Simmons, J. T. Finer, S. Chu, and J. A. Spudich, "Quantitative measurements of force and displacement using an optical trap," Biophysical Journal **70**, 1813-1822 (1996).

85. K. Svoboda, C. F. Schmidt, B. J. Schnapp, and S. M. Block, "Direct Observation of Kinesin Stepping by Optical Trapping Interferometry," Nature **365**, 721-727 (1993).
86. L. P. Ghislain, I. Brustmascher, and W. W. Webb, "Force and Membrane Compliance Measurements Using an Optical Trap and Laser Interferometry," Biophysical Journal **64**, A109-A109 (1993).
87. L. P. Ghislain, and W. W. Webb, "Scanning-Force Microscope Based on an Optical Trap," Optics Letters **18**, 1678-1680 (1993).
88. L. P. Ghislain, N. A. Switz, and W. W. Webb, "Measurement of Small Forces Using an Optical Trap," Review of Scientific Instruments **65**, 2762-2768 (1994).
89. N. A. Switz, J. Mertz, and W. W. Webb, "A feedback modified optical trap for probing local viscosity and examining diffusive behavior on cell membranes," Biophysical Journal **70**, TU414-TU414 (1996).
90. F. Gittes, and C. F. Schmidt, "Back-focal-plane detection of force and motion in optical traps," Biophysical Journal **74**, A183-A183 (1998).
91. S. M. Block, "Recent advances in optical trapping technology: Towards single angstroms and single photons," Biophysical Journal **88**, 386A-386A (2005).
92. F. Gittes, and C. F. Schmidt, "Interference model for back-focal-plane displacement detection in optical tweezers," Optics Letters **23**, 7-9 (1998).
93. V. Garbin, D. Cojoc, E. Ferrari, R. Z. Proietti, S. Cabrini, and E. Di Fabrizio, "Optical micro-manipulation using Laguerre-Gaussian beams," Japanese Journal of Applied Physics Part 1-Regular Papers Brief Communications & Review Papers **44**, 5773-5776 (2005).
94. P. A. Prentice, M. P. MacDonald, T. G. Frank, A. Cuschieri, G. C. Spalding, W. Sibbett, P. A. Campbell, and K. Dholakia, "Manipulation and filtration of low index particles with holographic Laguerre-Gaussian optical trap arrays," Optics Express **12**, 593-600 (2004).
95. A. T. O'Neill, and M. J. Padgett, "Axial and lateral trapping efficiency of Laguerre-Gaussian modes in inverted optical tweezers," Optics Communications **193**, 45-50 (2001).
96. N. B. Simpson, L. Allen, and M. J. Padgett, "Optical tweezers and optical spanners with Laguerre-Gaussian modes," Journal of Modern Optics **43**, 2485-2491 (1996).
97. K. Ladavac, and D. G. Grier, "Microoptomechanical pumps assembled and driven by holographic optical vortex arrays," Optics Express **12**, 1144-1149 (2004).
98. K. T. Gahagan, and G. A. Swartzlander, "Optical vortex trapping of particles," Optics Letters **21**, 827-829 (1996).
99. L. Jauffred, A. C. Richardson, and L. B. Oddershede, "Three-Dimensional Optical Control of Individual Quantum Dots," Nano Letters **8**, 3376-3380 (2008).
100. T. Iida, and H. Ishihara, "Optical manipulation of nano materials under quantum mechanical resonance conditions," Ieice Transactions on Electronics **E88C**, 1809-1816 (2005).
101. T. Yu, F. C. Cheong, and C. H. Sow, "The manipulation and assembly of CuO nanorods with line optical tweezers," Nanotechnology **15**, 1732-1736 (2004).
102. Y. Nakayama, P. J. Pauzauskie, A. Radenovic, R. M. Onorato, R. J. Saykally, J. Liphardt, and P. Yang, "Tunable nanowire nonlinear optical probe," Nature **447**, 1098-1101 (2007).
103. X. Huang, P. Jain, I. El-Sayed, and M. El-Sayed, "Plasmonic photothermal therapy (PPTT) using gold nanoparticles," Lasers in Medical Science **23**, 217-228 (2008).
104. N. Malagnino, G. Pesce, A. Sasso, and E. Arimondo, "Measurements of trapping efficiency and stiffness in optical tweezers," Optics Communications **214**, 15-24 (2002).

Chapter 2 –

Design and construction of an optical trapping system

2. Design and construction of an optical trapping system

2.1. Overview

There are three parts in this chapter. The first part covers the basic design considerations for the construction of a basic optical trap i.e. wavelength of the trapping laser beam, numerical aperture (N.A) of the microscope objectives and beam steering optics [1]. These deliberations are all crucial for the optical trapping of micrometre and nanometre sized particles. The high NA microscopy objective serves two purposes: trapping and imaging. The design of an imaging and illumination system for high resolution microscopic imaging is briefly discussed.

The second part of the chapter covers the use of an acousto optic modulator (AOD) and a stepper motor to automate the steering of the trapping beam in the transverse and the axial planes respectively. A single optical beam can then be steered with high precision using automation controls.

Significant attention in the field has been invested into the design of alternative trapping geometries: multiple optical traps [2]. The third part of the chapter presents the constructed optical trapping system based on the considerations discussed in part one and two. The optical trapping system comprises of two Gaussian beams, with orthogonal linear polarisations, that are focused through a single high NA microscope objective. This forms two independent optical tweezers [3]. The automated beam steering controls (part two) are built into one of the tweezers, while the other tweezers is steered manually. The semi-automated dual beam optical tweezers serves as the key instrument for the majority of the experiments in this thesis (chapter 3-7).

2.2. Design considerations

2.2.1. Laser wavelength and beam parameter

The early works of optical trapping by Ashkin [4-6] were made possible due to the invention of laser technology. There are two main considerations for the choice of trapping laser.

The first consideration is the wavelength of the trapping laser sources. It is ideal if the wavelength of the laser lies in low light absorption region of the trapped particle and the aqueous medium. Laser with wavelength close to the absorption band of the trapped particle creates undesirable thermal effects. These thermal effects can potentially damage the trapped particle and hence destabilised the trap. For example in trapping of biological particles, the trapping lasers are chosen in the near-infra red region to avoid dramatic damage to biological specimens.

Wavelengths of 830 nm and 970 nm have shown to be particularly favourable to the manipulation of the biological particles [7]. In the context of this thesis, I use a range of the non-biological particles for the optical trapping. The trapping laser beams generated from a Ytterbium-fiber laser (wavelength of 1070nm, YLM 5, IPG Photonics) are used to trap polymer microspheres (chapters 2-6), calcite microparticles (chapter 5), gold nanoparticles (chapter 6, 7), semiconductor nanoparticles (chapter 6) and polymer nanospheres (chapter 6,8). Only the gold nanoparticles and some semiconductor nanoparticles are non-transparent when exposed to this near infrared trapping wavelength. The absorption of the infrared light in these particles can result in residual heating.

Light absorption in the medium where the particles are suspended is important as well. In the domain of colloidal science, high power (≈ 5 W) green lasers (wavelength of 532 nm) are used for trapping due to the low amount of light absorbed by water. This reduces the surrounding heating effects (convection). Although near-infrared laser radiation (≈ 900 nm -1100 nm) absorbed by water (H_20) in my experiments (chapter 2 to 8), I have observed significant fluid convective effects only when the optical power at the sample exceeds ≈ 200mW. The convection effects are visualised with free floating particles that are in proximity (≈ 5-10 μm) to the optical trap. In chapter 8, I use a fiber laser with wavelength of 1090nm (SPI laser) and optical power of up to 600mW for optical trapping. The heating effects are suppressed by using heavy water (D_20), which absorbs very little infrared light radiation [8].

The second consideration is the quality of laser beam. The quality of the laser is assessed by the M^2 factor, beam pointing stability, intensity fluctuations and its maximum optical power. When the value of M^2 is equivalent to 1, the laser beam matches an ideal Gaussian beam profile [7]. An ideal Gaussian beam profile can be focused to a diffracted limited spot without any transverse aberrations (not considering any misalignment or additional optical aberrations). A good laser beam pointing stability removes any unnecessary spatial beam deviations. Intensity fluctuations in the laser beam cause unwanted temporal variations in the trap stiffness. The maximum optical power of the laser (in excess of 500mW), after accounting for the loss in power (unwanted reflections) in the optical train, defines the total amount of optical force that can be exerted. In this thesis, the near infrared fiber trapping lasers have an M^2 ~1.1, a beam pointing stability of < 10 nm, intensity fluctuations of ~ ±1 mW/ min and maximum optical power of 5 W (YLM 5, IPG Photonics).

The vast majority of optical trapping experiments use monochromatic continuous wave (CW) laser sources [9]. There are also emerging trends in using ultra-short pulsed lasers for optical trapping, as it can also be used as a multi-photon imaging laser source [10, 11]. It is possible to

simultaneously control the fluorescence excitation of a trapped object by apply pulse shaping technology with a femtosecond (≈ 12 fs) laser source.

2.2.2. Microscope objectives

The most crucial optical element of an optical trap is the microscope objective. It is used to focus the laser beam to form an optical trap. The choice of microscope objective determines the performance of the trap in three dimensions and the immersion medium of the objective (oil, water, or glycerol) sets limits on the axial depth to which particles can be trapped. In this section, I shall discuss the performance of the trap according to the N.A and the spherical aberrations of the microscope objective.

In 1872, Ernst Abbe defined a quantitative value for the angular aperture of a light called numerical aperture (N.A). The N.A of a lens is a measure of its ability to gather light at a fixed distance. N.A is given by $n_m \sin(\theta_1)$ where n_m is refractive index of medium (m=air, oil, water or glycerol) and θ_1 is the half-angle between the rays at the peripheral. Intuitively, the NA is also an important factor that defines the smallest region that light can be focused at its focal point. The theoretical achievable diffraction-limited beam spot using an oil-immersed microscope objective lens is given by $w_{XY-theory} = 0.55\left(\lambda / n_{oil} \sin(\theta_1)\right) / n_{water}$) (transverse full width half maximum of the beam) and $w_{z-theory} = 0.44\left(\lambda / (n_{oil} \sin^2(\theta_1 / 2))\right) / n_{water}$) the axial beam diameter (confocal parameter) at the focal plane [12] (n_{oil} is the refractive index of the oil medium). Appendix A (i) and A (ii) covers the measurements of the beam profile and optical power at the sample plane respectively.

Figure 2.1A illustrates a simple ray optics tracing schematic of the focusing light cone through a microscope objective when its back aperture is overfilled. The NA of modern microscope objectives is enhanced by using medium of a higher refractive index than air. An oil medium (n_m= 1.51-1.59) are often use to increase the N.A of the microscope objective. The invention of optical tweezers is made possible using high NA (typically ≥ 1) microscope objectives [6].

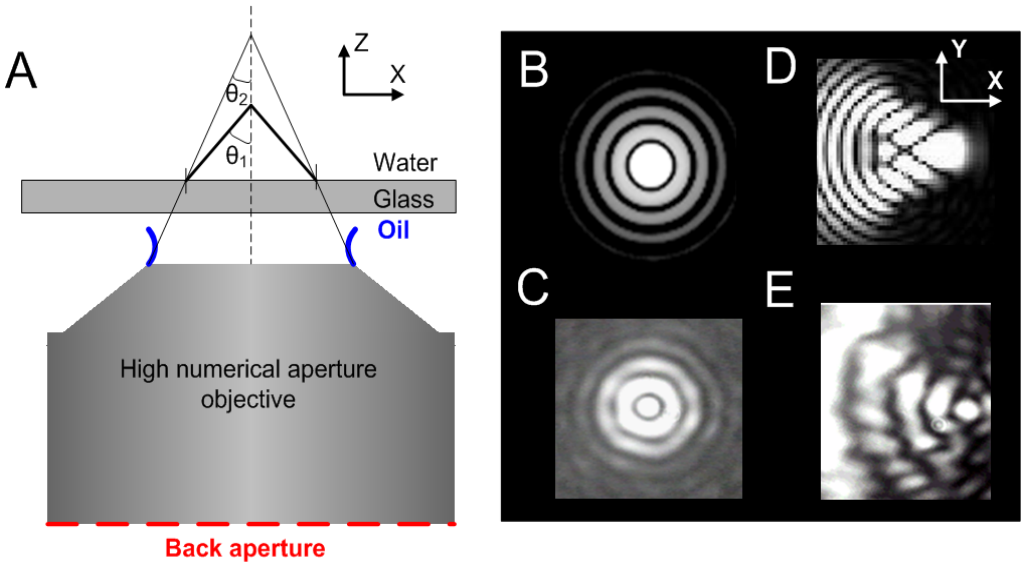

Figure 2.1. Focusing through a high N.A objective. A – illustrates the axial (spherical)aberrations and B-E shows Airy disk (an aligned beam onto back aperture of objective) and comatic aberration (misalignment onto the back aperture of the objective). In figure 2.1A, the light cone from the Gaussian beam during focusing (with the back aperture being overfilled to fulfil the NA). The light undergoes different medium (oil, glass and water) before reaching its focus point. θ_1 is the actual refracted half angle and θ_2 is the ideal refracted half angle when the NA is fulfilled (beam diameter = diameter of back aperture (red dash lines). The deviation of the half angle at region further away from the objective causes the spherical aberration. In figure 2.1 B-E, I shown the aligned beam (Airy disk - B,C) and misaligned beam (comatic aberration - D, E). The simulation (B, D) describes in appendix C. Note that the Airy disk is slightly defocused (resulting in the appearance of higher diffracting orders).

The back aperture of the microscope objective needs to be overfilled by the beam diameter of a laser beam in order to fulfil the NA of the microscope objective. Once the NA is satisfied, a steep intensity gradient is obtained in all three dimensions. This steep intensity gradient creates a three dimensional optical trap, optical tweezers [13, 14]. If the NA of the microscope objective is reduced to smaller than 0.8, the intensity gradient along the beam propagating direction would reduce and results in an optical trap in two dimensions (transverse plane) [15]. In this thesis, I use a number of microscope objectives with different NA values. In chapters 2, 3, 4 and 7, I use high NA (=1.25) objective to form an optical tweezers. In chapter 6, I use lower NA (0.75 and ≈ 0.25) microscope objectives to form two dimensional optical traps. In chapter 7, I use a single mode optical fiber (NA ≈ 0.2) to form a single optical trap.

Proper optical alignment of laser beam onto the microscopy objective is critical in obtaining a diffraction limited spot for optical trapping. Transverse misalignment (i.e. coma aberration) of a laser beam, at the back aperture of a high numerical objective, can be experimentally diagnosed by looking at the incident laser beam profile on a reflective glass slide (Figure 2.1 C, E). Figure 2.1 B

and C show a well aligned Gaussian beam onto the back aperture of the microscope objective (resulting in a well-defined Airy disk) in simulation and experiment respectively. Figure 2.1 D and E show the intensity pattern of a beam with comatic aberration due to misalignment at the back aperture in simulation and experiment respectively.

Although oil immersion objectives can offer higher NA (1.25 - 1.4) than water immersion objective, the oil immersion objectives are typically corrected for spherical aberration at a fixed distance for a given microscopy coverslip thickness (typically 0.17 mm). This means that it can still introduce spherical aberrations at other positions in the sample. The effects of spherical aberrations is due to the difference in the refractive index of the medium (oil) and interface (glass and water), would emerge as the focus is moved further away from the coverslip. In the case of oil immersion microscope objective, the trapping beam would propagate through a layer of oil, a thin piece of glass (coverslip) and then into the sample solution which is of a lower refractive index than the glass and oil. Thus the beam will, unsurprisingly, experience a large change in refractive index that generates spherical aberrations along the axial plane, broadening the beam spot along the axial plane when the focus is moved deeper into the sample. Hence, a well aligned optical tweezers may still suffer inherent axial aberrations due to refractive index mismatches. As the result, the trap performance of microparticles (diameter ≈ 1 μm) degrades (reduction in trap stiffness) when operating in deeper region (height above coverslip > 20 μm) of the sample [16-18]. Alternatively, water immersion objectives are corrected for the refractive index of water (removing the requirement of using immersion oil and a coverslip) which in turn reduces the spherical aberration [19]. Due to the choice of the inverted microscope platform and available of microscope objectives, I chose to use oil immersion microscope objective to form the optical tweezers. In chapter 3 section 3.7.2, I calibrate the effects of spherical aberration on my optical tweezers system by measuring the trap stiffness over a range of axial positions above the coverslip.

Most recently, Reihani and Oddershede [19] succeeded in minimizing spherical aberrations by using immersion oils with varying refractive indices (n_{oil}=1.53-1.59). They demonstrate efficient axial trapping over a longer axial distance than using typical immersion oil (n_{oil}=1.515). Alternative adaptive optical techniques to obviate these aberrations are available in the form of dynamic holographic elements [18] or the use of deformable mirror [20, 21] technology by imposing correction terms of the appropriate Zernike polynomials upon the input wavefront of the trapping beam. Finally, it is important to note that modern microscope objectives are designed to produce an image at infinity. With such “infinity corrected” objectives, researchers may add an additional telescope or other optical components (i.e. spatial light modulator or acoustic optical

deflector) to relay or modulate the laser source before the microscope objective (within the "infinity space") without affecting the bright-field or fluorescence imaging aspect of the system.

2.2.3. Conjugate optics: beam steering and imaging

In laser microscopy, the technique of laser beam steering is widely employed in confocal and multiphoton microscopy imaging for high speed raster scanning of a microscopic sample (point by point fluorescence excitation). In optical trapping, the precise and rapid steering of the focused beam (diffraction-limited spot) at the sample plane is crucial to accurate position and force measurements. As mentioned in the previous section, it is important to ensure that the back aperture is always fully filled to satisfy the N.A. In other words, the position of the input beam does not "walk off" or deviate away at the back aperture of the microscope objective. The use of optical conjugates optimises the steering of optical trapping beams.

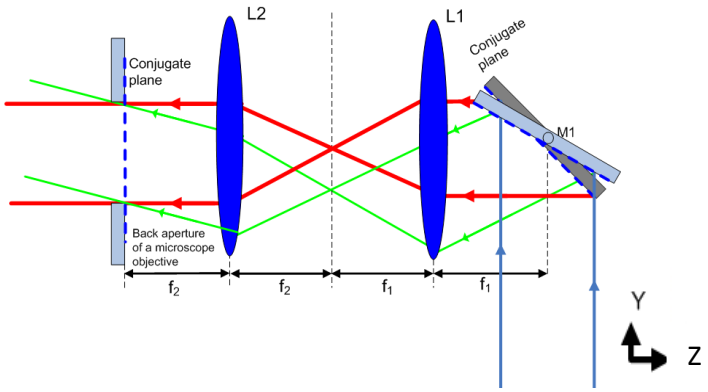

Figure 2.2 Beam steering lens relay system. Lenses L1 (focal length f_1) and L2 (focal length f_2) are used for imaging the steering mirror M1 onto the back aperture of the microscope objective (blue dash lines). Two sets of parallel laser beams (thick red and thin green lines) are drawn to show that the rays are position-invariant at the conjugate planes.

During beam steering, the input beam, that is overfilling the back aperture, needs to be centred upon the back aperture. This is so as to ensure a good quality optical trap at all times. In figure 2.2, I illustrate the idea of optical conjugates for the steering of the trapping beam with a mirror (M1). The back aperture of the microscope objective is imaged onto a mirror. This means that the positioning of the beam onto that mirror is equivalent to positioning the focused beam after the microscope objective. A tilt in the mirror translates to a lateral shift of the beam in the sample plane. Ideally, the beam position remains fixed onto the back aperture of the microscope objective. The beam steering system is made up of two lenses as seen in the figure 2.2, denoted as L1 and L2, and a rotating mirror M1. Each lens is placed at one focal length away from the other and the

rotating mirror M1 is positioned at one focal length away from one of the lens L1. By placing the back aperture of a microscope objective at one focal length away from lens L2, the mirror is imaged onto the back aperture. Here, the rotating mirror M1 and the back aperture of the microscope objective form conjugate planes. In figure 2.2, I illustrate two manners in which the rays are being redirected by the mirror M1 at an angle with respect to the principle axis of the beam steering lens systems: green thin line and red thick line. With the beam steering lens system, both rays maintain their spatial position onto the back aperture of the microscope objective. The central purpose of the conjugate planes is to ensure that a collimated beam light (blue line) before the mirror M1 maintains overfilling of the back aperture of microscope objective without any "walk off".

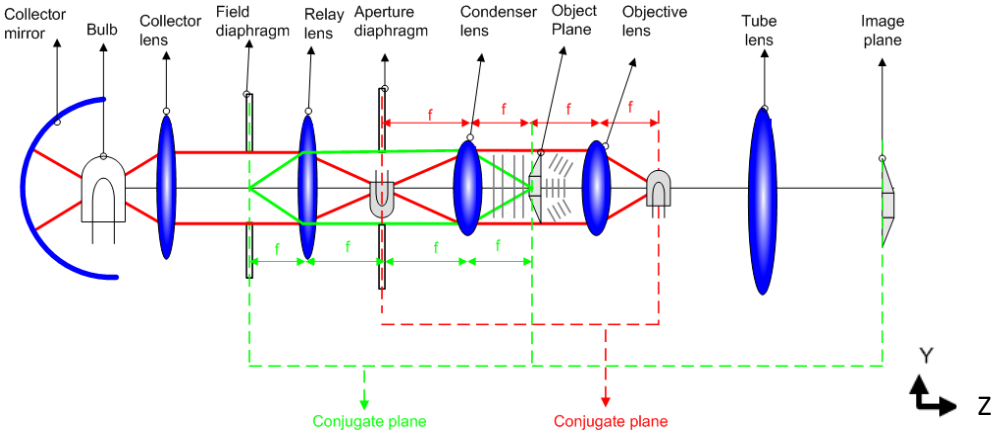

Figure 2.3 Köhler illumination with highlighted conjugate planes (illumination (red) and imaging (green)). The conjugate planes in the illumination paths include aperture diaphragm, back aperture of the microscope objective. The conjugates planes in the imaging path include field diaphragm, object plane and image plane.

The concept of conjugate planes is extensively used in microscope illumination and imaging. In figure 2.3, I illustrate the principles of the conjugate planes for the illumination and imaging for brightfield microscopy. The illumination conjugate is primarily based on Köhler illumination, which is to provide an even illumination right across the sample. The illumination provides the full resolving power of a lens (Abbe's law). From the figure 2.3, I illustrate the idea of the Köhler illumination by splitting the optical system into two separate sets of 4-f lens system (conjugate planes), each meant for illumination (red lines) and imaging (green lines).

In the illumination path, the collector lenses and mirrors seek to collimate the emitted light from a bulb filament. The image of the filament is relayed by a relay lens onto the front focal plane of the condenser (the position of the aperture diaphragm). The bulb appears in the conjugate

positions: the condenser aperture diaphragm (at the front focal plane of the condenser), the back focal plane of the objective. This set of conjugate plane arrangement is crucial in achieving an almost "planar" wave (grey lines before object plane) onto the sample plane (red solid line).

In the imaging path, the field diaphragm is first imaged onto the sample. This controls the area of illumination onto the sample. Any object at the sample scatters the incident planar light field. The scattered light field (spherical) interferes with the unscattered light (planar) and casts a "shadow" (interference pattern) on the image plane of the objective lens. The formation of the image (interference of the scattered and unscattered fields) at the image plane is relayed onto a second image plane by a tube lens. The image of field diaphragm appears at the conjugates imaging planes: object and image plane.

By changing the field and the aperture diaphragm, the field of illumination (green line) and the overall N.A of the condenser are altered respectively. It is possible to marginally improve the imaging quality or contrast of the final image by tuning the sizes of the two diaphragms. In conclusion, the use of Köhler illumination is important for brightfield microscopy contrast imaging methods especially for phase contrast imaging, differential interference contrast and Hoffman modulation contrast imaging (Appendix B (i)). The lateral resolution of brightfield illumination (based on wavelength of 532 nm that has a peak signal response in silicon based camera and NA of 1.25) is approximately 250nm.

2.3. Automated beam steering system

The use of automated beam steering systems provides a reliable and controllable way to manipulate trapped particles at discrete step sizes for measurements of positions and forces. In this section, I shall discuss two fundamental beam steering concepts for transverse and axial direction of the sample. The beam steering instruments used are acousto optic deflectors (AODs) or stepper motor.

2.3.1. Transverse

One of the earliest automation of optical tweezers was done by Sasaki *et al.* [21] who demonstrated that by scanning a single trap in a designed path, using a pair of fast scanning mirror driven by galvanometers. They observed that microspheres are seen to reside and align into the designated two-dimensional light patterns. In addition, they were also able to cage and transport reflective metallic particles or low refractive index microdroplets. Visscher *et al.* [22] integrated a

two-axis galvanometer mirror onto a confocal fluorescence microscope system to achieve rotational control of *E. coli bacterium* under fluorescence imaging. After which, Visscher *et al.* [23] further improved the scanning laser trapping system with acousto optic deflectors (AODs), where the optical trap can be steered at a rate of a few kHz (> natural frequency response of a micrometer sphere). These automated beam steering techniques (galvanometer, AOD) have since greatly improve the precision and repeatability of single molecule experiments [24]. In essence, these beam steering systems provide a reasonably accurate and reproducible two dimensional (x-y) intensity pattern (orthogonal to the beam propagation) by deflecting a single input beam.

There are number of ways to achieve to automated laser scanning such as using the galvanometer controlled mirror [25, 26], piezo-driven resonant scanning mirrors [27] or acousto optic deflector (AOD) [28]. The speed and accuracy of the beam positioning in the optical trapping of macromolecules is often very rapid (≈ 20ms) and precise (≈ 10nm) [28, 29].

The two axis mirror scanning techniques that operates by scanning a pair of oscillating mechanically controlled mirrors. The two highly reflective mirrors are aligned such that each provides scanning in each of the axis (x, y). The mechanical nature of mirror scanning technique limits the speed with which the beam can travel across the sample. Current resonator scanning mirrors can reach scan rate of up to ≈ 8- 12 kHz [30].

.

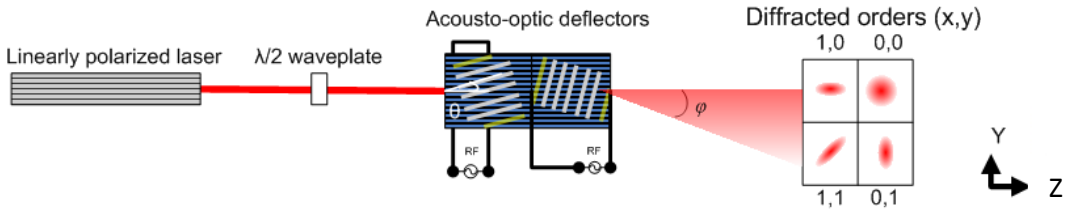

Figure 2.4 Operation of two axis (x-y) acoustic optic deflector (AOD). A single linearly polarised Gaussian beam enters a two axis acousto-optic deflector that subsequently yields the four diffraction orders arranged in a two (x, y) dimensional coordinate system. The half waveplate controls the input polarisation of the beam before entering into the AOD. The input laser beam is incident at the Bragg angle (θ), efficiently diffracted by the sound wave grating and deflected by an angle $\varphi = \lambda(f/v)$, f = frequency of the acoustic wave, v = velocity of the acoustic wave and λ is the wavelength of the input light. The diffracted orders illustrate the input beam being scanned along a linear path (line scan) on each of their respective axis (x and y).

On the other hand, the AOD operates by deflecting an input beam through a diffractive grating formed with acoustic wave. In figure 2.4, I illustrate a line scan operation of a two-axis AOD system. Within one AOD, a standing acoustic wave modulates the refraction index of the crystals which in turn diffracts the light propagating through it much like a phase grating. Tuning the depth of the phase change can also modulate the intensity of the laser beam. The steering of the

beam, formed at the first diffraction order, is accomplished by moving the grating. Two AOD's scanning in orthogonal directions can be combined in series to provide both x and y beam deflections as shown in figure 2.4. Each deflector consists of a crystal with piezoelectric transducers which are driven by radio frequency (RF) voltages. The RF voltage modulates the standing wave across the crystal. Figure 2.4 shows that a linearly polarised input laser beam that is incident at the Bragg angle (θ), efficiently diffracted by the sound wave grating at an angle φ and into the respective diffraction orders (x, y). A linearly polarised laser beam needs to be passed through a half waveplate ($\lambda/2$) controlling the direction of the polarisation of the light beam) before entering the pair of AODs.

When a slow linear scan (tens of Hz) is applied on each individual AOD, the diffractive grating from each AOD spreads the input beam into its individual diffracted orders. An example of the output diffracted patterns from a two axis AOD during slow scan is shown in figure 2.4. Typically there are four diffracted orders (x, y) arranged over a two dimensional grid (higher diffraction orders are present but much weaker in intensity). The intensity at the undiffracted Gaussian spot (0, 0) is strongest and does not change its position during scanning. On the other hand, the diffraction orders at (0, 1) and (1, 0) are the vertical and horizontal scanned line intensity from each of the individual AODs. The combined output of the two AODs are given as (1, 1) which is represented by a diagonal scanned line intensity as shown in figure 2.4. A binary aperture is placed to select the (1, 1) diffracted order, which is then relayed into the sample plane as the trapping beam. The crystals in the AOD used for steering an infrared laser can be either a tellurium dioxide (TEO_2) or Lithium Niobate ($LiNbO_3$).

The AOD system suffers from some optical efficiency trade off due to its diffractive nature and beam fluctuations within the crystals as compared with the galvanometer scanning mirrors. The first diffracted order which typically contains only around 40% of the total input optical power is used. In addition, the AOD optical efficiency gradual decreases with respect to the deflection angle of the grating. This creates a less than ideal spread of intensity distribution across the sample plane. Even though this can be compensated by imposing an amplitude modulation to even out the intensity, it means that each AOD needs to be characterized for the change of intensity versus deflection angle. This change of intensity has a marked effect on the stiffness of the trap generated. Furthermore, small intensity fluctuations can also be caused by the delayed response time of the all the optoelectronic components: the quality of the electronics and the programming aspects [31, 32]. Finally, a Fabry-Pérot type interference occurring within the pair of AOD can also create

undesirable intensity modulations. However, for very small displacement i.e. 50nm -100nm, the intensity of the beam changes by less than 5%.

A recent work by Valentine *et al* [33] suggests that an electro-optic deflector (EOD), where an external electrostatic field creates a refractive index gradient in an appropriate crystal, provides an even more precise beam steering than the AOD. So the EOD can help to increase the resolution in force and position measurements. However, the EOD does not offer a larger steering angle than the AOD. In general, the AOD is ideal for high speed steering of single beam optical trap over a small distance (≈500nm) and is often used in optical force feedback system [33, 34].

In addition, an AOD can easily accomplish a repetitive scan rate of the order of tens of kHz due to the fast travelling speed of the acoustic waves. At such high speed scanning, a single beam can be "shared" between different positions at milliseconds [2]. A time shared optical trapping system using AOD is discussed in Appendix D.

2.3.2. Axial

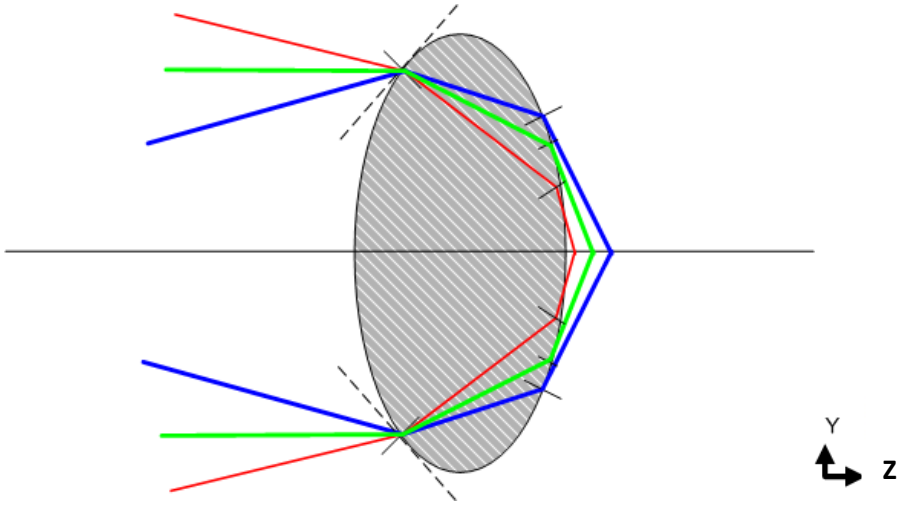

Figure 2.5 Axial beam shift due to divergence of beam before a focusing lens. The degree of divergence and convergence in the input beam before a focusing lens can shift the focal position in the sample plane along the axial direction (Z). Solid line indicates that the input beam is collimated (green line), diverging (blue ray) or converging (red ray)

The axial position of the beam focus (without altering the phase of the beam) can be changed by simply moving one of the lenses within a beam expansion lens systems. The change in the telescope lens system controls the divergence of the input beam before entering into the focusing lens (i.e. microscopic objective) as shown in figure 2.5 (red, green and blue). If the input beam is collimated, the output light will be focused onto the focal plane, indicated by the green

line in figure 2.5. The relative positions of one of the lenses in the telescope system can in turn result in a diverging (blue ray) or a converging (red ray) beam reaching the back aperture of the microscope objective. The divergence and convergence of beam (controlled through the movement of the lens) displaces the beam focus (trapping position) before or after the initial focus position. Schaffer *et al* [35] showed that the laser beam focus moves less than 20 nm per 1 μm of motion of the lens.

2.4. Dual optical tweezers system

A commercial microscopy body provides a high level of mechanical stability. It also offers multiple imaging ports (typically five) with built-in fluorescence and brightfield illumination modules. In addition, the microscope system provides a rotating microscope turret mount that accommodates up to five microscope objectives. By rotating the turret, one can switch between different microscope objectives easily. The combination of two types of automated sample holding stages, H117 Prior Scientific and 733.3D Physik Instrumente, can provide large steering range and high precision translation controls over the viewing location within the sample plane. It is important to build the optical trapping system on vibration damping table so as to provide isolation from the surroundings. The displacement of the optical table as a function of time is measured to be approximately 50 nm using a geophone, as shown in Appendix A.

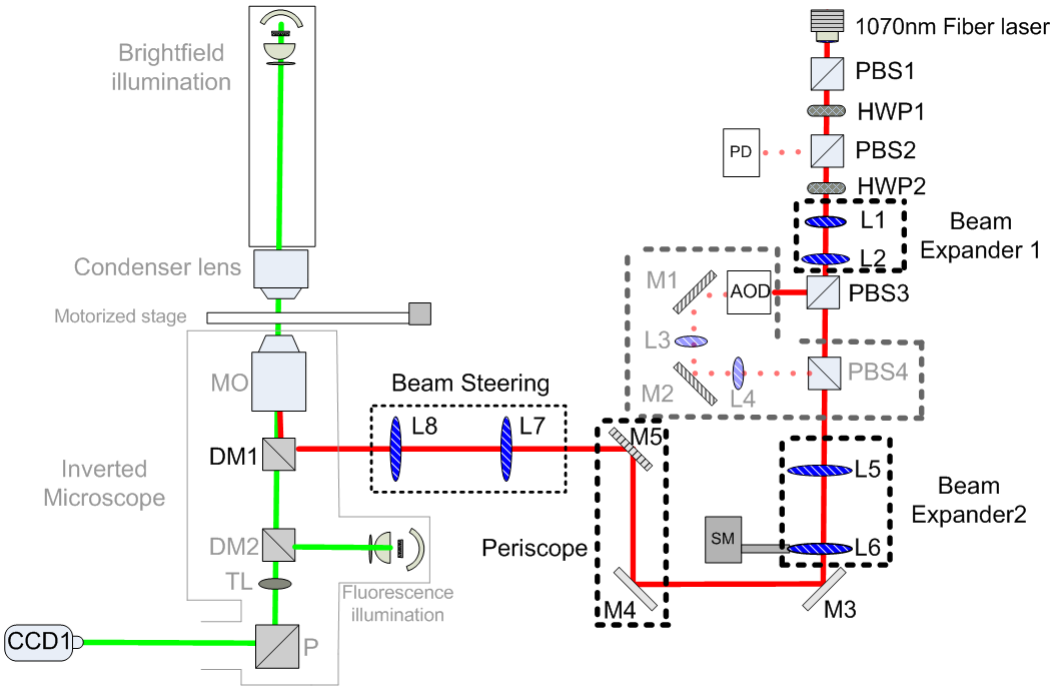

Figure 2.6: Dual beam optical tweezers setup with automated beam steering controls. A single infrared fiber laser is put through two polarising beam splitters (PBS1 and PBS2). PSB1 ensures a linearly polarised beam. The PBS2 works in conjunction with the HWP1 to control overall intensity of the beam. The HWP2 controls the polarisation direction of the beam. The beam is then expanded by lenses L1 and L2 (twice the input beam diameter ≈ 3.2 mm) before being split into two orthogonal polarised beams by PBS3. The deflected beam after the PBS3 fills the input aperture of the AOD. The exiting beam from the AOD is reflected by mirrors M1 and M2 and relayed by L3 and L4 to PBS4. PBS4 recombines the both the deflected and undeflected beams from PBS3. The two beams now have orthogonal polarisations and are expanded by three times using lenses L5 and L6. Lens L6 is attached to a stepper motor that translates it along the beam propagating direction. Mirrors M3, M4 and M5 reflect the two beams onto the dichroic mirror DM1 Mirrors. M4 and M5 form a periscope that elevates the height of the beam relative to the optical table. Lenses L7 and L8 forms the beam steering system that images the steering mirror M5 onto the back aperture of the objective MO. DM1 reflect the two beams onto the focusing objective (MO) and into the sample plane. On the imaging and illumination aspects, a bright field illumination assembly (Nikon) and condenser lens provide an illuminating light onto the sample plane and a tube lens TL images the light collected by the objective MO onto a digital camera CCD1. A separate fluorescence illumination with another dichroic mirror DM2 is used for fluorescence excitation.

In this section, I describe the construction of an optical tweezers system based on a commercially available inverted microscope system (TE2000E Nikon) with its supporting illumination and imaging setup. Instead of building just a single beam optical trapping system, I have decided to construct a dual beam optical tweezers system. This elegant and inexpensive approach creates two adjacent and independent optical tweezers. The dual beam optical tweezers is often desired by the biophysics community for stretching and holding macromolecules [3]. This dual beam optical tweezers is not to be confused with the counter-propagating dual beam optical trapping. Here, two beams are ***co-propagating*** in the same direction into a single microscope objective to form the two optical traps. On the other hand, the ***counter-propagating*** dual beam optical trapping makes use of two laser beam propagating in opposing directions to form a single optical trap.

Figure 2.6 shows the illustration of the dual beam optical tweezers setup. A single near infra-red fiber laser (YLM series, IPG laser, wavelength 1070nm) outputs a collimated Gaussian beam with beam diameter of 1.6mm. The beam is then directed onto a beam splitter cube (PBS1) that ensures a linearly polarised beam is generated. It is then directed onto a half waveplate (HWP) and a second beam splitter cube (PBS2) which controls the overall input power in the beam. A photodiode is placed at the deflected beam path of the PBS2 to monitor the power stability in the beam. The undeflected beam enters a second half waveplate (HWP2). The HWP2 controls the polarisation direction of the beam. It is then expanded by twice with a simple two lens telescope

(2X) made up of lenses L1 and L2, before being split up into two independent beams by the next polarisation beam splitter cube (PBS3). This expansion is necessary to ensure the right filling factor onto the entrance aperture of the AOD (DTD-274HA6B, Intraaction Corp).The AOD is controlled by a two channel variable frequency source (Intraaction, DVE120). A low filling factor on the AOD can significantly reduce the range which the beam can steer. A beam steering lenses system is set after the output of the AOD (lenses L3 and L4) after the mirror M1. The lenses help form an intermediate conjugate plane of the output face of the AOD, which is relayed onto the back aperture of the microscope objective. The optical power in each of the beam or trap can be controlled by rotating the HWP2. Both beams are recombined at the second polarisation beam splitter cube (PBS4) before entering a beam expansion system (X3) formed by lenses L5 and L6. The expanded beams are redirected by a dielectric mirror (M3 and M4) onto the steering mirror (M5). M4 and M5 form a periscope system that elevates the height of the beam, relative to the optical table, to reach the input beam port on the microscope system. A beam steering lens system, lenses L7 and L8, ensures that the expanded beam is well aligned onto the back aperture of the microscope objective (MO, NA.1.25, oil immersion, 100 X, Nikon) when the steering mirror (M3) is rotated. NIR dichroic mirror (DM, Chroma, z900dcp, reflectivity efficiency > 90% at wavelength of 1070 nm) reflects the two beams onto the back aperture of the MO. A bright field illumination and a condenser (CO) illuminate the sample. A fluorescence illumination module with a dichroic mirror (DM2) provides a fluorescence excitation light source. This fluorescent light illuminates the sample with the same microscope objective (MO). The image of the object is relayed onto digital charged coupled device (CCD) camera (HAD, Pulnix) via the tube lens (TL). The DM1 is designed to transmit the wavelength below 900nm, and this is coincidence with the typical wavelength of the excitation and emission fluorescence wavelengths (wavelength 350 nm to 600 nm). A stepper motor (SM, LS series, Zaber technology) is attached to lens L6. By shifting the position of L6, it changes the separation distance between L5, thus the divergence of the beam can be controlled. The stepper motor delivers the axial control of two beams, as mentioned in section 2.3.2. In this trapping system, one of the beam (deflected beam at PSB2) is steered by an AOD, while the other undeflected beam remains fixed [3]. Since the NA (=1.25) of the oil immersion MO is larger than 1, the two beam forms two independent optical tweezers [3].

Next, I show some initial trapping results using the constructed dual optical tweezers system. Figure 2.7 (A-C) shows the sequence stepping of a 0.5 μm (diameter) polymer sphere with the AOD trap (second optical trap) stepping away from a second 0.5 μm (diameter) polymer sphere static optical trap at 0.5μm steps. For beam displacements of up to 5 μm, the intensity of the

beam changes by less than 10% on both of the axes. Figure 2.7 D-F shows the sequential axial stepping of the two optically trapped 0.5μm (diameter) polymer spheres by 0.5 μm steps away from the imaging plane. This axial stepping is achieved by moving the lens L6 with a stepper motor moving at much large distance (≈ 70 μm). The overall trapping system is therefore semi-automated. A detailed calibration of the scanning trap using a quadrant photodiode (QPD) will be covered in the next chapter.

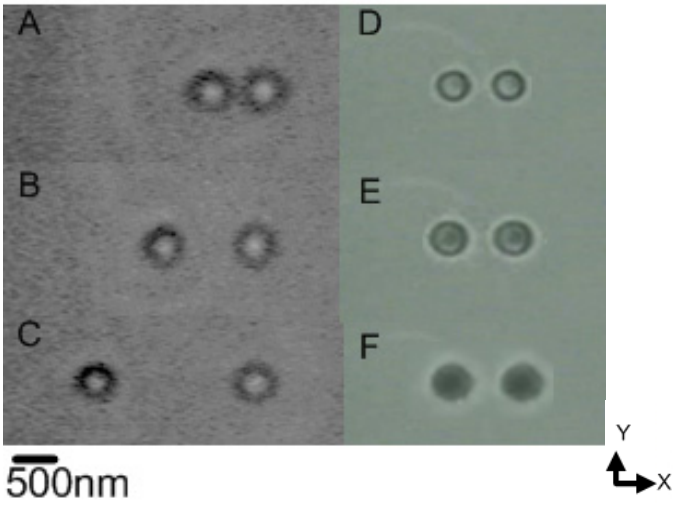

Figure 2.7 – Transverse and axial stepping of optically trapped microspheres (0.5 μm in diameter). A-C: transverse stepping of an optically tweezed sphere (0.5 μm) and D- F: axial displacement of the optically trapped spheres.

2.5. Conclusion

In this chapter, I have covered the design considerations for the construction of a basic optical tweezers and the construction of a dual beam optical trapping.

The selection of two of the most important components (laser and the microscope objective) in an optical trapping system is discussed in detail. In the first section, I discuss the choice of trapping laser beam such as the laser wavelength and laser beam parameter. The absorption of the wavelength by the trapping material is important to maintaining a stable trap. Laser in the infrared spectrum of 830 nm and 970 nm are particularly suited for trapping of biological particles. The absorption of light by the medium, in which the particles are suspended, plays a role in the surrounding thermal effects. At moderate optical power (< 200 mW), the heating effects of infrared lasers in water (H_20) are minor. In my experiments, I make use of laser with wavelength of 1070nm which are suitable for manipulating non-biological particles. At higher optical power (>300 mW), I make use of heavy water (D_20) that has lower light absorption at the infrared wavelengths. In the

same section, I discuss the NA of the microscopy objective lens to use. The NA of the objective lens determines the imposed optical gradient force on the trapped particle. A high NA (>1) microscope objective creates strong enough intensity gradient in three dimensional to form an optical tweezers. With microscope objectives at lower NA (< 1), the axial intensity gradient is reduced and a two dimensional optical trap is formed. In both case, the NA must be satisfied by overfilling the back aperture of the microscope objective.

Careful design of the optical system is important to achieve the best trapping and imaging performance. In final part of the first section, I explained the use of conjugate optics for beam steering and imaging. The beam steering optical setup ensures that the beam maintains an overfilling factor on the back aperture of the microscope objective during steering. So the trapping performance would remain unchanged during beam steering. Appropriate imaging and illumination system is important for the clear viewing microscopic particles. I illustrated the principles of the conjugate planes for the illumination and imaging upon a microscope sample. The correct design of the illumination provides an even illumination right across the sample, while exploiting the full resolving power of a lens (NA).

The majority of my experiments will be carried out on an inverted optical microscopy platform (Nikon, TE2000E) that is commercially available. The microscope system (Nikon TE2000) provided the proper illumination and imaging system for high and low NA microscope objectives. The microscope included an additional beam port for optical trapping without the need to compromise the use of any of the imaging and illumination paths. Furthermore, there are additional viewports in the microscope system and they are especially important when combining the optical tweezers with other imaging modalities: laser scanning confocal fluorescence microscopy (chapter.7) and digital holographic imaging (appendix G).

In the second section, I moved onto the explanation an AOD and stepper motor for automated beam steering in the transverse and axial plane. A two axis acousto-optic deflector was illustrated for the two dimensional beam steering in the transverse plane. The first diffraction orders from the acoustic grating formed by the two axes AOD is used as the trapping beam. The steering was performed by changing the separation of the gratings. A separate stepper motor was used for the control of the beam position in the axial plane. A stepper motor moved a lens that is part of a beam expansion lenses system. The position of the lens changed the divergence/convergence of the trapping beam at the back aperture of the microscope objective lens, which in turn controlled the beam focus position along the axial plane.

In the final section of the chapter, I described the experimental setup that is used in the majority of the experiments in this thesis. The experimental setup comprised of two independent optical trapping beam [3]. Using a set of polarisation optics and a Mach-Zehnder interferometer setup, a single Gaussian beam was split into two beams of equal power but each orthogonally polarised (to minimize optical interference effects). Each beam created an independently steerable optical tweezers, after being focused through the high NA microscope objective (MO). One of the beam (second optical trap) was steered by an AOD, while the other beam remained fixed [3]. The AOD beam steering controls (section 2.3.1) were built into one of the tweezers, while the other tweezers was steered manually. A single stepper motor (section 2.3.2) was used to move the axial position of two focused Gaussian beams simultaneously. Lastly, I demonstrated the automated trapping controls on polymer spheres (0.5 μm in diameter) using two optical tweezers formed by a single high NA (1.25) oil immersion microscope objective with an infrared laser (wavelength 1070 nm). I designed and performed all the experiments described in this chapter. A set of customised software was written by me to accomplish the automated beam steering.

2.6. References

1. W. M. Lee, P. J. Reece, R. F. Marchington, N. K. Metzger, and K. Dholakia, "Construction and calibration of an optical trap on a fluorescence optical microscope," Nat. Protocols **2**, 3226-3238 (2007).
2. K. Dholakia, and W. M. Lee, "Optical Trapping Takes Shape: The Use of Structured Light Fields," in *Advances in Atomic, Molecular, and Optical Physics, Vol 56*(Elsevier Academic Press Inc, San Diego, 2008), pp. 261-337.
3. E. Fallman, and O. Axner, "Design for fully steerable dual-trap optical tweezers," Applied Optics **36**, 2107-2113 (1997).
4. A. Ashkin, "Acceleration and trapping of particles by radiation pressure," Physical Review Letters **24**, 156-159 (1970).
5. A. Ashkin, and J. M. Dziedzic, "Stability of optical levitation by radiation pressure," Applied Physics Letters **24**, 586-588 (1974).
6. A. Ashkin, J. M. Dziedzic, J. E. Bjorkholm, and S. Chu, "Observation of a single-beam gradient force optical trap for dielectric particles," Optics Letters **11**, 288-290 (1986).
7. K. C. Neuman, E. H. Chadd, G. F. Liou, K. Bergman, and S. M. Block, "Characterization of photodamage to Escherichia coli in optical traps," Biophysical Journal **77**, 2856-2863 (1999).
8. A. C. Tam, and C. K. N. Patel, "Optical absorptions of light and heavy water by laser optoacoustic spectroscopy," Appl. Opt. **18**, 3348-3358 (1979).
9. M. Goksör, J. Enger, and D. Hanstorp, "Optical Manipulation in Combination with Multiphoton Microscopy for Single-Cell Studies," Appl. Opt. **43**, 4831-4837 (2004).
10. B. Agate, C. T. A. Brown, W. Sibbett, and K. Dholakia, "Femtosecond optical tweezers for in-situ control of two-photon fluorescence," Optics Express **12**, 3011-3017 (2004).
11. P. Li, K. B. Shi, and Z. W. Liu, "Manipulation and spectroscopy of a single particle by use of white-light optical tweezers," Optics Letters **30**, 156-158 (2005).
12. J. B. Pawley, "Fundamental and Practical limtis in Confocal Light-Microscopy," Scanning **13**, 184-198 (1991).
13. H. Kogelnik, and T. Li, "Laser beams and resonators," Applied Optics **5**, 1550-1567 (1966).
14. A. E. Siegman, "How to (maybe) measure laser beam quality," OSA TOPS **17**, 184-199 (1998).

15. H. Kress, E. H. K. Stelzer, G. Griffiths, and A. Rohrbach, "Control of relative radiation pressure in optical traps: Application to phagocytic membrane binding studies," Physical Review E **71** (2005).
16. A. Rohrbach, and E. H. K. Stelzer, "Trapping forces, force constants, and potential depths for dielectric spheres in the presence of spherical aberrations," Applied Optics **41**, 2494-2507 (2002).
17. K. C. Vermeulen, J. van Mameren, G. J. L. Wuite, and C. F. Schmidt, "Dependence of optical trap stiffness on focusing depth in the presence and absence of spherical aberrations," Biophysical Journal **88**, 663A-663A (2005).
18. K. D. Wulff, D. G. Cole, R. L. Clark, R. DiLeonardo, J. Leach, J. Cooper, G. Gibson, and M. J. Padgett, "Aberration correction in holographic optical tweezers," Optics Express **14**, 4169-4174 (2006).
19. S. N. S. Reihani, and L. B. Oddershede, "Optimizing immersion media refractive index improves optical trapping by compensating spherical aberrations," Optics Letters **32**, 1998-2000 (2007).
20. T. Ota, T. Sugiura, S. Kawata, M. J. Booth, M. A. A. Neil, R. Juskaitis, and T. Wilson, "Enhancement of laser trapping force by spherical aberration correction using a deformable mirror," Japanese Journal of Applied Physics Part 2-Letters **42**, L701-L703 (2003).
21. E. Theofanidou, L. Wilson, W. J. Hossack, and J. Arlt, "Spherical aberration correction for optical tweezers," Optics Communications **236**, 145-150 (2004).
22. K. Visscher, G. J. Brakenhoff, and J. J. Krol, "Micromanipulation by Multiple Optical Traps Created by a Single Fast Scanning Trap Integrated with the Bilateral Confocal Scanning Laser Microscope," Cytometry **14**, 105-114 (1993).
23. K. Visscher, S. P. Gross, and S. M. Block, "Construction of multiple-beam optical traps with nanometer-resolution position sensing," IEEE Journal of Selected Topics in Quantum Electronics **2**, 1066-1076 (1996).
24. K. C. Neuman, and S. M. Block, "Optical trapping," Review of Scientific Instruments **75**, 2787-2809 (2004).
25. K. Sasaki, M. Koshioka, H. Misawa, N. Kitamura, and H. Masuhara, "Pattern-formation and flow-control of fine particles by laser-scanning micromanipulation," Optics Letters **16**, 1463-1465 (1991).
26. K. Sasaki, M. Koshioka, H. Misawa, N. Kitamura, and H. Masuhara, "Optical Trapping of a Metal-Particle and a Water Droplet by a Scanning Laser-Beam," Applied Physics Letters **60**, 807-809 (1992).
27. C. Mio, T. Gong, A. Terray, and D. W. M. Marr, "Design of a scanning laser optical trap for multiparticle manipulation," Review of Scientific Instruments **71**, 2196-2200 (2000).
28. W. J. Greenleaf, M. T. Woodside, E. A. Abbondanzieri, and S. M. Block, "Passive all-optical force clamp for high-resolution laser trapping," Physical Review Letters **95**, 208102 (2005).
29. W. J. Greenleaf, M. T. Woodside, and S. M. Block, "High-resolution, single-molecule measurements of biomolecular motion," Annual Review of Biophysics and Biomolecular Structure **36**, 171-190 (2007).
30. C. K. Hitzenberger, P. Trost, P. W. Lo, and Q. Y. Zhou, "Three-dimensional imaging of the human retina by high-speed optical coherence tomography," Optics Express **11**, 2753-2761 (2003).
31. A. E. Wallin, H. Ojala, A. Korsback, E. Haeggstrom, and R. Tuma, "Real-time control of optical tweezers - art. no. 66441Y," in *Optical Trapping and Optical Micromanipulation IV*, K. Dholakia, and G. C. Spalding, eds. (2007), pp. Y6441-Y6441.
32. A. E. Wallin, and R. Tuma, "Beam-stabilized high resolution optical tweezers," Biophysical Journal **88**, 662A-662A (2005).
33. M. T. Valentine, N. R. Guydosh, B. Gutiérrez-Medina, A. N. Fehr, J. O. Andreasson, and S. M. Block, "Precision steering of an optical trap by electro-optic deflection," Opt. Lett. **33**, 599-601 (2008).
34. A. E. Wallin, H. Ojala, E. Haeggstrom, and R. Tuma, "Stiffer optical tweezers through real-time feedback control," Applied Physics Letters **92**, 224104-224103 (2008).
35. E. Schaffer, S. F. Norrelykke, and J. Howard, "Surface Forces and Drag Coefficients of Microspheres near a Plane Surface Measured with Optical Tweezers," Langmuir **23**, 3654-3665 (2007).

Chapter 3 -

Calibrating an optical tweezers with back focal plane interferometry

3. Calibrating an optical tweezers with back focal plane interferometry

3.1. Overview

In this chapter, I shall elaborate on an interferometric technique called back focal plane interferometry (BFP) [1] developed to calibrate an optical tweezers system. As discussed previously in section 1.5.2, this technique has been used to measure the position and stiffness of an optically trapped particle. This chapter is split into seven parts.

In the first section, I will introduce the various techniques that have been used for the calibration of an optically trapped particle. In the second section, I shall describe the technique and the basic setup to achieve BFP interferometry with a quadrant photodiode (QPD). In the third section, a QPD and a nanopositioning stage are used together to measure the change of intensity (interference patterns at BFP) with respect to the particle positions. This step provides a calibrated QPD (conversion factors). In the fourth section, I use the calibrated QPD to track vibrations and drifts in three dimensions on the surface of the sample chamber using a surface adhering microsphere. The basic optical tweezers geometry uses a Gaussian laser beam through a high numerical aperture (NA) microscope objective lens. This arrangement can only provide a single three dimensional trap with an approximately fixed ellipsoidal focal volume, thus constraining the ratio of particle position in lateral and axial directions within the trap. Using the calibrated QPD and a single beam optical tweezers, I measure the ratio of the trapped particle positions in three dimensions with respect to their sizes. After which, I show that by monitoring the position variance of the particle on the calibrated QPD, the presence of multiple particles entering into the trap is revealed.

In the fifth section, I describe two analysis methods that work in either time domain (equipartition method) or the frequency domain (power spectrum density). The equipartition method provides a straightforward and fast measurement of the thermal fluctuations based on the changes in the position of a trapped particle over a given time. On the other hand, the power spectrum density (PSD) method provides the amplitude of the position fluctuations over a given frequency range. This can supply information on both the trap stiffness and contribution of noises at various frequencies. I use the acquired signals from a QPD to derive the spring constant value of an optical trapped particle based on the two methods. I then make a choice on one of the techniques to measure the performance of an optical tweezers system (section 2.4) in the following section.

In the sixth section, the chosen analysis method (PSD) is used to measure the stiffness of the optical trap based on a two parameters: increasing optical power and spherical aberrations

(section 2.2.2). The recorded particle position over a given period of time in each direction can be described by a Boltzmann distribution (probability) that in turn will be directly related to the shape of the potential energy well of the optical trap. Using a position histogram plot and the trap stiffness, I can plot the optical potential energy well of a trapped particle.

In the final section, I make use of the QPD calibration methodology to calibrate the beam positioning of the acousto optic deflector (AOD) and stepper motor at the trapping plane. The stiffness of the trap, k, multiplied with the displacement of the particle, y, provide the values of exerted force, F (F=ky). Using the AOD and QPD, I translate and measure the trap stiffness (stiffness, k) and mean positions (y) of an optically trapped particle over one dimension so as to deduce the exerted optical force, F.

3.2. Introduction

In this section, I provide an overview of the past and present particle tracking methods in optical trapping systems. Ashkin [2] first used the far-field scattered light, collected in orthogonal to the trapping optics, to track the number of viruses entering into an optical tweezers system. Since then, there have been a range of techniques invented to improve the sensitivity in the tracking optically trapped particles. Particle position detections are carried out in a number of ways including digital video microscopy, differential optical interferometry, back focal plane interferometry and evanescent light scattering. Each technique differs in their time response and position sensitivity. It is important to consider the applications before choosing the appropriate methods. Next I give an overview of the different techniques.

The use of digital video microscopy is perhaps the most straightforward method of particle tracking [3]. A sequence of microscopic images is digitally recorded by a coupled charge device (CCD) camera placed at the image plane of the sample. A pattern recognition program is used to track the trapped particle. The pixels on the CCD camera are calibrated against a microscope ruler (typically ≈ 10 μm per division). Although it is possible to achieve sub-pixel resolution for the video tracking method, the response time (frame rate) is severely limited and often not suited for fast position feedback. A recent work by Leonardo *et al* [4] has successfully implemented multiple position measurements with a high speed camera under bright field illumination.. Keen *et al* [5] showed that particle tracking with a high-speed camera can reach an accuracy of 10 nm but with only a bandwidth of a few kilohertz. The main issue was the limitation on the size of the on-board memory buffer. This restricted the duration of data capture to only a few seconds. The high cost and

large amount of data-transfer/analysis associated with the high speed camera limits the number of users that can adopt the high speed camera particle tracking method.

Conventional brightfield differential optical interferometer has been used for enhancing contrast in microscopic imaging (appendix B (i)). Differential laser interferometry was developed by Webb and co-workers [6-10] for sensitive position-sensing along one axis. They measured small displacements and forces of an optically trapped particle with a differential laser interferometer. The differential interferometer operates by collecting the forward scattered light from two orthogonally polarised laser beams. Each laser beam acts as an individual probe beams illuminating the optically trapped particle (≈0.2 μm apart). Each beam would acquire a different phase shift after passing through the optically trapped particle. And when the two beams of orthogonal polarisations are recombined, the resulting beam polarisation would be elliptical. The elliptically polarised light is further split into its orthogonal polarisation components with each illuminating an independent photodetector. Any physical displacements of the trapping particle would alter the phase difference between the two probing beams. The phase differences would then result in a relative change of the intensity at the two detectors. This technique is extremely sensitive (pm) [6] and had been successful in high resolution position and force measurements of biological system [11, 12].

In 1998, Gittes and Schmidt [13] proposed the BFP interference technique for high resolution position mapping of the particle with nanometre accuracy. The technique takes advantage of the first order far-field interference between the scattered and the non-scattered components of the light being diffracted from a trapped microsphere. The interference pattern is mapped [13] onto an optoelectronic detector (quadrant photodiode (QPD) or position sensitive detector (PSD)) [14-20]. The photodetector receives the intensity signal and converts it into voltage. The voltage outputs are put through a differential circuit to indicate the direction of shift in the intensity signal. This gives the change in the particle position along the transverse plane. Due to the interference nature of the pattern, the sum of the intensity signals indicates the axial displacement of the particle. The interference pattern can be collected from either back scattered light (from the same trapping microscope objective used for) or forward scattered light (with another microscope objective). The back scattering geometry provide a weaker signal (intensity) than the forward scattering geometry. This is because it makes use of the weak reflective surface of the trapped particles [18, 21]. In addition, the BFP methods can use the light scattered from a trap that originated from the trapping beam or from a separate laser beam (probe beam). With one quadrant photodetector and the BFP interference patterns, it is possible to detect particle positions in all three directions. This technique also does not depend on the “optical resolution” of the imaging optics field of view. The BFP

detection scheme is by far the most popular technique in the optical trapping community when it comes to implementing position and stiffness measurements of optical traps [22].

A more specific surface positioning sensing method makes use of the light scattered from a trapped colloidal that is held close to the surface. Evanescent wave is generated at the interface where the refractive index of the medium changes from high to low. The intensity of an evanescent wave decays exponentially over a few hundred nanometres into the medium of lower refractive index. By monitoring the intensity of the scattering light from the illuminating evanescent field, it is possible to observe very weak surface forces between a single colloidal particle and a flat surface as a function of separation distance (≈100 nm) [22]. This type of surface particle detection geometry has been successfully applied for the direct determination of weak critical Casimir forces [23]. It is also worthwhile to note that all the techniques, mentioned in this section, do suffer from the lack of capacity in directly tracking multiple particles that are coaligned axially within a single trap. An emerging method called digital holography particle tracking [24] that is pioneered by the Grier group does address this issue. This method has achieved multiple particles tracking in both the transverse and axial plane.

In this chapter, I choose to work with BFP interferometry for position and stiffness measurement, due to its compatibility with the inverted microscope system (section 2.4). In addition, I use the forward scattered light (using a second objective lens) from the optical trapping beam for the BFP interference.

3.3. Back focal plane interference

In this section, I will explain the origins and the experimental setup of BFP interferometry. When a focused light beam from the microscope objective (MO) passes through a sphere, the diffracted light interferes with the undiffracted light. The Gouy phase [25, 26] at the beam focus position introduces an important π phase shift between scattered (spherical) and unscattered (planar) light at the focal region of the beam. The microsphere acts like a diffracting aperture. The phase difference creates a first order interference pattern at the BFP of the detection objective (DO) lens as seen figure 3.1A. The analytical approach, proposed by Gittes and Schmidt [13], follows the Rayleigh scattering of a small particle. They formalised that the average change in the interference of the scattered and unscattered light field ΔI onto a QPD detector over the total far-field interference signal I_{total} in a mathematical expression given in equation 3.1,

$$\frac{\Delta I}{I_{total}} = \frac{2k^3\alpha}{\pi r^3}\exp\left(\frac{-r^2}{w_o^2}\right)\sin(kr)\sin(\theta)\cos(\phi)\exp\left(\frac{-k^2 w_o^2\theta^2}{4}\right) \qquad (3.1)$$

where $k = 2\pi n/\lambda$, λ is the wavelength of the laser and n is the refractive index of the medium, $r = \sqrt{x^2 + y^2}$ where x and y are the transverse coordinates, θ is the angular aperture of the collecting lens, ϕ is the azimuthal phase variation, w_0 is the beam width of the trapping laser, $\alpha = r^3\left(m^2 - 1\right)/\left(m^2 + 2\right)$ is the polarisability of the object and m is the ratio of the refractive index $n_{particle}/n_{medium}$.

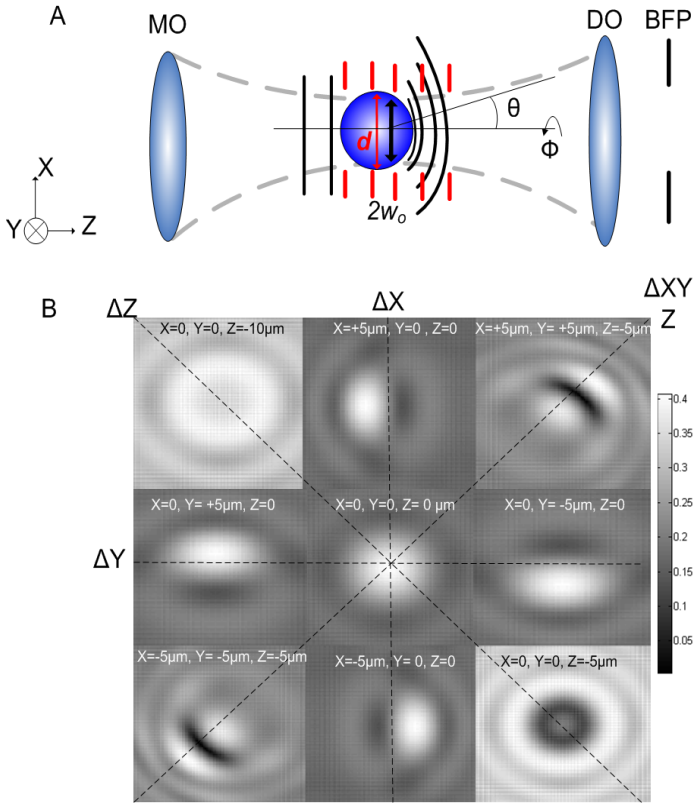

Figure 3.1 – BFP interference. (A) diagram illustrating the interference between the scattered light (black) and unscattered light (red) from an optically trapped sphere. The microscope objective (MO) lens focussed the beam into the sphere of diameter d.. The beam waist at the focus is given by w_o. The scattered light from the microsphere possess a spherical wavefront. The scattered light interferes with the beam at the focus position, which is planar. The interference light is then collected by a detector objective lens (DO). θ is the angular aperture of the DO lens, ϕ is the azimuthal phase variation. (B) shows the numerically calculated interference pattern of a spherical wave with a focused light field at different transverse and axial positions (X,Y,Z).

In figure 3.1B, I numerically calculated the BFP interference. This is done by numerically propagating a small spherical wave with a focused Gaussian beam (lens of focal length 170 µm)

located at the focus. The two fields are collected by a second lens at its BFP. A series of far-field interference patterns are calculated by moving the lateral (ΔX, ΔY) and axial position (ΔZ) of the spherical wave at discrete displacements about the focal volume of the beam. The discrete interference patterns (first order) are correlated with the movement of the spherical wave as shown in figure 3.1B. This intensity shifts in the interference pattern are correlated with the positional shift in the spherical wave, as illustrated in figure 3.1B, in all three dimensions (XYZ). A QPD placed at the plane of the interference patterns records this intensity shift as voltage signals in the respective quadrants. The output voltage signals are then differentially calculated to give values for X and Y position shifts in the transverse direction. The change in the sum of the voltage from all the quadrants gives the position shift in the axial (Z) direction.

Due to the optical nature of the technique, it is important to carefully select the appropriate microscope objectives (NA) lens to be the detection objective lens. This is so as to obtain maximum sensitivity in the interference pattern [5]. Rohrbach *et al* [27] performed the calibration of the polystyrene spheres of diameter of 0.7 μm to 2 μm. He concluded that an objective with an NA of 0.5 works best for this range of particle sizes. The reason behind this is because a relatively low NA (0.5) objective lens would collect more light over a larger depth of focus than the high NA objective lens (>0.9) [27]. So the interference between the plane wave and the spherical wave (from the particle) can be tracked over a long axial distance. In the detection setup described in figure 3.2, I use a microscope objective with a NA of 0.65 (40X, Nikon Eplan) as the DO lens. The NA of the chosen DO lens is close to the suggested NA by Rohrbach.

Figure 3.2 shows the actual setup (with illustrated schematic) that is used to relay the BFP of the DO into the QPD. A simple way to align the BFP onto the QPD is to use a phase contrast objective lens. The DO lens is first replaced by an identical (NA and magnification) phase contrast microscope objective lens. In a phase contrast objective lens, a phase ring is located at its BFP, as seen in figure 3.3A. **The image of the ring serves as the alignment marker for the QPD. Hence, it is possible pre-align the QPD accurately without using trapped spheres or laser beam.** In figures.3.3B and C, I show the BFP interference image of a single trapped 1 μm (diameter) sphere that is at two different axial planes captured by a digital CCD camera. Here, the trapping beam is used as the particle tracking beam. The optical trap here is generated by focusing the manually steered Gaussian beam (figure 2.6) through a microscope objective lens (MO) with a NA of 1.25.

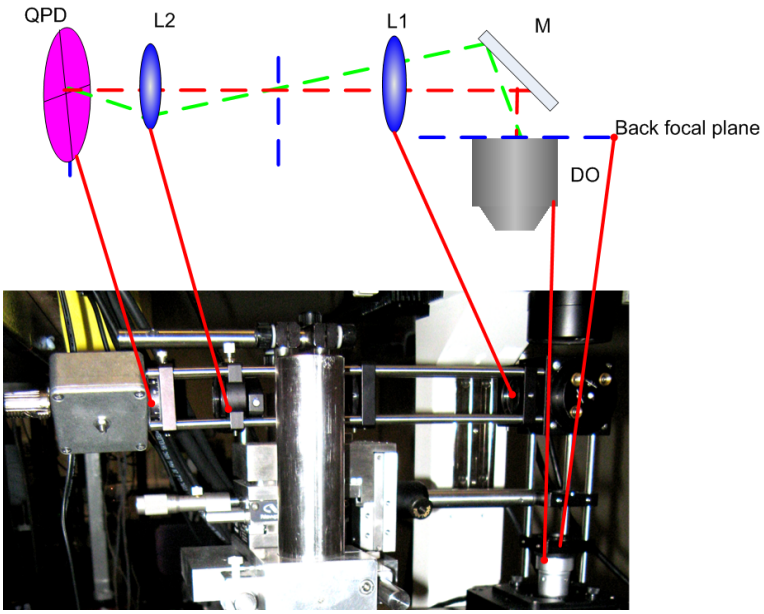

Figure 3.2 Back focal plane interference and quadrant photodiode setup. (Top) show a scehematic of a two lens relay (L1 and L2) system that demagnifes the image of the BFP of the detection objective (DO) lens onto the QPD after dielectric mirror M. The blue dotted line indicates the conjugate imaging planes of the BFP. (Bottom) shows the actual optical setup that collects the forward scattered light from the sample. The microscope objective MO is not shown in this diagram. The entire setup will be illustrated later in figure 3.19.

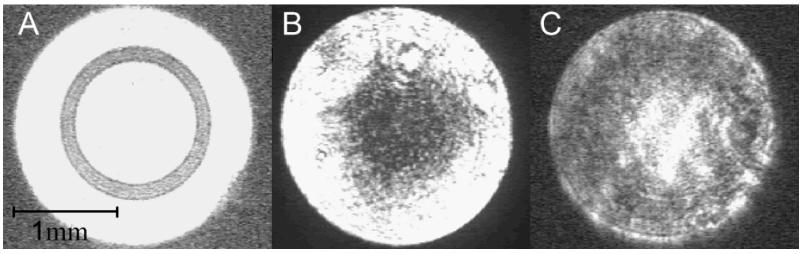

Figure 3.3 Back focal plane interference images. (A) show the phase contrast ring at the BFP at the QPD image plane and B, C is the interference patterns from a trapped 1 μm (diameter) sphere taken at two different axial planes.

3.4. Calibrating the quadrant photodiode (QPD)

In this section, I first explain my choice of the QPD used to capture the BFP interference. After which, I demonstrate how to calibrate a QPD with a particle stuck on the bottom of the sample chamber with a nanopositioning stage. The QPD measurement is done with ***the static optical trap (figure 2.6)*** formed by the beam after the PBS 3. The trapping beam used in the calibration is not steered with the AOD. The optical trap is formed with a high NA (1.25) microscope objective (MO) lens. The optical power at focus is 40±1 mW.

There are generally two types of semiconductor photodetectors i.e. silicon (Si) and indium gallium arsenide (InGaAs), each is optimised for visible (500-800 nm) and infrared (800-1300 nm) wavelength respectively. The choice of the quadrant photodetector is critical for optimal time response, reduced parasitic filtering effects and the high sensitivity of detector active area [28, 29]. The QPD has a typical bandwidth (> MHz) and fast response/rise time (≈ ns). The QPD essentially acts like a four pixel CCD. It easily exceeds the high frame rate camera (large array of pixel) in terms of data acquisition speed and cost. QPDs are placed in either an image or BFP for two- or three dimensional positions sensing respectively. In the current system, I have chosen the InGaAs QPD that is from Hamamatsu Pte Ltd (part no. G6849). The detector is ideally suited to detect intensity with the trapping laser beam (λ=1070nm). The parasitic filtering effects are reduced when using infrared light on the InGaAs QPD [30]. However, the total active area (sum of four quadrants) of InGaAs QPD (≈2 mm X 2 mm) is usually much smaller than silicon based detectors (≈ 10 mm X 10 mm). This means that additional optics is necessary to reduce the image of the back aperture of the DO as seen in figure 3.2.

As mentioned in the previous section, the interference of the scattered and unscattered light field can be use to infer onto the relative three dimensional positions of an optically trapped sphere. To accurately establish the position of the sphere with the interference pattern, a nanopositioning stage is used to move a fixed particle (for a given particle with refractive index n_p and size d) over the laser beam at sequential step sizes. By plotting the intensity change (QPD) versus the fixed particle displacement (nanopositioning stage) about the beam, the BFP interference patterns can be calibrated against particle positions. The plot of voltage (V) against particle displacement (μm) is a linear within a certain region in the beam. Using this linear relationship, a linear conversion factor (V/μm) is obtained ($V_{xcalib}, V_{ycalib}, V_{zcalib}$). It is then possible to map out the actual position of the trapped spheres [15-20].

Positions of the particle from the QPD, P_{QPD}, are read as voltage signals (μm) after the conversion factors are included. The voltage signal (V) from each individual quadrants are given as I_1 I_2 I_3 and I_4 (like quadrants in a two dimensional coordinate system). The values of the particle position are given as I_x, I_y and I_z . These values are derived from the difference and sum of the individual quadrants. With the conversion factor $V_{xcalib}, V_{ycalib}, V_{zcalib}$ (V/μm)., the position in voltage (V) are converted to physical displacement (μm) as shown in equation 3.2,

$$P_{QPD}(t) = \left(I_x(t)/V_{xcalib},\ I_y(t)/V_{ycalib}\ ,I_z(t)/V_{zcalib}\right)$$
$$= \left(\frac{I_1(t)-I_2(t)+I_3(t)-I_4(t)}{I_1(t)+I_2(t)+I_3(t)+I_4(t)} \frac{1}{V_{Xcalib}}, \frac{I_1(t)+I_2(t)-I_3(t)-I_4(t)}{I_1(t)+I_2(t)+I_3(t)+I_4(t)} \frac{1}{V_{Ycalib}}, \frac{I_1(t)+I_2(t)+I_3(t)+I_4(t)}{V_{Zcalib}} \right) \quad (3.2)$$
$$= \left(\langle X(t)\rangle, \langle Y(t)\rangle\ , \langle Z(t)\rangle\ \right)$$

The choice of a good nanopositioning stage is important in achieving the appropriate resolution in the calibration (accuracy of 5 nm or better). The precision of stage motion defines the accuracy of the conversion factor. In my experiment, I chose three axis nanopositioning stage (Physikinstrumente, 733.3D). The stage has a resolution of 0.1 nm for every axis and a repeatability of less than 2 nm.

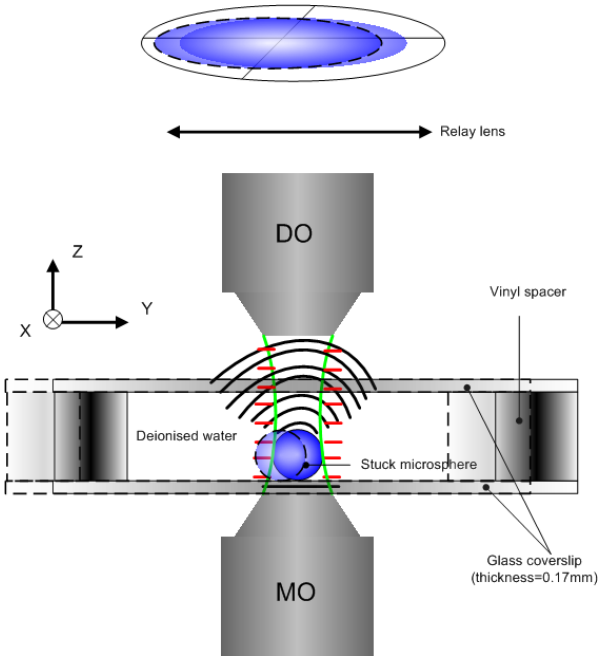

Figure 3.4 Stuck particle calibration. Illustration of the stage scanning process for a sphere stuck at the bottom coverslip. MO lens is used to focussed a Gaussian beam onto the stuck microsphere. The scatttered and unscattered are collected by the detection objetive (DO) lens. The interference at the BFP of the DO is relayed onto the QPD using the relay lens. The sample chamber is made up of a circular vinyl space with two microscope coverslips.

The scanning process to obtain the conversion value is illustrated in figure 3.4. Figure 3.4 shows a Gaussian beam focused through a microscope objective (MO) lens illuminating a sphere, which is adhered to the surface of a sample chamber. The microsphere is adhered onto the bottom surface of the chamber by dry sedimentation. The sample chamber is formed with two glass

coverslips and a single cylindrical vinyl spacer (1cm in diameter, 100 µm in depth). A detection objective (DO) lens is placed above the sample chamber. A relay lens lies after the DO lens that images the BFP of the DO onto the QPD. The scattered light and unscattered light emerging from the microsphere are led to interfere at the BFP of the DO lens. The interference pattern, indicated by the solid blue circle is projected onto a QPD. The sample chamber is mounted onto the nanopositioning stage. The stage movement in the transverse direction changes the position of the sphere in the trapping beam and therefore the interference pattern on the QPD, as indicated by the dotted circle. This schematic only illustrates the scanning procedure in one direction (Y). In practical, custom software (©Labview) is use to ensure that the QPD registers a voltage signal at every step the stage takes.

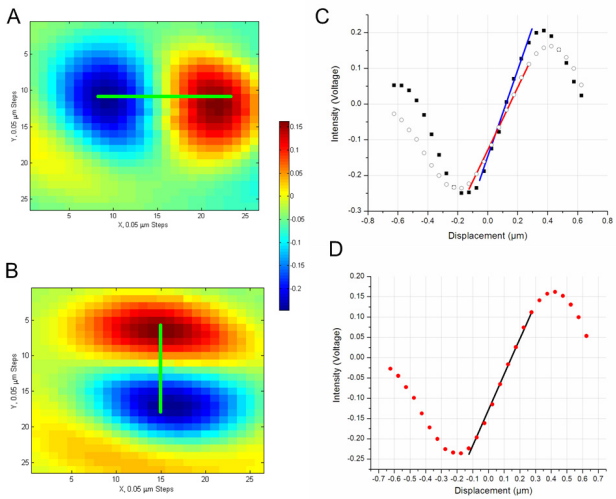

Figure 3.5 Calibration graphs for 0.78µm spheres. A and B shows a two dimensional plot for the transverse X, Y on a stuck 0.78µm (diameter) sphere obtained experimentally. The images of the two dimensional scan reflects the actual image seen by the QPD. The scan area is around 2.5 µm at a step size of 0.05 µm. C shows the linear plot for X (red) and Y(blue) each obtaining a calibration factor of 0.85 (red) and 1.15 (blue) respectively. D shows the axial calibration factor of 2.12. Each graph C,D is given a linear fit to measure the calibration factor.

In practice, the experiments are carried out with a stuck 0.78 µm (diameter) sphere. The scan area is around 2.5 µm at a step size of 0.05 µm. In figure 3.5 A and B, the intensity patterns recorded by the QPD on the transverse plane are calculated with respect to the differential voltage signals I_X and I_Y. Figure 3.5 C shows the one dimensional plot (dots) and linear fit (solid line) for transverse planes X and Y at the selected linear region (line in figure 3.5A and B). Figure 3.5D shows the one dimensional plot of the axial stepping. From the linear fit in figure 3.5 C, a linear conversion factor V_{xcalib} equals to 0.85 V/µm(red) and V_{ycalib} equals to 1.15 V/µm (blue) respectively. Figure 3.5 D shows the axial linear conversion V_{zcalib} is 2.12 V/µm. The trapping

beam power at the sample remains fixed at an optical power of 40mW. In figure 3.6, I performed a series of calibration for a range of the particle sizes along the transverse (X, Y) and axial position (Z) [27]. By taking a linear fit along the coloured (grey) regions on the graphs in figure 3.6, I obtained a list of the conversion factors (V/µm) based on particles size (µm) in table 3.1. The total lateral linear range for the different particle size (0.5 µm to 3 µm) varies between 0.5 µm to 1.6 µm and the axial linear range varies between 1 µm to 2 µm. In general, the particle size will affect the range detection range of the QPD and the NA of the detection lens will affect the calibration scaling factor.

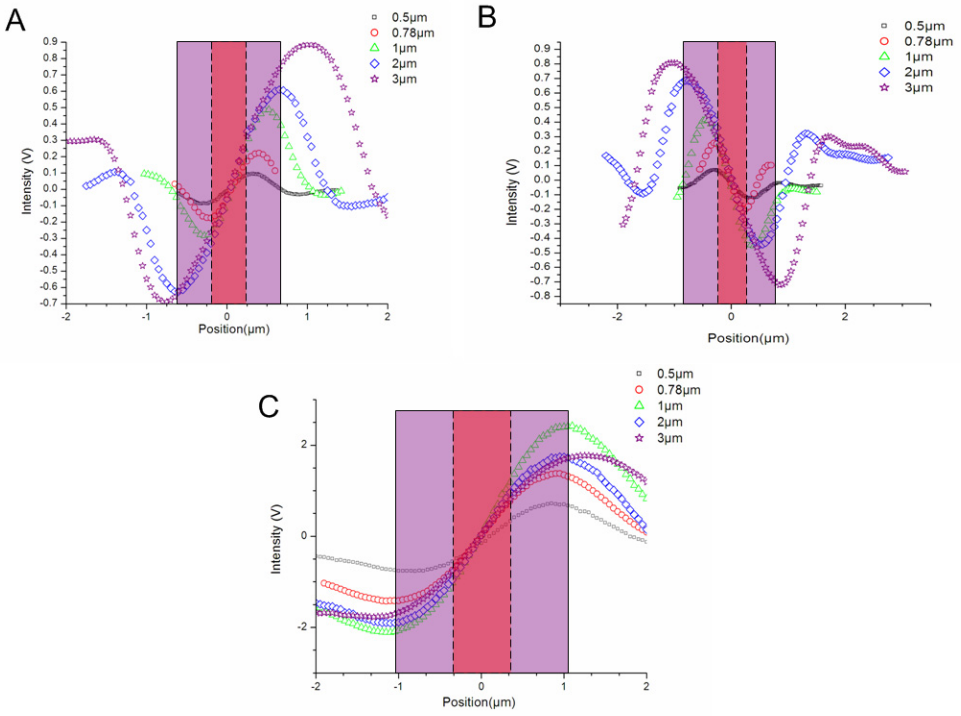

Figure 3.6 Calibration graphs. shows the one dimensional plot of five polymer spheres with different diameters (0.5, 0.78, 1, 2 and 3µm). (A) – X axis, (B) – Y axis and (C)- Z axis. The step size for each axis is 50nm for sphere sizes of 0.78 µm to 3 µm spheres. Only for 0.5 µm spheres, a step size of 10nm is used. Figure 3.6A and B show that the range where the linear region of the graph scales with the particle sizes. The calibration factor obtained from the three graphs listed in table 3.1. The highlighted box marks the approximate linear range for all the spheres size on the QPD.

Size (µm)	**V_{Xcalib} (V/µm)** ± 0.02	**V_{Ycalib} (V/µm)** ± 0.02	**V_{Zcalib} (V/µm)** ± 0.03
0.5	0.43	0.42	0.8
0.78	0.85	1.15	2.12
1	1.37	1.49	3.11
2	1.28	1.28	2.45
3	1.23	1.05	2.07

Table 3.1. List of conversion factors. This table lists the conversion factor of different particle sizes (diameter (µm) = 0.5, 0.78, 1 ,2 ,3) . The average variance of the measurements (five data set) is given in ±.

3.5. Measuring particle position with calibrated quadrant photodiode

This section covers the measurements of particle position using the calibrated QPD. There are three subsections in this section. As a first step, I track the position of a particle stuck at the bottom of the chamber (a glass coverslip). The position of the stuck particle reveals vibrations and drifts in the static stage. Next, I modulate the nanopositioning stage containing the stuck particle with a square wave (step function of positions) and track the changes on the QPD. This measures the accuracy of the conversion factor.

In the second step, I trap microspheres of different sizes using a single optical tweezers. By monitoring the position of the trapped particle, an asymmetry in the distribution in the particle position over three dimensions is observed. The symmetry of the position distribution of a different particle size (trapping volume) will vary for an optical trap of a fixed focal volume.

Finally, I monitor the position variance of a trapped particle along one dimension. The position variance shows evidence of multiple particles entering into the optical trap.

3.5.1. Position measurements with a stuck microsphere

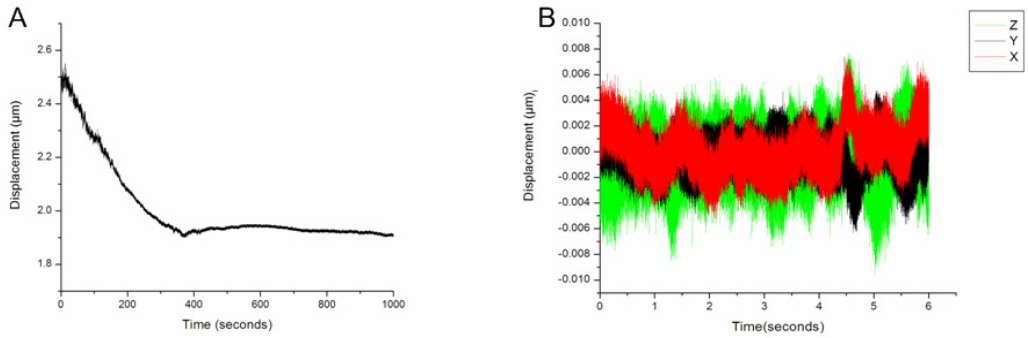

Figure 3.7 Drift and vibrations. The plots of a stuck 0.78µm polymer sphere position are plotted over time. (A) Axial position drift (displacement) over time (s). A large initial drift of about 600 nm lasted for approximately 400 s before stabilisation. (B) After stabilisation (1000 s), the position fluctuations of the stuck particle position (µm) over time (6 s) in three dimensions (XYZ) Red (X), black(Y) and Green (Z). The particle fluctuates approximate 5-8 nm in all three dimensions.

Illuminating the trapped beam (now acting like a probing beam) onto a single particle stuck on the surface of the sample chamber can reveal a range of background vibrations. These background vibrations include mechanical vibrations, temperature fluctuations and movement of the immersion medium (if using oil immersion objectives lens). The data collected over a given time period from the calibrated QPD measures the amount of background vibrations. It is important to

access the background noise before any trapping measurements are taken. These measurements can be done with an uncalibrated QPD so as to measure the shift of particle position relative to an initial start point (voltage readings).

Figure 3.7A shows the recorded position drift on a stuck sphere (diameter 0.78 μm) along the axial (Z) direction of the stage over 1000 s right after the sample is placed. The initial drift lasted for ≈ 400 s and over ≈ 600 nm. The initial drift in axial position is postulated to arise from the heavy mechanical mount used to mount the microscope objective turret. The initial transverse (XY) drift is low (< 200 nm) before stabilisation. The transverse drift is primarily affected by the viscous drag imposed of the oil immersion medium because it is being compressed in between the coverslip and front face of the microscope objective. The thermal gradient within the optical train can also cause miniscule expansion and drift in the optics. As there is very little temperature gradient in the sample around (no heated stage or in the incubation chamber (ΔT_{stage} = ± 1.5 ^{o}C/hr), I do not see a significant position change due to temperature. Figure 3.7B shows the positions of the stuck sphere over a 6 s period upon stabilisation. It indicates only a 5-8 nm change of the position variance in all three dimensions. In order to reduce the drift in the stage, it is possible to include active feedback/drift compensation software with an automated stage. This indicates a relatively low background noise on the surface. Other sources of noises include shot noise and amplitude noise resulting from statistical fluctuations at the detector from the source (trapping laser) is also measured without a sphere. The dark noise generated by the detector i.e. constant background signal is measured with the absence of any illumination. In addition, the electronics that process the intensity- voltage signal conversion can contain electronics and electrical noise (the detector is 1/f noise taken from the data sheet and external noise from power sources measured with a voltmeter). In our setup, the noises (dark, shot, amplitude, electronic and electrical) are reduced to ≈ 0.1 % (i.e. 1mV noise for the signal of 1V).

Before I start any position measurements of a trapped sphere, I first measure the displacement of the nanopositioning stage with a stuck particle. This tests the accuracy of the conversion factor. As an example, I showed the position tracking of an oscillating 3μm diameter sphere that is stuck on a surface of the sample chamber. The sphere is scanned over the trapping beam at 5 Hz in all three dimensions at a specific distance. The scanning process goes forward and backward like a square wave function as shown in figure 3.8A. From the conversion, in table 3.1, the step size that the particle has moved is calculated to be, X = 9.3 ± 0.5 nm, Y = 18± 0.5 nm and Z = 78 ± 0.5nm. The measured step size is within 15 % of the induced step size of 10 nm, 15 nm and

80 nm by the nanopositioning stage. Figure 3.8B shows the tracking of the same 3µm polymer sphere along the axial direction as the step size decreases from 40 nm to 20nm.

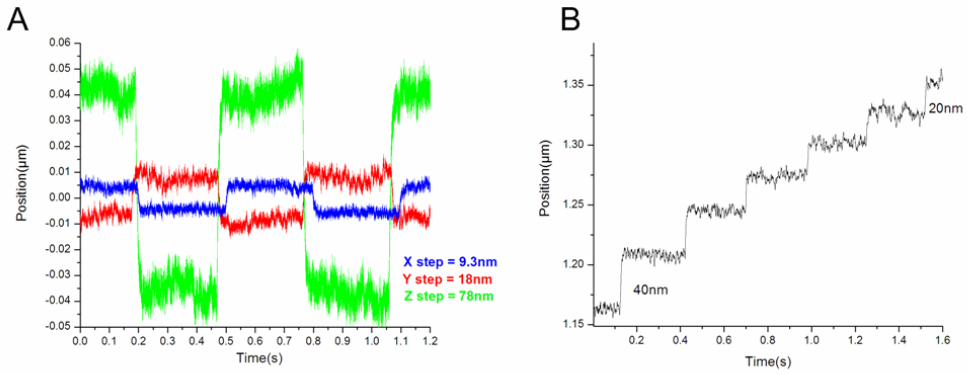

Figure 3.8 Measured stuck 3 µm particle displacement when moved by nanopositioning stage (A) The scanning process goes forward and backward like a square wave function (5Hz). The induced step size of by the nanopositioning stage 10 nm (X), 15 nm (Y) and 80 nm (Z). The measured displacement is X = 9.3 ± 0.5 nm, Y = 18± 0.5 nm and Z = 78 ± 0.8nm. (B) Decreasing step size of 5 nm step sizes over time (after averaging)

3.5.2. Particle size and trapping volume

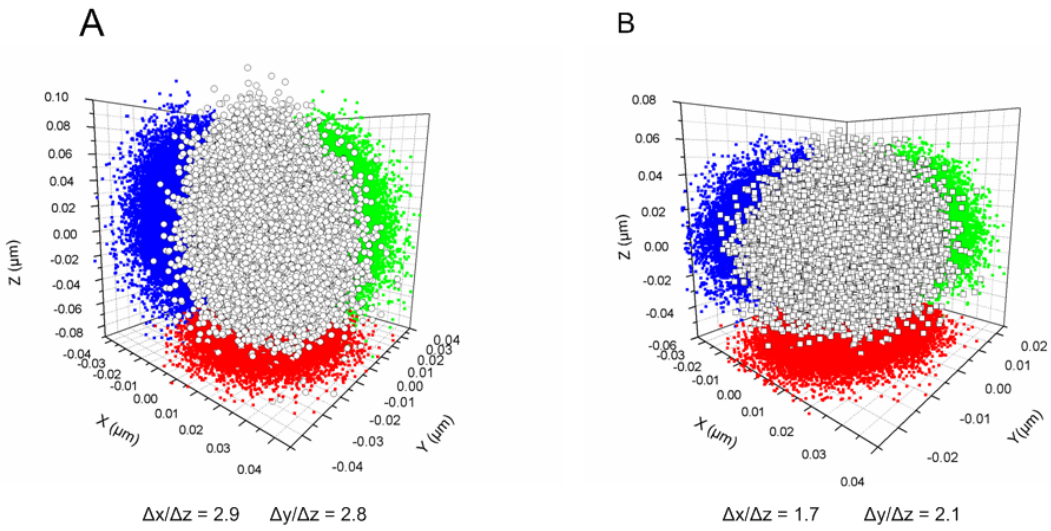

Figure 3.9 Scattered plot of the trapped trapped microsphere of diameter 0.5 µm and 1 µm positions. A shows the three dimensional distribution (XYZ) of the particle position different particle size for 0.5 µm and B for 1µm. The magnitude of the particle displacements in three dimensions defines the trapping volume. The coloured spots are the projected particle position in the respective axis.

A focused Gaussian beam provides a single three dimensional optical trap (optical tweezers). The focused Gaussian beam has an approximately ellipsoidal focal volume. The axial intensity gradient (confocal parameter) is larger than the transverse intensity gradient (beam waist)

and that causes the ellipticity in the trap. The area under the intensity gradient constrains the trapped particle displacements in lateral and axial directions. Particles of different sizes can still move within the intensity gradient of the optical trap. The magnitude of the movement defines the trapping volume. In other words, the size of the particle (dielectric without any enhanced polarisability) can influence the trapping volume. As such, the optimal trap volume for each particle size can vary for different of beam parameters. Intuitively, the particle would need to fill the entire focal volume of the trapping beam, so as to obtain the best optical trap i.e. rod-like particles.

Here, I illustrate by trapping two polymer spheres (1μm, 0.5μm in diameter) in two separate trapping experiments using a single optical tweezers. The acquisition parameters determine the ability to resolve particle position at a given time resolution. Here, I use 20,000 samples at a sampling rate of 50 kHz. The sample rate will provide a data point (particle position) every 20 ms. Increasing the number of samples can average any additional random fluctuations (longer acquisition time). The optical power at the sample is 40±1 mW. Each particle is held at a distance of up to ten times or more of their diameter away from the bottom coverslip, so as to reduce hydrodynamic corrections ($r/h < 0.1$) according to Faxen's correction. From figure 3.9, the transverse symmetry of the trap is observed to be more uniform for the 0.5 μm sphere (A) as compared to the 1 μm sphere (B). On the other hand, the asymmetry along the transverse versus axial dimension is larger for the 0.5 μm sphere than the 1 μm sphere. The ratio of the transverse displacement over the axial displacement: $\Delta x/\Delta z$, $\Delta y/\Delta z$ are consistent with previous experiments [31, 32]. The measured confocal parameter of the beam is Z= 0.985 +/-0.06 μm and the transverse beam parameters (full width half maximum) is X = 0.39 +/-0.01 μm and Y=0.28+/-0.01 μm nm. Hence, for the current trapping volume, the 1 μm sphere over-fills the focal volume and leads to a more symmetrical trap. However, the 0.5 μm sphere under-fills the area under the axial intensity gradient and therefore leads to large displacements in the axial direction than the transverse direction. The symmetry of the trapping volume (focal volume) is heavily dependent on the particle size.

3.5.3. Multiple trapped particle tracking

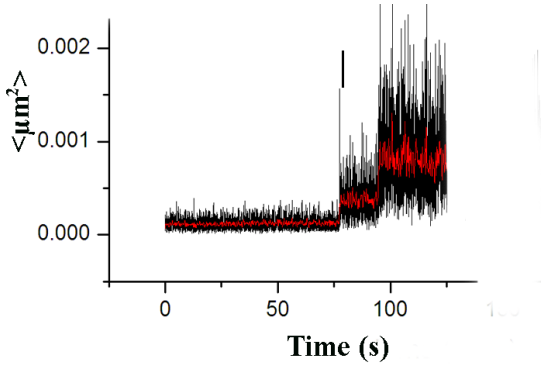

Figure 3.10- Position variance from single to three particles trapped in an optical trap. Position variance is plotted against time. The trap starts off with one sphere and after the observation of 150 s, there are two other particle entering into the trap. Each three discrete step increase in the variance indicates one additional 0.78 μm particles going into the optical trap. The red plot line references to the linearly averaged data.

When more than one particle resides within an optical trap, the degree of displacement measured at BFP interference pattern will increase. This means larger position variances. Hence, by observing the position variance over time, it is possible to trace the number of particles entering into the trap. Here I start off with one trapped particle and monitor the position variance over 150 s. The concentration of the sample is such that there are approximately 10 spheres within a 50 μm by 50 μm field of view. In figure 3.10, there are two distinct jumps in the variance over 150 s period, where each discrete jump indicates newly trapped spheres (diameter 0.78μm). This is confirmed with brightfield video imaging. This form of tracking is particularly useful in the tracking of nanoparticles [33]. However, this form of tracking is not able to differentiate the positions of the individual particles within the trap.

3.6. Trap stiffness analysis

This section is divided into three subsections. In first two subsections, I describe the two methods use for the analysing the stiffness (spring constant) of an optical trap. The two analysis methods analyses position fluctuations over a given period of time or a range of frequencies.

In the last part of this section, the analysis is carried out by measuring the trap stiffness of an optical trapped microsphere using a single optical tweezers. Based on the results from the two

methods, I then select a suitable trap stiffness analysis method that is to be use in the remaining part of the chapter for trap stiffness measurements.

3.6.1. Time domain

The equipartition theorem states that each degree of freedom (x, y, z) in a harmonic potential (optical trap) has $k_B T/2$ of energy. The magnitude of particle displacement within the trap in a given direction over a time can therefore indicate the strength of the trap. A particle held in a trap with a "stiffness" of k at position x possess a potential energy of $\left(k\left\langle(x-x_{mean})\right\rangle^2\right)/2$. Hence, a simple relationship is formed between the thermal energy (k_BT) at the medium temperature (room temperature, ~25 ^oC where $k_BT \sim 0.0041$pN μm), and the positional variance of particle $\left\langle x^2\right\rangle$ bound in the over-damped harmonic potential is established. The exerted force is then calculated to be kx .The stiffness of the trap derived using the equipartition theorem is show in equation 3.3

$$k = \frac{k_B T/2}{\left\langle(x-x_{mean})^2\right\rangle/2} \tag{3.3}$$

where k_B is the Boltzmann constant (1.380×10^{-23} J/K)and T is the temperature in Kelvin.

Using the conversion factors ($V_{Xcalib}, V_{Ycalib}, V_{Zcalib}$) in table 3.1 and the equipartition theorem, the position data from the QPD is use to measure the stiffness of the particle. By simply measuring the variance of the particle position, the trap stiffness, k, can be readily extracted. This particular calculation is independent of the viscous drag co-efficient and do not requires a correction for the proximity of the trap to the adjacent surface. However, the sensitivity of this technique depends on the intensity illuminating on the QPD. In some cases, a separate beam of a fixed power is used to probe the trapped particle so as to ensure the sensitivity of the technique is not compromise when the optical powers of the trapping beam changes. When the trapping beam is used as the probe beam, the voltage to position conversion factor needs to be constantly monitored at each trapping power [34].

3.6.2. Frequency domain

In the frequency domain [35], the modified Langevin equation of motion in one dimension (x) in section 1.4 is further developed. I first remove the inertial term which is negligible compared to the viscous drag and the new equation appears in equation 3.4:

$$\frac{\partial x(t)}{\partial t} + \frac{k}{\gamma} x(t) = \sqrt{\frac{4k_B T}{\gamma}}.n(t)$$
$$\frac{\partial x(t)}{\partial t} + 2\pi f_c x(t) = 2\left(D\right)^{1/2} n\left(t\right) \quad (3.4)$$

where γ is the drag coefficient; and the second term is the optical restoring force for the trap stiffness, k , is associated with the roll off frequency, f_c , by $f_c = k / 2\pi\gamma$ and the Brownian fluctuating force, $F_f\left(t\right)$ is at temperature T is associated with Einstein's diffusion coefficient, $D = k_B T / \gamma$ under Gaussian random process over time $n(t)$.

The Fourier transforms of $x(t)$ and $n(t)$ gives $x(w) = \int_{-T}^{T} x(t) e^{i2\pi f_w t} dt$ and $N(w) = \int_{-T}^{T} n(t) e^{i2\pi f_w t} dt$ respectively. The Fourier transform of equation 3.4 is rewritten as equation 3.5,

$$x(w) = \frac{\sqrt{D}.N(w)}{\pi(f_c - if_w)} \quad (3.5)$$

where $f_w = \frac{w}{T_{measured}}$, $T_{measured}$ is the measured time period and *w* data taken for each run.

The Gaussian uncorrelated noise $n(w)$ is dropping when solving for the power spectrum density. The power spectrum is the Fourier transform of the auto-correlation of the voltage signals over the range of frequency, *f*. For w>0, I obtain the equation 3.6 from equation 3.5,

$$PSF_w = \frac{\left|x(w).x'(w)\right|}{T} = \frac{D}{\pi^2(f_c^{\,2} + f_w^{\,2})} \quad (3.6)$$

Experimentally, the Fourier transform would be performed discretely than continuously as shown in equation 3.7,

$$x(w) = \frac{1}{f_{sample}} \sum_{j=1}^{N} e^{i2\pi j \frac{1}{f_{sample}} w} x(j) \quad (3.7)$$

where $T_{measured} = N\left(1/f_{sample}\right)$, w = -N/2+1,…N/2.. and f_{sample} is the sampling frequency which is twice the Nyquist frequency. Equation 3.6 is a Lorentzian equation that can be fitted using a least square procedure. The values from the fitting proceed will give the roll off frequency f_C and then obtain the trap stiffness $k = 2\pi f_c \gamma$ in equation 3.4.

Using this technique, the QPD need not be calibrated. Instead, the rough voltage values (I(t)) is used. In equation 3.8, I show the equation to solve for the power spectrum density (PSD) with fast Fourier transforms and the position values I_x, I_y and I_z from the QPD ,

$$PSD_{\mathrm{QPD}}(f) = \left(\left| \frac{\mathrm{FFT}(I_X(t)) \times conj(\mathrm{FFT}(I_X(t)))}{N} \right|, \left| \frac{\mathrm{FFT}(I_Y(t)) \times conj(\mathrm{FFT}(I_Y(t)))}{N} \right|, \left| \frac{\mathrm{FFT}(I_z(t)) \times conj(\mathrm{FFT}(I_z(t)))}{N} \right| \right) \tag{3.8}$$

where N is the number of samples (sampling frequency ≥ half of the Nyquist sampling frequency), FFT is the fast fourier transform and *conj* notates the complex conjugate. The experimentally obtained power spectrum density $PSD_{\mathrm{QPD}}(f)$ in one dimension (y) will have a Lorentzian form as shown in equation 3.9,

$$PSD_{\mathrm{QPD}}(f) = \frac{k_B T}{\pi^2 \gamma (f_c^2 + f^2)} \tag{3.9}$$

where $k_B T$ is the energy of the particle at room temperature (*T*), the corner (roll-off) frequency f_c is simply given by, $f_c = k_y / 2\pi\gamma$ and γ is the drag coefficient. Drag force given by $6\pi\eta r v$ where η is the viscosity of the medium, r is the radius of the particle, v is the velocity of the particle as it travels in the medium or the velocity of the fluid flow against the particle. As the corner frequency f_c, is independently derived from the power spectrum density. Hence the quality of the trap may be determined without the need for a calibrated detector in contrast to the equiparition theorem (time domain).

The two techniques work in tandem so as to provide an appropriate counter checking of the measurement of the trap stiffness. However, it is important to know that the calibration values used in the time domain analysis are different for each laser power. This would require a different calibration factor for each trapping power levels and particle sizes [34]. Such sensitivity considerations are not required for the Fourier domain analysis. In the following sections, the

experimental measurements of trap stiffness on a single trapped particle in an optical tweezers system are elaborated. From the results, the preferred analysis approach is chosen.

3.6.3. Measuring trap stiffness of an optically trapped microsphere

In this section, I look at the computation of the stiffness of the trap using both the equipartition and power spectrum methods. A single focussed Gaussian generated using a microscope objective with a NA of 1.25 is used to form the three dimensional optical trap.

As an example, an optically trapped polymer sphere (diameter 0.78µm, 10% size variations, Bangs Lab Pte Ltd) with a power of 40±1 mW is held at 8.5 µm away from the bottom coverslip with its displacement recorded by the QPD over a 6 s time period. The rate of acquisition is 50 kHz with 20000 data points. Figure 3.11 A shows the plot of the position of the polymer sphere over a 6 s acquisition time period and figure 3.11 B is the three dimensional scattered plot of the trapped particle over the same time period in all the three dimensions (XYZ).

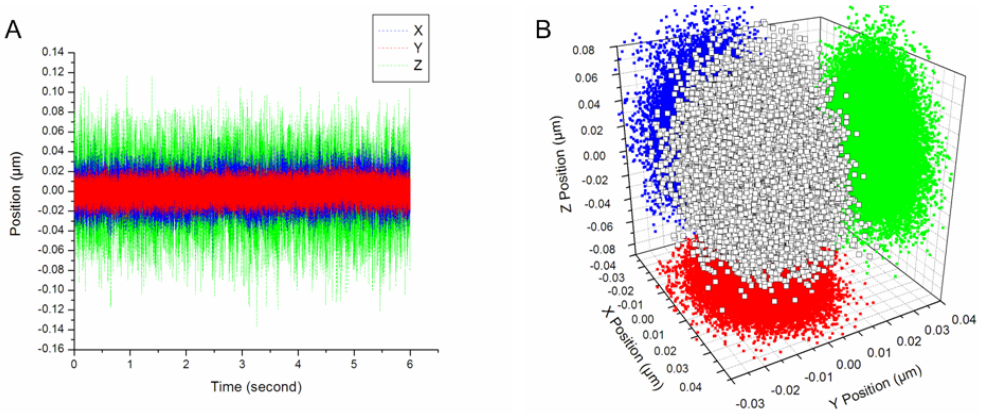

Figure 3.11 Trapped particle position in all three dimension (0.78µm polymer sphere) with trapping power 40±1 mW at the sample. (A) Trapped particle position over time (X blue, Y red, Z green). (B) Three dimensional plots of the time trace in (A). X red, Y blue, Z green

The trap stiffness for the 0.78 µm diameter sphere computed with the equipartition (time domain approach) is given to be k_X=25.0 pN/µm, k_Y= 59.2 pN/µm and k_Z= 5.1 pN/µm. The inequality in the lateral trap stiffness is due to the polarisation of the trap (X-polarised) and weak axial trap stiffness is due to the asymmetrical focal volume that is typical of highly focused beam (Appendix A). The equipartition method is a very straightforward way to determine the stiffness of a trap based on the particle position but does require a precise position calibrated detector.

To compute trap stiffness with the power spectrum method in the frequency domain, the frequency roll off, $f_c = k_y / 2\pi\gamma$, of the power spectra density plot is required. This method requires curve fitting procedures and is therefore less straightforward.

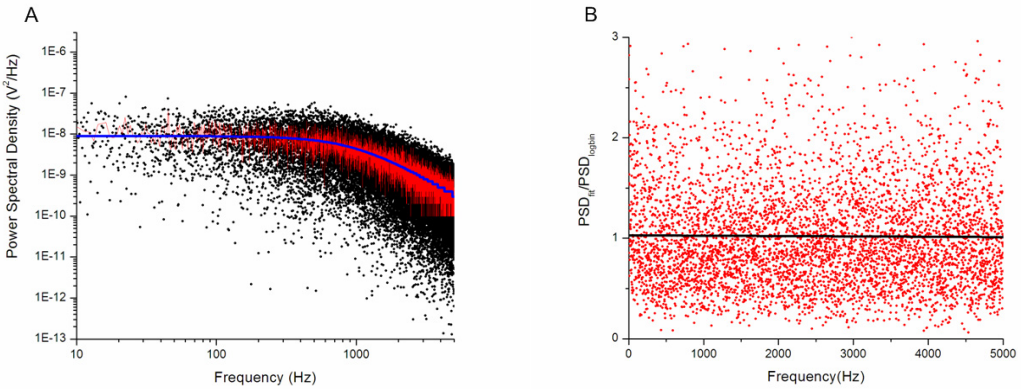

Figure 3.12 Binning of power spectrum graph and curve fitting. (A) shows the unbinned power spectra density plots (black dots), log-binned data (red line) and the nonlinear fitted curve (blue). (B) shows the division of power spectrum density values of fitted curve (blue line) over the log bin-data values (red line) and the linear fit (black line) is performed on the divided values. Ideal values of the slope and y intercept in graph B 0 and 1 respectively.

Typically, the acquired raw power spectrum, shown in figure 3.12 A (the black dot), is presented in a log-log plot (20 000 samples, acquisition rate of 50 kHz). To obtain the frequency roll off, a nonlinear fitting is performed based on equation 3.9. However, due to the large amount of points, it will be numerically tedious to obtain an equal weightage throughout the points during the curve fitting process. A direct strategy is to reduce the number of data from the raw data set. This reduction is performed using averaging or binning [35]. By choosing a set of points to average I can reduce the points to fit and increase the accuracy of the fitting procedures. Due to the logarithm nature of the plots, a logarithm binning sequence is chosen to reduce the length of the dataset. The logarithmic binning goes about choosing a specific bin size N from a certain block of data D. For each bin N, their mean in both X (frequency) and Y (PSD) is calculated and put forward as the new point. The vital part in the log-log binning technique is the choice of the start point of each bin steps. For a bin size N, the distribution would take the form X*(i-1)*(D+1) to i*D where i =1,…..N. This logarithm bin is shown as the red lines in figure 3.12. By performing the nonlinear fitting procedure (Lorentzian), blue line figure 3.12A, the roll-off frequency, f_c, is obtained.

Another way of checking the accuracy of the fitting curve is to perform a simple division of the fitting points (blue line) over the bin points (red line). The divided values are plotted over the

same frequency range, red dot in figure 3.12B. By performing a linear fit on the values(red dotted lines), the gradient of the slope and the y-intercept of the linear fit (black line in figure 3.12B) can quantitatively assess the overall distribution and accuracy of the nonlinear fitting procedure [35]. The y-intercept is at 1 while the slope of the fit is at 0.00001. These intercept and slope value in the final linear fit of the divided PSD values (red dot) means that most of the nonlinear fit curve passes through the log-binned data.

After obtaining the frequency of the roll off, the drag coefficient γ is still required to compute the trap stiffness. The Faxen correction factor takes into account the increased drag coefficient when an object is close to a planar surface i.e. coverslip interface. The hydrodynamic correction (fifth order correction) with the associated viscous drag γ in the transverse γ_{xy} and γ_z axial when close to surface is given in equation 3.10 [36],

$$\gamma_{x,y} = \frac{(6\pi\eta r)}{\left(1-\frac{9}{16}\left(\frac{r}{h}\right)+\frac{1}{8}\left(\frac{r}{h}\right)^3-\frac{45}{256}\left(\frac{r}{h}\right)^4-\frac{1}{16}\left(\frac{r}{h}\right)^5\right)} \quad \gamma_z = \frac{(6\pi\eta r)}{\left(1-\frac{9}{8}\left(\frac{r}{h}\right)+\frac{1}{2}\left(\frac{r}{h}\right)^3-\frac{57}{100}\left(\frac{r}{h}\right)^4-\frac{1}{5}\left(\frac{r}{h}\right)^5\right)} \quad (3.10)$$

where η is the viscosity of the medium, r is the radius of the particle and h is distance from the glass surface. The transverse correction factor $\gamma_{x,y}$ for 0.78um sphere at 8.5um above the bottom coverslip is 0.974 while the axial correction factor γ_z is 0.948. The relative position of the sphere is measured by incrementally moving sample stage using the piezo stage in the axial direction from the bottom of the coverslip to the trapping position. The starting position is first measured by observing the changes in the axial histogram of the trapped particle. As the trapped particle rest onto the bottom coverslip, an asymmetry in the histogram appears along the axial direction of the trapped particle. As the coverslip is incrementally moved away from the trapped sphere, the symmetry of the position histogram trap volume will be slowly restored. This is because the surface is no longer perturbing the particle position in the axial direction.

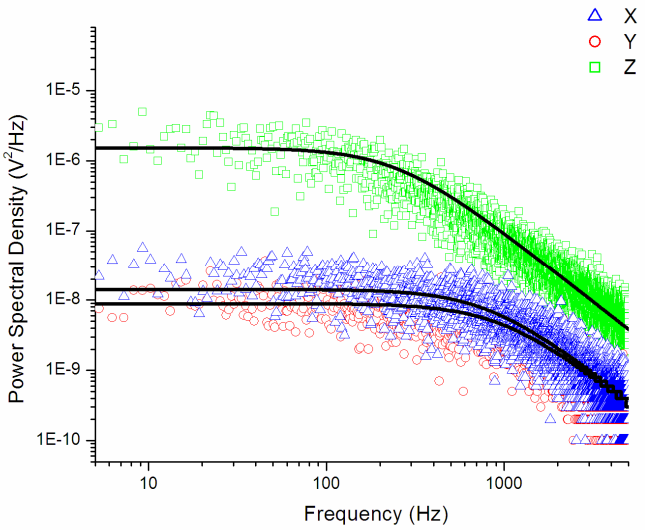

Figure 3.13 Power spectrum density plot and nonlinear curve fitting. An optically trapped 0.78µm polymer sphere with 40 mW at the sample for all the three axis (red circle(X), blue triangle (Y), green square (Z)). The black line indicates the fitted curve which gives the roll off frequency as X-800Hz, Y- 1000Hz, Z – 300Hz

The final calculated trap stiffness ($k = 2\pi f_c \gamma$), for the 0.78µm trapped at a height of 8.5um above the bottom coverslip, is calculated as k_X= 38.8 pN/µm, k_Y= 47.4 pN/µm and k_Z= 12.17 pN/µm as obtained from the nonlinear fit (black line) of the bin data (squares, triangle and circle) as shown in figure 3.13.

Both methods show a deviation of trap stiffness in all three directions in the same fashion i.e. same i.e. a weak axial trap and a stronger stiffness in the y direction than x direction. However, the values are comparatively different by Δk_x = 36%, Δk_Y = 21% and Δk_Z = 58%. Here the largest difference in trap stiffness is along the axial direction k_z. The difference (up to 50%) in trap stiffness is also observed by Appleyard *et al* [34] when trapping at lower optical powers (< 70mW).. The equipartition method makes use of conversion factor using a stuck sphere at the bottom surface of the chamber. But the trap stiffness is assessed at a different height above the surface. Intuitively, it is logical to attribute this discrepancy to the change of intensity on the QPD. Since the sphere is moved away from the surface of the sample chamber, the intensity at the QPD must have changed. Hence, a change of overall intensity must contribute to a change in the conversion factor. To prove this point, I measure the change in total intensity falling on the QPD as a trapped sphere moves away from the bottom coverslip.

Figure 3.14 shows total intensity of QPD as the trapped sphere (0.5µm in diameter) is moved incremental (10 nm) to around 2.5 µm above the bottom surface of the sample. The first two peaks in the signal are due to the coherent interference effects measured from the bottom of a

trapped microsphere (0.5µm in diameter) and the top surface of the coverslip (Fabry-Perot) interferometry [37]. At distances further away from the coverslip, the signal is seen to gradually decrease. This decrease in signal shows that the intensity of the light on the QPD has changed

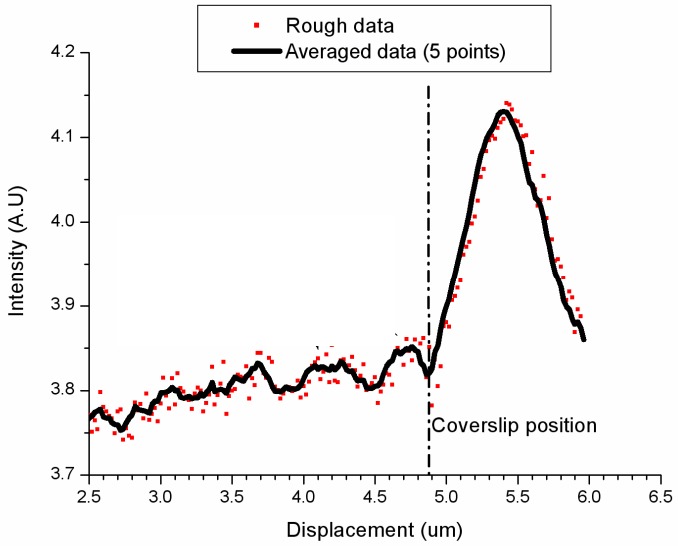

Figure 3.14 Changes in intensity over distance away from the coverslip. Red dot indicates the measured values and black line indicates the linearly averaged values (5 point) of the measured values

It is possible to reduce the discrepancy by calibrating the particle while it is being trapped above the coverslip. To do this, an independent laser beam is use to project the scattered light from the trapped spheres onto the QPD. The trapped particle needs to be steered with an AOD. Each AOD deflection angle (MHz) must first be already calibrated to a position shift (µm) using the particle of the same size. The trapped particle is then optically steered about the probe beam to obtain a calibration graph (V/µm).

A less complicated way to resolve is to retrieve the conversion factor (V/µm) using an uncalibrated QPD. Allersma *et al* [14] showed that it is possible to estimate the detector sensitivity β from an uncalibrated voltage power spectrum PSD_v. Considering the high frequency region ($f >> f_c$) of equation 3.6 from both the uncalibrated PSD_v and calibrated PSD_{nm}, as shown in equation 3.11. By multiplying the raw power spectrum with the square of the frequency, $PSD.f_w^2$, I can obtain a constant value, ρ, is obtained at plateau position of the graph, shown in figure 3.15. Using this information, I can then measure the detector sensitivity β based on the known size of the trapped bead as shown in equation 3.11 and shown in figure 3.15,

$$PSD_v(f >> f_c) = \beta^2 PSD_{nm}(f >> f_c)$$
$$PSD_v(f >> f_c) = \beta^2 \frac{D}{\pi^2}\frac{1}{(f_c^2)}$$
$$f^2.PSD_v = \beta^2 \frac{D}{\pi^2} \qquad (3.11)$$
$$\beta = \sqrt{\rho \frac{3\pi^3 \eta d}{k_B T}}$$

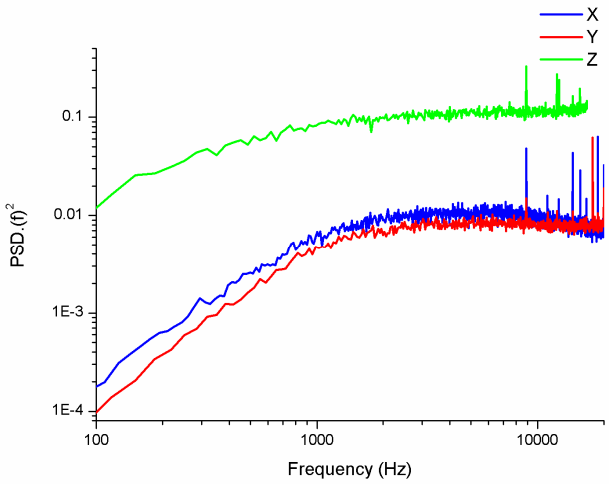

Figure 3.15 Power spectrum density multiplied by the square of the frequency, $PSD.f_w^2$ plotted against the range of frequency. The value at the plateau ρ is used to calculate the calibration factor for the three dimensions X (blue), Y (red) and Z (green)

Using this numerical technique, the calibration factors obtained for the three dimensions are V_{xcalib} =0.7 V/µm, V_{ycalib} = 1.05 V/µm, V_{zcalib} = 2.4 V/µm. The trap stiffness of X, Y and Z are then determine as follow 37.8 pN/µm, 53.12 pN/µm and 7.21 pN/µm. The stiffness values deviation is much lower as compared to the values obtain from the equipartition method (2% deviation for X and 10% deviation for Y and 40% for Z) [34]. However, the values of the axial stiffness still deviate from each other by a fair margin. Position conversion factor, especially in the axial direction, has always been an issue and is constantly being improved [37-40]. The values of the axial stiffness obtained (from the power spectrum) in this thesis does not account for any absolute physical measurements (i.e. biological forces or interaction forces), is instead used to reflect a relative trend in the optical trap. However, further improvement on the axial measurements needs to be made.

From the analysis carried out in this section, the trap stiffness measured using the power spectrum technique does not depend on any intensity variations or any additional QPD calibration. Hence, it appears to have a stronger advantage over the equipartition method for trap stiffness

measurements. Therefore, I choose to make use of the power spectrum technique to measure trap stiffness of a single beam optical tweezers system discussed in this thesis. The variation of the stiffness obtained using the power spectrum technique is around 5 %.

3.7. Trap stiffness measurements

In this section, I perform the trap stiffness measurements based two parameters: optical power, spherical aberrations. In addition, I also plot the optical potential energy well of the optical trap using the position histogram (Boltzmann statistics), calibration factor and stiffness of the trap obtained from the PSD analysis.

3.7.1. Optical power versus trap stiffness

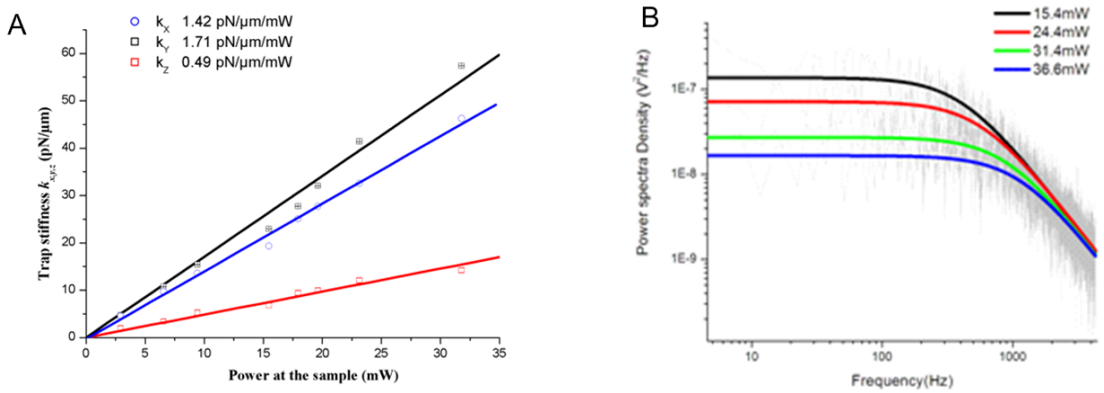

Figure 3.16 Trap stiffness and PSD with increasing optical power in the trap. A - the trap stiffness versus optical power for 1µm polymer sphere at 14 µm away from the bottom coverslip. The trends indicates a stiffer trap is the y (black) direction than x (blue). The axial trap stiffness is approximately 3 times smaller than the lateral trap stiffness. B – change in the power spectra density for Y axis as the power is increased at different power. The colour line shows the nonlinear fit on the PSD at different powers. Black – 15.4 mW, red – 24.4mW, green – 31.4 mW and blue – 36.6 mW The drop in the y intercept indicates a reduction in the particle position variance.

Based on the understanding of the optical forces (section. 1.3), the strength of the trap can be improved by increasing the optical power. In this section, I show that the stiffness of the optical trap increases linearly with optical power. A 1 µm (diameter) polymer sphere is trapped at 14 µm away from the bottom coverslip, where the hydrodynamic correction factor in all three dimensions ≈ 1. Figure 3.16 A shows the plot of the trap stiffness versus the optical power of the optical trap at the sample. The power at the sample is measured with a dual objective lens method (appendix A(ii)). From the graph in figure 3.16A, I can clearly observe a stronger stiffness in Y (1.71 pN/µm/mW) than X (1.42 pN/µm/mW). This is due to the linear polarisation of the trapping beam

[31]. The axial trap stiffness is 0.49 pN/µm/mW and is due to the ellipsoidal trapping volume. The results are consistent with past reported values [31]. In figure 3.16B, I show the changes in the power spectra density at different power level. The y intercept of the power spectrum is seen to drop in amplitude as the trapping power increases. The decrease in the y intercept means that the area (integral) under the Lorentzian curve is reducing. This reduction of the area under the curve is due to the decrease in the position variance as defined by Parseval's theorem.

3.7.2. Trap stiffness due to spherical aberrations

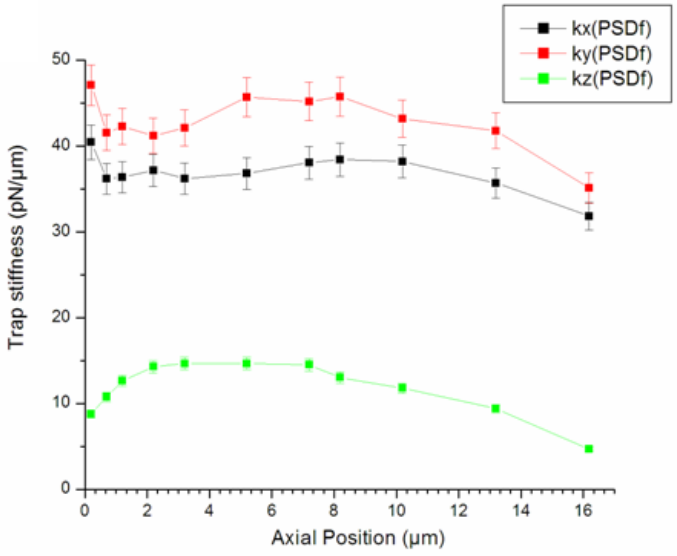

Figure 3.17 Measurements of the trap stiffness at different axial heights. Calculated trap stiffness (k_x, k_y and k_z)in the three dimensions from the power spectrum density (PSDf) at different height away from the bottom of the sample chamber. Decrease in axial trap stiffness k_z is due to spherical aberration in the optical trap.

In chapter 2 section 2.2.2, I explained that the spherical aberrations for an oil immersion objective can affect the optimal working position of an optical tweezers within the sample chamber. With the BFP and QPD, it is possible to measure the spherical aberration by measuring the stiffness of the trapped particle at different axial heights. The mismatch in the refractive index between the oil immersion, water and glass will reduce the axial trap stiffness at positions further away from the surface of sample. Figure 3.17, the trap stiffness of a 1 µm sphere is measured at a range of axial positions (0 to 16 µm) away from the surface of the bottom coverslip. From the calculated trap stiffness (based on the power spectrum method), the trap stiffness in the axial directions is reduces to less than 5 pN/µm at 16 µm and the transverse trap stiffness is only reduced to approximately 35

pN/µm (taken into account the Faxen correction factor, equation 3.10) [27]. Since every microscope objectives are corrected for their spherical aberration at a given axial depth, it is crucial to measure their individual spherical aberrations over a range of the trapping depths. The trapping power of 30 mW is maintained at the same level at the different axial positions.

3.7.3. Plotting the optical potential well

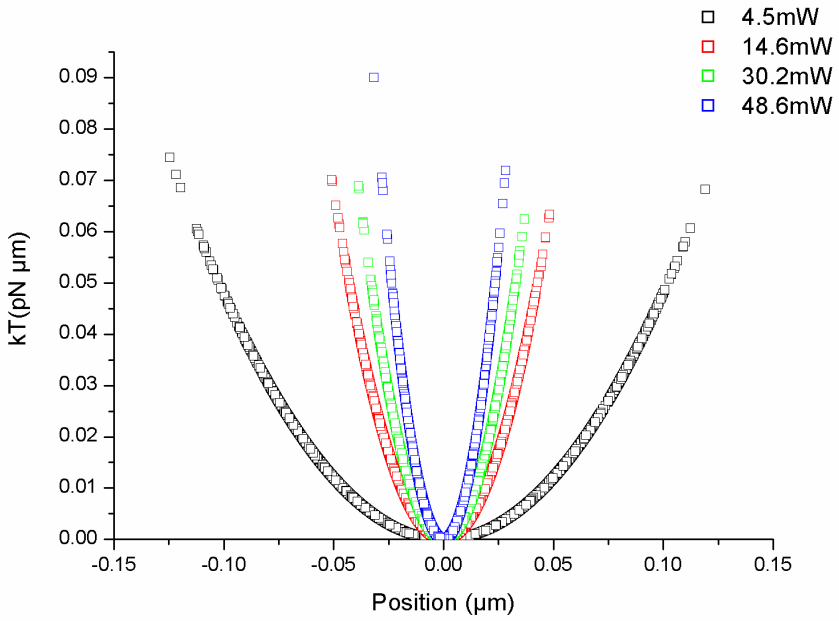

Figure 3.18 Optical potential energy well in the y axis with increasing optical powers. The plot shows the narrowing of the optical potential energy of the optical trap using a 0.78µm trapped sphere at 8.5µm above the coverslip as the power in the trap is increased from 4.5mW to 48.6mW.

The particle position over a given period of time in each direction may be recorded as a histogram that is described by a Boltzmann distribution (probability). This in turn will be directly related to the shape of the energy potential of an optical tweezers. The Langevin equation presented in chapter 1 describes the Brownian dynamics of a particle residing within harmonic potential well. However, the optical potential energy is only harmonic over a fraction of the trapping wavelength. Hence, the optical potential well is in itself not linearly scaled with the displacement from the centre to the perimeter of the trap**. I can translate the Boltzmann position plots (position histogram plot) into an optical potential energy plot by using the Boltzmann statistics.** Using Boltzmann statistics or distribution as shown in equation 3.12,

$$P(y) = Ae^{-\frac{E(y)}{k_B T}} \tag{3.12}$$

where $P(y)$ is the probability of finding the particle along the transverse dimension y, $E(y)$ is the potential energy of the particle within a given area, A is the normalized factor when $\int P(y)dy = 1$. The potential energy in this case is assumed to be a harmonic oscillator which is $k\left\langle y^2 \right\rangle$ based on the equipartition method as shown in equation 3.13,

$$k\left\langle y^2 \right\rangle = -k_B T.\ln(P(y)) + k_B T \ln(A) \tag{3.13}$$

The last term in equation 3.13 is the potential offset due to the normalization factor which can be ignored [16, 41]. Hence, from equation 3.13, it would be possible to plot the optical potential of trap with a given *k*. From the position trace of the trapped polystyrene sphere (diameter 1 μm), I can plot the number of times that a particle goes pass a location within the trap. The collection of the points at each location in the trap forms a histogram of the particle position versus counts. From the calibrated values obtained the power spectrum density (PSD), I can then convert the particle position in the histogram from voltage to micrometres. The plots of the optical energy potential in the one dimension (y) at different trapping powers are obtained by multiplying the stiffness of the trap k_y with the position variance of the particle $\left\langle y^2 \right\rangle$ as shown in figure 3.18

3.8. Calibrating the acousto optics deflector and stepper motor

In this final section of the chapter, I adopt the technique, described in section 3.5, to calibrate the beam positions on the sample (μm) versus the AOD scanning frequencies (MHz) and the step sizes of the stepper motor (μm). The beam steering devices (section 2.3) are used to move a trapped particle at sequential steps. By steering the trapped particle, with a stiffness k, at a distance of, y, I can then exert an optical force F given by k*y.

Figure 3.19 shows the inclusion of the QPD and DO lens (figure 3.2) onto the dual optical tweezers system described in section 2.4. A pair of telescope lens system (lens L9 and L10) relays the image at the BFP of the DO lens onto the QPD. A NIR dielectric mirror M6 is used to reflect the scattered infrared light and letting through the illumination from the bright field condenser. A single linear polariser is used for selecting the AOD automated trapping beam for QPD measurement. The

detection objective also serves as the condenser lens for the brightfield illumination. I use a microscope objective with a NA of 0.65 (40X, Nikon Eplan) as the DO lens. The NA of the chosen DO lens is close to the suggested NA by Rohrbach [27] that is suitable for tracking particles from diameter of 0.7 µm to 2 µm.

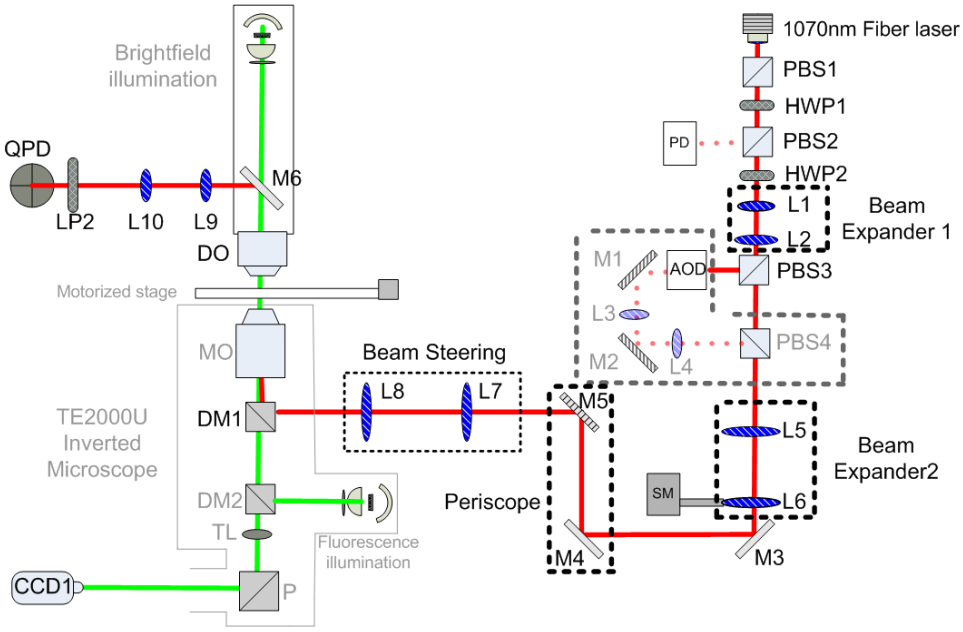

Figure 3.19- Dual tweezing beam with QPD and DO lens. The setup is the same as described in figure 2.6 except the optics for the QPD. A detection objective (DO) lens is used to collect the scattered light from the trapped particle onto the QPD. Lenses L9 and L10 de-magnify the image of the BFP onto the active area of QPD. The image is reduce by approximately 4 times (7mm to 2mm). M6 is a near infrared dichroic mirror that reflect light of wavelength >900nm. LP2 is a linear polariser that selects which trapping beam to let through to the QPD.

In the previous sections, the QPD measurements are done with the static optical trap is formed by the trapping beam that is not steered by the AOD. Since initially the two trapping beams are polarised in two orthogonal directions after the PBS3 and PBS4. Using the linear polariser (LP2) optics, I can remove the presence of the static trapping beam on the QPD. The polarisation of the steerable trapping beam does contain slight ellipticity after passing through acoustic gratings in the AOD. By rotating the linear polariser such that it is orthogonal to polarisation of the static trap, I can effectively "shunt" away >99% of the intensity from the static trapping beam.

First, the AOD scans the beam (in MHz) over a given scan area in the sample chamber that is centred on a stuck 1 µm (diameter) microsphere. A custom Labview project is written which records the voltage signal on the QPD and the scanned frequency that is send to the RF driver that drives AOD. By plotting the voltage signal pertaining to one dimension versus the scanned frequency, a linear dependence of the voltage to frequency can be identified (V/MHz) as shown in

figure 3.20A. For the stepper motor, the lens attached to the stepper motor is moved at incremental steps about the stuck particle. And the conversion factor is achieved by identifying the region when the QPD voltage signal scales linearly with the step size, as shown in figure 3.20 B

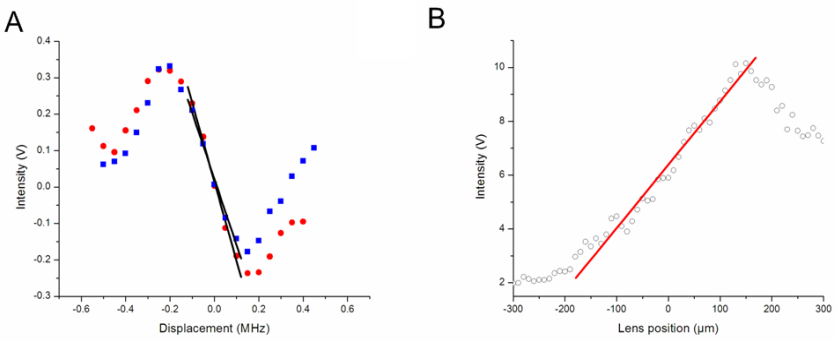

Figure 3.20- Calibration graph for AOD and stepper motor with a stuck 1µm sphere (A) shows the transverse calibration of MHz to voltage signal on the QPD (dotted points is the acquired data, red (X) and blue(Y) and black line is the linear fit) and (B) calibration of the step size of the stepper motor to the total intensity on the QPD for calibrating the axial direction. The red line indicates the linearity scaling region. The gradient of the linear fits are used as the calibration factors for the AOD and stepper motor.

The conversion factor for x and y are 2.18 V/MHz and 1.82 V/MHz respectively, as shown in figure 3.20A. For consistent with the QPD calibration technique, I use the calibrated conversion factors in table 3.1. By taking the conversion values (V/µm) from table 3.1 and dividing that by AOD conversion factor (the trapping laser is the same power), the frequency step (MHz) can be converted to displacement (µm) of the beam in the sample. On the transverse plane, the x direction is 0.63 MHz/µm and y direction is 0.82 MHz/µm. Using the same stuck particle, I scanned the stepper motor at an increment of 10 µm step over a range of 400 µm. The conversion factor in the lens displacement is given as 0.022 V/μm_{lens} , shown in figure 3.20 B. With the axial conversion factor of the QPD (V/µm) for 1µm sphere is given as 3.11 V/µm (table 3.1), I calculate the conversion factor for the stepper motor to be 141 $\mu m_{lens}/\mu m_{sample}$.

Next I move a trapped 1 µm fluorescence sphere with the AOD and stepper motor. The trap is located at around 3 µm above the bottom coverslip so as to reduce the variation in the conversion factor. I first apply a forward and reverse saw tooth function on y dimension of the AOD at a frequency step of 0.02MHz and 0.008MHz respectively. This forward and reverse frequency step movement should translate to a particle movement of ≈ 0.024µm and ≈0.0098 µm in y direction correspondingly. The optical power in the optical tweezers is measured to be

50±1mW at the sample. The related trap stiffness is calculated to be at ≈ 68±6pN/µm using the PSD method. The actual motion captured by the QPD is measured to be about 0.0210 ± 0.01µm (forward-red) and 0.0107± 0.005µm (backwards-blue) in y direction. The measured displacement from the QPD and desired imposed displacements from the AOD varies to within 15%. Since I know the distance, y, and the stiffness, k, I can compute the force exerted by the particle. The transverse force exerted, in figure 3.21A, will be about ≈ 1.63 ± 0.06 pN (forward) and 0.66 ± 0.01 pN (backwards).

Using the stepper motor with the lens (L6 in figure 3.19), I move the optically trapped particle along the axial direction at approximately 0.500 µm steps, as measured by the QPD as shown in figure 3.21B. The stepper motor is moved at around 50 µm which should equal to 0.35 µm. Here there is 30% difference in the measured and imposed particle motion. This is still due to the inaccuracy of the axial calibration that needs to be improved.

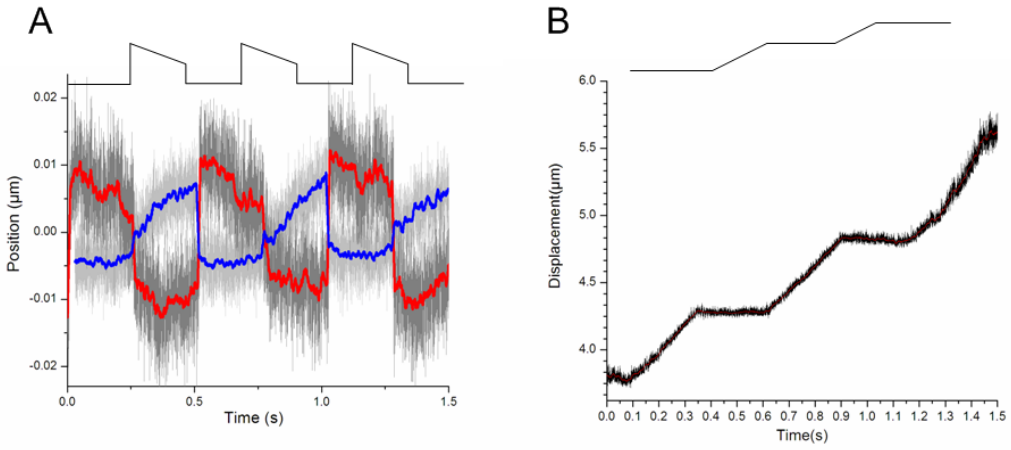

Figure 3.21 – Particle movement captured by the QPD. A trapped sphere 1 µm in diameter is moved to around 5 µm above the bottom of the sample chamber. (A) QPD position signal in the y direction is measured to be about 0.0210 ± 0.01µm (forward-red) and 0.0107± 0.005µm (backwards-blue). The imposed AOD frequency step is 0.02MHz and 0.008MHz from the AOD that should translate to a particle movement of ≈ 0.024µm and ≈0.0098 µm in y direction. (B) QPD measured displacement of the trap particle in the axial direction with a stepper motor. Each step is ≈ 0.5± 0.1µm. The stepper motor is moved at around 50 µm which should equal to 0.35 µm. The applied waveform imposed on to the deflected trapping beam is illustrated above the experimentally obtained graph.

3.9. Conclusion

In this chapter, I first introduced the calibration and analysis techniques for transforming an optical trapping setup into a powerful position and force measurement system [35]. From the overview given in section 3.2, it was clear from literature that the BFP interferometry is most suited for adapting an interferometric position measurement scheme onto a modern microscopy system.

The BFP technique made use of a single QPD and objective lens that are ideally suited for the standard microscopy system.

In the second section, I explained the BFP interference effects using an analytical, numerical model and experimental results. On the same note, I introduced a practical means of locating the BFP with aid of a phase contrast microscope objective. The BFP interference provided a first order interference pattern of a particle that registered a voltage signal on the QPD. The interference pattern was used to measure the particle position in three dimensions.

In the following third section, I described the steps to calibrate the QPD using nanopositioning stage and a sphere stucked at the bottom on the chamber. The stuck sphere was scanned in a square grid pattern by the stage, with the trapping beam located in the middle of the pattern. The resulting output position signal from the QPD was plotted over the scanning grid pattern to give a calibration graph. From a linear scaling factor between the voltage and distance, the conversion factor of the QPD was acquired. This conversion factor translated the voltage signal into position displacements. I performed the same calibration steps for different particle. The conversion factor was found to be different for different particle sizes.

Using the conversion factor, I carried out three experiments in the fourth section of the chapter. Firstly, I measured the background vibrations and drift using a stuck sphere. An initial axial drift of ≈ 600nm was observed which stabilised after 400 s. Once stabilised, the vibration or drift was brought down to a minimum of 5 to 8 nm. Secondly, I measured the trapping volume of the optical trap with two different particle sizes. The size of the particle (dielectric without any enhanced polarisability) is found to influence the trapping volume. The optimal trap volume for each particle size varied for different of beam parameters. Ideally, one needs to find a particle that filled the focal volume of the trap. In the experiments carried in section 3.5.2, the transverse symmetry of trap was more uniform for the 0.5 μm particle as compared to the 1 μm particles. And the asymmetry along the transverse versus axial dimension was larger for the 0.5 μm sphere than the 1 μm sphere. Finally, I monitored the position variance of an optical trap was a relatively concentrated microsphere sample. The position variance was shown to increase when more than one particle is in the trap.

The conversion of an optical trapped particle into a force transducer required the knowledge of the stiffness of the trap. In the fifth section, I introduced the numerical analysis of trap stiffness and measured the stiffness of an optically trapped microsphere. With the conversion factor, the position of the particle in voltage was translated to the position (μm). Using the equipartition theorem, the potential energy (k_BT) of a particle in a harmonic potential (optical trap) over a time

period divided by the position variance of the trapped particle gives the stiffness of the trap, $k = (k_BT)/\langle x^2 \rangle$. On the other hand, the uncalibrated position signal (in voltage) was analysed in terms of its power spectrum density (PSD). PSD is the Fourier transform of the auto-correlation of the voltage signal over the range of oscillating frequency, f. The power spectrum is a function in the frequency domain and allowed the full examination of both fast and slow oscillations. The plot PSD of an optically trapped particle over a range of frequency is of a Lorentzian form. A nonlinear curve fitting was done to obtain the roll off frequency, f_c, from the Lorentzian graph. The relationship of the roll off frequency to stiffness is given as $k= 2\pi f_c \gamma$. The two data analysis was carried out in time or frequency domain. The frequency domain measurement was less demanding on the light sensitivity of the detector and did not require any form of position calibration to be done [42]. I performed the analysis of the trap stiffness using both methods on a single trapped microsphere.

The time domain approach with the conversion factor was seen to have limitations in the assertion of the trap stiffness, when compared to the power spectrum. By scanning a trapped particle away from the bottom surface of the coverslip, I observed the decay in the collected intensity upon the QPD. This change in intensity caused a discrepancy between the stiffness values obtain from the two methods. A simple method to avert this discrepancy was to obtain a conversion value (V/μm) using the PSD data. With the new conversion factor, the difference in the values of the trap stiffness was much smaller.

After the comparison, I proceeded to make use of the PSD analysis method to assess the trapping performance of an optical tweezers system in the sixth section of the chapter. I measured the trap stiffness over a range of laser power and trapping depth (spherical aberration calibration). There is a linear relationship between the laser power and trap stiffness. From the trapping depth results, the axial trap stiffness of a 1 μm microsphere gradually dropped at around 8 μm. This indicated the presence of spherical aberration that reduced the steepness of the intensity gradient in the axial direction (axial gradient force). Using the conversion factor (PSD) and the histogram position plot of a particle, I also carried out the calculations of the actual optical potential energy well in the trap at increasing power. As the power got higher, the width of the potential energy well got narrower.

In the final section of the chapter, I calibrated the AOD and stepper motor using the stuck particle approach. I showed that the calibrated AOD can achieve nanometric position control. The AOD steered optical tweezers was shown to exert sub-piconewton (≈ 0.66 pN) forces and moved a trapped particle at only a few nanometres (≈ 9nm). In the current dual optical tweezers system, the QPD was shared between the trapping beams using a linear polariser. The two optical traps were

coaligned and moved in tandem with a stepper motor (T-LS Series Zaber). The axial stepping is important when combining with confocal microscopy imaging (chapter 7).

Further improvement can be used to increase the stability of the setup such as enclosure of the beam paths within experimental setup and active feedback control over the trapping beams. A second AOD and QPD can be used to automate and calibrate the current static trap. A feedback routine is currently being written and tested on the setup. With respect to the steering process, the current AOD digital conversion card (voltage to MHz conversion) does appear to have a low amplitude modulation over a longer period of time (minutes). This issue had also been observed by an independent group [43]. An improvement can be made by using a separate FPGA digital synthesis card (≈100MHz) and this can also provide high frequency force feedback [44].

One possible way to improve the axial calibration is use a separate detector (single photodiode) and reduced the NA of the detector lens (using an aperture) [45]. This will help in the collection of the signal from the central diffraction order and improve the axial calibration. In addition, the axial position should be controlled using a piezo motor instead of a stepper motor to increase repeatability of the lens movement.

I designed and performed all the experiments in this chapter. A set of customised software is written by me to accomplish the data acquisitions and beam steering. I acknowledge that the initial software for the data acquisitions from the QPD was developed in close collaboration with Dr Peter J Reece [20].

References

1. F. Gittes, and C. F. Schmidt, "Interference model for back-focal-plane displacement detection in optical tweezers," Optics Letters **23**, 7-9 (1998).
2. A. Ashkin, and J. M. Dziedzic, "Optical trapping and manipulation of viruses and bacteria," Science **235**, 1517-1520 (1987).
3. J. C. Crocker, and D. G. Grier, "Methods of digital video microscopy for colloidal studies," Journal of Colloid and Interface Science **179**, 298-310 (1996).
4. R. Di Leonardo, S. Keen, J. Leach, C. D. Saunter, G. D. Love, G. Ruocco, and M. J. Padgett, "Eigenmodes of a hydrodynamically coupled micron-size multiple-particle ring," Physical Review E (Statistical, Nonlinear, and Soft Matter Physics) **76**, 061402-061404 (2007).
5. S. Keen, J. Leach, G. Gibson, and M. J. Padgett, "Comparison of a high-speed camera and a quadrant detector for measuring displacements in optical tweezers," Journal of Optics a-Pure and Applied Optics **9**, S264-S266 (2007).
6. W. Denk, and W. W. Webb, "Optical measurement of picometer displacements of transparent microscopic objects," Appl. Opt. **29**, 2382-2391 (1990).
7. L. P. Ghislain, I. Brustmascher, and W. W. Webb, "Force and Membrane Compliance Measurements Using an Optical Trap and Laser Interferometry," Biophysical Journal **64**, A109-A109 (1993).

8. L. P. Ghislain, and W. W. Webb, "Scanning-Force Microscope Based on an Optical Trap," Optics Letters **18**, 1678-1680 (1993).
9. L. P. Ghislain, N. A. Switz, and W. W. Webb, "Measurement of Small Forces Using an Optical Trap," Review of Scientific Instruments **65**, 2762-2768 (1994).
10. N. A. Switz, J. Mertz, and W. W. Webb, "A feedback modified optical trap for probing local viscosity and examining diffusive behavior on cell membranes," Biophysical Journal **70**, TU414-TU414 (1996).
11. S. M. Block, L. S. B. Goldstein, and B. J. Schnapp, "Bead Movement by Single Kinesin Molecules Studied with Optical Tweezers," Nature **348**, 348-352 (1990).
12. R. M. Simmons, J. T. Finer, S. Chu, and J. A. Spudich, "Quantitative measurements of force and displacement using an optical trap," Biophysical Journal **70**, 1813-1822 (1996).
13. F. Gittes, and C. F. Schmidt, "Interference model for back-focal-plane displacement detection in optical tweezers," Opt. Lett. **23**, 7-9 (1998).
14. M. W. Allersma, F. Gittes, M. J. deCastro, R. J. Stewart, and C. F. Schmidt, "Two-dimensional tracking of ncd motility by back focal plane interferometry," Biophysical Journal **74**, 1074-1085 (1998).
15. P. C. Chaumet, A. Rahmani, and M. Nieto-Vesperinas, "Photonic force spectroscopy on metallic and absorbing nanoparticles," Physical Review B **71** (2005).
16. E. L. Florin, A. Pralle, J. K. H. Horber, and E. H. K. Stelzer, "Photonic force microscope based on optical tweezers and two-photon excitation for biological applications," Journal of Structural Biology **119**, 202-211 (1997).
17. A. Rohrbach, C. Tischer, D. Neumayer, E. L. Florin, and E. H. K. Stelzer, "Trapping and tracking a local probe with a photonic force microscope," Review Of Scientific Instruments **75**, 2197-2210 (2004).
18. G. Volpe, G. Kozyreff, and D. Petrov, "Backscattering position detection for photonic force microscopy," Journal of Applied Physics **102**, 084701 (2007).
19. G. Volpe, G. Volpe, and D. Petrov, "Brownian motion in a nonhomogeneous force field and photonic force microscope," Physical Review E (Statistical, Nonlinear, and Soft Matter Physics) **76**, 061118-061110 (2007).
20. W. M. Lee, P. J. Reece, R. F. Marchington, N. K. Metzger, and K. Dholakia, "Construction and calibration of an optical trap on a fluorescence optical microscope," Nat. Protocols **2**, 3226-3238 (2007).
21. J. H. G. Huisstede, K. O. van der Werf, M. L. Bennink, and V. Subramaniam, "Force detection in optical tweezers using backscattered light," Optics Express **13**, 1113-1123 (2005).
22. K. C. Neuman, and S. M. Block, "Optical trapping," Review of Scientific Instruments **75**, 2787-2809 (2004).
23. C. Hertlein, L. Helden, A. Gambassi, S. Dietrich, and C. Bechinger, "Direct measurement of critical Casimir forces," Nature **451**, 172-175 (2008).
24. S.-H. Lee, and D. G. Grier, "Holographic microscopy of holographically trapped three-dimensional structures," Opt. Express **15**, 1505-1512 (2007).
25. J. H. Chow, G. de Vine, M. B. Gray, and D. E. McClelland, "Measurement of Gouy phase evolution by use of spatialmode interference," Opt. Lett. **29**, 2339-2341 (2004).
26. A. R. Clapp, A. G. Ruta, and R. B. Dickinson, "Three-dimensional optical trapping and evanescent wave light scattering for direct measurement of long range forces between a colloidal particle and a surface," Review of Scientific Instruments **70**, 2627-2636 (1999).
27. A. Rohrbach, H. Kress, and E. H. K. Stelzer, "Three-dimensional tracking of small spheres in focused laser beams: influence of the detection angular aperture," Opt. Lett. **28**, 411-413 (2003).
28. K. Berg-Sorensen, L. Oddershede, E.-L. Florin, and H. Flyvbjerg, "Unintended filtering in a typical photodiode detection system for optical tweezers," Journal of Applied Physics **93**, 3167-3176 (2003).
29. E. J. G. Peterman, M. A. van Dijk, L. C. Kapitein, and C. F. Schmidt, "Extending the bandwidth of optical-tweezers interferometry," Review of Scientific Instruments **74**, 3246-3249 (2003).
30. K. Berg-Sorensen, E. J. G. Peterman, T. Weber, C. F. Schmidt, and H. Flyvbjerg, "Power spectrum analysis for optical tweezers. II: Laser wavelength dependence of parasitic filtering, and how to achieve high bandwidth," Review of Scientific Instruments **77**, 063106-063110 (2006).
31. A. Rohrbach, "Stiffness of optical traps: Quantitative agreement between experiment and electromagnetic theory," Physical Review Letters **95**, 168102 (2005).

32. A. Rohrbach, and E. H. K. Stelzer, "Three-dimensional position detection of optically trapped dielectric particles," Journal of Applied Physics **91**, 5474-5488 (2002).
33. K. Svoboda, and S. M. Block, "Optical Trapping of Metallic Rayleigh Particles," Optics Letters **19**, 930-932 (1994).
34. D. C. Appleyard, K. Y. Vandermeulen, H. Lee, and M. J. Lang, "Optical trapping for undergraduates," American Journal of Physics **75**, 5-14 (2007).
35. K. Berg-Sorensen, and H. Flyvbjerg, "Power spectrum analysis for optical tweezers," Review of Scientific Instruments **75**, 594-612 (2004).
36. E. Schaffer, S. F. Norrelykke, and J. Howard, "Surface Forces and Drag Coefficients of Microspheres near a Plane Surface Measured with Optical Tweezers," Langmuir **23**, 3654-3665 (2007).
37. K. C. Neuman, E. A. Abbondanzieri, and S. M. Block, "Measurement of the effective focal shift in an optical trap," Opt. Lett. **30**, 1318-1320 (2005).
38. C. Deufel, and M. D. Wang, "Detection of Forces and Displacements along the Axial Direction in an Optical Trap," **90**, 657-667 (2006).
39. J. K. Dreyer, K. Berg-Sorensen, and L. Oddershede, "Improved axial position detection in optical tweezers measurements," Applied Optics **43**, 1991-1995 (2004).
40. S. F. Tolic-Norrelykke, E. Schaffer, J. Howard, F. S. Pavone, F. Julicher, and H. Flyvbjerg, "Calibration of optical tweezers with positional detection in the back focal plane," Review of Scientific Instruments **77**, 103101-103111 (2006).
41. E. L. Florin, A. Pralle, E. H. K. Stelzer, and J. K. H. Horber, "Photonic force microscope calibration by thermal noise analysis," Applied Physics a-Materials Science & Processing **66**, S75-S78 (1998).
42. F. Gittes, and C. F. Schmidt, "Back-focal-plane detection of force and motion in optical traps," Biophysical Journal **74**, A183-A183 (1998).
43. Y. Huang, J. Wan, M.-C. Cheng, Z. Zhang, S. M. Jhiang, and C.-H. Menq, "Three-axis rapid steering of optically propelled micro/nanoparticles," Review of Scientific Instruments **80**, 063107-063108 (2009).
44. A. E. Wallin, H. Ojala, E. Haeggstrom, and R. Tuma, "Stiffer optical tweezers through real-time feedback control," Applied Physics Letters **92**, 224104-224103 (2008).
45. A. Rohrbach, H. Kress, and E. H. K. Stelzer, "Three-dimensional tracking of small spheres in focused laser beams: influence of the detection angular aperture," Optics Letters **28**, 411-413 (2003).

Chapter 4 –

Calibrating Laguerre-Gaussian (LG) beam optical tweezers with back focal plane interferometry

4. Calibrating Laguerre-Gaussian (LG) beam optical tweezers with back focal plane interferometry

4.1. Overview

In chapter 3, I implemented the use of back focal plane (BFP) interferometry and QPD to measure the position and trap stiffness of an optically trapped particle. In this chapter, I will use the same QPD calibration techniques and stiffness analysis (PSD) on a novel beam optical tweezers system. The novel beam discussed in this chapter is the Laguerre Gaussian (LG) beam. This chapter is divided into six sections.

In the first two sections, I will give an overview of the LG beam modes and its applications. In the third section, two techniques used to generate a LG beam from a Gaussian beam are described. One of the techniques is chosen to be integrated into the existing optical tweezers systems (figure 3.18). In the fourth section, I shall carry out the steps to obtain the conversion factor of the QPD with a focused LG beam. In the fifth section, the calibrated QPD and the position histogram is used to deduce the scattering forces of a particle trapped in a focused LG beam. The position histogram of the trapped particle is compared against its relative position in the linear region of the calibration graph. This comparison can indicate the strength of the scattering forces along the axial direction in the optical trap, as suggested by Kress *et al* [1]. An optically trapped particle in a LG beam optical tweezers can have a new equilibrium position. The technique of BFP interference makes use of the Gouy phase effect around the focus of the probe/trapping light field to provide the sensitive position measurement. The Gouy phase effects in LG beams have been shown before to create a spiral intensity pattern which is used in optical micromanipulation [2]. In the same section, I will also discuss the issues of cross talk along the transverse plane of the QPD due to the back focal plane (BFP) interference pattern using a LG beam. Finally in the last section, I shall compare between the trap stiffness (pN/μm/mW) of different trapped particles sizes using a focused LG beam and a Gaussian beam in all three dimensions.

4.2. Introduction

The use of a higher order laser mode beam (TEM*01), for optical trapping was first introduced by Ashkin [3]. The higher order laser mode exhibits an annular intensity pattern. As such, the low refractive index particle is repelled from the high intensity annular rings and confined within the dark core. A special class of high order laser modes: LG modes, also known as optical

vortices [4, 5], have been of interest for the orbital angular momentum of light (OAM) [6-9], wavefront studies [10, 11] and optical micromanipulation [4, 12-17] amongst other areas. In 1999, Gahagan and Swartzlander [18] used a focused LG beam (azimuthal index of 1) to trap both low and high refractive index particles. The low and high index refractive index particles were seen to be trapped at two different axial positions simultaneously. The high refractive index particle is located close to the focus of the beam while the low refractive index particle is seen trapped further away from focal plane as shown in figure 4.1.

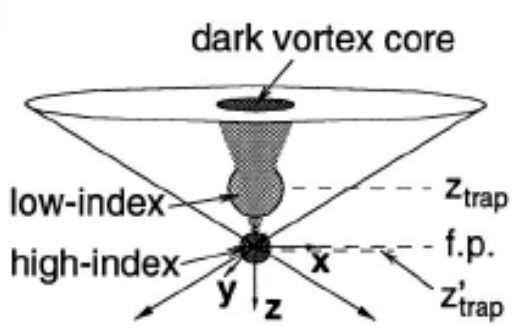

Figure 4.1 Stable trapping positions for low- (ztrap) and high-index (z'trap) particles respectively. The focal plane (f.p.) is assigned the position [18].

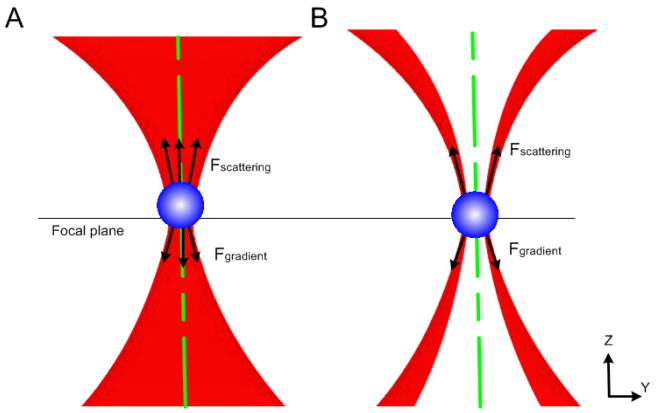

Figure 4.2 Balance of scattering and gradient forces in a Gaussian and LG beam optical tweezers along the beam axis. (A) Trapped microsphere with the balancing of the scattering and gradient forces in a focused Gaussian beam. (B) Trapped microsphere with the balancing of the scattering forces and gradient force in a focused LG beam. The optical forces along beam centre axis (green dash line) is not present for the LG beam optical tweezers. The particle trapped in the LG (B) will shift to a new equilibrium position.

The stable three dimensional optical trapping of a microsphere with an optical tweezers requires the balance scattering and gradient forces in all three dimensions. In the axial direction, the gradient force of a focused Gaussian beam balances the scattering force so that an optically trapped particle rest at an equilibrium position (figure 4.2 A). If the on-axis intensity in the Gaussian beam

is removed, the scattering forces would also be reduced (as in the case of a LG beam). The reduction of the scattering forces can cause the optically trapped particle to move to a new equilibrium position (figure 4.2 B).

So far, there have been only two experiments aimed at quantifying the reduction of the on-axis scattering force in the axial direction with a LG beam optical tweezers. Simpson *et al* [16] used the drag force method (Q values) and Friese *et al* [19] collected the back scattering light from optically trapped microspheres with an LG beam and image onto a single photodetector (not a QPD). Simpson *et al* [16] reported that for spheres sizes of 5 μm diameter, the axial Q values is improved by a factor of approximately two for the LG (azimuthal index of 3) beam optical tweezers as compared Q values from the Gaussian beam optical tweezers. The drag force measurement approach relies on the point when the optical force is equal to the drag force. One way to measure the drag force is to move the stage (to mimic fluid movement) and measure the point where the trapped particle falls out of the trap. The method has shown to give a large degree of variations due to the mechanical drift during sample translation [20]. Hence, the accuracy of the drag forces (Q values) in repeated measurements is low. Using the QPD technique and the PSD approach would be a much more deterministic approach.

Friese *et al* [19] used the PSD analysis approach to analyze the scattering light and calculate the trap stiffness. They have observed an approximate increase of ≈ 30% in the trap stiffness in optically trapped microsphere (diameter 2.58 μm) using a LG beam (azimuthal index of 1) optical tweezers. However, they did not use a calibrated QPD and BFP interferometry to measure the particle positions in the LG beam optical tweezers. To date, there have been a wide number of applications using LG beams [5, 12, 15, 17, 21, 22]. The quantification of the particle dynamics in LG beam optical tweezers is important in assessing their performance as force transducers. Before going into the stiffness and position measurements, I will first describe the LG beam modes and its generation methods.

It is worthwhile to note that a focused LG beam can also impart orbital angular momentum (OAM) to a trapped object due to the azimuthal phase variation in the field. Such light beams is a useful tool in the exertion of torques on particles in contrast to the optical torque arising from spin angular momentum (polarisation of the field) [23]. Angular momentum transfer on trapped particle is not considered in the experiments described in this chapter.

4.3. Laguerre-Gaussian (LG) beam modes

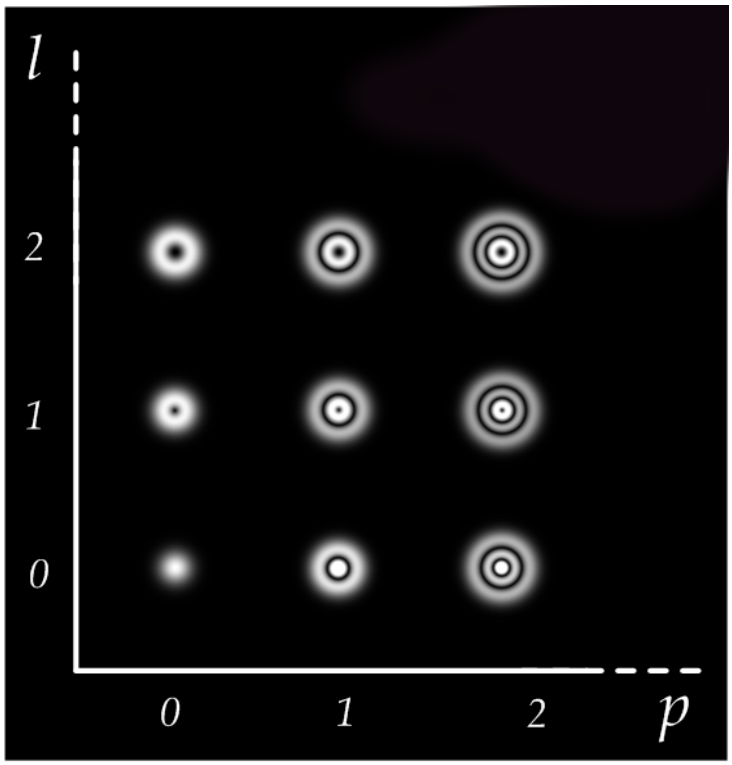

Figure 4.3: Various orders of the LG beams. In the paraxial approximation, LG modes are characterised by two integer indices namely *l*, azimuthal index, and *p* is the radial index, LG_p^l ..

In this section, I shall first explain the case of an ideal LG beam. Although the actual optical tweezers is considered a truncated beam due to the aperture effects (Airy diffraction pattern) of the microscope objective, it is useful to review the origins of the ideal LG beam modes for the purpose of its generation. Light beams emitted from a laser cavity are electromagnetic fields, which are solutions of the wave equations and satisfy appropriate boundary conditions. Some of the solutions form a complete and orthogonal set of functions [24] and are called the "higher modes of propagation". Essentially, any transverse mode optical distribution can be expanded in terms of these modes. These higher order transverse modes are often referred to as non-zero order mode light fields

In the context of the transverse laser mode theory, the circularly symmetric LG laser beam modes form a complete basis set for paraxial light beams and thus one may express any given light mode as a sum of them [6]. In this work, a given LG beam mode is denoted by LG_p^l where *l* and *p* are the two integer indices that describe the mode structure of the beam. The azimuthal index *l*

refers to the integer multiples of 2π phase variation that cycles around the circumference of the beam mode, while (p+1) indicates the number of radial nodes in the mode profile (see figure 4.4). For each increment of p, an additional concentric ring is added to the mode profile while an increment of l results in an increase in the diameter of the dark core, termed optical vortex, located on the beam axis. The azimuthal index l is often referred to as the topological charge of the optical vortex [25].

A general description of the electric field of an ideal LG mode $E(LG_p^l)$ of indices l and p may be written as shown in equation 4.1:

$$E(LG_p^l) = \sqrt{\frac{2p!}{\pi(l+p)!}}\left(\frac{\sqrt{2}r}{w(z)}\right)^{l/2} .L_p^l\left(\frac{2r^2}{w^2(z)}\right).\exp\left(-i\left[kz-(l+2p+1)\tan^{-1}\left(\frac{\lambda z}{\pi w_o^2}\right)\right]\right) \\ .\frac{w_o}{w(z)}.\exp\left(\frac{-r^2}{w^2(z)}\right).\exp\left(\frac{-kr^2}{2R(z)}\right).\exp-(\pm il\phi) \quad (4.1)$$

where z denotes the distance from the beam waist, z_r is the Rayleigh range, k is the wave number, ω is the radius at which the Gaussian term $\exp(-r^2/w^2)$ falls to 1/e of its on-axis value, r is the radius, ϕ is the azimuthal angle and L_p^l is the generalised Laguerre polynomial. The term $(2p+l+1)\arctan(z/z_r)$ is the Guoy phase of the LG mode that varies with the mode indices. From equation 1, I can directly locate the source of this azimuthal phase variation from $\exp(\mp il\phi)$.

The physical form (intensity and phase) of the LG_0^1 beams is shown in figure 4.4. Here, a three dimensional plot of the azimuthal phase variation of the LG_0^1 beam shows a linearly increasing phase change about the azimuthal direction (0 to 2π) over two periods, see figure 4.4. For the LG_0^1 beam, the 0 to 2π phase step along the beam circumference leads to destructive interference at the centre of the beam (π phase steps on opposite ends of the wavefront): a dark core. The numerical calculated intensity profile of the LG beam is shown figure 4.4 [6, 26, 27]. It shows a distinctive annular intensity beam that is directly due to the azimuthal phase variation.

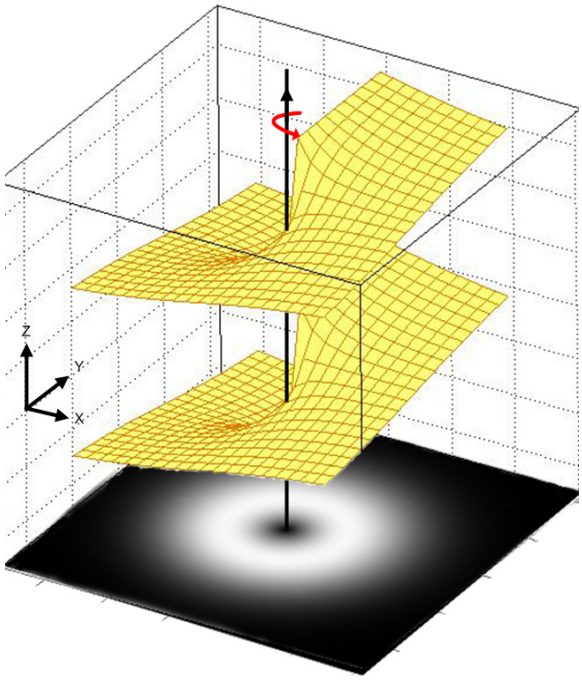

Figure 4.4: Intensity and phase of a beam LG_0^1. A beam LG_0^1 has a well defined orbital angular momentum (red arrow) due to the helical wavefront (yellow plot). The intensity distribution of LG_0^1 in the transverse plane is also shown.

The associated Poynting vector with an incident linearly polarised wave containing a planar wavefront would possess zero angular momentum. However, when there is a tilted or inclined wavefront of the planar wave in the azimuthal direction, it would translate to an azimuthal component in the Poynting vector [6, 10, 14, 28, 29]. The interpretation of the orbital angular momentum (OAM) in an LG beam can be described as a beam with an azimuthal inclining wavefront which leads to a uniform orbital angular momentum around the beam circumference. LG modes with $l \neq 0$ have garnered much interest owing to their $2\pi l$ azimuthal variation that gives rise to a well defined OAM, of $l\hbar$ per photon. Under the paraxial approximation, this form of angular momentum in the LG beam can be decoupled from spin angular momentum arising from its polarisation state [30].

This azimuthal phase variations also have direct consequence in its angular momentum energy transfer. These characteristics (phase and intensity) of the LG beam have lent themselves to the possibility of optical manipulation of low-refractive index particles [3, 4, 22] and optical torque transfer on microparticles [7, 14, 31]. In this chapter, I will restrict the discussions to the trapping dynamics arising from the intensity profiles of a LG_0^1 beam.

4.4. Generation of LG beams

Figure 4.4 shows that the individual wavefronts of the travelling beam are delayed at different phase steps in an azimuthal manner. However, the knowledge of the actual phase shift (i.e. 0-2π) would need to be assess by either interferometry[32], double slits[33] or microlens[11]. In chapter 5, I will describe the use of optically trapped microspheres for the measurement of the azimuthal phase variation. Before that, in this section, I describe the techniques use to create such an azimuthal phase delay.

There are several techniques that can be use to generate this form of azimuthal phase delay in conventional optics [34]. It is possible to generate the LG modes (circular symmetry) directly from within the laser resonator cavity by tuning the cavity mirrors [35, 36]. It is more convenient to generate LG beam modes directly from a fundamental Gaussian mode rather than a higher order HG mode due to accessibility of single mode Gaussian beam lasers. Here, I shall list out two common optical elements use to generate LG beams directly from Gaussian beam namely computer generated hologram and spiral phase plate.

4.4.1. Computer generated hologram

Holograms are often designed to reconstruct the phase and amplitude of an object. In conventional holography, the reference beam (recording beam) and the sample beam (object beam) are led to interfere at an angle to produce off-axis holograms. If the light field are temporally coherent, the interference patterns would result in a sinusoidal wave pattern (grating) that is imposed on to the holographic element. The grating pattern on the hologram acts as a diffractive element. This means that when the recording beam illuminates the hologram, the image would re-appear at an angle to the recording beam. This type of off-axis hologram aids in the clear separation of the image (first diffraction order) and recording beam (zeroth diffraction order). In most case, the zeroth diffraction order possesses higher intensity amplitude than the rest of the diffracting orders. On the other hand, it is also possible to carry out the interference without an angle: on axis hologram. The on axis separation can be made by using a reference beam with a spherical or conical wavefront [37]. However, the co-propagating zeroth and first diffracting orders could overlap and interfere, which would cause poor reconstruction of the image. With modern day computer and programming scripts, it is possible to “virtually” interfere the reference beam and the object beam, while directly recording it onto a light sensitive display i.e. spatial light modulators [38].

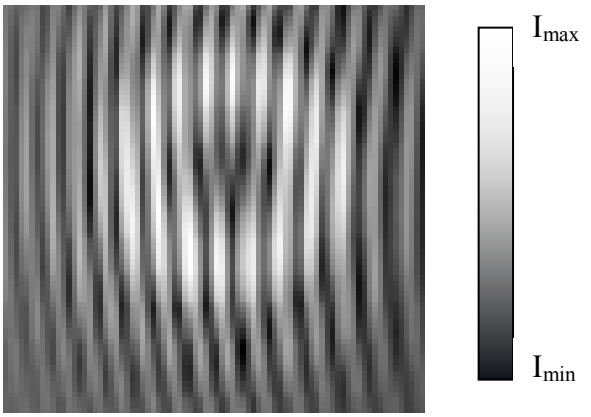

Figure 4.5- shows numerically calculated far-field diffraction of the pattern of interference between an plane wave and a LG_0^1 mode [39].

Figure 4.5 shows the computer generated off axis interference between a plane wave and a LG beam. The intensity pattern resembles a fork light pattern. For simplicity, a plane wave is often used to interfere at an angle with the spiral phase function ($\exp(\mp il\phi)$) to form a computer generated pattern as seen in figure 4.6. The central fork light interference pattern displayed in figure 4.6 contains the information of the azimuthal phase ($\exp(\mp il\phi)$) of a LG_0^1 beam.

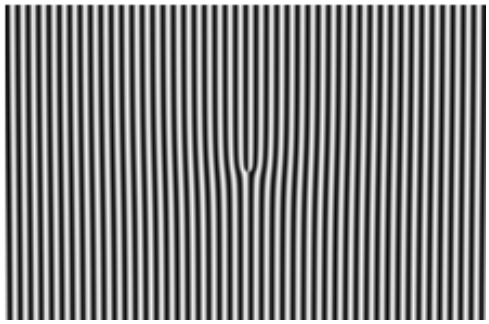

Figure 4.6 Computer generated hologram for LG_0^1 beam.. A shows the sinusoidal computer generated holograms for generating LG_0^1 beam where a plane wave interfered with the spiral phase function ($\exp(\mp il\phi)$)

The transmission function of the off-axis sinusoidal hologram in figure 4.6, would take the form of *T*, which is to generate a $LG_0^{\pm l}$ beam may be represented as in equation 4.2,

$$T = \frac{1}{2}\left(1 - \cos(k_x x \pm l\phi)\right) \tag{4.2}$$

where k_x defines the periodicity of the grating along x axis and l is the azimuthal order and ϕ is $\tan^{-1}(y/x)$. The holograms for LG_0^1 beam has l=1. By directing an expanded Gaussian beam (plane wave approximation), $G(r,\phi,z)$, upon the hologram with a transmission function of T, a number of diffracted orders, i.e. the zeroth order and the two conjugate orders, would emerge. The input Gaussian beam is diffracted into different orders of the beam with azimuthal phase variations. It is important to know that the azimuthal index from the two diffraction order are of equal in magnitude but opposite in sign (positive and negative) as shown in equation 4.3 and figure 4.7,

$$\begin{aligned} G(r,\phi,z).T &= G(r,\phi,z).\left[\frac{1}{2}\left(1-\cos(k_x x \pm l\phi)\right)\right] \\ &= G(r,\phi,z).\left[\frac{1}{2}-\frac{e^{i(k_x x\pm l\phi)}-e^{-i(k_x x_1\pm l\phi)}}{4}\right] \\ &= \left[\frac{1}{2}G(r,\phi,z)-\frac{1}{4}G(r,\phi,z)e^{i(k_x x\pm l\phi)}-\frac{1}{4}G(r,\phi,z)e^{-i(k_x x\pm l\phi)}\right] \end{aligned} \tag{4.3}$$

This holographic technique can be readily achieved using spatial light modulators (SLM) [40] which have gained more popularity due to the ease and versatility of LG beam generation [41].

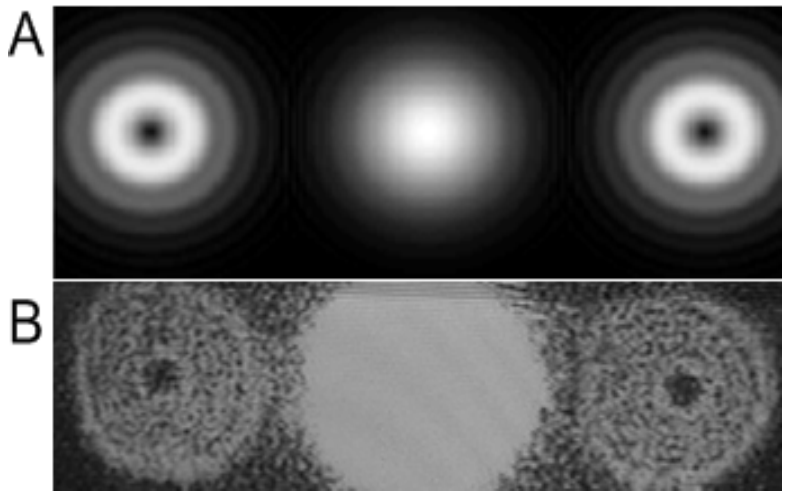

Figure 4.7 Intensity profile of the diffracting orders from a hologram for generating LG_0^1 beam as shown in figure 4.6. A - shows numerically calculated far-field diffraction B - shows the experimentally obtain far-field diffraction pattern (the beams are slightly defocused) [39]. The zeroth diffraction order (centre Gaussian beam) has the highest intensity. The hologram used to generate the LG beams are binary grating and thus the low efficiency in the first diffraction orders.

4.4.2. Spiral phase plate

A direct method would be to replicate the azimuthal phase variation ($\exp(\mp il\phi)$) on an optically transparent medium [24]. Such a phase element can directly imprint its phase onto the input beam. The phase imprinting process can be explained by simple refractive index change. If an input beam of wavelength λ with a planar wavefront illuminates a single piece of refractive element of a given thickness h_N, the glass plate will create a phase delay of θ based on the glass plate's thickness and n_{glass}, n_{air} is the refractive index of glass and air respectively as shown in equation 4.4,

$$\Delta\theta = \frac{2\pi(n_{glass} - n_{air})h_N}{\lambda} \tag{4.4}$$

If one is to subdivide the thickness of the refractive element into N number of steps and arrange them in a spiral pattern, it would form a spiral phase delay onto an input wavefront. For a quantized phase step *i*, the overall phase delay h_N would be given in equation 4.5,

$$h_N = \sum_{i=1}^{N} \Delta h_i \tag{4.5}$$

Substituting equation 4.5 to equation 4.4, the total phase shift in a spiral phase plate is given as $\Delta\theta_{spiral}$ in equation 4.6,

$$\begin{aligned} \Delta\theta_{spiral} &= \frac{2\pi(n_{glass} - n_{air})}{\lambda}\left[\left(\frac{\phi}{2\pi}\right)\sum_{i=1}^{N} h_i\right] \\ &= \frac{(n_{glass} - n_{air})}{\lambda}\left[(\phi)h_n\right] \end{aligned} \tag{4.6}$$

Equation 4.6 is the quantized summation of the individual phase step *h* over the beam circumference ($\phi = 0 - 2\pi$). From equation 4.6, the total phase change, $\Delta\theta_{spiral}$ will be equal to $l\phi$. The azimuthal phase will be directly dependent on the refractive index difference between the glass and air, the height of the refractive element and wavelength as shown in equation 4.7.

$$\Delta\theta_{spiral} = l\phi = \frac{(n_{glass} - n_{air})}{\lambda}\left[(\phi)\sum_{i=1}^{N} h_i\right]$$
$$l = \frac{(n_{glass} - n_{air})h_N}{\lambda} \qquad (4.7)$$

If the input beam is a Gaussian beam, the final electric field $E_{spiral}(r,\phi,z)$ will be given by equation 4.8,

$$E_{spiral}(r,\phi,z) = \left[\frac{w_o}{w(z)}.\exp(\frac{-x^2+y^2}{w^2(z)}).\exp(-i\tan^{-1}\frac{z}{z_R}).\exp(-i(\frac{-kr^2}{2R(z)}))\right].\exp(-ikz).\exp(il\phi) \quad (4.8)$$

where $r = \sqrt{x^2+y^2}$, $\phi = \arctan(y/x)$, l is the number of cycles of 2π phase around the optical beam circumference, k is the wave number, w_o is the radius at which the Gaussian term $\exp(-r^2/w^2)$ falls to 1/e of its on-axis value and *w(z)* is the radius of the beam waist at the propagation distance z, z_R is the Rayleigh range.

In many cases, the spiral phase element makes use of a high refractive index substrate that is shaped into the spiral phase ramp [24, 42]. With recent micro-fabrication techniques, the spiral phase element has been miniaturized [43, 44]. From Equation 4.7, it is also clear that the azimuthal order of the spiral phase plate is specific to the wavelength of the input beam. Hence, it is possible to access the "non-integer" azimuthal phase variation by changing the wavelength of the illuminating laser beam [42]. Due to the limitations of lithography (without stitching), the size of the phase plate cannot be too big (limited to hundreds of microns). The small aperture can introduce additional diffracting light pattern which interferes with the purity of the mode (asymmetrical shape of the dark core and strong intensity side-lobes). Figure 4.8 shows two images of the spiral phase plate for LG_0^1 at wavelength of 633 nm and their respective intensity pattern at the far-field. Figure 4.8 A and B shows the numerically calculated three dimensional spiral phase and a microfabricated spiral phase plate respectively. The respective LG modes (equation 4.8) created at the far-field in simulation and experiment are shown in figure 4.8 C and D.

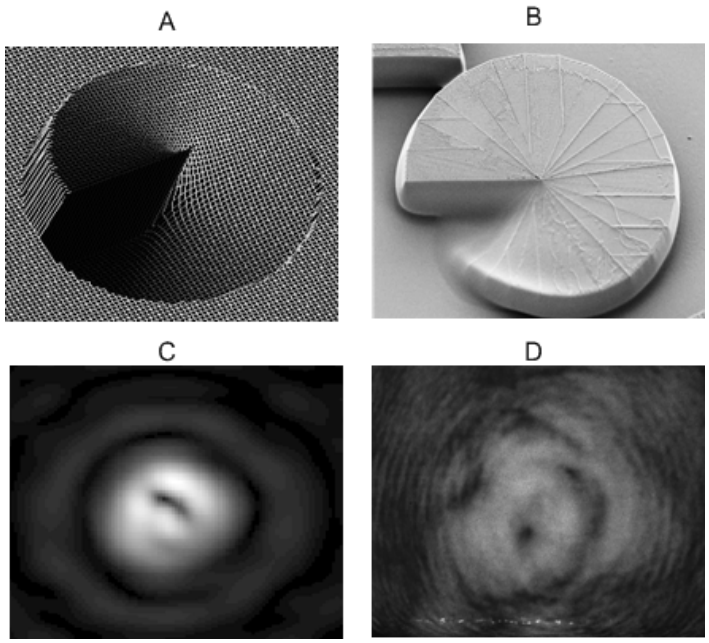

Figure 4.8 Spiral phase plate and the far-field intensity pattern. A is the numerically calculated of the spiral phase; B is the fabricated phase plate using e-beam lithography [Chris Readon]. C – is the numerically calculated LG_0^1 after passing through the micron sized spiral phase in A and D – experimentally obtained LG_0^1 beam with the microfabricated spiral phase plate [4].

The exact output laser mode from the spiral phase plate described here is a superposition of LG modes [24], as seen in figure 4.8 C and D. This mode mismatching is generally due to the discrete phase step or the aperture (optical window) introduced by the spiral phase element.

LG modes form a complete orthonormal basis. An experimentally generated LG beam using the spiral phase element (also with holograms) can contain higher order LG modes. By performing a mode decomposition (based on orthogonal operations) of the experimentally obtained LG modes (intensity pattern), the weightings of each higher order LG modes can be identified [10]. Current fabrication technology (>24 fine steps) can yield up to 80% mode conversion efficiency from Gaussian to LG_0^1 beam. An interferometer can reveal the quality of the azimuthal phase variations [32]. Here, I use a Michelson interferometer to interfere the LG beam with itself. This produces a dual fork intensity pattern [41], as shown in figure 4.9. From the interference pattern, I can see additional azimuthal phase variations besides the centre beam axial (dash circles and red dots). The wavelength of the laser used here is 633nm.

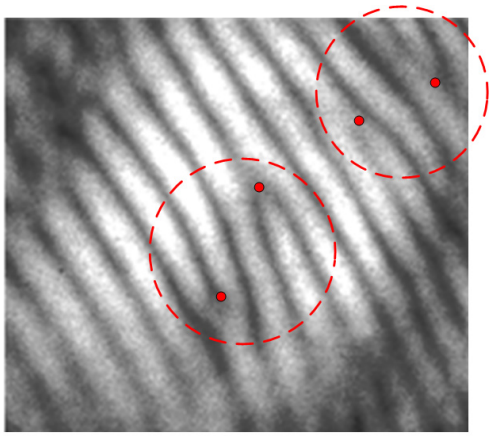

Figure 4.9- Interference patttern LG_0^1 using a Michelson interferometer. The ring circle indicates the presence of the azimuthal phase variations (double fork pattern). The red dot identify the location of each fork intensity pattern.

The complex expansion coefficients of the decomposition of the LG beam can be calculated by means of a scalar product [24, 42]. However, this decomposition is often used to assess to the quality of the free-space generated LG beam. In this thesis, the main concern is the experimental trapping performance of the generated LG beam, thus the detailed mode decomposition of the LG beam is not covered in this thesis. The quality of the LG beam is judged by measuring the intensity variations in the annular intensity pattern. The intensity distribution of the LG beam is critical to the trapping dynamics which is of concern in this chapter. In simulation and experiment (figure 4.8), the microfabricated spiral phase plate creates large beam asymmetry in the far-field. The symmetry in the intensity pattern can be attributed to the small aperture size of the microfabricated spiral phase plate. The small sized aperture introduces additional diffracting light that reduces the intensity and wavefront symmetry of the beam. To overcome this, a large aperture spiral phase plate is needed. In our current trapping experiment, I make use a large aperture spiral phase plate from RPC photonics to generate the LG_0^1 mode at wavelength 1070nm [45]. The large aperture (≈10 mm) reduces the distortion of the dark core and gives a smooth transverse intensity (5% intensity variation) around the beam circumference, as seen in figure 4.10. The high order modes (additional annular rings = higher radial modes p) are still present in the final beam. The intensity of the additional annular ring has amplitude of <20% than the first annular ring.

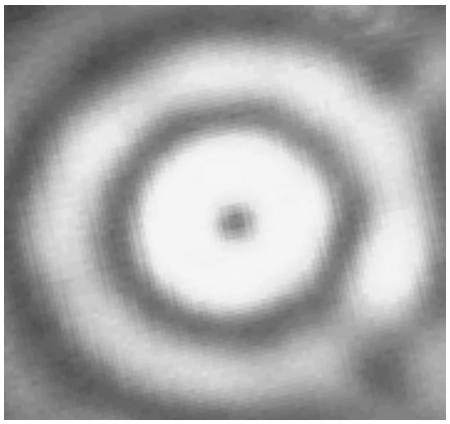

Figure 4.10- Improved LG_0^1 beam from large aperture spiral phase plate. The large aperture spiral phase plate is obtained from RPC photonics [45].

4.5. Calibrating LG beam optical tweezers with quadrant photodiode

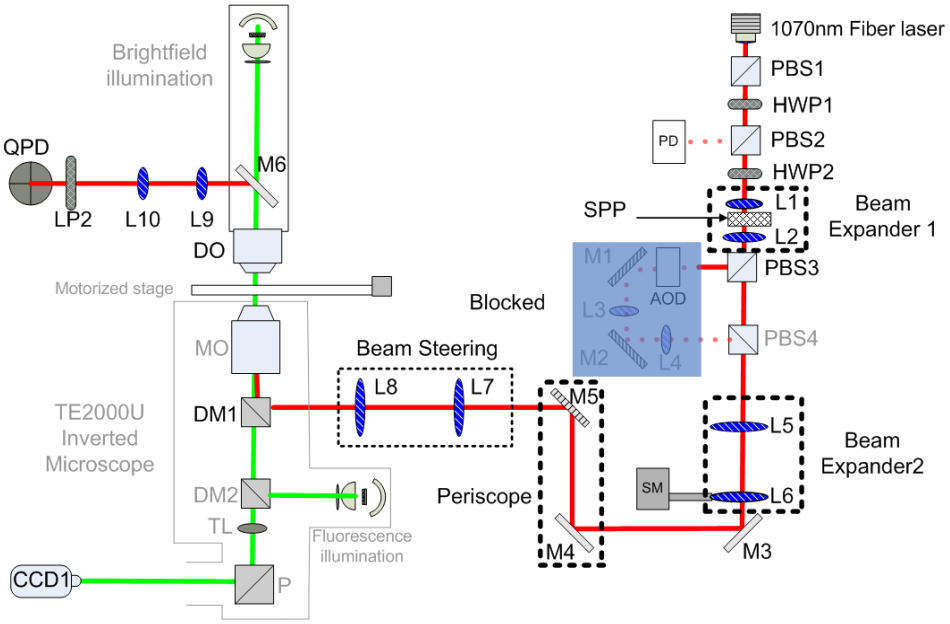

Figure 4.11 Experimental setup for calibrating a LG_0^1 beam optical tweezers. The spiral phase plate (SPP) [45] is placed at one focal length away from lens L1. The blue colour block indicates the deflected path after PBS3 that is not used in this experiment.

The experimental setup shown in section 3.8 is used for the calibration experiments. The spiral phase plate (SPP) is placed on the first beam expansion lens system. This converts the input Gaussian beam from the fiber laser into a LG_0^1 beam. The undeflected LG_0^1 beam passing through PBS3 is used for the calibration and trap stiffness measurements. The position of the SPP lies at

approximately one focal length away from L1. Using a high quality SPP (RP photonics), the insertion power loss is measured to be only 5%. Direct insertion of the spiral phase plate ensures a comparable back filling factor with the Gaussian beam. In other words, the beam diameters of the input LG_0^1 and Gaussian beam at the back aperture of the microscope objective are almost equal. Here the beam diameter of the LG_0^1 beams varies approximately 15% from the Gaussian beam. The almost matching back aperture filling factor is important so as to achieve a reasonable comparison between the two beams.

To obtain the conversion factor, I return the QPD calibration technique described in section 3.4. In this experiment, I make use of polymer microsphere of diameter 1 µm. Figure 4.12 shows the transverse and axial axes calibration graphs for 1µm sphere. From the plots, in figure 4.12, I carry out a linear fit to obtain the conversion factor. For consistency, I also repeated the calibration of the Gaussian beam. The power used for the calibration is 26mW at the sample. The X conversion factor for Gaussian and LG_0^1 beam are given as 0.85 V/µm and 0.86 V/µm. The Y conversion factors for Gaussian and LG_0^1 beam are 1.05 V/µm and 1.06 V/µm respectively. There are minor differences in the values of the conversion factors between Gaussian and LG beam. In the axial direction, the conversion factor for the Gaussian and LG beam are 2.5 V/µm and 1.3 V/µm respectively. The calibration result suggests good transverse and axial linearly scaling (V to µm) with a LG_0^1 beam using the QPD.

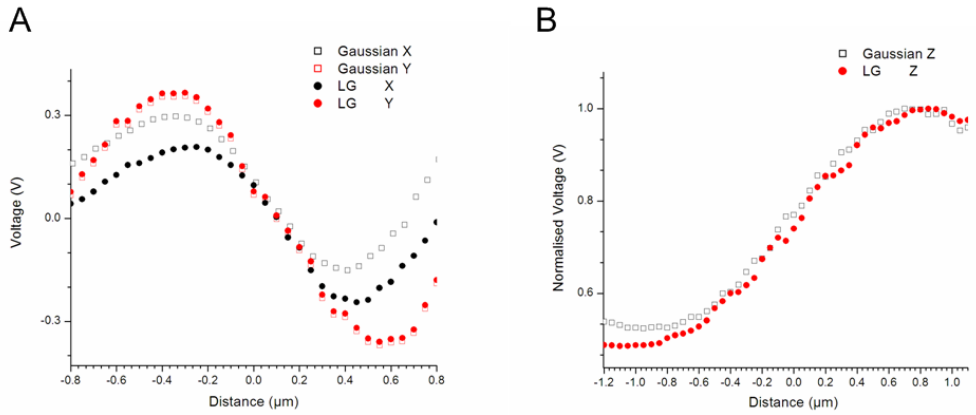

Figure 4.12 - Calibration for Gaussian and LG_0^1 beam for 1µm spheres. A - Black square and red square data for transverse plane for Gaussian beam and Black dots and red dots indicate data for transverse plane X and Y for LG_0^1 beam. B –black square and red dots indicate data for the axial plane for Gaussian and LG_0^1 beam.

The far-field interference of an LG_0^1 beam and Gaussian beam can exhibit a spiral intensity pattern [32]. Hence, it is logical to also expect that the interference at the back focal plane can produce a spiral like pattern. An ideal LG beam possess a different Gouy phase function ($1+ 2p + l \tan^{-1}(z/z_r)$) than the Gaussian beam. As such, a spiral intensity pattern can be generated with a LG beam upon interference with a plane wave or spherical wave (scattered light). This effect can pose an issue for the position measurement, i.e. transverse cross talk, when using the LG beam for position calibration [46]. The interference pattern can rotate when the particle moves transversely within the trapping beam. This effect might introduce ambiguity in the conversion factor [2, 47].

A direct way of quantifying the cross talk is to measure the cross correlation of the power spectrum density of the two axis (Px and Py) of a trapped microsphere [48]. This is done without going through the tedious two dimensional scans for different particle sizes, shown in figure 3.5 of chapter 3. Table 4.1 lists the cross-correlation of the power spectrum for different particle sizes over a given frequency range. In the conventional optical tweezers using a focused Gaussian beam, the cross-correlation factor between the two transverse axes should vary between 1-2% for the particles size from 1-3μm. However, in the LG_0^1 beam, the cross correlation factor is significantly higher as the particles size increases to 3 μm. This indicates that this cross talk between the two transverse axes would be significant for large sphere size. The logic of this result is that the larger sized microspheres will produce an increased scattered signal. This increase will contribute to an increased interference signal between the diffracted and undiffracted light fields. With the increased interference signals, the "spiral" intensity would because more prominent and therefore contribute to the cross talk (cross-correlations).

Diameter (μm)	Cross correlation over the frequency (5Hz-10000Hz) $Pxy/(PxPy)^{1/2}$
1	0. 1%
2	1.5%
3	19%

Table 4.1 – Measure of cross talk with trapped particles in the LG trap.

To further verify the effect cross talk in the 3 μm sphere at the back focal plane, I then carry out a two dimensional scan of the particle and collect the intensity signal at the back focal plane.

The interference of a LG_0^1 beam with a spherical wave at the BFP is numerically calculated using beam propagation method (section 3.3). I numerically calculated the back focal plane

interference by simulating the interference between a spherical wave (scattering from a Mie object) and a focused LG beam (using a lens of a focal length 170µm) at the focus as shown in figure 4.13 A. On the other hand, I also performed a two dimensional scan of a stuck 3µm which measures the interference intensity pattern detected by the QPD, as shown in figure 4.13 B. From the intensity pattern at the BFP in simulation and experiment, it is clear that the spiral interference fringe (indicated in the red dotted line) is present. From the data, it would be advisable to trap microspheres of diameter <3 µm with the focused LG_0^1 beam to avoid the cross talk.

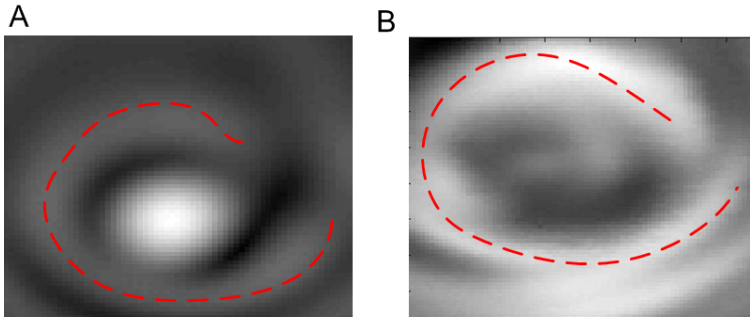

Figure 4.13 – Two dimensional plot of the interference pattern (spherical wave and LG beam) capture at the back focal plane A – Numerical calculations of interference pattern from scattered and unscattered light from Mie particle, B – Intensity of the back focal plane with the scanning of the stuck 3 µm sphere achieve experimentally using the QPD. The red dotted line indicates the intensity of the spiral pattern.

4.6. Measuring on-axis scattering with back focal plane interference

Using the BFP interferometry with a calibrated QPD, it is possible to directly infer onto the relative axial position shift of the microsphere within the optical tweezers due to scattering forces. Kress *et al* [49] showed that for the same particle type and at the same power, the BFP signal on a calibrated QPD can elucidate the scattering forces in an optical trap. They reduce the NA of the microscope objective used for optical trapping and steadily observed the increase in the asymmetry in the position distribution of the trapped particle over the axial position calibrated graph (V/µm). The asymmetry here means that the centre of the position histogram of the trapped particle moves further away from the mid point of the position calibration graph. Since the decrease in the NA of an objective, the balance of the scattering and gradient forces in the axial direction would start to change, i.e. scattering forces > gradient forces.

Here I repeated the same analysis for Gaussian and LG_0^1 beam optical tweezers with 1 µm diameter polymer sphere. The sphere is trapped at 10µm above the coverslip to reduce any surface hydrodynamic forces. Figure 4.14A shows that microsphere in a Gaussian beam resides at an asymmetrical position about the most linear part of the calibration graph. The ratio of asymmetry is

comparable with Kress et al [49] based on the same NA (1.25) used for the trapping beam. Figure 4.14 B shows the trapped microsphere residing in the LG_0^1 beam being located at a position that is closer to the centre of the linear region. The ratio of the particle position, with respect to the edges of the linearly scaled region, on the calibration graph is measured by 0.65 (Gaussian) and 0.93 (LG_0^1 beam). This strongly suggests that the on-axis scattering of a LG_0^1 beam is reduced to a minimum and thus permits the microsphere to reside close to the centre of the linear region. This graph is the first evidence of the reduced scattering forces imposed by a LG_0^1 beam using a calibrated QPD and BFP interferometry technique.

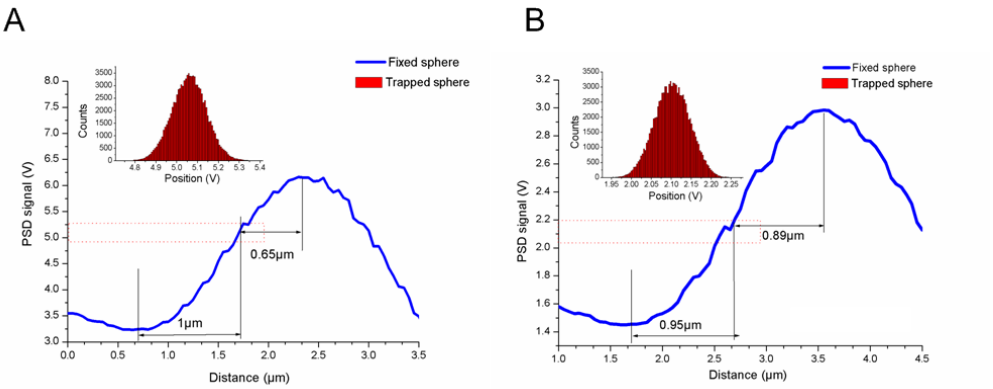

Figure 4.14 – Particle position with respect to calibration graph. The inset shown a histogram of the particle position. The centre position in the histogram is linked to the calibration graph. (A) Gaussian beam and (B) Sensitivity of the axial detection with A- Gaussian and B- LG_0^1 beam. The ratio of the particle position, with respect to the edge of the linearly scaled region, on the calibration graph is measured by 0.65 (Gaussian) and 0.93 (LG_0^1 beam).

.

4.7. Evaluation of trap stiffness

To assess the trap stiffness of the optical tweezers, the power spectrum analysis is first performed by Friese *et al* [19]. Both the focused Gaussian beam and LG beam are deployed to trap polymer spheres with sizes of 1 μm, 2 μm and 3 μm in diameter. A nonlinear fitting procedure is use to measure the frequency roll off, which is then use to calculate the trap stiffness. The data are presented as a block chart in figure 4.15. Judging from the plot in figure 4.15, the trends seem to indicate that for the trapping of 1 μm spheres, the Gaussian beam out performs, by ≈50%, the LG beam both transverse (XY) and axial (Z) stiffness. However, the LG beam seems to be comparatively better (≈ 40%) in stiffness along the axial (Z) for trapping of 2 μm spheres than the Gaussian beam. As for the trapping of 3 μm sphere, both beams offered the low stiffness in all three directions. However, a large amount of cross talk in the LG beam needs to be taken in account, see

table 4.1 for larger spheres sizes. The stiffness measurements are consistent with the results obtained by Friese *et al* [19].

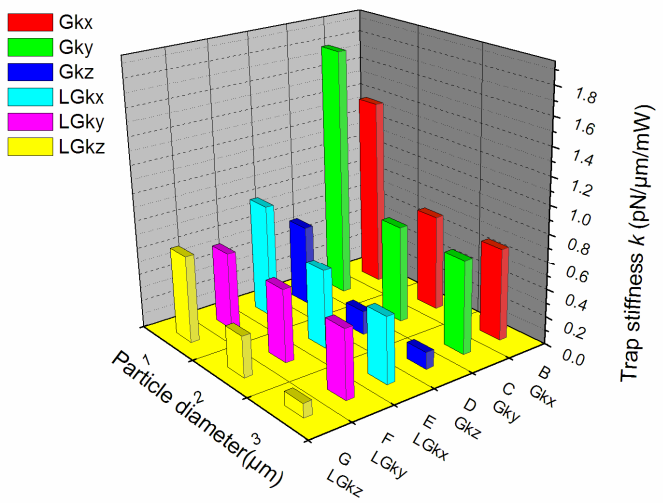

Figure 4.15 Trap stiffness per mW (pN/μm/mW) in XYZ for Gaussian and LG beam. (Gkx. Gky and Gkz refers to the trap stiffness of the Gaussian beam in x,y and z and LGkx. LGky and LGkz refers to the trap stiffness of the LG_0^1 beam in x,y and z)

Although it will be useful to measure the performance of larger azimuthal orders $l \geq 2$ LG beam, it is not appropriate as the LG beam waist would increase as well [50, 51].For higher order azimuthal modes, the beam waist would increase [50, 51] due to the beam scaling factor $r_l = w(z)\left(\sqrt{l/2}\right)$ where r_l is radius of the ring, $w(z)$ is the Gaussian bean waist in equation 4.1. Hence, an increase in l would increase the radius of the ring [27]. Also even if it is possible to match the increase beam waist to the back aperture of the microscope objective, the thin intensity ring for higher l would impose a weak transverse optical potential well for smaller microspheres and thus deem unsuitable for optical forces measurement schemes.

4.8. Conclusion

The conventional optical tweezers system does have some drawbacks such as trapping of only high refractive index particles and residual on-axis light scattering. The use of higher order laser beams primarily LG beam for optical trapping marks an important improvement in development of the optical tweezers systems. A focused LG beam can manipulate particles of either high or low refractive indices within its annular intensity pattern. In addition, the intensity minimal at the centre of the beam can potentially reduce the residual on-axis scattering force.

In this chapter, I started off by reviewing the higher order LG beam modes and paid close attention to the formation of the azimuthal phase variation and its annular intensity pattern. In the next section, I described two elements, computer generated hologram and spiral phase plate, for generating LG_0^1 beams from Gaussian beam. From the two techniques, I chosen to implement the spiral phase plate in the conversion of the Gaussian beam into a LG_0^1 beam. The generated LG_0^1 beam had a smooth intensity distribution in the annular intensity ring (≈5% variations) and low insertion loss. In addition, the spiral phase plate was directly integrated into the existing optical tweezers system, as described in section 3.8, without any realignment. To date, there had been a wide number of application using LG beams [5, 12, 15, 17, 21, 22] but none has shown within the context of a calibrated optical force measurement tool with BFP interferometry. In the following sections, I used the QPD calibration scheme in section 3.4 and power spectrum analysis in section 3.6.2 to study optical tweezers formed with a focused Gaussian beam and LG beam.

Next, I performed steps to obtain the calibration graph with the BFP interferometry technique. The calibration graph (V/μm) obtained from the QPD with a LG_0^1 beam was comparable to the Gaussian beam, using 1 μm stuck sphere, in all three dimensions. The interference of the LG_0^1 beam created a spiral intensity pattern. This effectively increased the cross talk between the transverse planes. By analyzing the cross-correlation of the LG_0^1 beam for different spheres size, I found that the 3μm diameter sphere contains the highest crosstalk. The cross talk was reduced for smaller sized particles.

After which, I performed the mapping of the axial position histogram (uncalibrated) of the trapped 1 μm onto the axial calibration graph of a LG_0^1 beam and Gaussian beam. This mapping helped to infer the axial scattering forces present in the trap [52]. The ratio of the particle positions, with respect to the edge of the linearly scaled region on the calibration graph, was measured to be 0.65 for Gaussian and 0.93 for LG_0^1 beam. The ratio of the positions strongly suggested that the on-axis scattering of a LG_0^1 beam was reduced to a minimum and thus permitted the microsphere to reside close to the centre of the linear region. This graph is the first evidence of the reduced scattering forces imposed by a LG_0^1 beam using a calibrated QPD and BFP interferometry technique.

Finally, I used the PSD analysis (chapter.3.6.2) to measure the trap stiffness with both the LG_0^1 beam and a Gaussian beam optical tweezers for range of particles sizes: 1, 2 and 3μm. From

the measurements, the optical stiffness of the LG_0^1 had ≈ 40% higher axial trap stiffness for 2μm spheres as compared with the Gaussian beam. On the other hand, Gaussian beam performed 50% better than LG_0^1 beam when trapping 1 μm spheres. However, both beams provided poor trap stiffness for 3 μm spheres. This is consistent with the results obtained by Friese *et al* [19] using back scattering geometry and PSD analysis.

With the results reported in this chapter, there are a number of future works that can continue:

Using defocusing microscopic imaging and two photon fluorescence imaging, Kress *et al* [53] measured that a trapped 1 um sphere lies at 150 nm above the focused Gaussian beam. A future work is to quantify the exact position shift of the trapped particle with respect to the focal point of the LG beam.

Another future work can include the calibration of optical tweezers formed LG beam with larger azimuthal index (l >1). However, special care needs to be taken to match the increase beam waist to the back aperture of the microscope objective. This is to satisfy the NA requirements of the microscope objective lens. It is also possible to improve the tracking of the trapped particle by using an independent laser beam as a probe beam (decoupled from the trapping probe beam). The independent probe can also provide a direct observation of the axial position shift between the Gaussian and LG beam trap.

Orbital angular momentum of the high order LG modes beam can be transferred via scattering [54]. It would be also useful to calibrate the rotating trapped microspheres, due to orbital angular momentum using the BFP and QPD technique. One possibility technique to measure transverse rotation in a symmetrical microsphere is through the spiral intensity at the BFP. The spiral intensity pattern could rotate due to a rotating microsphere. This proposed experiment is similar to the recent work done by Garbin *et al* [46]. They showed that the scattered signal off a metallic sphere (absorbing particle) in a LG trapping beam can have an asymmetry. The scattering signal was used to infer onto the azimuthal phase of a LG beam. In the next chapter, I use the interference patterns from the forward scattered light of trapped microsphere to measure the azimuthal phase of a LG beam. In this chapter, I have designed and performed the simulations and experiments.

4.9. References

1. H. Kress, E. H. K. Stelzer, G. Griffiths, and A. Rohrbach, "Control of relative radiation pressure in optical traps: Application to phagocytic membrane binding studies," Physical Review E (Statistical, Nonlinear, and Soft Matter Physics) **71**, 061927-061910 (2005).

2. L. Paterson, M. P. MacDonald, J. Arlt, W. Sibbett, P. E. Bryant, and K. Dholakia, "Controlled rotation of optically trapped microscopic particles," Science **292**, 912-914 (2001).
3. A. Ashkin, and J. M. Dziedzic, "Stability of optical levitation by radiation pressure," Applied Physics Letters **24**, 586-588 (1974).
4. W. M. Lee, B. P. S. Ahluwalia, X. C. Yuan, W. C. Cheong, and K. Dholakia, "Optical steering of high and low index microparticles by manipulating an off-axis optical vortex," Journal of Optics a-Pure and Applied Optics **7**, 1-6 (2005).
5. K. T. Gahagan, and G. A. Swartzlander, "Optical vortex trapping of particles," Optics Letters **21**, 827-829 (1996).
6. L. Allen, M. W. Beijersbergen, R. J. C. Spreeuw, and J. P. Woerdman, "Orbital angular-momentum of light and the transformation of Laguerre-Gaussian laser modes," Physical Review A **45**, 8185-8189 (1992).
7. N. B. Simpson, K. Dholakia, L. Allen, and M. J. Padgett, "Mechanical equivalence of spin and orbital angular momentum of light: An optical spanner," Optics Letters **22**, 52-54 (1997).
8. V. Garces-Chavez, K. Volke-Sepulveda, S. Chavez-Cerda, W. Sibbett, and K. Dholakia, "Transfer of orbital angular momentum to an optically trapped low-index particle," Physical Review A **66**, 063402 (2002).
9. B. Jack, M. J. Padgett, and S. Franke-Arnold, "Angular diffraction," New Journal of Physics **10**, 103013 (2008).
10. M. W. Beijersbergen, L. Allen, H. Vanderveen, and J. P. Woerdman, "Astigmatic Laser Mode Converters And Transfer Of Orbital Angular-Momentum," Optics Communications **96**, 123-132 (1993).
11. F. A. Starikov, G. G. Kochemasov, S. M. Kulikov, A. N. Manachinsky, N. V. Maslov, A. V. Ogorodnikov, S. A. Sukharev, V. P. Aksenov, I. V. Izmailov, F. Y. Kanev, V. V. Atuchin, and I. S. Soldatenkov, "Wavefront reconstruction of an optical vortex by a Hartmann-Shack sensor," Opt. Lett. **32**, 2291-2293 (2007).
12. K. Ladavac, and D. G. Grier, "Microoptomechanical pumps assembled and driven by holographic optical vortex arrays," Optics Express **12**, 1144-1149 (2004).
13. V. Bingelyte, J. Leach, J. Courtial, and M. J. Padgett, "Optically controlled three-dimensional rotation of microscopic objects," Applied Physics Letters **82**, 829-831 (2003).
14. A. T. O'Neil, I. MacVicar, L. Allen, and M. J. Padgett, "Intrinsic and extrinsic nature of the orbital angular momentum of a light beam," Physical Review Letters **88**, 053601 (2002).
15. A. T. O'Neill, and M. J. Padgett, "Axial and lateral trapping efficiency of Laguerre-Gaussian modes in inverted optical tweezers," Optics Communications **193**, 45-50 (2001).
16. N. B. Simpson, D. McGloin, K. Dholakia, L. Allen, and M. J. Padgett, "Optical tweezers with increased axial trapping efficiency," Journal of Modern Optics **45**, 1943-1949 (1998).
17. N. B. Simpson, L. Allen, and M. J. Padgett, "Optical tweezers and optical spanners with Laguerre-Gaussian modes," Journal of Modern Optics **43**, 2485-2491 (1996).
18. K. T. Gahagan, and J. G. A. Swartzlander, "Simultaneous trapping of low-index and high-index microparticles observed with an optical-vortex trap," J. Opt. Soc. Am. B **16**, 533-537 (1999).
19. M. E. J. Friese, H. RubinszteinDunlop, N. R. Heckenberg, and E. W. Dearden, "Determination of the force constant of a single-beam gradient trap by measurement of backscattered light," Applied Optics **35**, 7112-7116 (1996).
20. D. C. Appleyard, K. Y. Vandermeulen, H. Lee, and M. J. Lang, "Optical trapping for undergraduates," American Journal of Physics **75**, 5-14 (2007).
21. V. Garbin, D. Cojoc, E. Ferrari, R. Z. Proietti, S. Cabrini, and E. Di Fabrizio, "Optical micromanipulation using Laguerre-Gaussian beams," Japanese Journal of Applied Physics Part 1-Regular Papers Brief Communications & Review Papers **44**, 5773-5776 (2005).
22. P. A. Prentice, M. P. MacDonald, T. G. Frank, A. Cuschieri, G. C. Spalding, W. Sibbett, P. A. Campbell, and K. Dholakia, "Manipulation and filtration of low index particles with holographic Laguerre-Gaussian optical trap arrays," Optics Express **12**, 593-600 (2004).
23. M. E. J. Friese, T. A. Nieminen, N. R. Heckenberg, and H. Rubinsztein-Dunlop, "Optical alignment and spinning of laser-trapped microscopic particles," Nature **394**, 348-350 (1998).
24. M. W. Beijersbergen, R. P. C. Coerwinkel, M. Kristensen, and J. P. Woerdman, "Helical-Wave-Front Laser-Beams Produced With A Spiral Phaseplate," Optics Communications **112**, 321-327 (1994).

25. G. Molina-Terriza, J. Recolons, J. P. Torres, L. Torner, and E. M. Wright, "Observation of the dynamical inversion of the topological charge of an optical vortex," Physical Review Letters **8702**, Art. No. 023902 (2001).
26. J. Arlt, K. Dholakia, L. Allen, and M. J. Padgett, "The production of multiringed Laguerre-Gaussian modes by computer-generated holograms," Journal of Modern Optics **45**, 1231-1237 (1998).
27. J. Arlt, R. Kuhn, and K. Dholakia, "Spatial transformation of Laguerre-Gaussian laser modes," Journal of Modern Optics **48**, 783-787 (2001).
28. L. Allen, M. J. Padgett, and M. Babiker, "The orbital angular momentum of light," in *Progress in Optics, Vol XXXIX*(1999), pp. 291-372.
29. A. Mair, A. Vaziri, G. Weihs, and A. Zeilinger, "Entanglement of the orbital angular momentum states of photons," Nature **412**, 313-316 (2001).
30. S. M. Barnett, "Optical angular-momentum flux," Journal of Optics B-Quantum and Semiclassical Optics **4**, S7-S16 (2002).
31. A. T. O'Neil, and M. J. Padgett, "Three-dimensional optical confinement of micron-sized metal particles and the decoupling of the spin and orbital angular momentum within an optical spanner," Optics Communications **185**, 139-143 (2000).
32. M. Padgett, J. Arlt, N. Simpson, and L. Allen, "An experiment to observe the intensity and phase structure of Laguerre-Gaussian laser modes," Am. J. Phys. **64**, 77-82 (1996).
33. H. I. Sztul, and R. R. Alfano, "Double-slit interference with Laguerre-Gaussian beams," Opt. Lett. **31**, 999-1001 (2006).
34. S. Franke-Arnold, L. Allen, and M. Padgett, "Advances in optical angular momentum," Laser & Photonics Review **2**, 299-313 (2008).
35. A. Ishaaya, N. Davidson, and A. Friesem, "Very high-order pure Laguerre-Gaussian mode selection in a passive Q-switched Nd:YAG laser," Opt. Express **13**, 4952-4962 (2005).
36. O. T. Okida M, Itoh M, and Yatagai T,, "Direct generation of high power Laguerre–Gaussian output from a diode-pumped Nd:YVO4 1.3-μm bounce laser," Opt. Express **15**, 7616-7622 (2007).
37. R. Piestun, B. Spektor, and J. Shamir, "On-axis binary-amplitude computer generated holograms," Optics Communications **136**, 85-92 (1997).
38. G. Tricoles, "Computer generated holograms: an historical review,," Appl. Opt. **26**, 4351-4360 (1987).
39. W. M. Lee, X. C. Yuan, and D. Y. Tang, "Optical tweezers with multiple optical forces using double-hologram interference," Optics Express **11**, 199-207 (2003).
40. E. Martin-Badosa, M. Montes-Usategui, A. Carnicer, J. Andilla, E. Pleguezuelos, and I. Juvells, "Design strategies for optimizing holographic optical tweezers set-ups," Journal of Optics A: Pure and Applied Optics **9**, S267-S277 (2007).
41. W. M. Lee, X. C. Yuan, and K. Dholakia, "Experimental observation of optical vortex evolution in a Gaussian beam with an embedded fractional phase step," Optics Communications **239**, 129-135 (2004).
42. S. S. R. Oemrawsingh, J. A. W. Van Houwelingen, Eliel E. R, J. P. Woerdman, Verstegen. E. J. K, Kloosterboer, and 't Hooft.G. W, "Production and Characterization of Spiral Phase Plates for Optical Wavelengths," Appl. Opt. **43**, 688-694 (2004).
43. W. C. Cheong, W. M. Lee, X. C. Yuan, L. S. Zhang, K. Dholakia, and H. Wang, "Direct electron-beam writing of continuous spiral phase plates in negative resist with high power efficiency for optical manipulation," Applied Physics Letters **85**, 5784-5786 (2004).
44. W. M. Lee, X. C. Yuan, and W. C. Cheong, "Optical vortex beam shaping by use of highly efficient irregular spiral phase plates for optical micromanipulation," Optics Letters **29**, 1796-1798 (2004).
45. http://www.rpcphotonics.com/vortex.asp.
46. V. Garbin, G. Volpe, E. Ferrari, M. Versluis, D. Cojoc, and D. Petrov, "Mie scattering distinguishes the topological charge of an optical vortex: a homage to Gustav Mie," New Journal of Physics **11**, 11 (2009).
47. M. P. MacDonald, K. Volke-Sepulveda, L. Paterson, J. Arlt, W. Sibbett, and K. Dholakia, "Revolving interference patterns for the rotation of optically trapped particles," Optics Communications **201**, 21-28 (2002).
48. K. Berg-Sorensen, and H. Flyvbjerg, "Power spectrum analysis for optical tweezers," Review of Scientific Instruments **75**, 594-612 (2004).

49. H. Kress, E. H. K. Stelzer, G. Griffiths, and A. Rohrbach, "Control of relative radiation pressure in optical traps: Application to phagocytic membrane binding studies," Physical Review E **71**, 061927 (2005).
50. R. K. Singh, P. Senthilkumaran, and K. Singh, "Effect of primary coma on the focusing of a Laguerre-Gaussian beam by a high numerical aperture system; vectorial diffraction theory," Journal of Optics a-Pure and Applied Optics **10**, 9 (2008).
51. D. Ganic, X. Gan, and M. Gu, "Focusing of doughnut laser beams by a high numerical-aperture objective in free space," Opt. Express **11**, 2747-2752 (2003).
52. H. Kress, E. H. K. Stelzer, G. Griffiths, and A. Rohrbach, "Control of relative radiation pressure in optical traps: Application to phagocytic membrane binding studies," Physical Review E **71** (2005).
53. H. Kress, E. H. K. Stelzer, and A. Rohrbach, "Measuring and adjusting the trapping position in optical tweezers," DGaO Proceedings **ISSN: 1614-8436** (2005).
54. K. Volke-Sepulveda, V. Garces-Chavez, S. Chavez-Cerda, J. Arlt, and K. Dholakia, "Orbital angular momentum of a high-order Bessel light beam," Journal of Optics B-Quantum and Semiclassical Optics **4**, S82-S89 (2002).

Chapter 5 -

Optically trapped micro-apertures for phase and coherence measurements

5. Optically trapped micro-apertures for phase and coherence measurements

5.1. Overview

In the previous chapter 3 and 4, the BFP interference patterns from the diffracting light fields of a trapped microsphere is used for position and trap stiffness measurements. The measured and calculated BFP intensity pattern resembles an Airy disk, figure 3.1. An Airy disk pattern is the Fourier transformation of a circular aperture. Hence, the trapped microsphere is acting like a diffracting aperture [1, 2]. If two microspheres are trapped alongside each other in one optical trap, the interference between the diffracting light (Airy pattern) from each microsphere will form a sinusoidal intensity fringes pattern. The two microspheres have in fact formed a microscopic Young's slit type interferometer. The visibility and arrangements of the interference fringes reflect the correlation of the phase and coherence between the light fields that is emerging from the two microspheres respectively. The sphere can be either trapped by sampling light field or separate optical traps.

In this chapter, I demonstrate two sets of experiments that use optically trapped microparticles as micro-apertures for phase and spatial coherence measurements. The first set of experiments use a LG beam to trap the two or more microspheres within its annular intensity pattern. The microspheres acts like self-aligned apertures and ***samples the trapping beam***. In contrast to the first set of experiments, I next make use of two independent optical traps (dual Gaussian beam optical traps) to manipulate two microparticles individually. The optically controlled micro-apertures (microparticle) are independently used to sample the spatial coherence on a separate sampling light field (LG beam). In the second set of experiments, ***the independent optical traps that are separated from the sampling light field*** offer more controllability over the position in which the microparticles are positioned.

5.2. Introduction

Conventional interferometric system makes use of beam splitter cubes, pinhole and slits for measurement of spatial, temporal coherence and phase change (wavefront) within a given light field. In this particular chapter, I shall restrict to interferometer formed with pinholes and slits: Young slits interferometer [3]. Young's double slits experiment is often used as a map of the spatial coherence of a light field that is well known to result in co-sinusoidal intensity fringes modulated by a sinc function. The lateral shifting and the visibility of the intensity fringes can be used to infer the

phase difference and the spatial coherence between the emerging light fields from the two slits respectively. Traditionally, the Young's interferometer comprises of two rectangular apertures or slit. With current microlithography techniques, the size of the slits can be reduced to smaller symmetrical apertures or pinhole. The quality of the pinholes (≈10 μm) often relies on good fabrication technique. In addition, precise optical alignment of the aperture within the sample beam is important. This alignment helps to increase the intensity of the transmitted light. Microspheres (polystyrene and silica) are widely available from a large number of companies and they come in a range of size selection (typically from 20 nm to 20 μm). These microspheres serve as the ideal pinholes (soft Gaussian type aperture) for probing the phase and coherence properties of a sample light field. Using optical traps, the controllability of the micro-aperture (microsphere) positions around a sample beam is increased. Next I shall briefly explain the concept of phase and coherence measurements with interference.

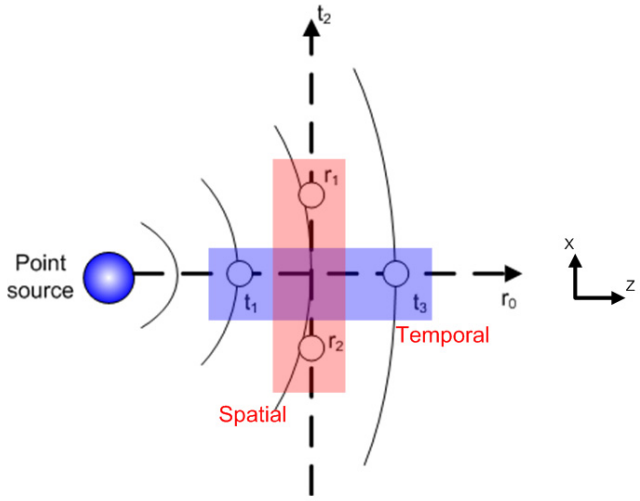

Figure 5.1 Spatial (red box) and temporal (blue box) sampling of a point source. The interference between the light fields from points denoted by $t_{1,2,3}$ and $r_{1,2,3}$ indicates points is time and space. $t_{1,3}$ at r_0 indicates to sampling point at different time in z and $r_{1,2}$ at t_2 refers to the sampling points at different spatial positions (x)

Classical optical interferometry describes the coherent interference of two sets of points, (E_1, E_2) or E_1, E_3, within a coherent light field. The interference pattern generated from the two sets of points is used to sample the spatial coherence or the temporal coherence of the input light. The interference of the fields results in an intensity pattern at an observation plane given as I_p. The intensity pattern is a way of deducing the state of coherence or phase difference between the two

points. Depending on the position of the two points (sampling points); it can refer to either the spatial, $I_{spatial}$ or temporal, $I_{temporal}$, interference as described in equation 5.1 or figure 5.1. By spatial interference, I refer to the sampling of r_1 and r_2 at the same frame of time t_2. On the other hand, temporal interference refers to the sampling of t_1 and t_3 at the same position r_0 ,.

$$I_p \begin{cases} I_{spatial}(r_1, r_2, t_2) = \left|E_1(r_1, t_2)\right|^2 + \left|E_2(r_2, t_2)\right|^2 + 2.\left|\gamma_{12}\right|\left(E_1(r_1, t_2)\right).\left(E_2(r_2, t_2)\right).\cos(\Delta\phi_{12}) \\ I_{temporal}(r_0, t_1, t_3) = \left|E_1(r_0, t_1)\right|^2 + \left|E_3(r_0, t_3)\right|^2 + 2.\left|\gamma_{13}\right|\left(E_1(r_0, t_1)\right).\left(E_3(r_0, t_3)\right).\cos(\Delta\phi_{13}) \end{cases} \quad (5.1)$$

From the interference equation (for temporal and spatial) given in equation 4.1, the cosine and gamma terms determines the phase difference and degree of the coherence between the two electric fields, E_1 and E_2, at sampled points respectively. ***A difference in the phase between the sampling points would result in a spatial shift in the intensity patterns and the degree of the coherence between the points change in the visibility of the interference fringes.***

A simple means of measuring the azimuthal phase variation is to use a Young's double slits experiment to sample the phase difference at the opposing sides of the beam (spatial sampling)[4]. In figure 5.2 A, the interference pattern after a spatially coherent Gaussian beam incident passes through two pinholes is numerically calculated. In figure 5.2 B, the interference fringe pattern (shifted by π as compared to figure 5.2A) of an LG beam that is incident on the same pinholes. Due to the phase difference (π) between the two points, the resulting interference pattern is shifted by a single interference fringe.

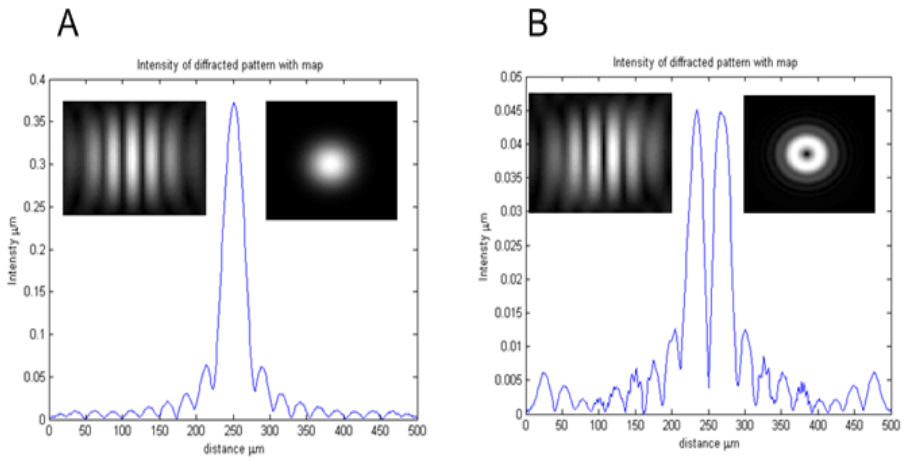

Figure 5.2 Young's slit interference with two pinholes. The cross-sectional plot of interference pattern between two coherent points in a monochromatic Gaussian beam **(A)** and a LG_0^1 beam (B). Left inset shows the interference pattern. Right inset shows the incident beam. The two pinholes are separated by one beam waist and centred to beam central axis.

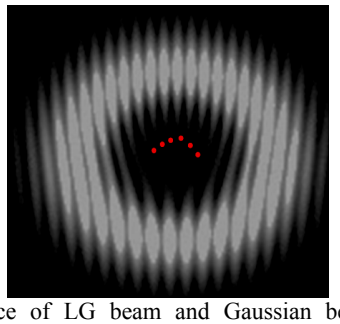

Figure 5.3 Temporal interference of LG beam and Gaussian beam. The numerically calculated interference between a LG_0^6 and a plane wave at an angle [5, 6]. The number of bifurcations, 6, (red dot) in the fork intensity patterns shows the azimuthal phase variation of the LG_0^6 beam.

On the other hand, by temporally interfering the LG beam with a plane wave (Mach Zehnder or Michelson interferometer), the intensity pattern (fork like pattern) can measure the degree of azimuthal phase variation, l [5-7] based on the number of bifurcations. Figure 5.3 shows the numerical simulation of a LG_0^6 beam interfering with a plane wave. A fork facing upwards indicates a positive azimuthal phase variation while the reverse indicates a negative azimuthal phase variation. The level of azimuthal phase variation (l) is signified by the number of bifurcations in the fork pattern. This particular temporal interference method was first used to measure the azimuthal phase variation in the LG beam modes [5]. The limitation lies in stability of the interference pattern and difficult to use to measure polychromatic LG sources (short coherence length ≈10μm). Aperture based wavefront sampling techniques (i.e. Young's slits type experiment [4] or Shack-Hartmann wavefront sensor [8]) are suited to diagnose the wavefront curvature of a monochromatic and polychromatic sources. I aim to further develop the aperture-based interferometry technique using optically controlled microapertures.

In the next two sections, I use the trapped microspheres to perform two phase measurements. The first experiment is to perform discrete phase measurement about a LG_0^1 beam with two optically trapped microspheres (Young's slits). This demonstrates that the microspheres can be optically controlled onto a chosen position on the LG_0^1 beam. The second experiment is to use multi-point interferometry with several trapped microspheres. Using several optically trapped spheres (all of which resides on the circumference of the same beam), I analysed the far-field interference pattern that elucidates the sign of the azimuthal phase variations of the trapping LG_0^3 beam. The array of microspheres here can be considered to perform a variant of the Shack-

Hartmann wavefront measurement. Using the optical forces, it is possible to "tune" the number of optically trapped microspheres within the LG_0^1 trapping beam.

5.3. Optically trapped microspheres for Young's slits type interferometry

In this section, I describe a microscopic version of Young's double slit experiment performed by two optically trapped colloids. I investigate the far-field interference intensity fringes, between the forward scattered light from two optically trapped colloids. The far-field interference pattern from the two colloids can provide a direct correlation to azimuthal phase shift in the LG beam. First I shall explain the theoretical aspect of treating Mie particles as diffracting apertures.

The forward scattering light arising from microspheres are well defined by Mie scattering and can be easily modelled like a diffracting disk diffracted as suggested by Chevaillier et al [1]. The numerical method works on the proposed Fourier decomposition of a given amplitude distribution into plane waves in x, y and z (also see Appendix C). The plane wave of each vector space is propagated to a certain distance and then a superposition to realize the far-field intensity pattern. This technique has been acknowledged as a useful and important tool for detailed analysis of wave propagation. The final mathematical expression of a propagating light field $E(x_0, y_0, 0)$ propagated towards the far-field at incremental z values, Δz is given as

$$E_0(x_1, y_1, z_1) = \frac{1}{2\pi}\iint \tilde{E}(k_x, k_y, 0).\exp\left(ik_x + ik_y\right).\exp\left(ik_z \Delta z\right)dk_x dk_y$$
$$= \frac{1}{2\pi}\iint \tilde{E}(k_x, k_y, 0)\exp(ik_x + ik_y)\exp\left(i\left(\Delta z\sqrt{2\pi/\lambda - k_x^2 - k_y^2}\right)\right)dk_x dk_y \tag{5.2}$$

where $k_x = 2\pi/\lambda x$, k_x, k_y are the transverse wave vectors, the longitudinal wave vector $k_z = \sqrt{(2\pi/\lambda)^2 - k_x^2 - k_y^2}$ where λ is the wavelength of the monochromatic optical field and $\tilde{E}(k_x, k_y, 0)$ is the representation of $E(x_0, y_0, 0)$ in the frequency spectrum (fourier transform). Hence, by replacing the $E(x_0, y_0, 0)$ with an analytical expression for an LG beam containing diffracting disks, I am able to numerically simulate the propagation of the LG beams diffracted by microspheres towards the far-field in free space. By using the Fourier transform method based on equation 5.2, I first numerically propagate the Gaussian beam containing microspheres in its annular

intensity ring towards the far-field ($z >> z_R$) with increments of z values, given as Δz. Since the microspheres are well described in the Mie Regime and the scattering angle is small, I consider mainly the diffracted rays from the microspheres in the simulation. The scattering geometry is illustrated in figure 5.4. From the simulation results, the gradual interference between the diffracted light from two spheres (half of the Gaussian beam waist) is observed towards the far-field.

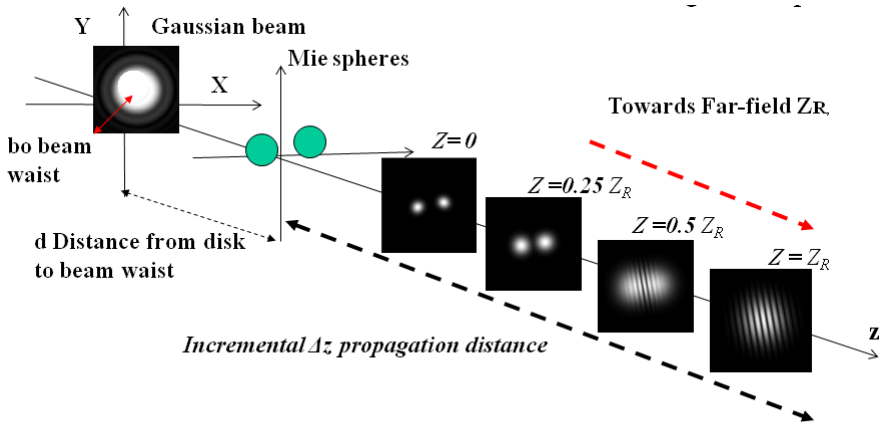

Figure 5.4 – Numerical simulation of two diffracting aperture (Mie particles) in a Gaussian beam. Two spheres positioned on opposite sides of a Gaussian beam. The scattered fields from the microspheres are led to interfere towards the far-field, Z_R. The interference between scattered light field began interfering at 0.5 Z_R

For the initial experiment, I set up a low NA optical trapping system with a short focal length lens as shown in figure 5.5. The low NA optical trap forms a two dimensional (2D) optical trap. In addition, silica microspheres of 6.84μm diameter are used as the micro-aperture. The diffusion coefficient for the size of the silica sphere will be low. The low diffusion rate of the large microsphere (< 6 $\mu m^2/s$) should result in the stable formation of the interference patterns.

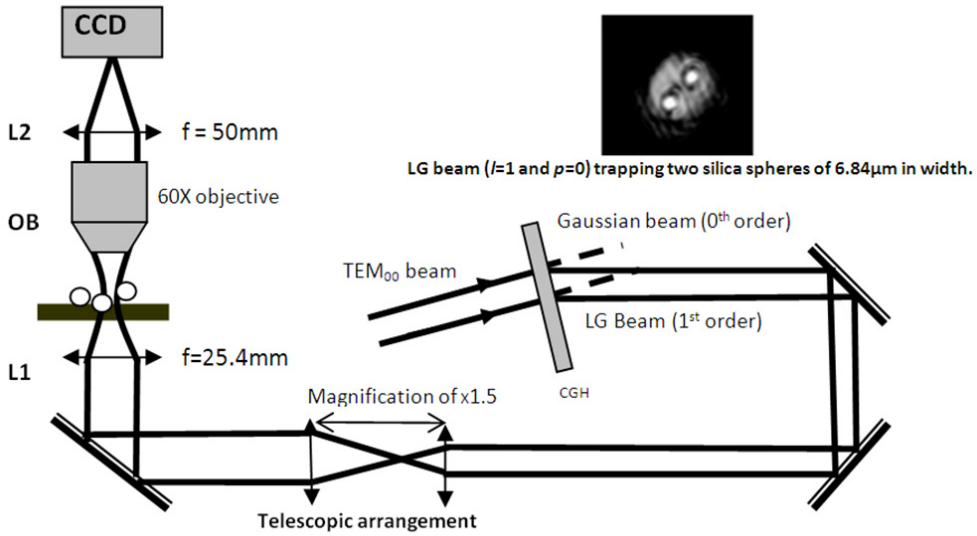

Figure 5.5 shows the experimental setup. A TEM00 beam is directed onto a high efficiency blazed computer generated hologram (CGH) that creates a LG_0^1 beam in its first order diffracts at an angle to the incident beam. The LG beam expanded to fill approximately the back aperture of the plano-convex lens, L1 of focal length 25.4mm. The diffraction pattern is collected from OB, 60X microscope objective (NA = 0.85), and relay far-field diffraction pattern of the colloids onto the imaging CCD through a second plano-convex lens, L2 of focal length 50mm, at its back focal plane (far-field diffraction patterns). Inset: LG beam (l=1 and p=0) trapping 2 spheres, each of diameter 6.84μm.

The experimental setup, shown in figure 5.5, is carried out without the use of high numerical aperture objectives (chapter 4). Instead I use a plano-convex lens (L1) to focus a low divergence LG beam onto the sample plane. An approximation to a single ringed LG_0^1 beam is generated using a highly efficient blazed computer generated hologram (CGH) [9] on glass, see section 4.4.1. The spiral phase plate element is not available during the experiment. The illuminating Gaussian laser beam has optical power of 1 W and wavelength of 1070 nm (laser source: max 10W, Yb-fiber CW, laser, IPG Corporation). The LG_0^1 beam is expanded to fill up the back aperture of the plano-convex lens, L1, and hence achieve a focused spot with diameter of around 15μm. The role of the lens (L2) is to relay the scattered light that is collected by a 60X microscope objective (OB) with an NA of 0.85 onto the observation plane (CCD camera). By shifting the position of the relay lens, I can image the optically trapped particles in the LG beam and the different propagation plane towards the far-field (back focal plane) using the relay lens. The size of the microsphere is chosen to approximately match the width of the annular intensity profile of the LG_0^1 beam and the beam waist of the Gaussian beam. These parameters are matched to the numerical model. The particles are dispersed in a heavy water (D_20) solution to reduce heating

effects and placed in a cylindrical sample chamber of diameter 1cm and depth 100μm. The average optical power required to levitate the colloidal microparticles away from the bottom side of the sample coverslip is typically around 100mW. The inset of figure 5.5 shows a LG_0^1 beam trapping two silica colloids of 6.84μm at opposing sides of the beam circumference.

Based on $I_{spatial}$ of equation 5.1, the added azimuthal phase variation from the LG_0^1 beam itself, will shift the interference fringes by π. Using the optical gradient force from the LG_0^1 beam, I controllably load the annular intensity profile of single ringed LG beams with two colloidal microspheres at different spatial positions by moving the sample stage. In figure 5.6, I show the far-field interference fringes when the two microspheres are placed at different positions of a LG_0^1 beam. The series of experiment images reveal a clear π phase shift in the interference fringes when the microspheres are directly opposite each other. The fringes gradual shifts from 0 to π, and back to 2π. The shift in the interference fringes begin with an intensity maximal to minimal at the centre (on the dash red line in figure 5.6). Hence, this result shows the possibility of controllable measurement of the phase shift within a trapping light beam.

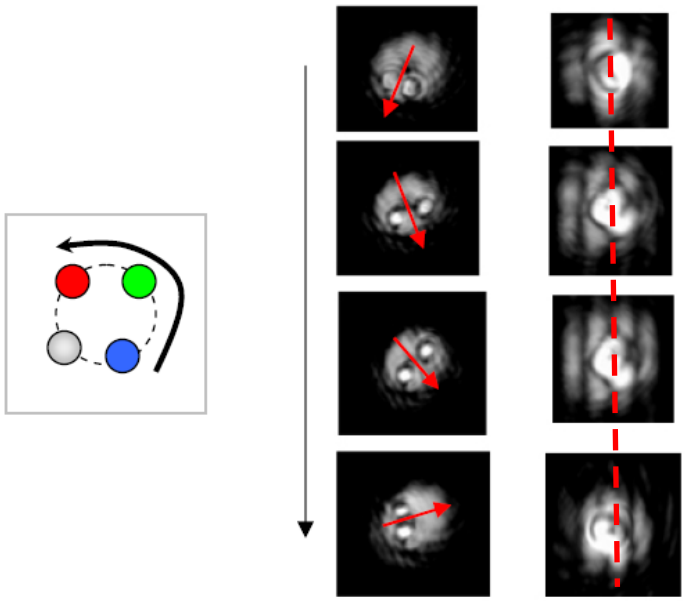

Figure 5.6 – Optically trapped microspheres as Young's slits. The far-field diffraction intensity pattern of two colloids trapped at different position in a LG beam (l=1, p=0) respectively.. The true orientation of the interference fringes is indicated along the red arrow. In inset illustrates the orientation of the microspheres around the LG_0^1 beam (blue-green –red circles). Red dash line indicate the position of the fringe shift.

To further prove that this phase shift is solely due to the azimuthal phase variation in the LG beam. I positioned two microspheres at opposing positions of a Gaussian beam, which resulted in the shifting of the intensity minima back to the maxima. In figure 5.7 A,C and B, D, I show the theoretical and experimental results with a Gaussian beam (LG_0^0) and a LG_0^1 beam respectively. In both the simulation and experiment, each of the beams is been apertured by two microspheres at opposite sides of the diameter of the beam. The relatively small separation between the colloids about the LG_0^1 beam means that the interference patterns from Gaussian and LG_0^1 will have a relatively similar pitch of interference fringes.

From the cross sectional plot of the average intensity variation in the transverse plane (X), figure 5.7E, the interference fringes are shifted by π, when an LG_0^1 beam is apertured as compared with a Gaussian beam. I also notice a slight tilt in the interference fringes and this is attributed to the finite sampling area of the beam. This means that the sampled phase from each aperture covers a larger phase shift than ideally desired. However, the overall shift in the fringe would correlate directly to the relative phase difference sampled by the two colloids is π. The average fringe visibility is measured to be 0.67 i.e. a high fringe visibility/contrast. The size of the microspheres is relatively large and so the Brownian motion (particle diffusion) is not as large which supports the stability of the interference fringes. One may potentially map out the azimuthal phase of an arbitrary complex beam while the phase mapping resolution may benefit from improvement with use of different sphere sizes.

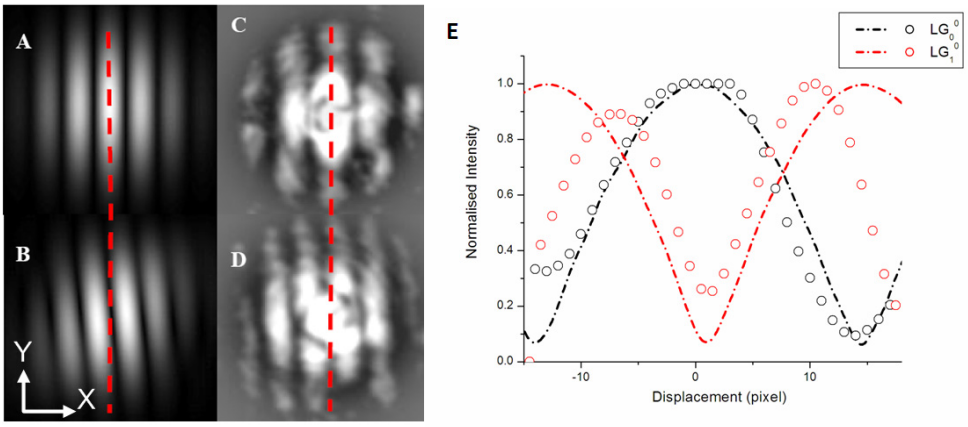

Figure 5.7 Microscopic Young's slits with optically trapped particles. A and B shows far-field diffraction (simulation) of two colloids trapped in a Gaussian (LG_0^0) and a LG_0^1 beam, C and D shows the experimental results respectively. Red line indicates the shift in the fringes due to the π phase between the two opposing points in the LG_0^1 beam. E shows the cross section of the average intensity variation across the transverse (X) at the observation plane (experiment - circle, theory – dot-dash line).

5.4. Multipoint interferometry with microspheres

The Young's type interferometer illustrated above makes use of only two apertures to measure the phase difference of the beam interferometer. However, if one is able to use multiple apertures onto a input, one could gain access to different part of the beam simultaneously. G. Gbur *et al* [10] used the resulting interference patterns from three apertures to reveal information about the coherence properties of the illuminating beam. Using multiple apertures, Berkhout and Beijersbergen [11] extended to the study of a multiple apertures interference pattern to probe LG beams of different azimuthal orders. In this section, I reported the interference patterns arising from multiple apertures residing within the LG beam and more importantly assessing the sign of the azimuthal winding of the LG beam. This work is done prior to the work done by Berkhout and Beijersbergen [11].

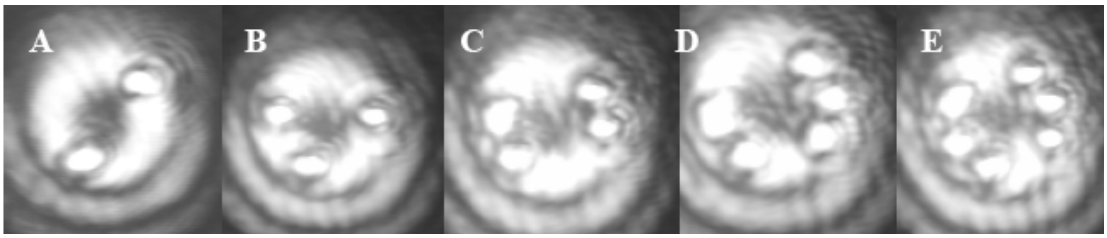

Figure 5.8 A- E, LG_0^3 beam trapping 2 to six silica colloids of 6.84μm around its annular intensity profile in a controlled manner using optical gradient forces.

In figure 5.8(A) to (E), I showed the arrangement of two to six colloid positions (static) at will around the LG_0^3 beam. The LG_0^3 beam extends the beam waist by more than twice so as to accumulate multiple spheres. Here a single ringed LG_0^3 beam is generated using another blazed computer generated hologram (CGH). The experimental setup is in figure 5.5 is used for this experiment. By translating the beam or sample stage, I am able to organize the annular beam profile of the LG mode with a range of colloidal particles. Transfer of the orbital angular momentum of light through scattering is observed (only when the annular rings are totally filled) but at a very slow rate due to our enlarged trapping beam and relatively low power density for these given sphere sizes [12, 13].

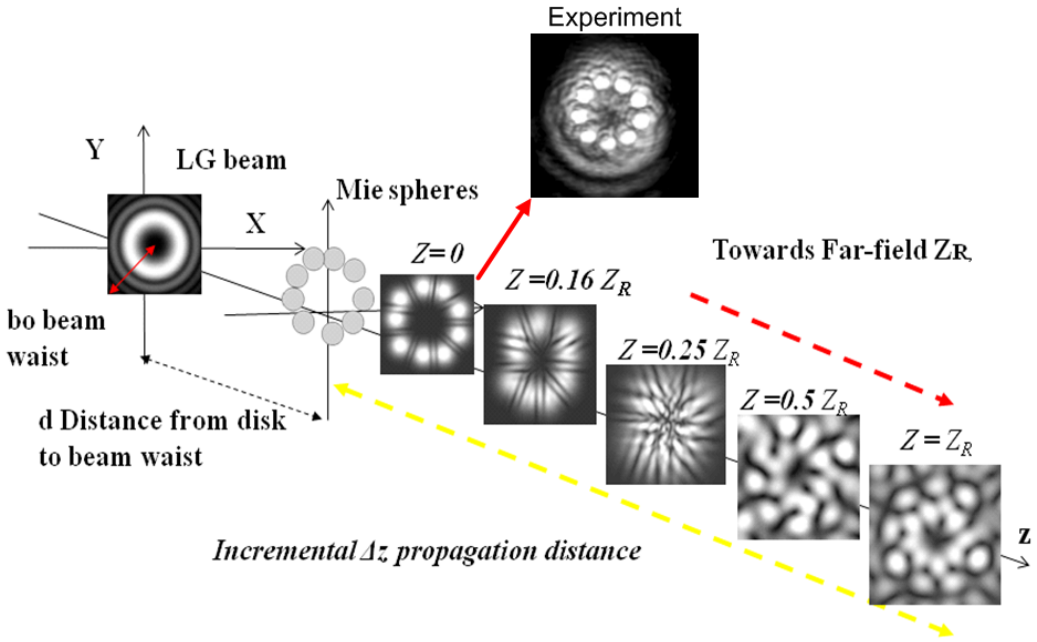

Figure 5.9 shows the scattering geometry of nine disks placed off the central axis of the LG_0^3 beam (red annular ring). bo denote the beam waist of the LG beam and d denotes the distances from the beam to the microsphere (treated as a diffracting disk) and Z_R denotes far-field. The scattering geometry are calculated in Cartesian coordinates (x,y,z). Experimentally obtained image of the 9 trapped spheres in the beam is indicated by the red block arrow

In figure 5.9, I show the numerical model of the scattering geometry where nine spheres filling up the annular beam. From the same figure, each colloid is observed to interfere with its neighbor, which in turn yields a rich intensity patterns in the far-field. From the simulation shown in figure 5.9, I can see an interesting interference pattern arising from multiple apertures residing within the LG_0^3 beam at a half Rayleigh range, z_R which resembles the spiral intensity pattern [14]. This spiral intensity could be important in the assessment of the sign of the azimuthal index of the LG_0^3 beam.

Note that this pattern only arises when the annular intensity rings is filled up with colloidal microspheres (nine spheres). The number of spiral arms observed is correlated to the number of colloids being trapped within the LG_0^3 beam. The direction of the spiral arms could possible infers the direction of the azimuthal index *l*. In experiment, I study the case where nine colloids are being trapped around the LG_0^3 beam and fully covering the entire beam. By reversing the azimuthal phase variation using a dove prism, I observed that the nine spiral intensity arms reverses at $0.5Z_R$. In

figure 5.10 (A), (B)) and figure 5.10(C), (D), I showed both simulation and experiment results from LG_0^{-3} and LG_0^3 respectively.

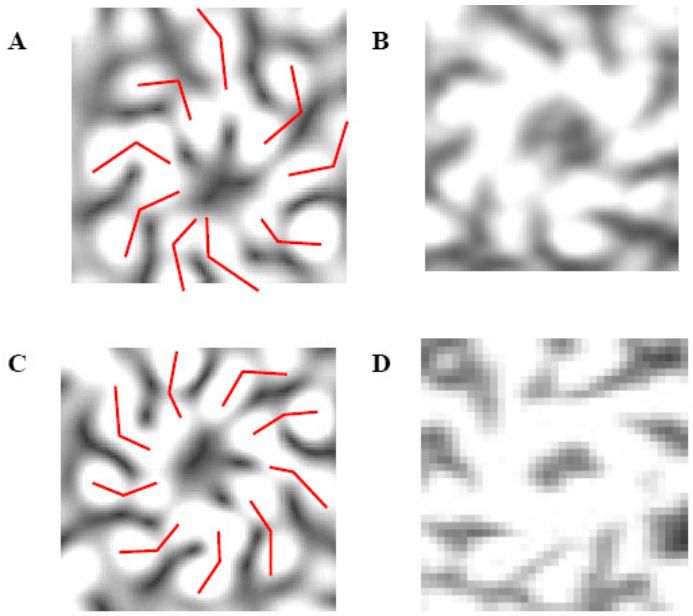

Figure 5.10 shows the simulation and experimental results of the spiral wave pattern. A, C (simulation) and B, D (experiment). The spiral intensity arms indicate the helicity of the trapping light. A & B are for as trapping beam of l=+3, C &D l=-3. The nine spiral arms correspond to the nine colloids trapped along the annular intensity profile, denoted by the red lines.

The interference pattern from the multiple trapped spheres (microlens) is a variant form of wavefront measurement scheme that is similar to Shack Hartmann wavefront system (regular spaced microlens on a rectangular grid) [8]. Additional interference pattern from other spheres arrangements are in appendix F of the thesis. From figure 5.10, the multiple trapped microspheres perform a wavefront measurement of the LG_0^3 beam to determine the sign of the azimuthal index.

5.5. Measuring spatial coherence using independently optically trapped apertures

The first two experiments prove that a combination of optically microspheres can be use to carry out localised measurement of the phase and wavefront of a sample light field. Young's slits is also a test for the spatial coherence of a given light field. Even though the process of self alignment of the microspheres (apertures) onto the sample beam is convenient, the position of the probe area is less controllable. This is because the distribution of the gradient forces acting on the microsphere

lies anywhere in the sample beam circumference. The degree of controllability over which position of the microsphere will reside in is much lower. ***The control positioning can be improved by using an independent set of optical traps to place the microspheres onto the sample beam.*** The independent optical trapping beams are necessary so that one is able to change and measure the spatial coherence on a specific location within an arbitrary light beam. The next question is: How the spatial coherence of a monochromatic laser beam can be manipulated?

Previous works have shown that a rotating diffuser is known to impart random phase fluctuations on a monochromatic laser beam, over a given time of observation. With increasing rotation rates of the diffuser [15, 16], the phase correlation between the any two points is reduced. As such, the spatial coherence is reduced over the time of observation. Hence, I need to control the rotation rates of a "micro-diffuser" and use that as one of the apertures within a Young's slit's type experiment. The micro-diffuser will in turn control the local spatial coherence or phase correlations within an arbitrary optical beam at will. The interference of the diffracting light from a microsphere (fixed phase) and a micro-diffuser (changing phase) will exhibit linear interference fringes.

The micro-diffuser is realised through the controlled trapping and rotation of a birefringent microparticle (calcite) (discussed in chapter 1, section 1.3.2.1) held in an optical trap. The calcite is set into rotation by using a circular polarised light. By varying the rotation rates (optical power) of our trapped calcite particle, a varying wavefront deformation (fine and random phase fluctuations) is controllably introduced upon a localized region of an arbitrary beam. I employed the use of a dual beam trapping system (as described in Chapter.1, 2) to trap two microparticles: a microsphere and a calcite individually upon the sample LG beam. Before I began the coherence measurements, I first use two 0.5 μm polymer microspheres to measure the quality of the interference fringes at the far-field.

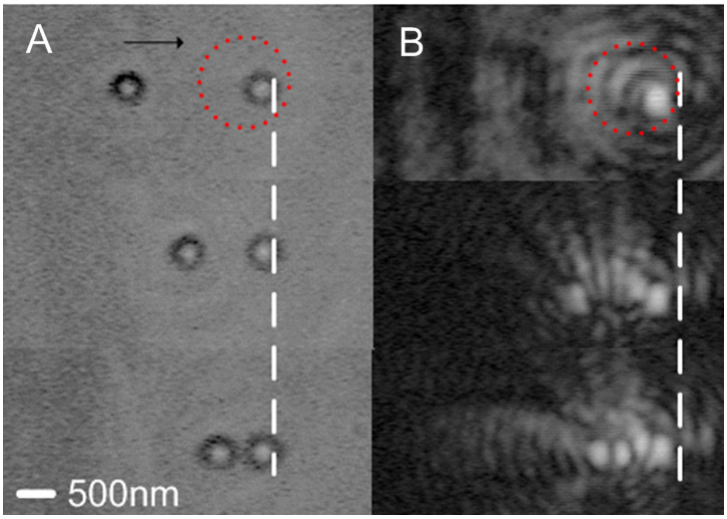

Figure 5.11 – Interference of a Gaussian beam using independently trapped 0.5µm spheres. (A) Sequentially reduction the separation between the two optical trapped spheres within a focussed sampled He Ne Gaussian beam and (B) the subsequent far-field diffraction between the two spheres.

In figure 5.11 A, I trapped two polymer spheres (0.5 µm diameter) at 3µm apart. By using an acousto-optic deflector (AOD), I sequentially reduce the separation between the two optical trapped spheres using two optical traps (λ= 1070nm) within a focused sampled Gaussian beam (λ=6.33nm). Both the trapping beam and the sample beam goes through a high NA objective (100X, NA 1.25). The optical power in each trapping beam is 50 mW. The sample beam is under-filled at the back aperture so that the beam diameter at the sample is approximate 1.5µm. This is so as to accommodate for the microsphere sizes. By observing the far-field diffraction pattern from the 633nm laser beam using a CCD, I observed the coherent interference between the two trapped spheres (figure 5.11B). The high NA objective restricts the sample beam diameter to within a few micrometres and also introduces higher order aperture effects due to the highly converging rays [17, 18]. On top of that, the interference fringes are of poor visibility. To simplify matter and improve the visibility of the fringes, I reduced the NA trapping microscope objective and created a two dimensional trap. A low NA (0.75) objective lens would expand the sampling range (beam waist) by minimum of two folds. The low NA optical trap will push the particles against the top of the sample chamber. Using the two dimensional trap, I will trap large spheres (5 µm) as apertures. The scattered signals from the larger spheres will be stronger and likely improve the visibility of the fringe. The two dimensional confinement ensures that the trapped particles are resting along the same axial position (top of sample chamber) and reduces temporal interference effects. In the following sections, I shall describe the probing of the spatial coherence of a light field (LG beam) within a pair of optically trapped microparticles.

The theory of optical coherence is central to the study of the cross-correlation of randomly fluctuating light fields [16, 19]. The fundamental properties of propagating light fields such as their directionality and polarisation are strongly correlated to the spatial coherence of the light field. A key experimental test of the spatial coherence of any light field is through the classical Young's double slit experiment [19]. The degree of spatial coherence is measured by the visibility of the far-field interference fringes from the Young's slits as shown in equation 5.1. When the wavefronts from the different spatial points in the light field are correlated, the light field is considered spatially coherent. However, when the correlations between the sampling points are randomized, the beam would be rendered spatially incoherent. When a coherent light field passes through the double slit, a set of co-sinusoidal intensity fringes emerges in the far-field, with the total amplitude of the envelope dictated by the size of each aperture. ***As the spatial coherence of the incident field decreases, so does the visibility of the intensity fringe.*** The degree of spatial coherence is thus measured by the visibility of the far-field interference fringes from the Young's slits. Equation 5.3 describes the visibility V(r) of the interference fringes in the far-field as the division of the difference and sum of the maximum, $\mathrm{I}_{\max}(r)$, and minimum, $\mathrm{I}_{\min}(r)$, of the intensity of the fringes on point P at position r, where $r = \sqrt{x^2 + y^2}$. $|\gamma_{12}|$ is the modulus of the mutual complex coherence between the optical field emerging from two apertures at a given time, thus ignoring the effects from temporal coherence.

$$V(r) = \frac{\mathrm{I}_{\max}(r) - \mathrm{I}_{\min}(r)}{\mathrm{I}_{\max}(r) + \mathrm{I}_{\min}(r)} = |\gamma_{12}| \tag{5.3}$$

As a monochromatic light field propagates through a dense scattering medium (e.g. a rotating diffuser), the wavefront of the light field is altered due to the scattering medium [20].. The time-average of the total fluctuations in the wavefront of a monochromatic light field generated by the rotating diffuser would then be approximately equivalent to the fluctuations from a thermal light source [20]. The face of a large diffuser contains fine granular structures that introduce uneven deformation onto the entire wavefront of the monochromatic light field. By rotating a diffuser, the wavefront of the light field will be randomized. This will in turn generate a quasi-thermal light source from a monochromatic beam. If we are to reduce the size of the diffuser to micrometers, I would then be able to control the spatial coherence at a much localized position of the light field. A microscopic technique would need to be used such as to remotely control a small piece of a diffuser.

Previous studies measured the mutual coherence function by placing apertures at varying distance apart after a collimated thermal light source [19] or a quasi-monochromatic light source

generated from a rotating diffuser [20]. In our case, I probe the mutual coherence through the diffracting properties of the apertures where one aperture acts as the diffuser that creates a quasi-monochromatic point source. I start by modelling a forward scattering geometry with two apertures: one clear (microsphere) and other randomized (a micro-diffuser) as shown in figure 5.12. Considering a double diffracting aperture system, E_1 and E_2, each creating its own scattered field that interferes in the far-field, the intensity pattern observed at a position I_P in the far-field is given in equation 5.4.

$$I_p(r_1,r_2) = |E_1|^2 + |E_2|^2 + 2(I_1)^{\frac{1}{2}}.(I_2)^{\frac{1}{2}}.\mathrm{Re}\left(\frac{\langle E_1(r_1).E^*{}_2(r_2)\rangle}{(I_1)^{\frac{1}{2}}.(I_2)^{\frac{1}{2}}}\right)\cos(\Delta\phi_{12}) \qquad (5.4)$$

$$= |E_1|^2 + |E_2|^2 + 2(I_1)^{\frac{1}{2}}.(I_2)^{\frac{1}{2}}.|\gamma(r_1,r_2)|\cos(\Delta\phi_{12})$$

where I_1 and I_2 are the intensity of E_1 and E_2 at position P, $E_1(r_1)$ and $E_2(r_2)$ denotes electric field distribution from the two apertures at different space, r_1 and r_2 are the radial coordinates, and the angle bracket denotes the time average over an interval larger than the coherence length. The mutual coherence term $|\gamma(r_1,r_2)|$ is also the normalized complex amplitude of the interference pattern itself. Hence the significance of equation.5.4 is that the visibility of the interference pattern in the far-field is directly related to the correlation of the fluctuation between the two apertures E_1 and E_2.

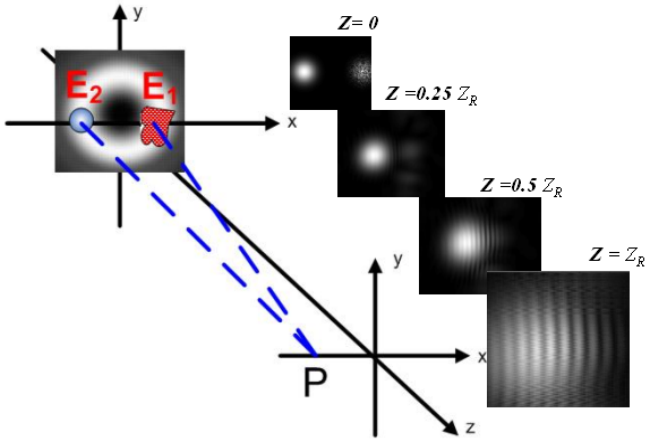

Figure 5.12 Numerical calculation of the clear and randomized aperture. A LG_0^3 that has been apertured by E_1 and E_2 and propagated towards the far field.Z_R E_1 and E_2 contains a clear aperture and a randomized aperture.

In figure 5.12, a "micro-diffuser" (E_1, red) and a clear aperture (E_2, blue) are placed at the annular intensity rings of the LG_0^3 beam. A randomized aperture E_1 is generated by multiplying the complex amplitude of the diffracting disk with a randomized phase function given by $\exp(-irand[\alpha,\beta])$, where $rand[\alpha,\beta]$ is a random phase generator and α,β are the lower and upper limit of the phase variation (α is set at zero and β is left to vary). The random phase aperture E_1 aims to simulate the random phase fluctuation introduced by a rotating micro-diffuser. The output fields from the apertures, E_1 and E_2, are then propagated numerically towards the far-field, P, using Fourier method [21]. These two apertures create a Young's slits interference that samples the wavefront of the LG_0^3 beam at two specific points over a given time, where the visibility, V(r), of the interference fringes indicates their degree of spatial coherence $|\gamma_{12}|$. Figure 5.12 and equation. 5.4 ignores the effects from temporal coherence.

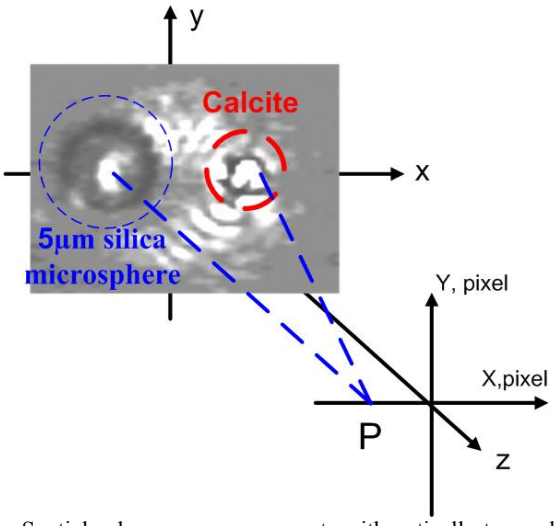

Figure .5.13 – Spatial coherence measurements with optically trapped particles. A "micro-diffuser", calcite (E1, red) and a clear aperture, microsphere (E2, blue) are placed at the annular intensity rings of the LG_0^3 beam. X and Y indicates the sxis in the sample and Xpixel and Ypixel denotes the observation plane on a camera.

A calcite microparticle is akin to a diffuser but on a micron scale and possesses a minuscule granular surface that deforms the wavefront of the incoming light field. By trapping a birefringent particle (e.g. calcite) with a circularly polarised light beam, one may impart spin angular momentum of light onto a trapped birefringent particle and induce particle rotation about its own optical axis [22] (see chapter 1, section 1.3.2.1). In this way I may influence both the positional and rotational control over the trapped particles. By varying the optical power of the trap, I am able to control the rotation rates of our trapped calcite particle. With that I can controllably introduce wavefront

deformation upon a localized region of an arbitrary beam. In the previous sections, I have shown how the far-field diffraction pattern from optically trapped microspheres may be used to infer the azimuthal phase of a LG beam in-situ [21]. The controlled rotation of the calcite using the second trap means that it can acts as both a micro-diffuser and diffracting aperture at the same time. Hence, the trapped calcite and the microsphere forms an optically trapped Young's double slit for modulating and measuring the spatial coherence of light as shown in figure 5.14. Next I will describe the experimental setup in figure 5.14 to achieve the spatial coherence measurements in figure 5.13.

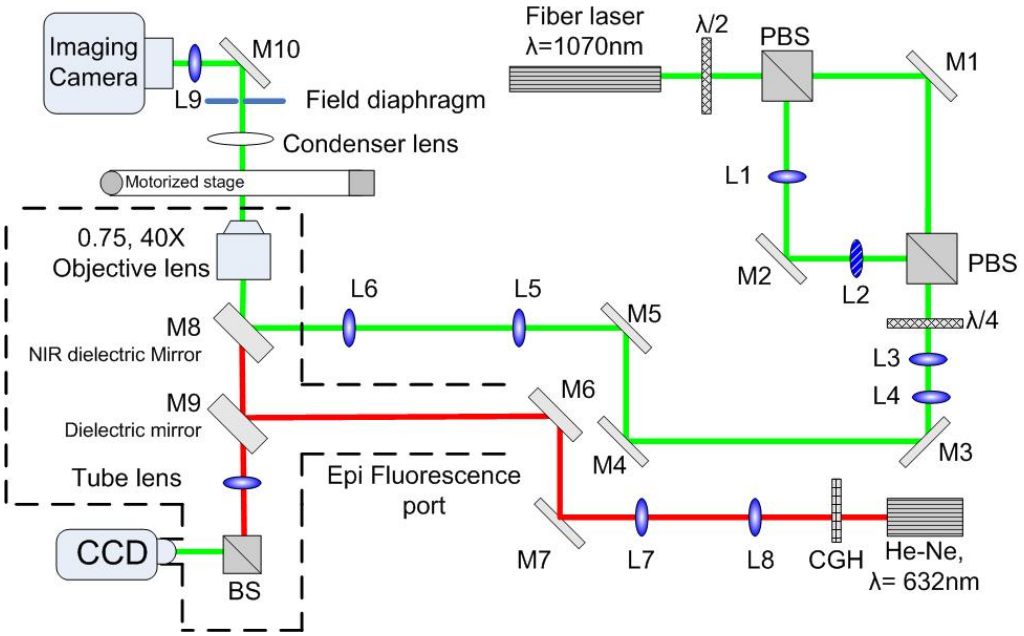

Figure 5.14 Experimental setup. The λ/2 controls the output polarisation direction of the output fiber laser. The polarising beam splitters (PBS1 and 2) splits and recombine two beam of orthogonal polarisation . A quarter waveplate (λ/4) is placed to create circularly polarised optical trap. Lenses L1 & L2 form a 1: 1 telescope to adjust the axial trapping position of one of the trapping beams. Lenses L3 & L4 form a telescope that expands the trapping beams to fill the back aperture (1:6). Lenses L5 & L6 are used to image the steering mirror onto the back focal plane of the objective. A CCD camera (Basler A622f) is placed at the back imaging plane of lenses L9. A probe LG_0^3 beam is generated using a He-Ne (λ=633nm) laser beam with a CGH and expanded (1:2) by the telescope system (L7 & L8) before entering into the objective lents. M1 to M4, M5, M8 and M9 denote dielectric mirrors to reflect the infrared trapping beam. M6 and M7 denote sliver mirrors for reflecting probe beam. Another CCD camera (30Hz) is used to capture the approximate rotation rate of the rotating calcite

In figure 5.14, I illustrate the experimental configuration of the simulated scenario in figure 5.13 used to achieve the required trapping requirement. The experimental setup is primarily based the dual beam trapping system (similar to chapter.2) is formed by two orthogonal polarised beams from a 1070nm fiber laser (5W, IPG, Photonics), built around a Nikon inverted microscope platform as described in chapter.1. The two orthogonally linearly polarised beams are formed using

two polarising beam-splitters placed in a Mach Zender interferometer arrangement [23]. Both beams then enter a microscope objective (numerical aperture (NA) 0.75, 40X) to form two independent optical traps (the AOD, extra PBS are not used in the experiment and hence removed from the figure for simplicity). The sample is a mixture of crushed calcite and 5μm silica microspheres that are dispersed in a D_20 solution, used to reduce heating effects from laser absorption. I note that the coarseness (granularity) [16] of the calcite is an important part of reducing the coherence as oppose to the use of a more uniform birefringent particles such as Vaterite [24]. The particles are placed in a cylindrical sample chamber of diameter 1cm and depth 100μm. A quarter-waveplate is then inserted to generate circularly polarised trapping beams. One of the beams traps and rotates the calcite particle through the transfer spin angular momentum, whilst the other beam forms a single beam trap to trap a 5μm silica microsphere, as shown in figure 5.13. As noted above, the light field which I choose to sample here is a LG_0^3 beam generated using a computer generated hologram (CGH) [25] at a wavelength of 633nm (He-Ne, Spectra Physics, USA). The sampling beam is simultaneously focused through the same objective as the trapping beams but via the epi-fluoresence port of the microscope. In the far field, I obtain fringes from the light diffracted by micro-apertures placed within the LG_0^3 beam using a charge coupled device (CCD, Basler 602f) camera (Imaging Camera) operating at a low frame rate (1-5Hz). Another CCD camera (30Hz) is used to capture the approximate rotation rate of the rotating calcite. This new trapping geometry allows us to separate the trapping beam from the probe beam; I use a 633nm He-Ne laser as our LG_0^3 probe beam and a 1070nm laser for our two orthogonally polarised trapping beams. Spin angular momentum is transferred onto the calcite particle fully only when it completes a half wave retardation of the circular polarised trapping beam. Thus, for the wavelength of 632nm, the calcite could cause the beam to undergo a full wave retardation. Hence, using two separate laser wavelengths for the trapping beam and to create the probe light field reduces any additional interference effects on the fringe visibility due to polarisation. The changes in the fringes are solely be due to phase fluctuations.

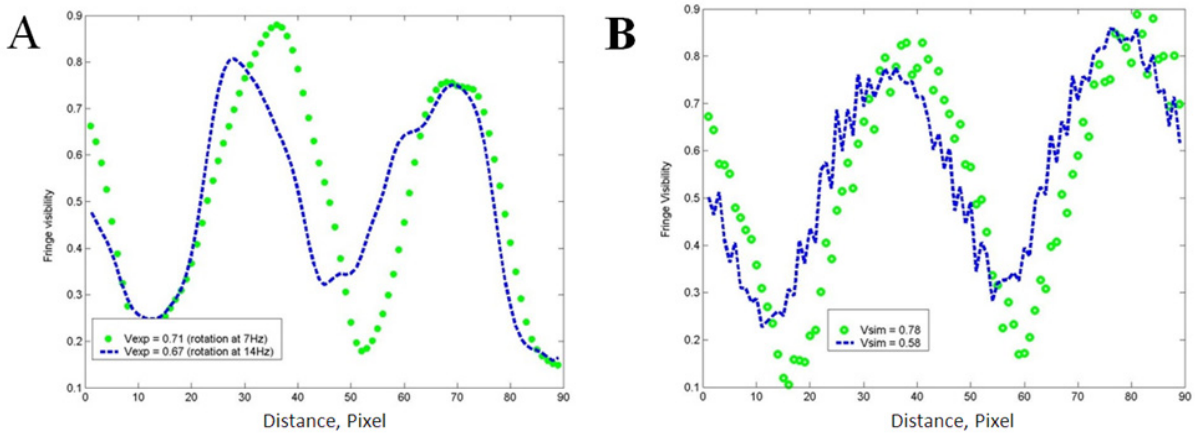

Figure 5.15 Cross sectional plot of the interference intensity pattern. (A) is the experimental data of the interference fringes from two apertures place around the annular ring of the LG_0^3 beam. (B) shows the numerically calculated far-field interference fringes when one of the apertures possesses a random complex phase. (A) shows that increasing the rotation of the calcite particle, a decrease in the fringe visibility V_{exp} is observed. This is seen numerically as well in V_{sim} as shown (B), increasing the phase variation in one of the apertures. (Vexp denotes the average fringe visibility obtained experimentally and V_{sim} denotes the average visibility obtained numerically).The interference fringes are distributed transversely across the X-axis, which is measured in pixel size for both (A) and (B). The small intensity fluctuation in the simulation is due to the pixilation of the simulation.

From our experimental observation, I have observed that at higher spin rates of the calcite the corresponding far-field interference fringes show a significant decrease in their visibility see figure 5.15. From figure 5.15A, I show that when the calcite is being spun at a spin rate of around 7Hz, we observe that the visibility of the interference fringes drops to V_{exp}=0.71 ± 0.01. Without any calcite spinning, the fringe visibility is approximately 0.9± 0.01. With a further increment of the spin rate of the calcite to approximately 14Hz, I can see that the visibility drop further to V_{exp}=0.67 ± 0.01. In figure 5.15B, we numerically calculate the expected visibility that we might expect from a simulated micro-diffuser (random phase) and a second clear aperture (fixed phase) placed in a LG (l=3, p=0) beam. The numerical calculation indicates a clear decrease in the visibility of the far-field interference fringes is observed by increasing the random phase variation $\exp\left(-irand[0,\beta]\right)$ of E_1, where $0.32\pi \le \beta \le 0.95\pi$. This decreases the phase correlation between the two sampling points E_1 and E_2 [14]. By generating a random phase where α=0 and β=0.32π, we observe that an increase of the random phase variation β to 0.64π and β to 0.95π, results in the fringe visibility dropping to V_{sim} =0.78 and V_{sim} =0.58, denoted by green circle and the blue dotted line respectively.

From both the experimental results and the numerical results, I can see that the visibility of the interference fringes reduces with increasing phase fluctuations in one of the sampling apertures. By comparing the numerical calculations (V_{sim}) and experiment results (V_{exp}), I can see that a

rotating calcite at rates from 7 to 14 Hz can approximately introduces a random phase variation β from 0.64π to 0.95π.

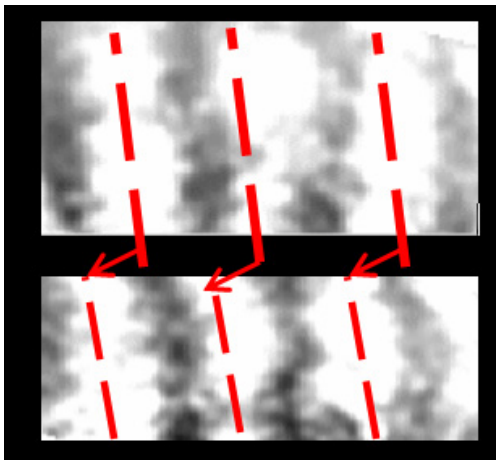

Figure 5.16 Doppler-like effect. The microscopic implementation of the Doppler effect when the trapped calcite is spun at around 7Hz, where the interference fringes shift in a periodic manner (denoted by the arrows)

The fringe visibility before is observed at low frame rate (1-5 Hz) (i.e. time-averaging). By controlling the rotation rate of the calcite particle in one of the optical traps at around 7 Hz (with relative good fringe visibility) and increasing the frame rate of the CCD (30 Hz) camera, I obtain reasonably good fringe visibility (≈0.9). I can start to observe that the interference fringes start to move laterally in a continuous manner, as shown in figure 5.16 (denoted by the red arrow). In this case, the birefringent particle behaves like a rotating aperture, with slight diffusing properties. The fringe motion as observed is due to the phase difference between the two apertures, realising a microscopic version of the rotational Doppler-like effect [7].

5.6. Conclusion

Optically trapped micro-apertures are simple to control and possess a high degree of localisation and manoeuvrability within a probed light field. The works presented here offers a generic technique to probe the phase and coherence of light fields.

To summarize this chapter in short, I have discussed the implementation of optical trapped particles as diffracting aperture for localized phase and coherence measurements within a given light field e.g. LG beam. Three experiments were carried to measure phase and coherence within the LG beam: 1) microscopic Young's slits with two optically trapped microspheres, 2) multi-point interferometry with multiple trapped microspheres and 3) spatial coherence measurement with optically trapped microsphere and calcite using a dual beam optical trapping system. The analysis of

the far-field interference between the microparticles was sufficient to elucidate the azimuthal phase variations and coherence of a LG beam.

In the first two microsphere experiments, the trapped sphere scattered light from the trapping beam. From the cross sectional plot of the average intensity variation in the transverse plane in the first experiment, I observed a shift in the interference fringes by π, when an LG_0^1 beam is apertured as compared with a Gaussian beam. I also noticed a slight tilt in the interference fringes and this is attributed to the finite sampling area of the beam. This meant that the sampled phase from each aperture covers a larger phase shift than ideally desired. However, the overall shift in the fringe would correlate directly to the relative phase difference sampled by the two colloids is π. The average fringe visibility was measured to be 0.67 i.e. marginal visibility / contrast. The size of the microspheres was relatively large and so the Brownian motion was not as large which supported the stability of the interference fringes. The stability of the spheres (also the visibility of the fringe) can be improved with independent optical traps, as I have shown in the third experiment. One may potentially map out the azimuthal phase of an arbitrary complex beam and the phase mapping resolution may benefit from improvement with use of different sphere sizes.

Extending from the two microsphere interferometer technique, I moved onto the assembly of multiple microspheres into the same LG beam in the second experiment. In conventional Shack-Hartman microlens, an array of microlens is illuminated by an input and the far-field pattern maps out the aberrations in the wavefront. Here, the optical forces were responsible for organizing the microspheres in the high intensity regions of the sample beam. The microspheres (i.e microlens) were purposefully arranged in a circular fashion, followed the annular intensity pattern of the LG beam. When the full annular intensity ring of the LG beam was filled, the resulting intensity pattern at half Rayleigh range indicated a spiral phase pattern that had direct correlation with the sign of the azimuthal index of the trapping beam.

The distribution of the transverse gradient forces acting on the microsphere lies anywhere in the beam circumference which means that a trapped microsphere would move in any position in the transverse plane of the trapping beam. The degree of controllability over which position of the microsphere should reside needed to be enhanced. This led me to the third experiment: decoupling the trapping beam from the sample beam. A dual beam optical trapping system generated two optical traps that independently assisted in the controlled loading of microparticles onto a separate sampling beam: a LG beam. To modulate and measure the spatial coherence of light, I used an optically trapped micro diffuser. An optically rotating birefringent particle (calcite) was capable of

imparting fine phase fluctuations on a probe beam, thus fulfilled the role of a "micro-diffuser". Using optical forces and torques in this way, it was possible to locally vary or modulate the spatial coherence in the light field. From both the experimental results and the numerical results, the visibility of the interference fringes was reduced with increasing phase fluctuations in the micro-diffuser. By comparing the numerical calculations (V_{sim}) and experiment results (V_{exp}), I saw that a rotating calcite at rates from 7 to 14 Hz can approximately introduce a random phase variation from 0.64π to 0.95π respectively. The fringe visibility dropped from V_{sim} =0.78 to V_{sim} =0.58. One possible application that can arise from this experiment is the measurement of spatial coherence in vertical-cavity surface-emitting laser (VCSEL) [26]. It has been known that VCSEL can be used to trap microparticles. Hence, it would be possible to use trapped microparticle to measure the spatial coherence of an array of VCSEL using their far-field diffraction pattern in an in-vivo manner.

I have designed the first two experiments with advice from Dr Veneranda Garcés-Chávez. I performed all of the experiments and analysis of the data in this chapter.

5.7. References

1. J.-P. Chevaillier, J. Fabre, and P. Hamelin, "Forward scattered light intensities by a sphere located anywhere in a Gaussian beam," Appl. Opt. **25**, 1222-1225 (1986).
2. S.-H. Lee, Y. Roichman, G.-R. Yi, S.-H. Kim, S.-M. Yang, A. van Blaaderen, P. van Oostrum, and D. G. Grier, "Characterizing and tracking single colloidal particles with video holographic microscopy," Opt. Express **15**, 18275-18282 (2007).
3. A. Howie, and J. E. F. Williams, "Interference: 200 years after Thomas Young's discoveries - Preface," Philosophical Transactions of the Royal Society of London Series a-Mathematical Physical and Engineering Sciences **360**, 805-806 (2002).
4. H. I. Sztul, and R. R. Alfano, "Double-slit interference with Laguerre-Gaussian beams," Opt. Lett. **31**, 999-1001 (2006).
5. M. Padgett, J. Arlt, N. Simpson, and L. Allen, "An experiment to observe the intensity and phase structure of Laguerre-Gaussian laser modes," Am. J. Phys. **64**, 77-82 (1996).
6. W. M. Lee, X. C. Yuan, and D. Y. Tang, "Optical tweezers with multiple optical forces using double-hologram interference," Optics Express **11**, 199-207 (2003).
7. J. Arlt, M. MacDonald, L. Paterson, W. Sibbett, K. Dholakia, and K. Volke-Sepulveda, "Moving interference patterns created using the angular Doppler-effect," Optics Express **10**, 844-852 (2002).
8. F. A. Starikov, G. G. Kochemasov, S. M. Kulikov, A. N. Manachinsky, N. V. Maslov, A. V. Ogorodnikov, S. A. Sukharev, V. P. Aksenov, I. V. Izmailov, F. Y. Kanev, V. V. Atuchin, and I. S. Soldatenkov, "Wavefront reconstruction of an optical vortex by a Hartmann-Shack sensor," Opt. Lett. **32**, 2291-2293 (2007).
9. H. He, M. E. J. Friese, N. R. Heckenberg, and H. Rubinszteindunlop, "Direct Observation Of Transfer Of Angular-Momentum To Absorptive Particles From A Laser-Beam With A Phase Singularity," Physical Review Letters **75**, 826-829 (1995).
10. G. Gbur, T. D. Visser, and E. Wolf, "Complete destructive interference of partially coherent fields," Optics Communications **239**, 15-23 (2004).
11. G. C. G. Berkhout, and M. W. Beijersbergen, "Method for Probing the Orbital Angular Momentum of Optical Vortices in Electromagnetic Waves from Astronomical Objects," Physical Review Letters **101**, 100801-100804 (2008).

12. V. Garces-Chavez, K. Volke-Sepulveda, S. Chavez-Cerda, W. Sibbett, and K. Dholakia, "Transfer of orbital angular momentum to an optically trapped low-index particle," Physical Review A **66**, 063402 (2002).
13. A. T. O'Neil, I. MacVicar, L. Allen, and M. J. Padgett, "Intrinsic and extrinsic nature of the orbital angular momentum of a light beam," Physical Review Letters **88**, 053601 (2002).
14. M. P. MacDonald, K. Volke-Sepulveda, L. Paterson, J. Arlt, W. Sibbett, and K. Dholakia, "Revolving interference patterns for the rotation of optically trapped particles," Optics Communications **201**, 21-28 (2002).
15. W. Martienssen, and E. Spiller, "Coherence and Fluctuations in Light Beams," American Journal of Physics **32**, 919-926 (1964).
16. W. Martienssen, and E. Spiller, "Intensity Fluctuations in Light Beams with Several Degrees of Freedom," Physical Review Letters **16**, 531 (1966).
17. B. Jia, X. Gan, and M. Gu, "Anomalous phenomenon of a focused evanescent Laguerre-Gaussian beam," Opt. Express **13**, 10360-10366 (2005).
18. D. Ganic, X. Gan, and M. Gu, "Focusing of doughnut laser beams by a high numerical-aperture objective in free space," Opt. Express **11**, 2747-2752 (2003).
19. L. Mandel, and E. Wolf, "Coherence Properties of Optical Fields," Reviews of Modern Physics **37**, 231 (1965).
20. W. Martienssen, and E. Spiller, "Coherence and Fluctuations in Light Beams," Am. J. Phys **32**, 919-926 (1964).
21. W. M. Lee, V. Garces-Chavez, and K. Dholakia, "Interference from multiple trapped colloids in an optical vortex beam," Optics Express **14**, 7436-7446 (2006).
22. M. E. J. Friese, T. A. Nieminen, N. R. Heckenberg, and H. Rubinsztein-Dunlop, "Optical alignment and spinning of laser-trapped microscopic particles," Nature **394**, 348-350 (1998).
23. E. Fallman, and O. Axner, "Design for fully steerable dual-trap optical tweezers," Applied Optics **36**, 2107-2113 (1997).
24. A. I. Bishop, T. A. Nieminen, N. R. Heckenberg, and H. Rubinsztein-Dunlop, "Optical Microrheology Using Rotating Laser-Trapped Particles," Physical Review Letters **92**, 198104 (2004).
25. H. He, N. R. Heckenberg, and H. Rubinsztein-Dunlop, "Optical-particle trapping with higher order doughnut beams produced using high-efficiency computer-generated holograms," Journal of Modern Optics **42**, 217-223 (1995).
26. A. L. Birkbeck, R. A. Flynn, M. Ozkan, D. Q. Song, M. Gross, and S. C. Esener, "VCSEL Arrays as micromanipulators in chip-based biosystems," Biomedical Microdevices **5**, 47-54 (2003).

Chapter 6 -

Optical trapping of nanosheets and nanotubes

6. Optical trapping of nanosheets and nanotubes

6.1. Overview

In this chapter, I use the optical tweezers system (chapter 2) to demonstrate the stable trapping of semiconductor nanosheets and nanotubes. Using both the BFP interferometry (chapter.3) and conventional brightfield video microscopy, I monitor the trapping of these semiconductor nanoparticles in an aqueous environment. In addition to the optical trapping technique, I also make use of chemical processes to increase the dielectric constant of the nanoparticle in a direct and indirect way. In the direct process, a layer of silica material is coated on the nanoparticles. In the indirect process, chemically treated silica microspheres are functionalised so that it draws affinity (Van der Waals attraction) to the nanoparticles. The nanoparticles used in the experiments are cadmium selenide (CdSe) nanosheets and vanadium oxide nanotubes (VOx-NTs, where $x \approx 2.4$). The silica layer is coated onto the CdSe nanotubes while silica microspheres are functionalised to tag onto the VOx-NTs. The BFP and QPD are used to measure the trap stiffness of the silica coating nanosheets. Brightfield images are used to evaluate the optical manipulation and transport of the nanotubes tagged with silica microspheres.

In the first section of the chapter, I provide an overview of the optical manipulation of nanoparticles. In the second section, I perform the trapping of 100nm diameter dielectric and gold nanoparticles. I compare the trap stiffness (PSD analysis) of the two nanoparticles and comment on the effects of enhanced trapping due to the polarisability of gold nanoparticles. In the third section, I move onto manipulation of the nanosheets and nanotubes.

6.2. Introduction

Nanoparticles refer to particles at the size scale of 1 to 100 nm. Nanoparticles are often referred to as the bridge between bulk material and atomic or molecular structures. At such a size scale, there are ample phenomenons such as localised heating, quantum confinement and surface plasmon resonance that can be studied. Through chemical synthesis, it is possible to produce nanoparticles such as quantum dot [1], metallic nanospheres and semiconductor nanoparticles (nanowires, nanotubes and nanorods) [2] readily. Semiconductor nanoparticles may present themselves as the ideal candidates for creating the basic nanostructures. Full three dimensional positional controls over an individual nanoparticle would naturally be beneficial in the construction of photonics and electronics micro/nanodevices. Several non-optical manipulation methods such as

microfluidics and electrics fields have been used to perform the task of assembling these 1D nanostructures [3].

Over the last three decades, the single beam optical tweezers technique has proven both powerful and versatile in many areas of physical and biological sciences, as described in chapter. 1. The collection of particles that is within the trapping range of a single beam optical tweezers extends from the size scale of micrometres to nanometres. Svoboda and Block [4] first demonstrated the three dimensional optical trapping of gold nanoparticles (36nm in diameter) with an optical tweezers and QPD. This pioneering work spawns the possibility of using optical forces to manipulate nanoparticles. The size of particles that is within the trapping range of a single beam tweezers now extends towards tens of nanometres (i.e. quantum dots) [5, 6].

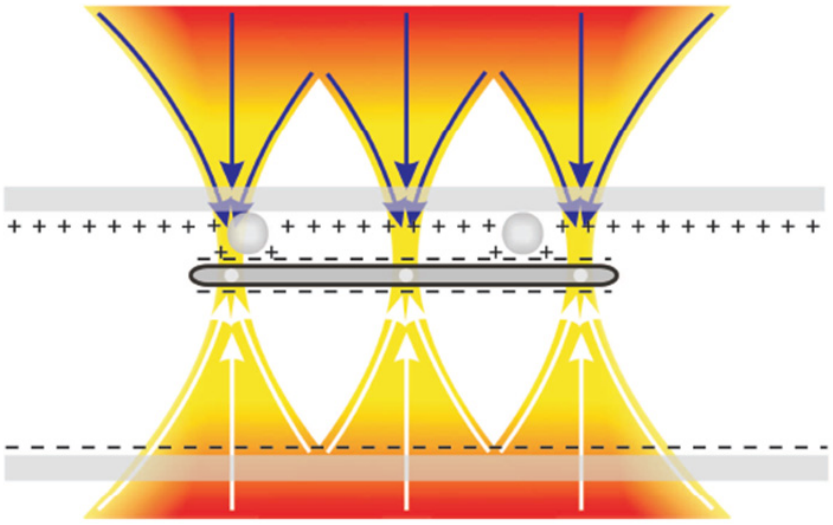

Figure 6.1 A sketch showing a Zinc oxide (ZnO) nanowire trapped in counter-propagating traps. Optical traps (orange) transported the nanowires onto the top surface of the cell and the silica particles deposited onto it, have been coated with PAH to give them a positive charge. When pressed against the top surface the nanowire will stick through electrostatic interactions. Here the nanowire is shown forming a bridge between two spheres.[7]

In recent years, a number of groups [7-13] have been using the optical trapping technique for direct manipulation of semiconductor nanostructures. Semiconductor 1D nanostructures (e.g ZnO, GaAs, Si) exhibit a relatively high refractive index at the near infrared wavelength which is ideal for trapping. However, their overall aspect ratio (diameter to length of 1:20) still poses a substantial hurdle to their efficient manipulation [11, 12]. An immediate solution would be to use multiple optical tweezers systems, e.g. holographic optical tweezers or time-shared optical tweezers

to tackle this concern. By distributing either a discrete number of optical tweezers or an elongated optical trap (a line intensity pattern) over the nanostructures, the 1D nanostructure is optically confined in either two or three dimensions [7, 13]. In figure 6.1, Van der Horst *et al* [7] used an AOD to create multiple optical traps in a counter-propagating beam trapping geometry. The nanowires are transported to the top of the sample and deposited onto two microspheres. Recent advancements in optoelectronic tweezers have also shown the ability to manipulate a large number of single nanowires simultaneously in two dimensions [14]. In addition, optical tweezers have shown to be able to transport and deposit bundles of single or multi walled carbon nanotubes onto a substrate [15-19].

In this chapter, I work on an alternative solution to enhance the trapping of nanoparticles which is via dielectric enhancements. I made use of two processes namely: silica coating and direct dielectric sphere tagging. The layer of silica material is coated onto the CdSe nanosheets via chemical synthesis. On the other hand, a direct tagging process with functionalized microspheres is used to indirectly manipulate the VOx-NTs. The optical trap is used to trap the CdSe nanosheets directly and the microspheres tagged to the VOx-NTs.

6.3. Trap stiffness of nanoparticles with back focal plane interference

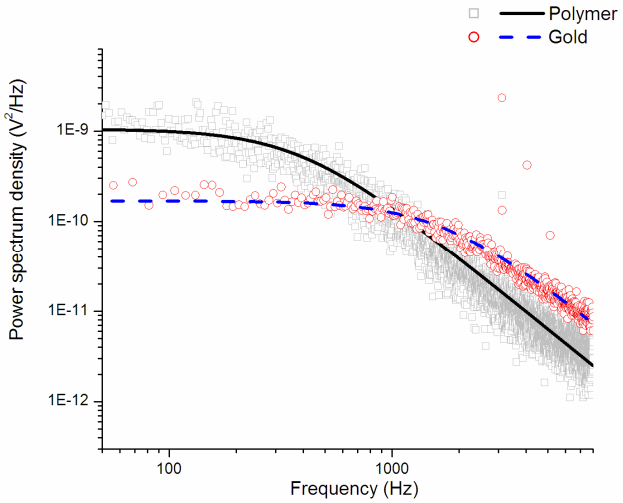

Figure 6.2 shows the roll off frequency for the two types of nanoparticles of the same size. (solid and dotted line are the nonlinear fit for polymer and gold respectively). The optical power in the optical tweezers is 101mW.

The preferred approach to measure the stiffness of the nanoparticle is using the PSD analysis [4, 20, 21]. As mentioned in section 1.3.2.2, gold nanoparticles have an enhanced trapping

capability as compared to the polymer sphere of the same size, due to the polarisability of gold [4, 20, 21]. Here I repeat the comparison study with 100nm (diameter) gold nanoparticles and polymer spheres, as shown in figure 6.2. The trap is located at 3μm away from the bottom coverslip with an optical power of 101mW at the sample. The roll-off frequency and trap stiffness for the polymer is measured to be 340 Hz and 2.03 pN/μm. On the other hand, the gold nanoparticle is measured to give a roll-off frequency and trap stiffness of 1700 Hz and 10.16 pN/μm respectively. Here, I see a five fold trapping enhancement of the metallic nanoparticles which in consistent with previous experiments [4, 20, 21]. This result shows that the BFP and QPD system can readily measure stiffness for particles down to 100 nm. As such, I can make use of the technique to measure the trap stiffness of the silica coated nanosheets in the next section. Note that in the appendix E(iii), I demonstrate the trap stiffness analysis for 48 nm nanoparticles.

6.4. Dielectric enhanced semiconductor nanoparticles

In this section, I demonstrate the trapping of dielectric enhanced semiconductor nanoparticles. The two processes aimed at enhancing the dielectric constant of the semiconductor nanoparticle are: silica shell coated CdSe nanosheets and direct dielectric sphere tagging onto VOx-NTs The back focal plane interferometry [22, 23] and brightfield microscope images are used to assess the trapping dynamics of the nanoparticles respectively.

6.4.1. Silica coated nanosheets

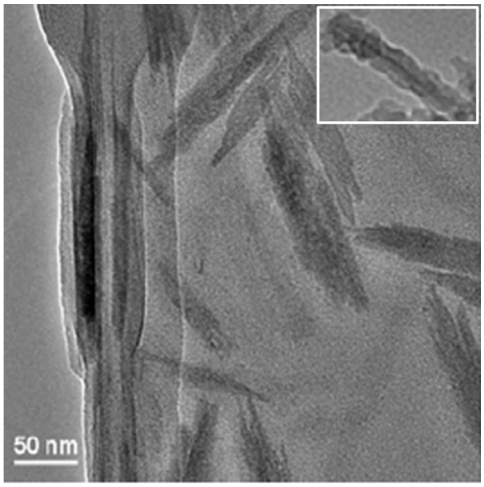

Figure 6.3 TEM image of CdSe nanosheets. Cadmium selenide (CdSe) nano sheets without silica coating and inset shows nanosheets after being coated. Notice the bumpy edges on the coated nanosheets are due to emulsion process.

Fluorescent semiconductor nanocrystals (also known as quantum dots) have improved the resolution, sensitivity and versatility of fluorescence microscopy. These nanocrystals are observed to provide a large stable photoluminance with a narrow emission spectrum under a broad excitation spectrum. Colloidal nanocrystals are single crystals of a few nanometres in diameter. Different size of nanocrystals can be made by controlling the duration, temperature of the synthesis process and also the ligands molecules. Absorption of any photons with wavelengths above this specific wavelength causes the formation of an electron-hole pair (exciton). These semiconductor crystals are excellent fluorescence markers to visualize biological systems. Only recently, it has been shown possible to optically trap these nanocrystals experimentally with an infrared optical tweezers [8]. On the theoretical front, there has been suggestions that the excitons created during resonant excitation in these nanocrystals can improve their optical trapping efficiency [24]. In this section, I shall explore the optical trapping of single nanosheets form with semiconductor nanocrystals using an infrared laser beam (wavelength 1070nm). The nanosheets are enhanced dielectrically with a thin coat of silica material. A layer of silica coating can often protect the nanoparticles from the surrounding medium due to issues with solubility and the toxicity.

Recently, Bormuth *et al* [25] have shown that a silica coating on a polystyrene microsphere provides a substantial improvement in the axial trap stiffness of the microsphere. In our current proposed experiment, a layer of silica coating is applied over the CdSe nanoparticles. This is to increase the effective refractive index or the dielectric constant of the nanoparticle. The coating process is carried out by Dr Pascal Andre and Mr Chen Shu. I will only elaborate the chemical synthesis process briefly. The CdSe nanoparticles were prepared by thermal decomposition of cadmium oxide, selenium, di-octylamine, tri-octylphosphine oxide, and hexadecylamine at 280 °C. The chemical were purchased from Sigma-Aldrich, used without further purification and the nanoparticles were extracted by centrifugation [26, 27] (1)(2). Silica coating of the nanoparticles (NPs) was carried out using a modified reverse microemulsion method based on work Yi *et al* [28]. A reverse microemulsion was prepared with NP-5 as surfactant and cyclohexane as the oil phase, the NPs solution was injected drop wise, while tetraethyl orthosilicate (TEOS) and ammonium hydroxide solutions were injected separately to start the hydrolysis reaction. The mixture was kept under stirring for 48-72 h to allow silica coating to grow. Silica coated nanoparticles were washed and extracted by centrifugation. From the TEM images of the CdSe quantum dots (4nm each), it appears that clusters were observed to form thin “nanosheets”. These nanosheets are formed when during the initial mixing (synthesis), the ligands meant for binding of the Cd and Se atom. Currently, steps are made to improve to the synthesis to obtain spherical Cd-Se nanoparticles. The average

length of the sheet is around 100-150nm with a thickness of about 4nm and length of about 25-50nm as shown in figure 6.3, inset show the silica coated nanosheets.

In this study, the static optical tweezers is used for the trapping (section 3.5). The power at the sample is around 150mW. The samples are prepared in a seal glove box to ensure cleanliness of the sample. The trapping of the nanosheets are carry out at 3μm above the coverslip. As an initial step, the trapping of the CdSe nanosheets is carried out but did not result in a stable three dimensional confinement (see appendix E(iv)). One of the reasons could be the low dielectric constant of the nanosheets. Hence, I move to use the silica coated CdSe nanosheets for trapping. The scattered light from the trapped silica coated nanosheets registers a PSD graph with a reasonable roll off frequency, shown figure 6.4. This indicates stable three dimensional trapping. In addition, a strong two photon signal is observed during the process. The signal drops to minimal (photobleaching) after 40 s (with sudden intensity dip at 25 s). These nanosheets are photo-bleached by the trapping laser beam due to strong two photon absorption. Fluorescence emission due to two photon absportion is often more efficiently carried out using ultrafast laser beams [29]. However, with enough optical power in a focussed continuous wave laser beam (optical tweezers), it is also possible to initiate two photon absportion [30]. Florin *et al* [30] first observed the two-photon absorption of a fluorescent dye for the 1064 nm continuous wave trapping beam that is chosen to fulfil the two photon criterion. Similarly, since the Cd-Se nanosheets possess a strong absportion band at 543nm, which is close to half of the wavelength of the trapping beam (1070nm), I am able to observe the excited light field (633 nm) with a Peltier cooled (-87 ^{o}C) electron-multiplying charge couple device (EMCCD) camera. In figure 6.4, a captured axial PSD (light gray) graph that belongs to an optical trap without any nanosheets in the trap (dark gray). The graph is plotted for comparison with the PSD graph of the trapped nanosheets. The PSD is fitted and a roll-off frequency 2000 Hz is derived. Based on the size of the nanosheets (assuming it is aligned along the beam axial direction), the axial trap stiffness is calculated to be 11.9 pN/μm.

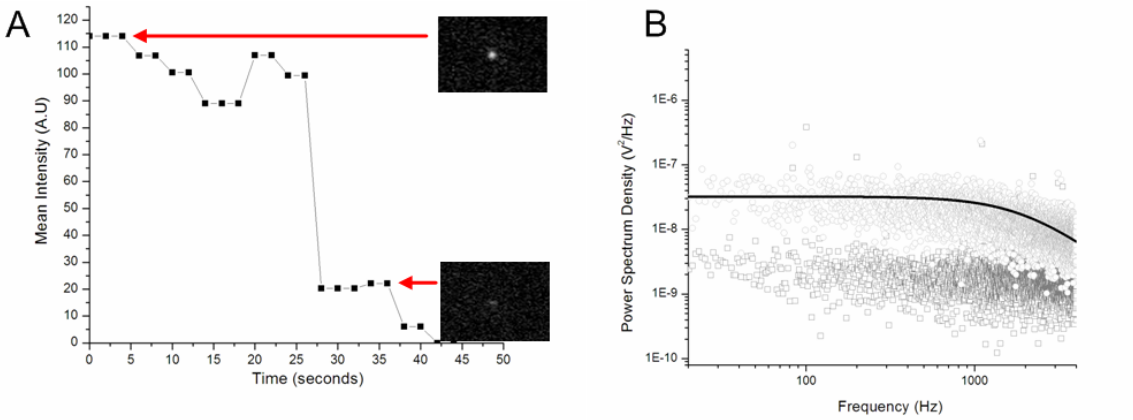

Figure 6.4 Fluorescence intensity and PSD graph of trapped silica coated CdSe nanosheets. (A) Mean intensity variation of the trapped CdSe nano-sheet being trapped over a given time as captured by the EMCCD (inset) with an exposure time of 2s.(B) Power spectrum density of the CdSe nano-sheet during the trapping in z (bin data- light gray circle and fit – black line) and an empty trap (bin data – dark grey squares)

From the current result, the silica coated nanoparticles has shown to be well confined within the optical tweezers. However, the photobleaching would render the nanoparticles ineffective for fluorescence applications. Jauffred *et al* [8] confirmed the trapping of CdSe/ZnS composite (15-20nm in size) and the subsequent fluorescence excitation with photobleaching at periods longer than 30 mins[31]. The main reason for this is because of the structure of the ZnS can increases photoluminance of the CdSe as well as protecting it from fast photobleaching [32]. Hence, it would be beneficial to carry out the trapping and photoluminance study for a combination of CdSe/ZnS composite nanoparticles (see chapter 9, section 9.5). The purpose of this section is to show that CdSe nanosheets, after dielectric enhancement with silica coating, can be stably trapped with a single optical tweezers. Hence, it is possible to trap and organise these CdSe nanosheets on a given substrate. However, the photobleaching effects in the trap restrict the use of the trapping technique for the assembling of these nanosheets as photonics devices. Other means of indirect trapping of the nanosheets (without causing photobleaching) might need to be used. This leads us to the next section where microspheres are tagged onto absorptive VOx-NTs and used as optical handles.

6.4.2. Dielectric microsphere tagging nanotubes

Newly emerging multi-walled vanadium oxide nanotubes (VOx-NTs, where $x \approx 2.4$) have been synthesized for a variety of applications: electrodes for Lithium (Li+) batteries, optical limiting and spin control via a transition from a semiconductor to a ferromagnet [33-35]. Essentially, these nanotubes are formed by lamellar structures of vanadium oxide to which amine molecules

have been intercalated. The amine molecules in the VOx-NTs can be substituted with several cations [35].

In this section, I describe a simple but powerful microsphere tagging technique to manipulate these absorptive VOx-NTs. **The VOx-NTs are highly absorptive at the NIR wavelength, which leads to direct laser ablation when exposed to the optical tweezers**. Direct illumination of the trapping beam at a mere 20mW results in the immediate ablation of the nanotubes (results not shown here). A systematic tag and removal procedure by means of a single optical tweezers system is shown for the efficient trapping and transportation of these nanotubes. This method has direct analogies with the manner by which single molecules are studied in optical traps [5]. The microspheres are chemically tagged to the particle of interest. A moving optical trap manipulates the microsphere which in turn moves the particles. The versatility of this microsphere tagging technique is now applied to the transport of independent nanotubes or bundles of nanotubes onto a chosen substrate. Since VO_x-NTs have high absorptions,the very same optical tweezers serves as a form of optical scissors that performs precise trimming of these VO_x-NTs . The optical tweezers can possibly remove the tagged dielectric microsphere after being transported to a desired location. The ablation is done with minimal optical contact (short exposure time) upon the nanotubes so as to incur minimal damage due to any absorption. The methodology of trapping and removal should be readily extendable to the trapping and transport of other absorptive nanotube structures.

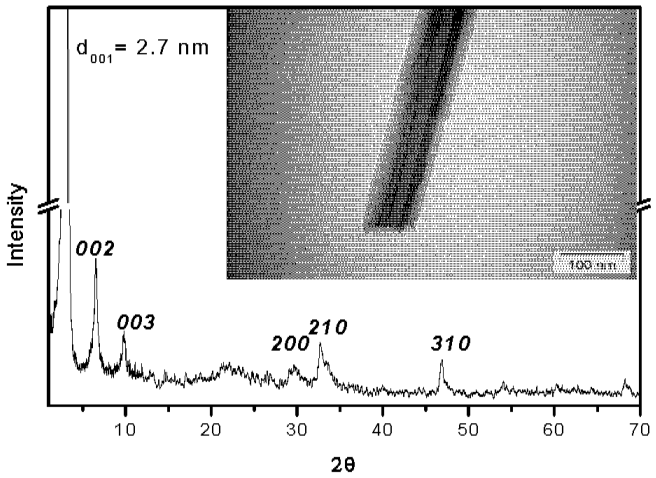

Figure 6.5- Typical X-ray diffraction pattern, inset shows a TEM image of vanadium nantotube. (Courtesy of Jose Luis Hernández-Pozos, Mexico)

The fabrication of the nanotubes and functionalized of the microspheres were carried out by Dr. Jose Luis Hernández-Pozos and Dr. Liliana Irais Vera-Robles from Universidad Autónoma

Metropolitana-Iztapalapa. Here I shall briefly describe the fabrication and functionalization processes. The details on the formation process are described elsewhere [35]. The VOx-NTs were synthesized with the following chemical process: Firstly, 1.82 grams (0.1 molar) of V_2O_5 was added to 3.3 ml (0.0565 molar) of ethanol. After which, 1.85 grams (0.1 molar) of dodecylamine (C12H27N) was added. The mixture was stirred for 2 hours before mixing it with 10 milliliters of water. The final mixture was left to age for 2 days. Afterwards, the mixture is further heated to 160 degree Celsius for 7 days in a Parr vessel. Finally, the remaining solution was filtered, washed with ethanol and dried in an oven at 70 oC for over 6 hours. The structures of the nanotubes are verified through the use of TEM imaging and X-ray diffraction. In figure 6.5, a typical X-ray diffraction pattern and the inset shows a TEM image of VOx-NTs is shown. From the X-ray diffraction pattern, it is possible to see three reflections at low angle (lattice structure indexed here as 001, 002 and 003). These reflections indicate the layered structure of the walls within the VOx-NTs. In this case the position of the first peak corresponds to an interlayer distance of 2.7 nm. At higher angles, the peaks indexed as *hk*0 corresponds to the crystalline structure of the walls. Such walls consist of layers of V_7O_{16} formed by two sheets of VO_5 square pyramids pointing in opposite directions which are joined by VO_4 in form of tetrahedron. X-ray diffraction patterns were taken with a Siemens D-500 diffractometer using the Kα line (λ=1.54 angstrom), the micrographs were taken with a Carl-Zeiss EM-910 Transmission Electron Microscope operated at 120 kilovolts. Typically, the thickness of these nanotubes ranges from ~20 nm; the tubes diameter varies between 50 to 120 nm and their lengths between 0.5 to 4 μm. The tube diameter (~0.5 - 1 μm) will vary with respect to the degree of unfolding that it may acquire over a given time [33]. A calibrated CCD is use to analysis the imaging of the nanotube in brightfield. Since the typical lateral resolution of brightfield is around 200 nm, the size of the nanotubes measured in this section serves as an estimate.

Next the functionalization of silica microspheres (2.7 μm in diameter, Bangs Labs) is explained. A molecule that would attach to the nanotubes is APTES (3 amino-propylethoxysilane) that contains an amine groups ($-NH_2$). This particular molecule will have high affinity (attraction) towards the VO nanotubes surface via Van der Waals interactions (see figure 6.6). A solution of the functionalized silica microspheres were suspended into 1ml of deionized water and the VO_x-NTs are suspended in an aqueous solution (1ml) containing a mixture of 70% ethanol and 30% deionized water. Both samples were sonicated before mixing together in an enclosed chamber as described before [36].

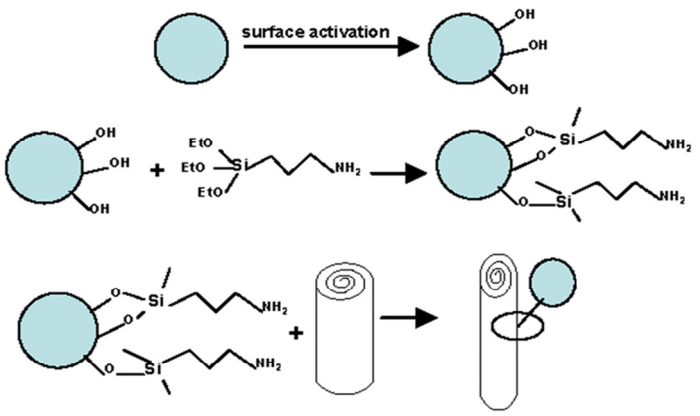

Figure 6.6- Illustration of APTES coating onto silica microspheres. Silica microspheres are cleaned to expose silanol groups and remove any contamination at the surface. They are then functionalized with APTES, the union between the bead and the APTES is a covalent bond. Once functionalized, the amine group (-NH_2) of the APTES molecule interacts with the vanadyl groups (V=O) at the tube´s surface. The close contact adhesion process is due to interacting Van der Waals forces (Courtesy of Jose Luis Hernández-Pozos)

Figure 6.7 shows the controlled tagging process. Here, a single optically trapped APTES-coated silica sphere (2.7 μm in diameter) is carefully positioned approximately 10 μm (by moving lens L6 with stepper motor as shown in figure 2.7)) above a single VOx-NTs (length ~ 5 μm, diameter ~ 0.5 μm). The slightly large diameter of this tube indicates a minor unrolling of the tubular structure. The nanotube is observed to be pulled towards the focused light beam. Upon contact, the nanotube is seen to attach itself onto the microsphere as seen in figure 6.7 A-B. In figure 6.7 C, I show the microsphere with the tagged nanotube being optically steered away as indicated by the orientation of the nanotube. Figure 6.7 D shows a graphical illustration of how the nanotubes are attached to the silica microsphere. In figure 6.7 E-H, I show a nanotube (length~ 5 μm, diameter ~ 0.5 μm) being transported around the sample by the optically trapped silica microsphere at velocities of up to 20 μm per second. Importantly, this form of tagging process is completely reversible. In figure 6.7 I-K, I show a single silica sphere with an attached nanotube (length of approximately 5 μm and diameter of around 0.5 μm) deposited onto a top coverslip. By carefully scanning a weak optical tweezers (<10 mW) across the junction where the nanotubes is attached to the microsphere, the nanotube is controllably detached from the microsphere and leaving minimum damage. Figure 6.7 L shows a graphical illustration of how the nanotubes are detached from the silica microsphere at the top coverslip.

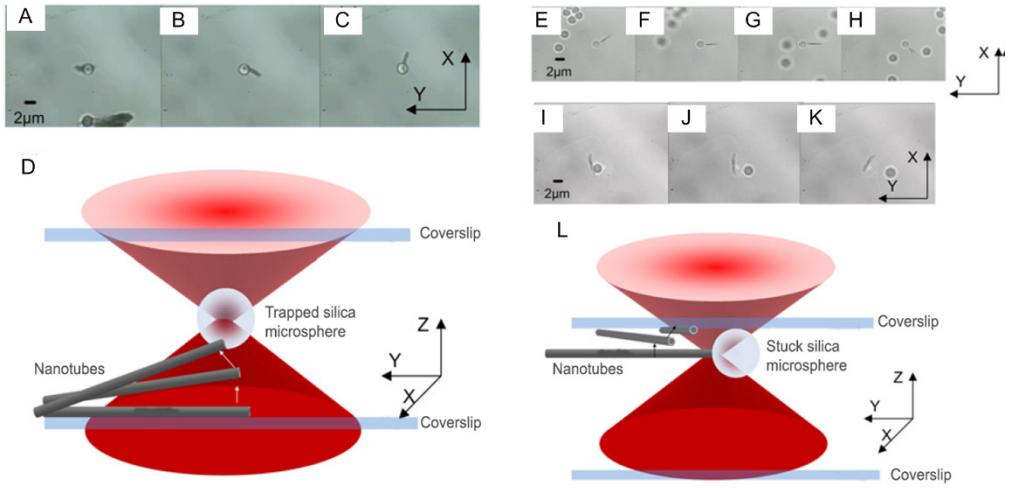

Figure 6.7 - Illustrate the tagging and untagging procedure of the nanotube onto a trapped coated silica microsphere. A - C shows a single nanotube being picked up by a trapped functionalized dielectric silica sphere. D shows a 3D illustration of the entire tagging process. E – H shows a large nanotube transported in both the lateral and the axial planes by a trapped silica microsphere. I – K shows the experiments results of the controlled removing of the nanotubes from their dielectric microspheres. L shows a 3D illustration of this removal process.

In figure 6.8, I show a series of images that depict the manipulation of the nanotubes in three dimensions. In figure 6.8A-D, I show the two functions in which a single optical tweezers serves both as the trapping beam and the optical scissors. A cluster of nanotubes tagged to a single silica microsphere is positioned around 2 μm above the bottom coverslip. By swiftly scanning the trapping beam across a small section of the cluster and back onto the microsphere, a small piece of nanotube (length: 2 μm, width: 0.5 μm) is trimmed and removed from the large cluster. As the trapping beam is scanned back onto the microsphere, the trimmed section of the nanotube is re-attached onto the optically trapped silica microsphere.

Figure 6.8 E-H shows the manipulation of a single nanotube (length: 5 μm, diameter: 0.5 μm) where one end of the nanotube is anchored onto a cluster of silica microsphere adhered to the bottom coverslip. An optically trapped microsphere (marked by a red dot) is moved onto the free end of the nanotubes for attachment, figure 6.8 F. Such an optical trapping configuration allows a three dimensional angular tilt position of the nanotube over a substrate of interest.

In figure 6.8 I - L, I illustrate the controlled rotation, at an incremental angle of 10 degree, of a bundle of nanotube with two microsphere tagged onto opposite ends of the bundle of nanotubes. With the help of a dual optical tweezers, in figure 2.7, one of the microspheres is translating at 1 μm incremental steps. This shows the angular positioning of the bundle of nanotubes with this technique. By shifting the axial position of two trapped microsphere away from the bottom of the

coverslip by 5 μm, the bundle of nanotubes is stably lifted off the bottom coverslip as seen in figure 6.8M and 6.8N. Next, I demonstrate the possibility of controlled patterning of the nanotubes onto a given substrate. The substrate here refers to the glass coverslip at the top of the sample chamber. I have transported and deposited a bundle of nanotubes onto the top coverslip. By using the trapping beam as an optical scissor, I am able to trim small piece of the tubes and thereafter position them into a desired pattern. In figure 6.8 O and P, I show the controlled two dimensional patterning of the nanotubes using an optical tweezers into T-shape and triangle respectively. These nanotubes have a small attraction to the silica coverslip. The fine positioning of the nanotubes into its desired shape is done by carefully steering a slightly defocused beam (with an AOD) at the perimeter of the nanotubes. In that way, the nanotubes are seen to be gently pushed away (due to scattering) from the beam without being ablated.

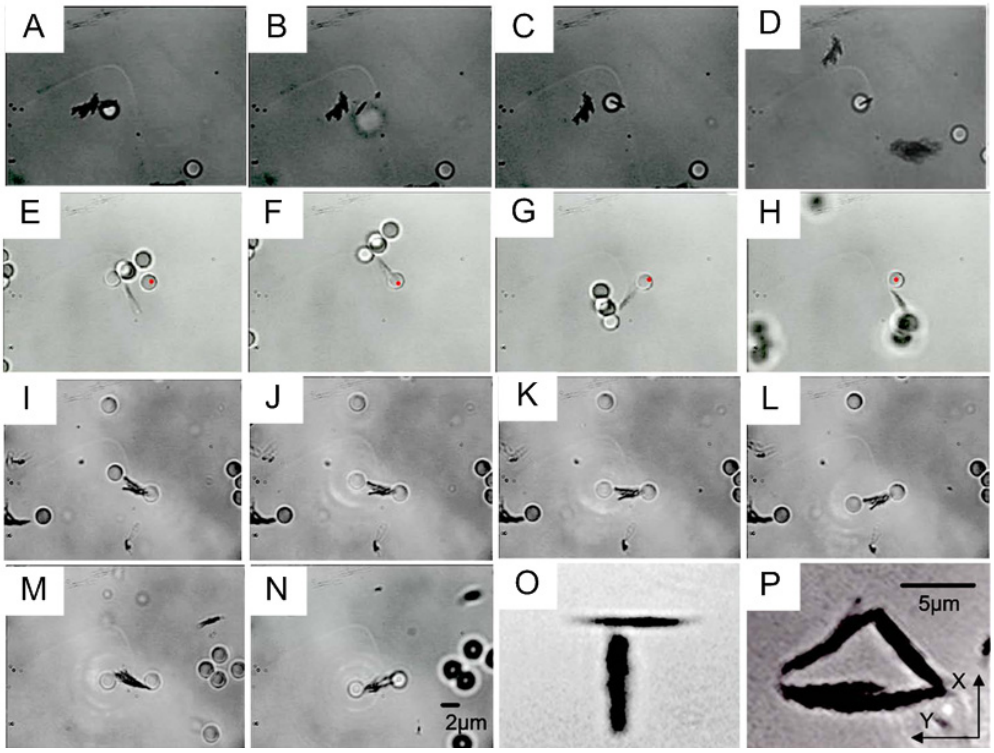

Figure 6.8- A series of images depicting the manipulation of the nanotubes in three dimensions (A) – (D) shows selective trapping and trimming of a single nanotube from a cluster of nanotubes and subsequent tagging to a optically trapped single silica microsphere. (E)-(H) shows the manipulation of a single nanotube over the bottom coverslip (I) – (N), rotation and controlled levitation of a bundle of nanotubes held with two optical tweezers via the two microspheres tagged onto opposite ends of the bundle of nanotubes. (O) and (P) shows the two dimensional patterning of the nanotubes into T-shape and triangle respectively.

6.5. Conclusion

In recent years, the field of optical tweezers has been actively used to explore the manipulation of nanoparticles. At the nanoscale dimension, the optical tweezers have proven to have an effective three dimensional control of their positions.

In this chapter, I seek to explore the manipulation of particles with sizes much smaller than the trapping wavelength. First, I measured a 5-fold increase of the stiffness for gold nanoparticles as compared with polystyrene nanospheres of the similar size (≈100nm in diameter).

Using the same instrument (a single optical tweezers), I went on to demonstrate the optical trapping of CdSe nanosheets that are silica coated. From the current result, the silica coated nanoparticles was shown to be well-confined within the optical tweezers: axial stiffness of 11.9 pN/μm with 150mW. The purpose of this section was to show that CdSe nanosheets, after dielectric enhancement with silica coating, can be stably trapped with a single optical tweezers. Hence, it is possible to trap and organise these CdSe nanosheets on a given substrate. However, the photobleaching effects in the trap will restrict the use of the trapping technique for the assembling of these nanosheets as photonics devices. In the next step, it would be beneficial to carry out the trapping and photoluminance study for a combination of CdSe and ZnS nanoparticles (i.e. CdSe/ZnS, ZnS). This will allow us to assess the photobleaching effects of the optical trap on different semiconductor nanosheets.

Next I qualitatively demonstrated a simple but powerful microsphere tagging technique to manipulate absorptive VOx-NTs. A systematic tag and removal procedure using an optical trapping system was shown for the efficient trapping and transportation of these nanotubes. The very same optical tweezers served as a form of optical scissors that performs precise trimming of these VOx-NTs, due their high optical absorption. The versatility of this optical technique allowed the selective tagging, manipulation and trimming of independent or bundles of VOx-NTs onto a chosen substrate, and minimized physical damage due to any absorption. Using a dual optical tweezers system (with one controlled by an AOD), I stably manipulated a bundle of VOx-NTs in three dimensions via the tagged microspheres. This approach can be extended to the manipulation and transportation of any types of nanostructures regardless of their material composition. One of the key advantages of this microsphere tagging is that there is no additional treatment need to be carried out on the nanoparticles. Unlike other dielectric microsphere tagging process, both the object and microspheres might need to be coated i.e. biotin or streptavidin.

One limitation of this technique is the strength of the affinity. In our experiments, the average tagging success was around 40%. This is due to the fact that the attraction relies on the amount of charge on the VOx-NTs which varies from particle to particle. Future experiments should carry out the quantification of the strength of the affinity using the dual optical tweezers system. Using the knowledge of the affinity, it would be possible to find a molecule with a higher attraction to VOx-NTs and possibly increase the binding efficiency.

In this chapter, I have designed and performed the experiments. The nanoparticles were obtained from various collaborators: CdSe nanosheets are obtained from Dr Pascal Andrea and Mr Chen Shu, University of St Andrews (UK) and the VOx-NTs with the functionalised microspheres are provided by Dr. Jose. Lius. Hernandez-Pozos and Dr. Liliana Irais Vera-Robles from the Universidad Autónoma Metropolitana-Iztapalapa (Mexico).

6.6. References

1. R. Bratschitsch, and A. Leitenstorfer, "Quantum dots: Artificial atoms for quantum optics," Nat Mater **5**, 855-856 (2006).
2. J. Tersoff, "Nanotechnology: Less is more," Nature **412**, 135-136 (2001).
3. Y. Cui, and C. M. Lieber, "Functional nanoscale electronic devices assembled using silicon nanowire building blocks," Science **291**, 851-853 (2001).
4. K. Svoboda, and S. M. Block, "Optical Trapping of Metallic Rayleigh Particles," Optics Letters **19**, 930-932 (1994).
5. K. C. Neuman, and S. M. Block, "Optical trapping," Review of Scientific Instruments **75**, 2787-2809 (2004).
6. K. Dholakia, and P. Reece, "Optical micromanipulation takes hold," Nano Today **1**, 18-27 (2006).
7. A. van der Horst, A. I. Campbell, L. K. van Vugt, D. A. Vanmaekelbergh, M. Dogterom, and A. van Blaaderen, "Manipulating metal-oxide nanowires using counter-propagating optical line tweezers," Opt. Express **15**, 11629-11639 (2007).
8. L. Jauffred, A. C. Richardson, and L. B. Oddershede, "Three-Dimensional Optical Control of Individual Quantum Dots," Nano Letters **8**, 3376-3380 (2008).
9. T. Iida, and H. Ishihara, "Optical manipulation of nano materials under quantum mechanical resonance conditions," Ieice Transactions on Electronics **E88C**, 1809-1816 (2005).
10. T. Yu, F. C. Cheong, and C. H. Sow, "The manipulation and assembly of CuO nanorods with line optical tweezers," Nanotechnology **15**, 1732-1736 (2004).
11. P. J. Pauzauskie, A. Radenovic, E. Trepagnier, H. Shroff, P. Yang, and J. Liphardt, "Optical trapping and integration of semiconductor nanowire assemblies in water," Nat Mater **5**, 97-101 (2006).
12. Y. Nakayama, P. J. Pauzauskie, A. Radenovic, R. M. Onorato, R. J. Saykally, J. Liphardt, and P. Yang, "Tunable nanowire nonlinear optical probe," Nature **447**, 1098-1101 (2007).
13. R. Agarwal, K. Ladavac, Y. Roichman, G. Yu, C. Lieber, and D. Grier, "Manipulation and assembly of nanowires with holographic optical traps," Opt. Express **13**, 8906-8912 (2005).
14. C. W. Ming, "Optoelectronic Trapping of Cells, Nanowires, and Nanoparticles," in *Optical Trapping Applications*(Optical Society of America, 2009), p. JMB1.
15. Y. G. Zhang, "Optical trapping and in-situ Raman spectroscopy of soluble carbon nanotubes," Abstracts of Papers of the American Chemical Society **229**, U92-U93 (2005).
16. D. L. Andrews, and D. S. Bradshaw, "Laser-induced forces between carbon nanotubes," Optics Letters **30**, 783-785 (2005).

17. L. F. Zheng, S. D. Li, J. P. Brody, and P. J. Burke, "Manipulating nanoparticles in solution with electrically contacted nanotubes using dielectrophoresis," Langmuir **20**, 8612-8619 (2004).
18. S. D. Tan, H. A. Lopez, C. W. Cai, and Y. G. Zhang, "Optical trapping of single-walled carbon nanotubes," Nano Letters **4**, 1415-1419 (2004).
19. J. Plewa, E. Tanner, D. M. Mueth, and D. G. Grier, "Processing carbon nanotubes with holographic optical tweezers," Optics Express **12**, 1978-1981 (2004).
20. P. M. Hansen, V. K. Bhatia, N. Harrit, and L. Oddershede, "Expanding the optical trapping range of gold nanoparticles," Nano Letters **5**, 1937-1942 (2005).
21. Y. Seol, A. E. Carpenter, and T. T. Perkins, "Gold nanoparticles: enhanced optical trapping and sensitivity coupled with significant heating," Opt. Lett. **31**, 2429-2431 (2006).
22. M. W. Allersma, F. Gittes, M. J. deCastro, R. J. Stewart, and C. F. Schmidt, "Two-dimensional tracking of ncd motility by back focal plane interferometry," Biophysical Journal **74**, 1074-1085 (1998).
23. E. J. G. Peterman, F. Gittes, W. Moehler, and C. F. Schmidt, "Optical tweezer experiments: Temperature effects and back focal plane interferometry," Biophysical Journal **80**, 73A-73A (2001).
24. T. Iida, and H. Ishihara, "Theoretical Study of the Optical Manipulation of Semiconductor Nanoparticles under an Excitonic Resonance Condition," Physical Review Letters **90**, 057403 (2003).
25. V. Bormuth, A. Jannasch, M. Ander, C. M. van Kats, A. van Blaaderen, J. Howard, and E. Schäffer, "Optical trapping of coated microspheres," Opt. Express **16**, 13831-31844 (2008).
26. Z. A. Peng, and X. Peng, "Nearly Monodisperse and Shape-Controlled CdSe Nanocrystals via Alternative Routes: Nucleation and Growth," Journal of the American Chemical Society **124**, 3343-3353 (2002).
27. F. Wang, R. Tang, and W. E. Buhro, "The Trouble with TOPO; Identification of Adventitious Impurities Beneficial to the Growth of Cadmium Selenide Quantum Dots, Rods, and Wires," Nano Letters **8**, 3521-3524 (2008).
28. D. K. Yi, S. T. Selvan, S. S. Lee, G. C. Papaefthymiou, D. Kundaliya, and J. Y. Ying, "Silica-Coated Nanocomposites of Magnetic Nanoparticles and Quantum Dots," Journal of the American Chemical Society **127**, 4990-4991 (2005).
29. B. Agate, C. T. A. Brown, W. Sibbett, and K. Dholakia, "Femtosecond optical tweezers for in-situ control of two-photon fluorescence," Optics Express **12**, 3011-3017 (2004).
30. E. L. Florin, A. Pralle, J. K. H. Horber, and E. H. K. Stelzer, "Photonic force microscope based on optical tweezers and two-photon excitation for biological applications," Journal of Structural Biology **119**, 202-211 (1997).
31. L. Oddershede, personal communications (2009).
32. B. O. Dabbousi, J. Rodriguez-Viejo, F. V. Mikulec, J. R. Heine, H. Mattoussi, R. Ober, K. F. Jensen, and M. G. Bawendi, "(CdSe)ZnS Coreâ^'Shell Quantum Dots: Synthesis and Characterization of a Size Series of Highly Luminescent Nanocrystallites," The Journal of Physical Chemistry B **101**, 9463-9475 (1997).
33. S. Webster, R. Czerw, R. Nesper, J. DiMaio, J. F. Xu, J. Ballato, and D. L. Carroll, "Optical properties of vanadium oxide nanotubes," Journal of Nanoscience and Nanotechnology **4**, 260-264 (2004).
34. P. B. R. N. M. M. F. K. H. U. N. Michael E. Spahr, "Redox-Active Nanotubes of Vanadium Oxide," Angewandte Chemie International Edition **37**, 1263-1265 (1998).
35. L. I. Vera-Robles, and A. Campero, "A Novel Approach to Vanadium Oxide Nanotubes by Oxidation of V4+ species," Journal of Physical Chemistry C **112**, 19930-19933 (2008).
36. W. M. Lee, P. J. Reece, R. F. Marchington, N. K. Metzger, and K. Dholakia, "Construction and calibration of an optical trap on a fluorescence optical microscope," Nat. Protocols **2**, 3226-3238 (2007).

Chapter 7 -

Combining optical tweezers with advanced optical microscopy imaging techniques for studies in nanoparticle cell hyperthermia

7. Combining optical tweezers with advanced optical microscopy imaging techniques for studies in nanoparticle cell hyperthermia

7.1. Overview

In this chapter, I enhanced the imaging capabilities of the inverted microscope system (TE 2000) that were previously restricted to brightfield and epi-fluorescence imaging. Bright-field imaging uses Kohler illumination to provide an even illumination onto an object on the sample and collect the object's image with a conventional charged coupled device (CCD) camera. Epi-fluorescence imaging makes use of a broadband light illumination, dichroic mirrors and long/short/band pass filter to select the appropriate fluorescent excitation and collect the emitted light onto a conventional CCD camera or an electron-multiplying charged coupled device (EMCCD). The additional imaging system is laser scanning confocal fluorescence imaging.

The improvements made with the laser scanning confocal fluorescence imaging is the added ability to reconstruct the three dimensional fluorescent image of a fluorescent particle. Using the confocal arrangement and the point by point excitation methodology, it is possible to provide a high resolution imaging of the fluorescent particles (transverse resolution ≈ 100nm), as seen in appendix A. In the first part of the chapter, I describe the integration of a commercial confocal scan head (Nikon C1Si) into dual optical tweezers system (chapter 3) via an imaging port to carry out fluorescent imaging on trapped biological particles. I also use the BFP interferometry to perform particle-cell adhesion experiment simultaneously with the confocal fluorescence imaging system.

In the second part of the chapter, I use this integrated manipulation and imaging instrument, termed as biophotonics workstation, to measure effects of biological cell when exposed to a heated trapped gold nanoparticle (as mentioned in section 6.3). The heated trapped gold nanoparticle serves as a single localised heating point that initiates selective cell hyperthermia (cell death due to heat). Using the time-lapse fluorescence imaging using the confocal scanning system, it is possible to track the changes to the cell membrane over a given time period.

7.2. Introduction

In 1676, Antonie van Leeuwenhoek became one of the first to have ever set his eyes on the bacteria with a home-made microscope. He later reported to the Royal society and ignited the field of microbiology [1]. As I now know, many biological microparticles are often difficult to see due to their refractive index being very close to that of their surrounding medium. It took another two hundred years before Frits Zernike invented an imaging technique that circumvented these issues with an elegant physics solution: converting faint phase gradients into intensity variations by the method of phase contrast with phase contrast technique [2]. Now the introduction of laser into modern fluorescent microscopy has greatly enhanced our capability to capture the beauty of the invisible world at much higher clarity and depth.

Laser microscopy has unravelled a wealth of complex processes in cell and molecular biology. The prominent laser imaging method such as laser scanning confocal fluorescence imaging and two-photon fluorescence excitation are established techniques for visualizing cells and macromolecules. Combination of optical imaging modalities and optical trapping system has come into interest due to the demands of modern interdisciplinary research: biophysics [3, 4] and material sciences [5].

The combination of the two important biophysical techniques: optical micromanipulation and fluorescence imaging in a single assay offers a powerful tool for studying cellular, molecular systems and even nanostructures. The combination of optical trapping and single-molecule fluorescence has revealed remarkable insight in the molecular mechanics of biological motors i.e. conformational and structural changes occurring within proteins and nucleic acids [6-8]. The integration of confocal laser scanning or multiphoton microscopic imaging and optical micromanipulation had led to insights into cellular activities [9, 10]. Eriksson *et al* [11] recently combined multi-point holographic optical tweezers with fluorescence image analysis, where each tweezers are adjusted axially to bring all of the fluorescence cell nuclei into a single imaging plane.

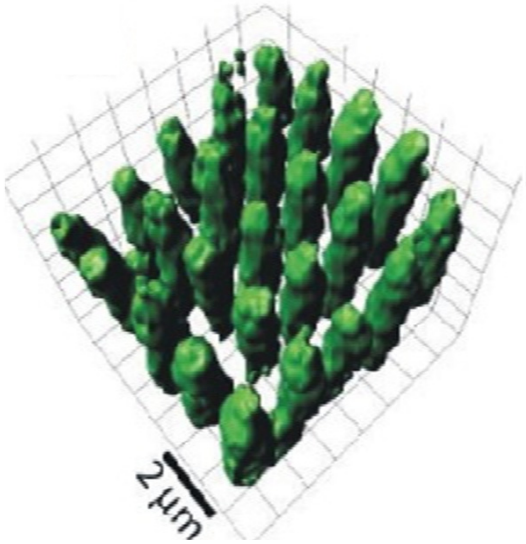

Figure 7.1 - A false-color iso-surface 3D representation image of optically assembled P. aeruginosa with optical traps. Volumetric data obtained from deconvolved confocal images of a 5x5 microarray of P. aeruginosa assembled with a 100X, 1.3NA oil immersion (Zeiss Plan-Apo) objective at λ= 514nm using <2mW per trap, and embedded in hydrogel. The average center-to-center distance is 1.52±0.06μm and average space between each bacterium is 354±134nm.[12]

Akselrod *et al* [12] used a novel combination of both a SLM and an acousto-optic deflector (AOD) to create living cell microarrays in a hydrogel. The AOD produced large arrays in 2D and the SLM was used to generate axial planes. With this arrangement and confocal laser imaging, Akselrod and colleagues [12] created and imaged heterotypic microarrays of living cells using multiple optical traps for exact positioning of hundreds of cells at the same time. Figure 7.1 shows the reconstructed volumetric imaging of large numbers of Pseudomonas aeruginosa bacteria which were trapped and imaged simultaneously. The average center-to-center distance is 1.52±0.06 μm and average space between each bacterium is 354±134 nm

Combining optical tweezers and Raman spectroscopy has also been an active area of research. This is because the optical tweezers can be used to fixed and translate a cell about the spectroscopy probe beam. The spectroscopy technique can show other interesting dynamics in cell studies down to its molecular composition. Ramser *et al* [13] had control over the medium surrounding the cell in their microfluidic chamber that was defined by electron beam lithography that subsequently moulded into rubber silicon. Different buffers flowed through the channels, while the resonance Raman response of an optically trapped red blood cell (RBC) was recorded. The authors were able to monitor the oxygenation cycle of the cell in real time and understand the effects of photo-induced chemistry. This system has prospects for *in vivo* monitoring of cellular drug response [13]. Jess and co-workers [14] were able to combine the dual beam counter-

propagating trap with simultaneous Raman spectroscopy creating a form of Raman flow cytometer. They were also able to take definitive Raman spectra from local parts of the trapped cell. The multivariate analysis obtained from the spectra provided valuable information of the chemical composition of the specific regions in the cell. Optical tweezers have found its niche in the immobilization of cell over a probe or imaging beam [9, 10, 14-17] [9, 10].This form of optical trapping, imaging and detector techniques opens up a new range of imaging and spectroscopy technique where the optical traps are used to fix cell in three dimensions. In this chapter, I shall restrict to the combination of the microscopy imaging with the optical trapping technique.

7.3. Optical tweezers with confocal fluorescence imaging

The confocal laser scanning microscope operates by first scanning a highly focused laser beam using an infinity corrected microscope objective (MO). The focused laser beam excites a given fluorphore at a localized part of the biological object. The emitted fluorescent signals (longer wavelength) is then collected by the same MO by a bandpass filter which rejects the excited wavelength. The emitted light is focused onto the pinhole and then the detector (a photomultiplier tube). The pinhole allows only the in-focus rays to illuminate the photomultiplier tube. The design of confocal laser scanning system (typically termed as the confocal scan head) is often the heart of the system. The scan head is responsible for rasterizing (two dimensional patterns) the excitation laser using a pair of galvanometer-based raster scanning mirror system and a variable pinhole apertures are included to tune to the appropriate confocal parameters. A set of photomultiplier tube detectors is use to detect different fluorescence wavelengths. Current detection system on the confocal microscopy system includes diffraction gratings or prisms coupled with slits positioned near the photomultipliers to enable spectral imaging [18]. It is worthwhile to note that the EMCCD can also be used in confocal microscopy imaging using the spin-disk technology [19] .

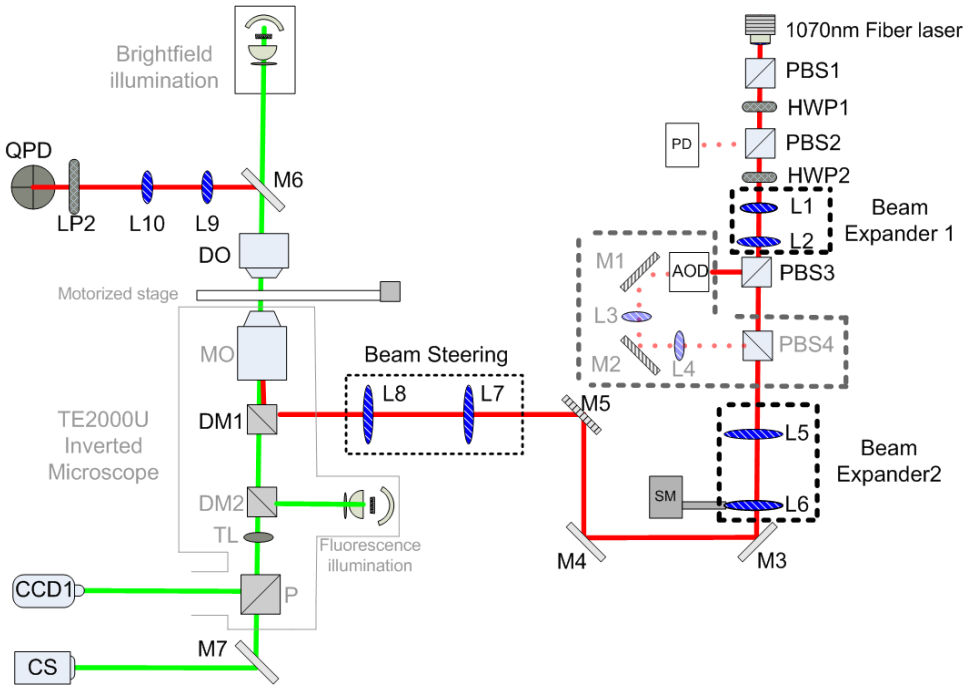

Figure 7.2 - Confocal optical trapping system. The description of the other optical elements of the setup besides the confocal scanning (CS) system is given figure 2.6 and figure 3.19. The confocal laser scanning microscopy system (CS) is mounted on a second imaging port on the microscope system. M7 is a mirror that reflects the fluorescence emitted light into the confocal scanning system.

Figure 7.2 shows the setup of the dual optical tweezers system with the BFP detection scheme and fluorescence confocal laser microscope system. The confocal laser scanning microscopy system (C1Si) is mounted on a second imaging port on the microscope system. A pinhole, just before the detector, filters out the out of focus rays so as to only select the fluorescent signal at the imaging place i.e. high spatial selectivity. The trick to merge the confocal laser scanning imaging technique and optical tweezers is to enable the trapped particles to be positioned about the axial direction. The traps are scanned along the confocal imaging plane (transverse). In the confocal scanning system (CS), there are fiber optic connectors that are links to the laser input (single mode fiber) and to the standard detector units (multimode fiber with GRIN lens). Within the CS unit, there are also an interchangeable scan head dichroic mirrors, and a motorized rotation stage with 3 confocal pinholes (100 µm, 50 µm and 10 µm). The fiber coupled 3 channel standard detector unit contains 3 photon multiplier tubes. The emission filters and dichroic mirrors are mounted in standard filter blocks in the detector unit. Three lasers with wavelengths 405 nm (diode), 488 nm (diode), and 532 nm (He-Ne) are mounted on the laser input unit. Commercial based software (Visual basic) EZ-C1 acquisition and analysis software is used to capture the confocal fluorescence images, perform volumetric rendering and provide time-lapse fluorescence imaging. In

the normal confocal imaging operations, the focusing unit (mounted on the objective) is scanned at 50 nm step size to achieve axial stepping during transverse laser scanning. This stepping of the microscope objective is not used when I combined with the optical traps. Instead, the optical traps are being stepped along the axial direction.

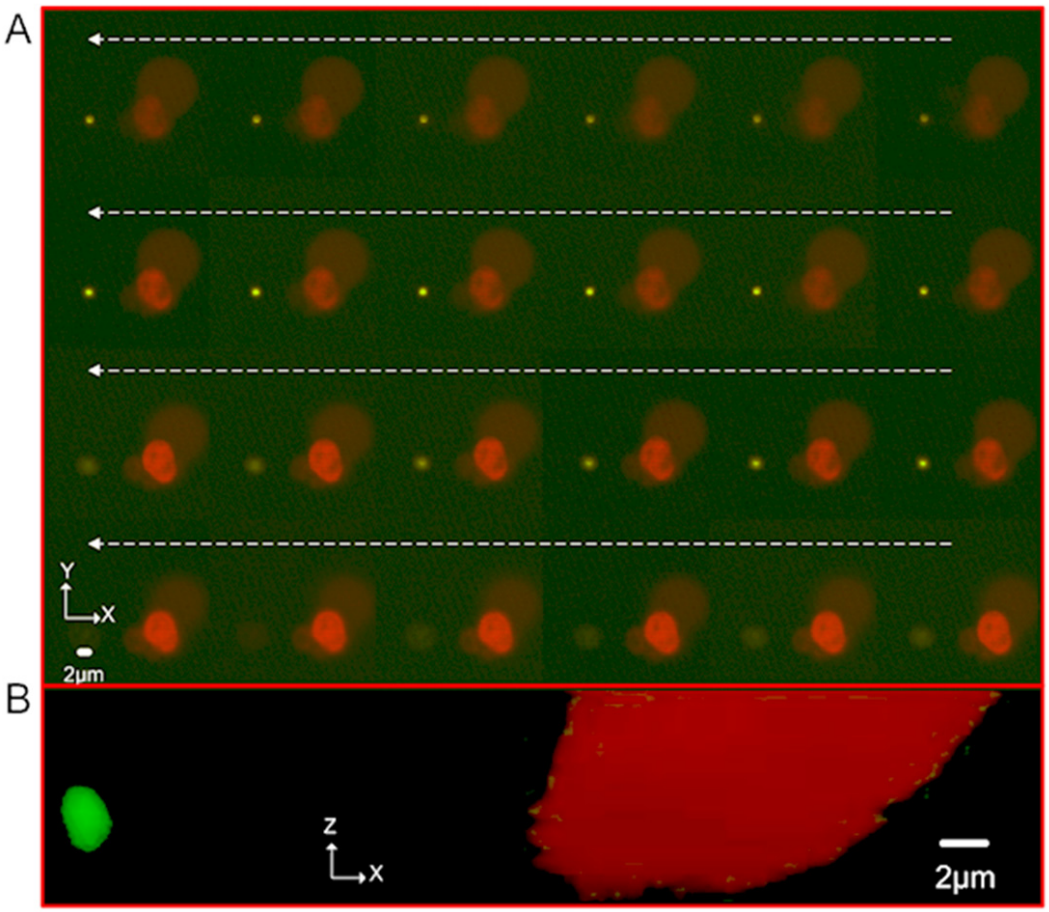

Figure 7.3- Confocal fluorescent images of a single trapped necrotic CHO cell (right) and 2 μm polymer green fluorescent sphere (left). (A) Series of laser induced fluorescence excitation images of optically trapped spheres and cell in a two independent traps. White dotted line indicates the scanning direction. The axial spacing between each interval of 250 ± 75 nm step size. The two particle are separated by around 10μm (B) is the slice of the stacked image from the images from A.

With the optical trapping system, I trapped two objects of interest simultaneously and scan their position along the confocal imaging plane. First of all, I chose to individual trap a single red fluorescent (after propidium iodide staining) Chinese hamster ovary (CHO) cell and a green fluorescent sphere in each tweezers respectively. The two trapped objects are then axially stepping along the confocal scanning plane at 250 ± 75 nm step size. At each axial position, a confocal fluorescent image is collected, as shown in figure 7.3A. By stacking all the images with EZ-C1 and

ImageJ software, I can recreate the three dimensional fluorescent images (with false colour volumetric plots) of the trapped sphere and necrotic CHO cell as shown in a single axial slice of the stack, figure 7.3B. From the slice of the reconstructed image, I can see a physical displacement of the trap sphere with respect to the cell. The difference in the axial position between two optically trapped objects is probably due to the different distribution of the optical forces in each particle. The necrotic CHO cell has a damaged membrane. This means that the surrounding medium has entered into the cell and thus reduced its overall refractive index difference with the medium. This translates to low gradient forces and the cell does not stay in the focus of the beam. In comparison, the microsphere has a much higher refractive index and therefore a stronger gradient force. This pulls the particle closer to the focus of the beam. The disparity in the exact particle position is directly revealed in confocal fluorescence imaging that might have been difficult to achieve otherwise.

The BFP interferometry is ideal to tracking position of trapped spheres and their interactions. Next I track the adhesion of a microsphere onto a bleb portion of a necrotic CHO cell. A bleb is an irregular bulge in the membrane of a cell that can be caused by localized decoupling of the cytoskeleton from the plasma membrane. Large blebs can be formed leading to sudden cell death (necrosis) due to heated gold nanoparticles [20]. This is different from the programming cell death (apoptosis) that is part of the natural cell life cycle.

In our experiment, the propidium iodide is used to stain both DNA and RNA of a dead Chinese hamster ovary (CHO) cell. Propidium iodide is an intercalating agent, non-membrane permeable and a red fluorescent molecule that is often used to test cell viability i.e. necrotic, apoptotic and normal cells [2]. Since RNA is present in the cytoplasm, the fluorescence signal will also be contained within the bleb, as seen in figure 7.4A. The boundaries of the blebbing are clearly highlighted due to the propidium iodide dye (which binds to both DNA and RNA) as shown in figure 7.4A. With brightfield microscopy, the visualisation of the bleb lacks contrast and clarity. Next in figure 7.4B, I illustrate an experiment that measures the position of an optically trapped microsphere as it makes contact to the bleb. By using the QPD, I track an optically trapped sphere as the cell is being moved toward the trapped bead, at a step size of 100 nm. In figure 7.4C, I show the position variance plots of the trapped spheres over time. When the microsphere makes contact with the cell and get adhere to the vesicle from the cell, both the mean position of the trapped particle shifts ($\Delta x \approx 0.1 \mu m$) and a drop in position variance ($\langle x^2 \rangle \approx 7.89$ nm to 2.07 nm) are recorded. The 2 μm sphere green fluorescence is trapped with stiffness of ≈ 60 pN/μm (see inset figure 7.4C) and at a height of around 5 μm above the coverslip. This experiment demonstrates the imaging sensitivity of the fluorescence imaging (bleb formation) using confocal

laser scanning fluorescence imaging system and accuracy of the nanoparticle position tracking with the BFP and QPD.

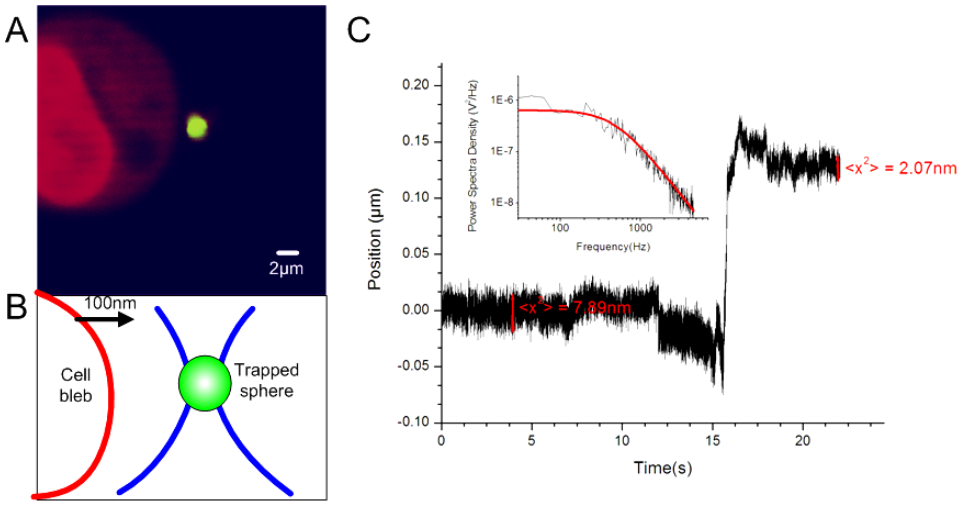

Figure 7.4- Confocal fluorescent imaging and BFP interferometry position tracking (A) Cell with bleb and trapped green sphere, (B) illustrate of the experiment of stepping the cell bleb towards the trapped sphere. (C) shows the X position of the sphere as it touches the bleb perimeter. As the sphere touches the bleb, there is a reaction force that pushed it back slightly before adhesion occurs (sudden drop in the variances of the position of the spheres) ($\Delta\langle x^2\rangle \approx 5.8$ nm)

7.4. Controlled single nanoparticle cell hyperthermia

In-vitro cell hyperthermia techniques have numerous therapeutic purposes especially in the controlled destruction of cancerous cells [21]. Gold nanoparticles have also been frequently used as an optical contrast agent for spectroscopy and fluorescence imaging due to its optical resonance wavelength. Gold nanoparticle, with relatively high absorption co-efficient at a given optical wavelength, can create highly localised thermal bath. However, the current techniques rely on ingested (phagocytosis or endoscytosis) nanoparticles within a cell [21]. Hence conventional biological techniques cannot allow the study of a biological cell when exposed to a single heating source. The combined optical force manipulation and confocal fluorescence imaging is combined to form a biophotonics workstation. This system can be used to the study complex biophysical systems. As a first step, I aim to study localised cell hyperthermia with a heated gold nanoparticle using the instrument, as described in figure 7.2.

In this work, I seek to focus the heat exchange between a single heating point and the consequential functional changes in a healthy CHO cell [20]. Using a single optically trapping metallic nanoparticle, as mentioned in section 6.3, I can controllably expose the cell to a single heat

source at a selected location. This is in stark contrast in other gold nanoparticle mediated cell hyperthermia studies that uses high quantities of gold nanoparticle [20, 22]. Here I take the first step to quantify by controlling the heating exchange between a single optically trapped 100nm (diameter) gold particles and CHO (Chinese hamster ovary) cell. The experiments are carried out with a trapping laser at a wavelength 1070nm. Dramatic heating has been observed in gold nanoparticle trapped with a focused infrared laser beam [23]. The focused light field (power density) [23] can induce a relatively large thermal heating effect [24]. Seol *et al* [24] formalised the increase in temperature (ΔT) of a gold nanoparticle based on its absorbed optical power as follows, $\Delta T(r) = P_{abs} / 4\pi rC$ where P_{abs} is the absorbed power, r is the radius of the sphere and C is the conductivity of the medium. With this formula, they calculated a 266 ^{o}C/W based on a 50 nm (radius) gold nanoparticle with an illuminating near infrared beam (wavelength of 1064 nm, beam waist of 427 nm).

With confocal laser scanning fluorescence imaging, I measure the permeability of the membrane of a cell due to a heated gold nanoparticle using a non-permeable membrane fluorescence marker (propidium iodide). The propidium iodide fluorescence marker is used to provide exact details of any breakage of the membrane and subsequently death of the cell. Propidium iodide is a non-membrane permeable red fluorescent molecule that is often used to test cell viability i.e. necrotic, apoptotic cells. An increase in the fluorescence amplitude from the propidium iodide staining can indicate that the cell membrane permeability is severely compromised and therefore possibly leading to cell death. The BFP interferometry system can assist in the accurate tracking of the gold nanoparticles as it is comes into contact with the membrane of the cell.

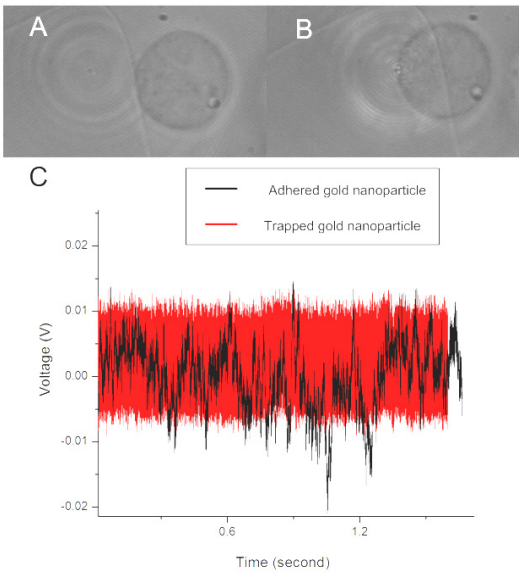

Figure 7.5 – A single trapped gold nanoparticle and contact with cell membrane. A and B I show the bright field imaging of an optically trapped gold is being held close (A) and pressed against to the cell membrane (B) and (C) shows the position trace over time. Red line shows trapped particle in medium (A) and Black line show trapped particle in contact with cell membrane (B). The contact point is judged from the asymmetrical distribution of the particle position. The trap stiffness (force over distance) of the gold nanoparticle is measured to be 6 pN/µm.

In this work, I make use of confluent Chinese hamster ovary (CHO) cells that were trypsinised and re-suspended using fresh medium (Minimum Essential Media (MEM), 10% Fetal Bovine Serum (FCS)+antibiotics). I diluted 20 µl CHO-K1 (~8000 cells) on fresh medium mixed with 20µl of fresh medium and 1.3 µl Propidium Iodide (PI) with a final concentration of 50µM. PI can be excited by the confocal laser (λ=488nm) and after binding to DNA, the fluorescence emission is observed at 617nm. A series of control experiments were performed. The trapping power leads to CHO cell death only with up to 500 mW of optical power and over 1 hour of exposed time (without any trapped nanoparticle). The scanning excitation laser has a wavelength of 488 nm which is off the resonance wavelength of gold (≈ 532 nm). The continuous scanning of excitation laser (at the powers used in the experiment) on a gold nanoparticle adhered on CHO cells did not contribute to any sudden cell death over a course of 2 hours.

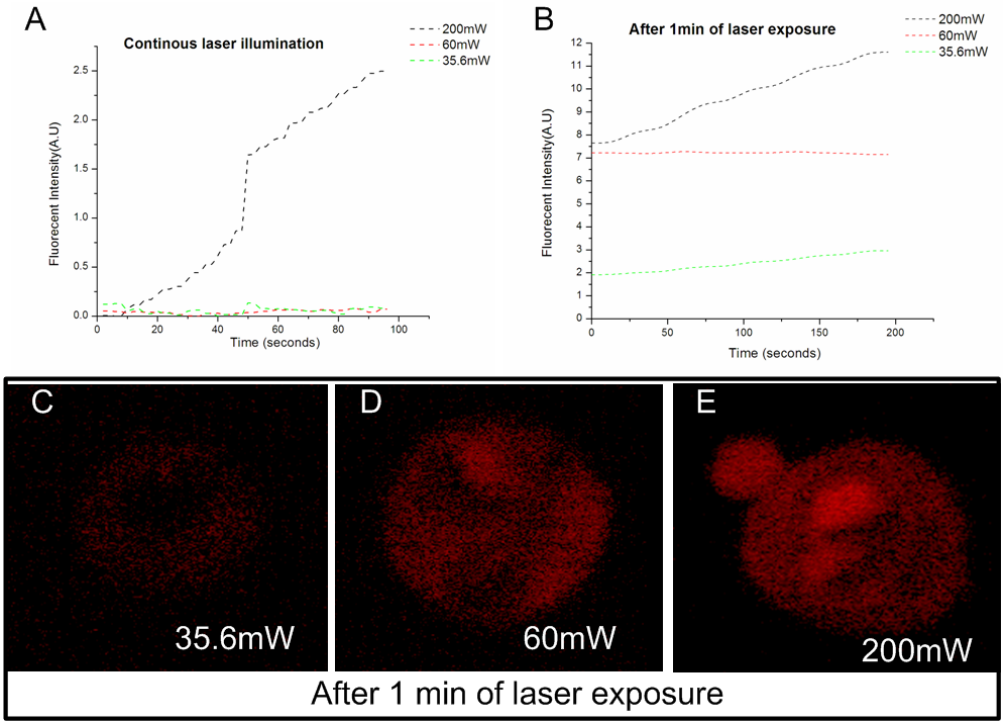

Figure 7.6- Amplitude of fluorescence over time. By simply controlling the exposure time over the gold nanoparticle that is adhered to the surface of the cell, I can directly active cell hyperthermia . (A) shows the fluorescent illumination after 90 seconds of continuous laser exposure. (B) The laser is then switch off and the cell fluorescent is being monitored for a period of over 200 seconds. C –E shows the fluorescent imaging of the cell at 30 seconds after the laser is being exposure for each given power. The time lag between A and B is around 1 min and the fluorescent signal during the lag time is not recorded.

For each fixed power (35.6 mW, 60 mW and 200 mW), I carried out the following experiments: a single 100 nm gold particle is trapped and move onto a selected cell where it is adhered. The selected cell did not exhibit any PI fluorescent signal. The attachment of the nanoparticles to cell membrane is performed by moving the trapped nanoparticle close to the membrane as shown in figure 7.5A and B. Once nanoparticle comes into direct contact and adhere onto the cell membrane (measured with the position signals from the QPD), the confocal imaging starts. The contact point is judged from the asymmetrical distribution of the particle position as shown in figure 7.5C. The delay between the particle contact and confocal imaging is approximately 10 s. The confocal imaging is carried out over a period of 90 s (interval of 5 s), as shown in figure 7.6A. During this time, the trapping laser is still illuminating the nanoparticles. The trapping ***laser is switched off after the initial 90 s illumination***. After which, the confocal imaging continues for another 200 s, shown in figure 7.6B. Figure 7.6C, D and E shows the fluorescent image of the cell at 30 s after the laser is being exposure to the initial 90 s laser illumination of power 35.6 mW, 60 mW and 200 mW respectively. From the temperature increase indicated by

Seol *et al*, [24], I estimate that the absolute temperature of the gold nanoparticle is given as 29^{o}C, , 39^{o}C, and 75^{o}C. The power density illuminating the nanoparticle is given as 130 mW/um^{2}, 210 mW/um^{2}, 714 mW/um^{2} respectively for the trapping power of 35.6mW, 60mW and 200mW and the beam parameters in appendix A.

At optical power of 200 mW, I can see a large bleb formed at the site where the gold nanoparticle is being located (which I attribute to necrosis) during the first 90 s illumination. The CHO cell seems to be undergoing a significant amount of change due to the heated gold nanoparticle at 200mW illumination that is not present in the other two powers. This effect is further supported by figure 7.7. In figure 7.7, I show the time sequence fluorescent images of the CHO cell, that was initially heated to an estimate 75^{o}C (200 mW), over the course of 240 s (at 30 s/frame) where there is no longer any illuminating laser. From series of fluorescence images shown in figure 7.7, the size of the bleb in the cell seems to still undergoing a significant amount of increase, just due to the initial heating. This suggests that the cell membrane is permanently damaged (necrosis) and the rapid growth of the bleb shown especially without any trapping laser illumination indicates a permanent damage of the cell (hyperthermia). This effect of a growing bleb is not present in the other two illuminating powers.

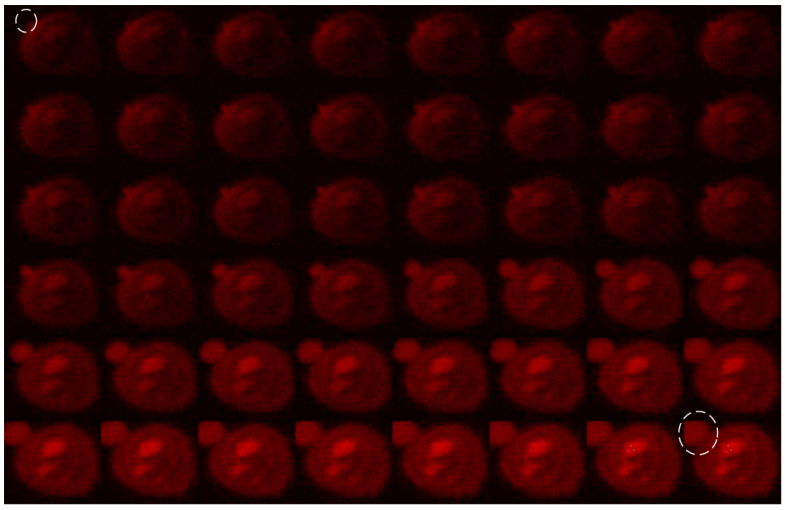

Figure 7.7 – shows the montage of the confocal fluorescent image observed (at 30 s/frame). The initial exposure time is 90seconds of 200mW. The constant expansion of the bleb (white dotted circle) shown the sudden cell death that suggest necrosis.

7.5. Conclusion

This chapter focused mainly on the integration of advance microscopy imaging with optical manipulation into a single apparatus: BFP interferometry and dual optical tweezers system are

integrated with confocal fluorescence to form a one single instrument.

In the first section, I used the calibrated stepper motor (section 3.8) to perform axial positioning of trapped particle for confocal fluorescence imaging. I trapped two fluorescent objects and sequentially moved the optically trapped particles across the scanning plane of the confocal microscope. The collected images were subsequently reconstructed to form a three dimensional fluorescent image of the optically trapped particles. With optical tweezers, it would be immensely useful to the study of the fundamental three dimensional organizations of cells and cell structure with fluorescence microscopy [25]. In the same section, I used the BFP interferometry to track a trapped microsphere as in come into contact with a cell bleb. The cell bleb was formed after I induced direct gold nanoparticle heating on the cell. Using a microsphere, I measured the adhesion contact point of microsphere and cell bleb by monitoring the position variances of the trap. The fluorescence imaging of the cell helped in the identification of the region where the cell bleb was located, which was hardly visible in bright field imaging.

In the second section, I performed selective cell hyperthermia with optically trapped gold nanoparticles. Using the back focal plane interference, I accurately tracked the gold nanoparticle as it came into contact with the surface of a given cell. By using confocal fluorescence imaging, I tracked the uptake of propidium iodide (non-membrane permeable) over time. The uptake of the propidium iodide indicated the permeability of the cell membrane (lipid bilayer) when exposed to a heated gold nanoparticle. From the results, the CHO cell was seen to undergo severe necrosis (growing size of bleb and increasing fluorescent amplitude signal) when the heated gold nanoparticles reach ≈ 70 ^{o}C. At optical power of 200 mW, I observed a large bleb formed at the site where the gold nanoparticle is being located during the first 90 s laser illumination. From series of fluorescence images shown in figure 7.7, the size of the bleb in the cell seemed to have undergone a significant amount of increase (size and fluorescent signal) for the next 240 s just due to the initial heating. At lower temperature of 29 ^{o}C and 39 ^{o}C, the cell bleb form formed in the initial 90 s of laser illumination does not grow in size and contains a fixed fluorescent level over the next 240 s. The results from the localised heating might indicate that the thermal heat required in reaching sudden cell death (necrosis) is at 70 ^{o}C. However, more experiments are needed to be made using other forms of fluorescence dye to track the membrane changes. Hence, I propose the use of a different (GFP) fluorescence dye [26, 27]. This can possibly elucidate the dynamics of the membrane of the cell during the heating process. In this chapter, I have designed and performed the experiments. The cell samples are prepared by Miss Leilani Torres.

7.6. References

1. G. Pontecorvo, "The Leeuwenhoek Lecture: Microbial Genetics: Retrospect and Prospect," Proceedings of the Royal Society of London. Series B, Biological Sciences (1934-1990) **158**, 1-23 (1963).
2. F. Zernike, "How I Discovered Phase Contrast," Science **121**, 345-349 (1955).
3. K. Visscher, and G. J. Brakenhoff, "Single beam optical trapping integrated in a confocal microscope for biological applications," Cytometry **12**, 486-491 (1991).
4. A. Hoffmann, G. Meyer zu Hörste, G. Pilarczyk, S. Monajembashi, V. Uhl, and K. O. Greulich, "Optical tweezers for confocal microscopy," Applied Physics B: Lasers and Optics **71**, 747-753 (2000).
5. D. L. J. Vossen, A. van der Horst, M. Dogterom, and A. van Blaaderen, "Optical tweezers and confocal microscopy for simultaneous three-dimensional manipulation and imaging in concentrated colloidal dispersions," Review of Scientific Instruments **75**, 2960-2970 (2004).
6. R. R. Brau, P. B. Tarsa, J. M. Ferrer, P. Lee, and M. J. Lang, "Interlaced optical force-fluorescence measurements for single molecule biophysics," Biophysical Journal **91**, 1069-1077 (2006).
7. T. T. Perkins, "Optical traps for single molecule biophysics: a primer," Laser & Photonics Reviews **3**, 203-220 (2009).
8. M. J. Lang, P. M. Fordyce, A. M. Engh, K. C. Neuman, and S. M. Block, "Simultaneous, coincident optical trapping and single-molecule fluorescence," Nature Methods **1**, 133-139 (2004).
9. M. Goksör, J. Enger, and D. Hanstorp, "Optical Manipulation in Combination with Multiphoton Microscopy for Single-Cell Studies," Appl. Opt. **43**, 4831-4837 (2004).
10. A. Hoffmann, G. M. Z. Horste, G. Pilarczyk, S. Monajembashi, V. Uhl, and K. O. Greulich, "Optical tweezers for confocal microscopy," Applied Physics B-Lasers and Optics **71**, 747-753 (2000).
11. E. O. Eriksson, D. Engström, J. Scrimgeour, and M. Goksör, "Automated focusing of nuclei for timelapse experiments on single cells usingholographic optical tweezers," Opt. Express **17**, 5585-5594 (2009).
12. G. M. Akselrod, W. Timp, U. Mirsaidov, Q. Zhao, C. Li, R. Timp, K. Timp, P. Matsudaira, and G. Timp, "Laser-guided assembly of heterotypic three-dimensional living cell microarrays," Biophysical Journal **91**, 3465-3473 (2006).
13. K. Ramser, J. Enger, M. Goksor, D. Hanstorp, K. Logg, and M. Kall, "A microfluidic system enabling Raman measurements of the oxygenation cycle in single optically trapped red blood cells," Lab on a Chip **5**, 431-436 (2005).
14. P. R. T. Jess, V. Garces-Chavez, D. Smith, M. Mazilu, L. Paterson, A. Riches, C. S. Herrington, W. Sibbett, and K. Dholakia, "Dual beam fibre trap for Raman microspectroscopy of single cells," Optics Express **14**, 5779-5791 (2006).
15. E. O. Eriksson, D. Engström, J. Scrimgeour, and M. Goksör, "Automated focusing of nuclei for timelapse experiments on single cells using holographic optical tweezers," Opt. Express **17**, 5585-5594 (2009).
16. C. G. Xie, M. A. Dinno, and Y. Q. Li, "Near-infrared Raman spectroscopy of single optically trapped biological cells," Optics Letters **27**, 249-251 (2002).
17. C. M. Creely, G. P. Singh, and D. Petrov, "Dual wavelength optical tweezers for confocal Raman spectroscopy," Optics Communications **245**, 465-470 (2005).
18. J. B. Pawley, "Fundamental and Practical limtis in Confocal Light-Microscopy," Scanning **13**, 184-198 (1991).
19. D. R. Sisan, R. Arevalo, C. Graves, R. McAllister, and J. S. Urbach, "Spatially resolved fluorescence correlation spectroscopy using a spinning disk confocal microscope," Biophysical Journal **91**, 4241-4252 (2006).
20. G. S. Terentyuk, G. N. Maslyakova, L. V. Suleymanova, N. G. Khlebtsov, B. N. Khlebtsov, G. G. Akchurin, I. L. Maksimova, and V. V. Tuchin, "Laser-induced tissue hyperthermia mediated by gold nanoparticles: toward cancer phototherapy," Journal of Biomedical Optics **14**, 021016-021019 (2009).
21. X. Huang, P. Jain, I. El-Sayed, and M. El-Sayed, "Plasmonic photothermal therapy (PPTT) using gold nanoparticles," Lasers in Medical Science **23**, 217-228 (2008).
22. R. K. Visaria, R. J. Griffin, B. W. Williams, E. S. Ebbini, G. F. Paciotti, C. W. Song, and J. C. Bischof, "Enhancement of tumor thermal therapy using gold nanoparticle-assisted tumor necrosis factor-alpha delivery," Molecular Cancer Therapeutics **5**, 1014-1020 (2006).
23. Y. Seol, A. E. Carpenter, and T. T. Perkins, "Gold nanoparticles: enhanced optical trapping and sensitivity coupled with significant heating," Optics Letters **31**, 2429-2431 (2006).

24. Y. Seol, A. E. Carpenter, and T. T. Perkins, "Gold nanoparticles: enhanced optical trapping and sensitivity coupled with significant heating," Opt. Lett. **31**, 2429-2431 (2006).
25. U. Mirsaidov, J. Scrimgeour, W. Timp, K. Beck, M. Mir, P. Matsudaira, and G. Timp, "Live cell lithography: Using optical tweezers to create synthetic tissue," Lab on a Chip **8**, 2174-2181 (2008).
26. J. A. Theriot, and T. J. Mitchison, "Comparison of actin and cell surface dynamics in motile fibroblasts," J Cell Biol **119**, 367 - 377 (1992).
27. S. Felder, and E. L. Elson, "Mechanics of fibroblast locomotion: quantitative analysis of forces and motions at the leading lamellas of fibroblasts," J Cell Biol **111**, 2513 - 2526 (1990).

Chapter 8 –

Nonlinear response with nanosuspension

8. Nonlinear response with nanosuspension

8.1. Overview

In chapter.6, I discussed the optical trapping of single nanoparticles with a focused Gaussian beam. In the same chapter, I have used the trapping technique to assembly nanotubes into a designed pattern onto a substrate. The ability to assembly nanostructures from individual nanoparticles would form an important platform for nanophotonics. Each dielectric nanoparticle possesses a discrete refractive index. With the increasing number of the nanoparticles entering into the optical field due to optical gradient force, the local particle density would increase and subsequently change the local refractive-index along the beam propagation axis. The formation of the chain of nanoparticles could act as a self-assembling waveguide. This localized refractive index change that is intensity dependent change can be characterized as a nonlinear response: photorefractivity.

In this chapter, I report the experimental and theoretical progress towards elucidating the nonlinear optical response of nanosuspensions. By nanosuspension, I mean the nanoparticles suspended in an aqueous medium. The chapter is split into four sections. In the first section, I introduce the past experiment and theoretical efforts meant to determine the nonlinear nature of the self organising nanoparticles. In the second section, I provide a brief explanation of the non-ideal gas approach at modelling the nanosuspensions. The new theoretical approach allows the inclusion of compressibility (packing of nanoparticles) in the medium.

In the third section, I describe a newly devised a fiber-optic method that can accurately measure the nonlinearity of liquid nanosuspensions. The beam from the output of the first fiber propagates across the nanosuspension to the second fiber where the power collected is measured as a function of the input power. This arrangement is a fiber-optic analogue of the classic Z-scan method [1] that is well adapted to measurements in aqueous solutions. The fiber-based scheme provides an ideal platform for the measurements within an aqueous medium. Here, a diverging beam from a single mode fiber is use to confine the nanoparticles instead of a focussed laser beam as shown before in chapter.6. Finally in the last section of the chapter, I compare my experimental results with the results generated from the proposed non-ideal gas model. From the experimental results and the current numerical model, the virial coefficients (particle-particle interaction) in the nanosuspension can be properly accounted for. The model yields an effective or renormalized Kerr effect that is an improvement from the previous theoretical model, exponential Kerr, which does not account for particle-particle interactions. It is important to note that the beam emerging from a

single mode fiber is a very close approximation to the ideal Gaussian beam. For convenience, I shall term the output mode of the single mode fiber as a Gaussian beam.

8.2. Introduction

The colloidal nanosuspension can be treated as a form of nonlinear medium. The use of optical forces to initiate nonlinear responses in nanoparticle suspension (nanosuspension) using a continuous-wave (cw) laser beam was first explored by Ashkin and co-workers [2-5]. They demonstrated that nonlinear effects (self-focusing, photorefractivity and filamentation) using aqueous suspensions of nanoparticles. Furthermore, Ashkin and co-workers were able to demonstrate some interesting nonlinear characteristics of nanosuspension and sodium vapor such as optical bistability [6] , self guiding [5] and four wave mixing [4]. These experimental demonstrations showed that the optical forces are a strong contributing factor in inducing a strong nonlinear response from colloidal nanosuspensions at relatively low average power (~1-2W). Through the observation of the Rayleigh scattering from the nanoparticles, Ashkin and others [2, 7, 8] have interpreted the nanosuspension as an artificial Kerr medium.

In the presence of an optical field, the nanoparticles experience an electrostrictive volume force (optical gradient forces) that attracts them into the spatial regions of high intensity, thereby increasing the local density and subsequently the local refractive-index. To the lowest order, this leads to the modelling of colloidal suspensions as an artificial Kerr media in which the induced change in refractive-index, n, is proportional to the applied light intensity I, $\Delta n = n_{2K} I$, with $n_{2k}>0$ the Kerr coefficient. However, just considering the dominant optical forces would result in a lead to an exponential variation of index change with intensity ($\Delta n = n_{2K} \exp((\alpha / 4k_B T) I)$), where α is the polarisability of the particle, k_B is Boltzmann constant and T is temperature of the medium.

In response to this conflicting issue (pure exponential or Kerr), a number of theoretical efforts have been drawn to the understanding of the behaviour of the nonlinear response from such Kerr mediums. The seminal work of Smith et. al [3, 4] mentioned the exponential model but they only considered the dominant Kerr nonlinearity. Recently, both El-Ganainy *et al* [9] and Gordon *et al* [10] have suggested that the full exponential model should be employed to investigate the nonlinear responses in a colloidal suspension at low colloidal densities. However, including the full exponential model renders the nonlinear responses highly unstable. This is in apparent contradiction with recent experimental observations of relatively stable one dimensional Kerr medium with evascent fields [11] that seem to agree reasonably with the Kerr model. Matuszewski *et. al* [12] have shown that by treating the nanosuspension as a hard sphere gas, it is possible to include the

compressibility of the system. This would in turn result in saturating the exponential nonlinearity at high intensities and at exceedingly particle densities, taking in consideration the particle-particle interaction.

8.3. Theoretical understanding

The theoretical model has been developed by Mr R. El-Ganainy, Professor D. N. Christodoulides and Professor Ewan M Wright. I aim to compare and analysis the nonlinear dynamics of the nanosuspensions with their model against my experimental results

R. El-Ganainy *et al* [9] proposed the theory where the optical gradient forces dominates the system and acts to pull particles towards the highest intensity of the input beam. In the initial steady state conditions, the particle drift is zero: meaning that the particles that are moving into the beam equivalent to the particles diffusing out. The size of the nanoparticles used in this work needs to be much smaller than the wavelength of the laser. For general notation, the colloidal nanosuspension is assumed to be at temperature T that composed of a host liquid of refractive-index n_b and nanoparticles of refractive index is given as n_p with a radius of a and volume $V_p = 4\pi a^3 / 3$, ε_0 is the free space permittivity, α is the polarisability of the particle and the dimensionless parameter $m = n_p / n_b$ which accounts for the relative-index.

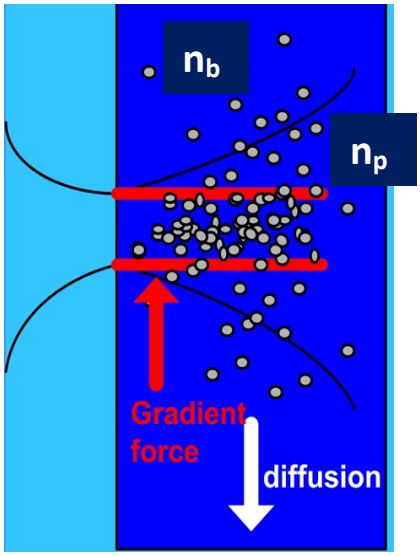

Figure 8.1.- shows a schematic illustration of the system. A suspension of nanoparticles (gray circles) with refractive index n_p that are suspended in an aqueous solution of refractive index n_h ($n_p > n_h$). Upon reaching the critical power, the gradient force (red arrow) acts to draw the diffusing nanoparticles (white arrow) into the highest intensity of the beam axis.

When a beam is introduced into the sample, as shown in figure 8.1, the volume filling factor

of the particles within the beam, given by $f(I)$ is related the intensity of the beam I by an exponential term given by

$$f(I) = f_o \exp\left(\left(\alpha / 4k_B T\right) I\right) \tag{8.1}$$

where k_B is Boltzmann constant and $\alpha = 3V_p \varepsilon_0 n_b^2 \left(m^2 - 1/m^2 + 2\right)$.

The initial filling factor is given as $f_o = \mathrm{V_p}\rho_0$, where $\mathrm{V_p}$ is the volume of the sphere (cm^3) and ρ_0 is the density of the particles (particles/cm^3) at zero intensity. Hence equation (8.1) can be rewritten as equation (8.2) by considering the refractive index difference between the nanoparticle and medium,

$$\Delta n(I) = (n_p - n_b) V_p \rho_0 e^{\frac{I}{I_c}} \approx n_{2K}(I_c + I) \tag{8.2}$$

where $I_c = \alpha / 4k_B T$ and $n_{2K} = (n_p - n_b) V_p \rho_0 / I_c$.

The two main nonlinearities that are of interest: the exponential nonlinearity and artificial Kerr medium, each corresponds to $\exp(I / I_c)$ and $(I_c + I)$ (first order approximation of the exponential term) from equation 8.2. In a recent work, El-Ganainy *et al* [13] treated the colloidal suspension as a non-ideal "Van der Waals" gas to allow for compressibility of the colloidal suspension. The detailed theoretical work can be found in the paper [13] . Here, I will only briefly discuss the key equations necessary at deriving the new nonlinear coefficient. In the equation 8.3, El-Ganainy *et al* [13] included the virial coefficient into I_c in equation 8.2,

$$\frac{\alpha I}{4k_B T} = \ln(r) + 2\left(\frac{B_2}{V_p}\right) f_0 \left(r - 1\right) + \frac{3}{2}\left(\frac{B_3}{V_p^2}\right) f_0^2 \left(r^2 - 1\right) \tag{8.3}$$

Here p is the pressure of this gas, k_B is the Boltzmann constant, ρ is the particle density and B_2, B_3 are the second and third virial coefficients respectively. The factor r=f/f_0 is the ratio of the volume filling factor of particles f to the field-free background value $f_0=V_p\rho_0$, so that r=1 for zero optical intensity. Here the dominant effect of the second virial coefficient is considered for the expansion. Starting from the the second virial coefficient given by $B_2(T) = -2\pi \int_0^\infty (e^{-U(r)/k_B T} - 1) r^2 dr$ [14], equation (8.2) can be rewritten as equation (8.4)[13]

$$\begin{aligned} \Delta n(I) &= (n_p - n_b) V_p \rho_0 \left(1 + r' I + ...\right) \\ &= \Delta n(0) + n_2 I + ... \ , \end{aligned} \tag{8.4}$$

where $r' = (dr / dI)|_{I=0}$, From equation 8.3 and 8.4, the second order nonlinearity is given in equation 8.5

$$n_2 = \left(\frac{n_{2K}}{1 + 2(B_2 / V_p) f_0 + 3(B_3 / V_p^2) f_0^2} \right) \tag{8.5}$$

These formulae reveal that including the virial coefficients softens the effective Kerr nonlinear optical response with respect to the exponential model since $n_2 < n_{2K}$. The relative role of the exponential nonlinearity depends on the magnitude of the first virial coefficients B_2 and B_3 is seen in equation 8.5 In the simulation, B_3 kept at 0.

For the numerical beam propagation, the recently developed theory of El-Ganainy *et al.* [9] for field propagation in a colloidal suspension is used. In particular, consider propagation of a linearly polarised field of frequency ω and free-space wave vector $k_0=\omega/c=2\pi/\lambda 0$ along the z-axis in a colloidal suspension. The electric field envelope is denoted as $\varphi(x, y, z)$ in such a way that $|\varphi|^2$ is the field intensity. Then the paraxial wave equation governing field propagation may be written as

$$\frac{\partial \varphi}{\partial z} = \frac{i}{2k_0 n_b} \left(\frac{\partial^2}{\partial x^2} + \frac{\partial^2}{\partial y^2} \right) \varphi + \alpha_0 \left(i\beta - \frac{1}{2} \right) r\varphi \ , \tag{8.6}$$

where $\alpha_0 = \sigma \rho_0$ is the linear (intensity) absorption coefficient accounting for low power Rayleigh scattering losses, ρ_0 being the equilibrium colloidal density in the absence of any illumination and

$$\sigma = \frac{128\pi^5 a^2 n_b^4}{3} \left(\frac{a}{\lambda_0} \right)^4 \left(\frac{m^2 - 1}{m^2 + 2} \right)^2 \ , \tag{8.7}$$

is the Rayleigh scattering cross section, and $\beta = k_0 (n_p - n_b) V_p / \sigma$ is a dimensionless constant that reflects the strength of the self-focusing nonlinearity to the nonlinear Rayleigh scattering losses. ***Equations 8.4 and 8.5 are incorporated into equation 8.6 through β .*** The intensity loss coefficient due to Rayleigh scattering is $\alpha_R = \alpha_0 r$ and r = f/fo which is the ratio of the filling factor. For comparison with the experiment that is described later, the parameters used are listed as follows: $\lambda = 1.09\,\mu m, n_p = 1.57, n_b = 1.33, \rho_0 = 1.9 \times 10^{13}\, cm^{-3}, a = 50\, nm, \mathrm{f}_0 = 0.01$ and $\mathrm{D} = 110\ \mu\mathrm{m}$. At this wavelength, the nanoparticles introduces very small amount of Rayleigh scattering losses. This have verified in both numerical simulations and in experiments. The measured scattering loss is $3.91\mathrm{cm}^{-1}$. Note that this much lower than the previously reported scattering loss, $15\mathrm{cm}^{-1}$, using a wavelength of 532nm on 100nm diameter nanoparticles [2, 7, 8].

Our probing of the nonlinear optical response of colloidal suspensions is based on two oppositely directed and aligned single-mode optical fibers (identical mode field diameter and core) that are inserted into the nanoparticle suspended in aqueous solution in a fine capillary tube, as shown in figure 8.2. The fibers are well separated by a distance D, shown in the inset of figure 8.2.

The input fiber to the left serves to launch a beam having the well defined beam profile of the single-mode fiber and the collecting fiber to the right is use to measure the power coupled into the same single-mode beam profile after propagating the distance D. In our experiments, the fiber mode profile was well characterized by a Gaussian field of spot size w_0, and the distance D was typically a few times the Rayleigh range of the initial Gaussian beam.

Our experimental scheme is reminiscent of the classic Z-scan method for measuring Kerr nonlinearities with the collecting fiber playing the role of the aperture in the Z-scan method [1, 15]. In our case, however, it is the input power that is scanned. Next equation (8.5) is employed for the beam propagation between the input and collecting fibers along with the initial Gaussian field representing the field launched by the input fiber at z=0

$$\varphi(x,y,0)=\sqrt{\frac{2P_{in}}{\pi w_0^2}}e^{-(x^2+y^2)/w_0^2} \quad , \tag{8.8}$$

with input spot size w_0 and input power P_{in}. Once the propagated field $\varphi(x,y,D)$ is calculated and the power at the collecting fiber is calculated via the integral as shown in equation (8.6),

$$P_{coll}=\left|\sqrt{\frac{2}{\pi w_0^2}}\int dxdye^{-(x^2+y^2)/w_0^2}\varphi(x,y,D)\right|^2 \quad , \tag{8.9}$$

which is the modulus squared of the propagated field projected onto the collecting fiber mode. For comparison with the experiment, a spot size w_0=3.4 μm is used.

8.4. Experimental approach with single mode fiber

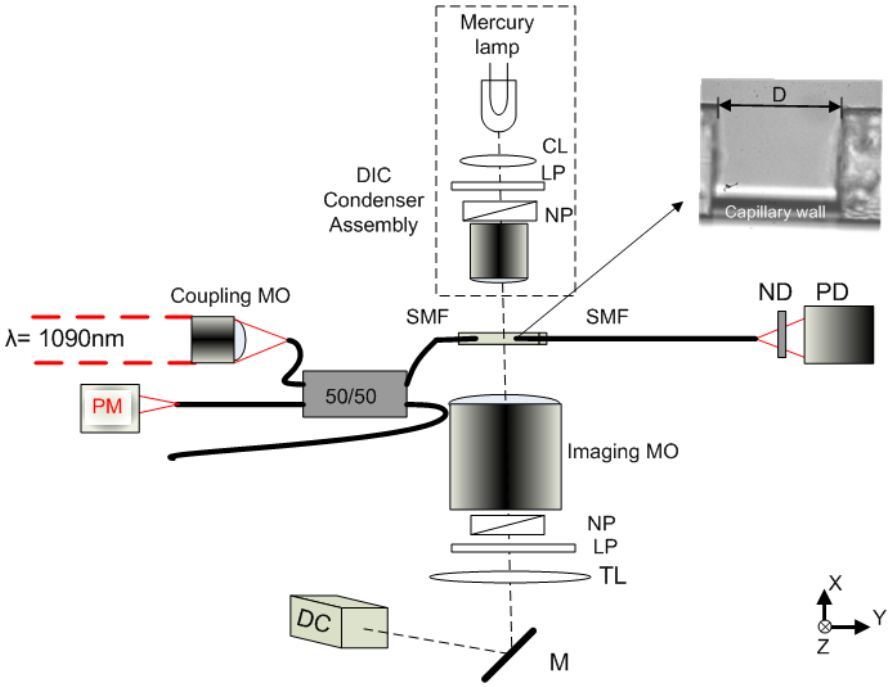

Figure 8.2 shows the experimental setup. Two oppositely directed and aligned identical single-mode optical fibers (SMF) that are inserted into the colloidal suspension and separated by a distance D, shown in the inset. The input fiber to the left launches a well defined Gaussian beam (wavelength, λ=1090nm, spot size w_0=3.4 μm) at variable input power (monitored through the 50/50 fiber splitter and Power meter (PM)) directly into the colloidal suspension, and the collecting fiber to the right is used to measure the power coupled into the same single-mode beam profile after propagating the distance D using a photodetector (PD). An orthogonal differential interference contrast (DIC) imaging is used to detect subtle phase variations (from the accumulated nanoparticles) within the sample with a digital camera (DC).

In the experimental setup shown in figure 8.2, a linearly polarised laser (10 W, 1090 nm, SPI laser) is coupled into a 50/50 fiber splitter (FC1064-50-FC- 2x2 SM Coupler) using a three positioning fiber coupling stage (MDE122, Elliot scientific) with a microscope objective and coupling objective (10X, 0.25NA, Comar). The beam profile of the single-mode fiber is well characterized as a Gaussian with spot size w0=3.4 μm at the wavelength λ=1.09 μm. One end of the fiber splitter is directed onto a power meter, PM (Melles Griot) to monitor the power fluctuations in the laser and fiber coupling stage (< 2%). The other end of the splitter is coupled, via FC connector, into a single ended cleaved SMF (1060XP, Thorlabs, mode field diameter to 6.8 μm). The cleaved end of the fiber is then inserted into a capillary of inner diameter of 200 μm (Invitrocom) as shown in the inset. The sample is mounted onto an X-Y translations stage (H117, Prior Scientific) within an inverted microscope platform (TE2000E, Nikon). A microscope objective (imaging MO) (20X,

NA DIC 0.50 NA, Nikon) is used to image the sample onto a high speed digital camera (DC) (A622f Basler) via a tube lens (TL). A condenser assembly to support differential interference contrast (DIC) illumination is used (LP – linear polariser, NP – Nomarski prism). The same polarisation optics is placed in the imaging path so as to pick up the small phase difference within the sample. The DIC illumination technique has previously been used to visualize single nanoparticles [16].

The cleaved end of a second identical SMF (1060XP, Thorlabs, mode field diameter) is inserted into the other end of the capillary and brought to a known distance away from the input face of fiber. Once the two fibers are aligned, the whole chamber is subsequently sealed with epoxy to reduce fluctuations. The output of the second fiber illuminates PD (PDA10CS-EC, Thorlabs), which in turn measures the coupled power. A set of calibrated neutral density filter (ND) is used so as to prevent over exposure onto the PD. A custom Labview program is used to remotely control the input power and capture the coupled power at the PD using a data acquisition device (National instruments NI USB-6009). The nanoparticles used here are polystyrene plain spheres of diameter $2a = 0.099\mu m$ (10% coefficient of variation), a being the radius (PS02N/6391, Bangs Lab). The spheres are treated with sulfate groups: 0.1% SDS (sodium dodecyl sulfate) and 0.05% sodium azide anti-microbial agent. The initial concentration is 1.921 X 10^{14} particles/cm^3. For each dilution step, heavy water (D20) is used as the diluting agent so as to reduce thermal convection flow. For the coupling power measurements, I prepared two samples with colloidal densities of $\rho 0 = 1.921 \times 10^{13}$, 1.921×10^{12} particles/cm3. The collecting fiber is placed at a distance D=110±10 μm away from the input fiber. For each run, a total of 200 data points are taken and averaged over a 1 second acquisition time. At lower input powers (< 400 mW), the collected power varies linearly with the input power (the difference in the power plots is due to minor misalignment in z). The nanosuspension is loaded into the capillary by capillary forces while the fibers are inserted thereafter. The key advantage of this setup is to gain direct access to the nonlinear suspension within the aqueous medium. In addition, this approach eliminates any spherical aberration due to beam propagation through the glass and water interfaces present for cuvette-type geometries, and by using thinner chambers in contrast to more standard rectangular cuvette, convection roles may be suppressed. Due to the thin capillary walls, I can observe the alignment of the nanoparticles under DIC illumination for the concentration of 1.921×10^{13} particles/cm^3. In figure 8.3, I show two brightfield images for input powers of 0 W and 0.514 W. When the input is at 0.514 W, I can see a

fine track in the refractive index from the DIC illumination upon the sample, this corresponding to the formation a fine channel of increased nanoparticle density.

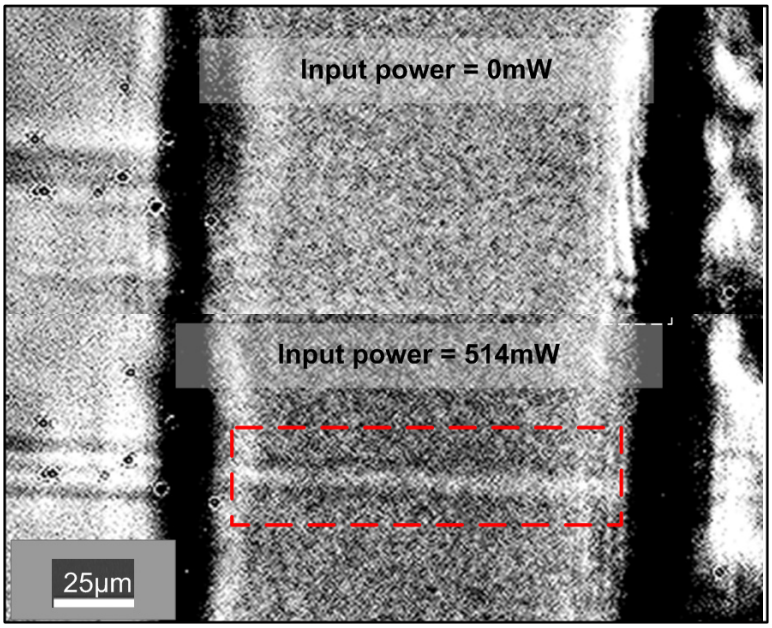

Figure 8.3. DIC images of the two countering single fiber aligned (input fiber on the left and collecting fiber on the right) in the nanosuspension. The top image indicates no accumulation of nanoparticles when input power is at 0 mW. The bottom image indicates a fine channel of accumulating nanoparticles (highlighted by the red box) when the input power is at 514 mW.

8.5. Comparing theory and experiment

Figure 8.4A shows the experimental results for the power measured at the collecting fiber (P_{coll}) versus input power (P_{in}) for the two concentrations above. For the lower density (dash-dot line) the input power remains well below the critical power (0.5 W) and the collected power scales linearly with the input power. For the higher density (solid line) I see that that the collected power scales linearly for lower input powers, rises above the low concentration linear plot for higher powers, and finally there is a peak in the plot of P_{coll} versus P_{in} akin to that discussed above for the case of a Kerr medium, the rollover occurring at $P_{in} \approx 0.5$ W.

The reasoning behind this change is that for input powers much less than the critical power, the power at the collecting fiber P_{coll} will be a fixed fraction less than unity of the input power. This fraction is determined by the linear beam spreading and wavefront curvature that accumulate over the distance D. However, as the input power is increased towards the critical power, the input beam waist start to maintain its input beam waist (towards non-diffraction), and the fraction of power at

the collecting fiber will increase with input power. For the special case that the input power equals the critical power for self-trapping the input beam should propagate with unchanging beam profile between the fibers leading to, in principle, perfect power coupling. Increasing in the input power beyond the critical power leads to further contraction of the propagating beam spot size between the fibers so that the fraction of power coupled into the collecting fiber should therefore decrease with increasing input power. Thus, for a Kerr medium the critical power for self-focusing can be estimated experimentally by looking for a peak or rollover in the plot of the measured power P_{coll} at the collecting fiber versus input power P_{in}.

One general finding from the numerical study of our experiment is that beam propagation method simulations on the exponential nonlinearity do not resemble the obtained experimental results. No amount of fine tuning of parameters can make it to resemble the experimental results in figure 8.4A. The reason is very simple, namely, since the exponential nonlinearity includes arbitrarily high orders of self-focusing nonlinearity, once self-focusing collapse starts, it is immediately super-critical [17], leaving no room for the relatively smooth rollover seen in figure 8.4A. Rather, using the exponential nonlinearity the plot of the power measured by the collecting fiber versus the input power is initially linear with input power. Then it increases very sharply with increasing input power, and finally drops abruptly to zero above a given power. (This plot is not included since it was virtually impossible to maintain numerical accuracy once the collapse initiated). Hence, it is concluded that the pure exponential model is therefore not a good representation of the nonlinear optical response of our experiment. Next, I consider the numerical results treating the colloidal suspension as an artificial Kerr medium for which the exponential nonlinearity is truncated to the first nonlinear term shown in equation 8.2. For the sample filling factor of 0.099, the BPM shows a critical power of $P_{roll\ over} = P_{in} = 0.53$W, figure 8.4B, that is within reasonable agreement (3%) with the experimentally obtained result of 0.51W, as shown in figure 8.4.

In addition, by including the non-ideal gas model, the same beam propagation mode provide includes the varying values of the second virial coefficient (B_2/Vp) (equation 8.4 and 8.5). For this study, B_3 is set to 0. This will in turn provide the numerical solution as follows as: $P_{rollover}$ = 0.4,0.51,0.62 W for (B_2/Vp)=15,25,35, respectively. Using the roll over point, I can directly infer on the second order virial coefficient. Here, the value of $P_{rollover}$ =0.51 W, I obtained a coefficient of (B_2/Vp)=25. From the values of the coefficient, I can then calculate the nonlinear coefficients n_2

which give the nonlinear coefficients n_2=1.7x10^{-9} cm^2/W, n_{2K}= 4.2x10^{-16} cm^4/W^2. This value for n_2 is in reasonable agreement with an independent value n_2=2.0x10^{-9} cm^2/W obtained with a separate Z-scan method [1].

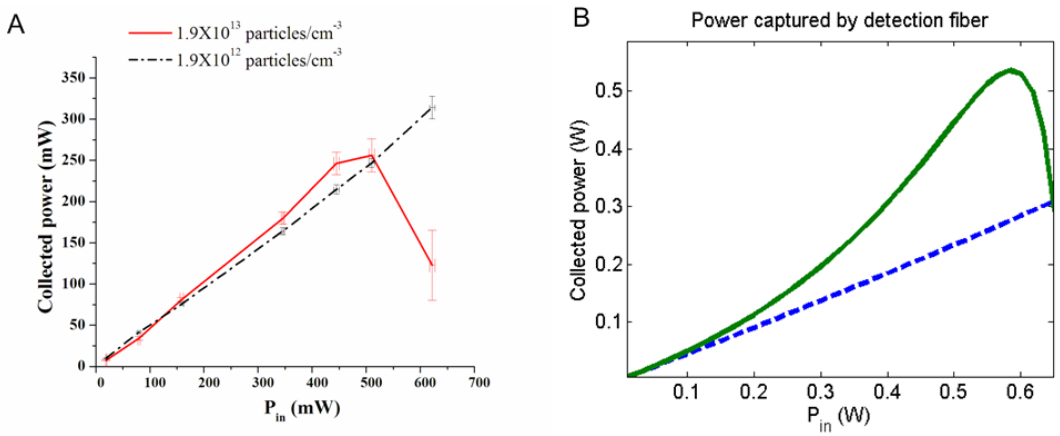

Figure 8.4(A) experimental and (B) numerical plot of power measured at collecting fiber with a photodetector versus the input power for the two concentrations: 1.921x10^{13}, 1.921x10^{12} particles/cm^3 (solid and dash line respectively)

8.6. Conclusion

There was a fundamental rift between theory and experiment regarding the nature of the nonlinearity of such nanosuspensions [11]. In particular, carried to its logical conclusion the electrostriction model for the nonlinear optical response leads to an exponential model for the nonlinear optical response for a colloidal suspension at a given temperature. However, including the full exponential model rendered the nonlinear system highly unstable. This theoretical prediction was in apparent contradiction with recent experimental observations of relatively stable one dimensional nonlinear medium that seemed to agree reasonably with the Kerr model. On the modelling aspect, Matuszewski *et al* [12] had shown that by treating the liquid suspension as a hard sphere gas they can include the compressibility of the system and this has the effect of saturating the exponential nonlinearity at high intensities. However the saturation effects resulting from this type of interactions are only important at exceedingly high filling factors.

In this chapter, I had addressed the issue on the nature of the nonlinear optical response of aqueous nanosuspensions (exponential or Kerr response) with an experimental setup. I had achieved reliable experimental results which compared well with an improved theoretical model which treats nanosuspension as non-ideals gases [13]. The compressibility factor of the nanosuspension was included in the non-ideal gas model. The successful inclusion on the level of particle

compressibility with experimental parameters marked an important step towards resolving which theoretical model best described the nanosuspension as it address particle-particle interactions.

The devised dual beam fiber approach: two single-mode fibers (identical core diameter) were immersed in the liquid and co-aligned with their fiber core facing each other. One fiber provided a well characterized input beam which propagates across the nanosuspension to the second fiber where the power collected was measured as a function of the input power. This arrangement was a fiber-optic analogue of the classic Z-scan method that is well adapted to measurements in aqueous solutions. The fiber-based scheme provided an ideal platform for the measurements within an aqueous medium. The exponential nonlinearity model was found to have the least correlation with our experiment, followed by the artificial Kerr medium approach. Including the effects of compressibility via the second virial coefficient in the non-ideal gas model was found to yield good agreement with the experiment, and in turn can be used to infer values for the second virial coefficient (B_2/V_p), and the nonlinear coefficients.

In this chapter, I have designed and performed the experiments. I performed the analysis of the results and compared with the theoretical predictions obtained by Mr R. El-Ganainy, Professor D. N. Christodoulides and Professor Ewan M Wright.

References

1. M. Sheik-bahae, A. A. Said, and E. W. Van Stryland, "High-sensitivity, single-beam n2 measurements," Opt. Lett. **14**, 955-957 (1989).
2. A. Ashkin, J. M. Dziedzic, and P. W. Smith, "Continuous-wave self-focusing and self-trapping of light in artificial Kerr media," Opt. Lett **7**, 276-278 (1982).
3. P. W. Smith, P. J. Maloney, and A. Ashkin, "Use Of A Liquid Suspension Of Dielectric Spheres As An Artificial Kerr Medium," Optics Letters **7**, 347-349 (1982).
4. P. W. Smith, A. Ashkin, and W. J. Tomlinson, "4-Wave Mixing In An Artificial Kerr Medium," Optics Letters **6**, 284-286 (1981).
5. J. E. Bjorkholm, and A. A. Ashkin, "cw Self-Focusing and Self-Trapping of Light in Sodium Vapor," Physical Review Letters **32**, 129 (1974).
6. P. W. Smith, A. Ashkin, J. E. Bjorkholm, and D. J. Eilenberger, "Studies of self-focusing bistable devices using liquid suspensions of dielectric particles," Opt. Lett **9**, 131 - 133 (1984).
7. V. E. Yashin, S. A. Chizhov, R. L. Sabirov, T. V. Starchikova, N. V. Vysotina, N. N. Rozanov, V. E. Semenov, V. A. Smirnov, and S. V. Fedorov, "Formation of soliton-like light beams in an aqueous suspension of polystyrene particles " Opt. Spectrosc. **98**, 511-514 (2005).
8. R. Sigel, G. Fytas, N. Vainos, S. Pispas, and N. Hadjichristidis, "Pattern Formation in Homogeneous Polymer Solutions Induced by a Continuous-Wave Visible Laser," Science **297**, 67-70 (2002).
9. R. El-Ganainy, D. N. Christodoulides, C. Rotschild, and M. Segev, "Soliton dynamics and self-induced transparency in nonlinear nanosuspensions," Opt. Express **15**, 10207-10218 (2007).

10. R. Gordon, J. T. Blakely, and D. Sinton, "Particle-optical self-trapping," Physical Review A (Atomic, Molecular, and Optical Physics) **75**, 055801-055804 (2007).
11. P. J. Reece, E. M. Wright, and K. Dholakia, "Experimental Observation of Modulation Instability and Optical Spatial Soliton Arrays in Soft Condensed Matter," Physical Review Letters **98**, 203902 (2007).
12. M. Matuszewski, W. Krolikowski, and Y. S. Kivshar, "Soliton interactions and transformations in colloidal media," Physical Review A (Atomic, Molecular, and Optical Physics) **79**, 023814-023816 (2009).
13. R. El-Ganainy, D. N. Christodoulides, E. M. Wright, W. M. Lee, and K. Dholakia, "Nonlinear optical dynamics in nonideal gases of interacting colloidal nanoparticles," Physical Review A **80**, 053805 (2009).
14. J. A. Barker, and D. Henderson, "What is "liquid"? Understanding the states of matter," Reviews of Modern Physics **48**, 587 (1976).
15. Y. X. Wang, and M. Saffman, "Experimental study of nonlinear focusing in a magneto-optical trap using a Z-scan technique," Physical Review A **70** (2004).
16. P. M. Hansen, V. K. Bhatia, N. Harrit, and L. Oddershede, "Expanding the optical trapping range of gold nanoparticles," Nano Letters **5**, 1937-1942 (2005).
17. W. M. Lee, R. El-Ganainy, D. N. Christodoulides, K. Dholakia, and E. M. Wright, "Nonlinear optical response of colloidal suspensions," Opt. Express **17**, 10277-10289 (2009).

Chapter 9 –

Conclusion and future works

9. Conclusion and future works

In this chapter, I aim to provide a short conclusion and future experimental works, with respect to the techniques developed in each of the chapters.

9.1. Dual optical tweezers

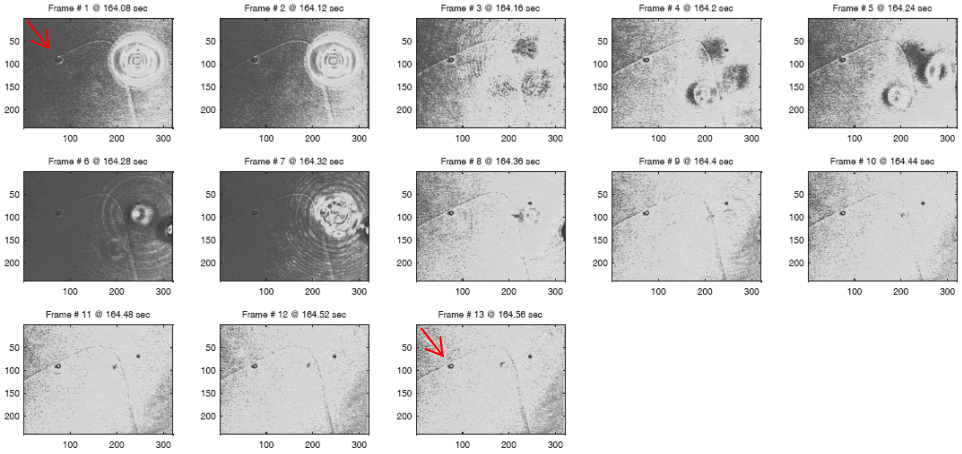

Figure. 9.1 shows a sequence of images (13 frames at 0.04s apart) of two 1 µm spheres held in two separate optical tweezers at around 15 µm apart. One of the trapped sphere (right) is broken down using the nanosecond laser. Residual bubble formation can be seen in frames 4-8. The second trapped particle (red arrow) is remained held in place after the LIB event. The figures are processed with help from Dr Y.Arita.

Conclusion - In chapter.2, I have list out the main design considerations required to construct a semi-automated dual optical tweezers system on a commercial inverted microscope system (Nikon TE 2000). The key equipment considerations in that chapter include the choice of laser and microscope objective lens. The important design considerations include the design of a dual beam optical tweezers system using a Mach Zehnder interferometry setup and beam steering optics with acousto optical deflector. Using the procedures describe in chapter.2, it is possible to build a high resolution optical tweezers for probing of biomechanical forces.

Future works – Using a dual beam optical tweezers system, it is possible to study both long and short range interactions between two particles held within each of the optical tweezers. The setup illustrated in figure 2.6 has now been used to study long range pressure waves during laser induced break down. Laser-induced breakdown (LIB) occurs when a high enough laser power density is absorbed by a given medium. Typically, a Q-switched (nanosecond) laser is used. The process of the LIB can lead to plasma formation, emission of an acoustic transient, which is followed by generation of a cavitation bubble [1]. The cavitation bubble can create a significant

pressure waves propagating in the medium can increase the membrane permeability of cells. In the current study, I have incorporated, via the epi-fluorescence port, a frequency doubled Q-switched Nd:YAG laser 532 nm with 1 ns pulse width carrying 1 mJ (Elforlight Ltd., Model SPOT) that is co-aligned onto one of the optical tweezers. Using one of the optical tweezers, I hold a single microparticle (1 µm in diameter) and localised the LIB on the trapped sphere. Using the dual optical tweezers system, the second particle is held at a distance and is used to measure the extent of the pressure being induced away from the LIB trapped sphere. The preliminary measurement of the pressure wave is to be covered in the future works pertaining to chapter.3. In the current system, there are two optical tweezers: one static and other steerable in the transverse directions. Both tweezers can be steered in the axial direction. The current dual optical tweezers system can be converted into a fully automated system by separately building lateral and axial steering devices into each of the beam path. In other words, the ideal system allows steering of two trapping beams in both the lateral and axial direction independently. This step will increase the flexibility of the position of a second probe particle in the experiment shown in figure 9.1.

9.2. Back focal plane interferometry

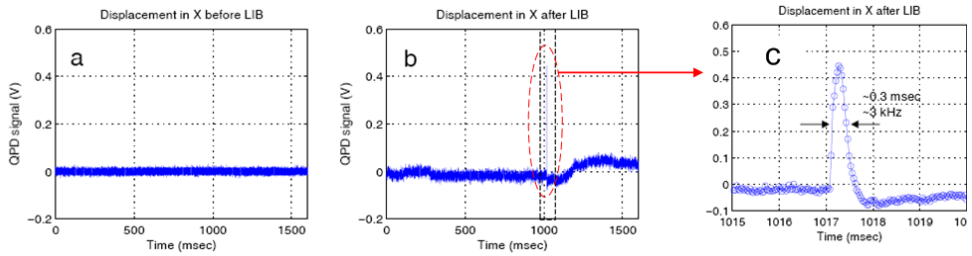

Figure. 9.2 Position displacement from the probe microsphere (left particle figure 9.1 indicated by the red arrow). From the analysis of the particle position (before LIB (a) and after LIB(b)) shows that there is large displacement of around 400 nm during the blast and a secondary displacement of 100nm before returning back to the stable trapping position. The time frame that the recorded displacement occurs is shown in c, which is 0.3 ms. The figures are processed with help from Dr Y.Arita.

Conclusion – In chapter.3, I have introduced the techniques that have been used to measure the position and stiffness of an optically trapped particle. The main instrument used in this chapter is achieved using the BFP interferometry setup and a quadrant photodiode (QPD). I first use a nanopositioning stage so as to measure the change of intensity (interference patterns at BFP) with respect to the particle positions. The linearity region, where the change of intensity versus particle position is linear, is used as a calibration scaling to directly assess the position of a particle in an optical trap. For the calibration of the trap stiffness of the optically trapped object, there are two

methodologies used i.e. time and frequency domain. I then performed the two analysis method on a single trapped particle to assess the suitability of the methods. From the result, it appears that the frequency method can provide a more reliable and easier assessment of the trap stiffness. Using the frequency analysis method, I measure the variation of stiffness with respect to increasing optical power and axial trapping height. Using the Boltzmann distribution (particle position histogram over time), it is possible to directly plot the actual optical potential energy of the trapped particle at different optical powers. Finally, the calibration technique is used to calibrate the AOD steered optical tweezers. The optical tweezers system can experimentally measure particle displacement of up to 9 nm and mechanical force of up to 0.66 pN.

Future works –The framework of optical force measurement scheme provides unprecedented access to micro-mechanical effects in a non-invasive manner. In chapter.1 section 1.5.2, I have discussed on the use of the BFP interferometry system for the measurement of biomechanical forces of cells. In current work, I have extended the use of the BFP system onto the measurement of laser induced pressure waves. Current techniques on measuring these pressure waves requires the indirect imaging of free floating tracer particles with video tracking technique or the measurement of the expansion of the residue bubble formed after the breakdown. These techniques lack deterministic measurements of the actual forces that is important to assess the magnitude of the breakdown. Considering the use of the dual optical tweezers in section 9.1, I can directly use the BFP interferometry system and measure the displacement of a probe microsphere. The probe microsphere is held stably in an optical tweezers and positioned at a pre-determined location from the particle is being broken down. Based on the measured displacement (using the conversion table in table 3.1) in figure 9.2 b, c, I estimated that the pressure induced on the trapped particle is around 182 Pa. This is around an order of magnitude smaller than currently measured pressure based on the LIB of bulk material, which is reasonable. In figure 9.3, I showed the corresponding power spectrum density graph before and after the LIB event.

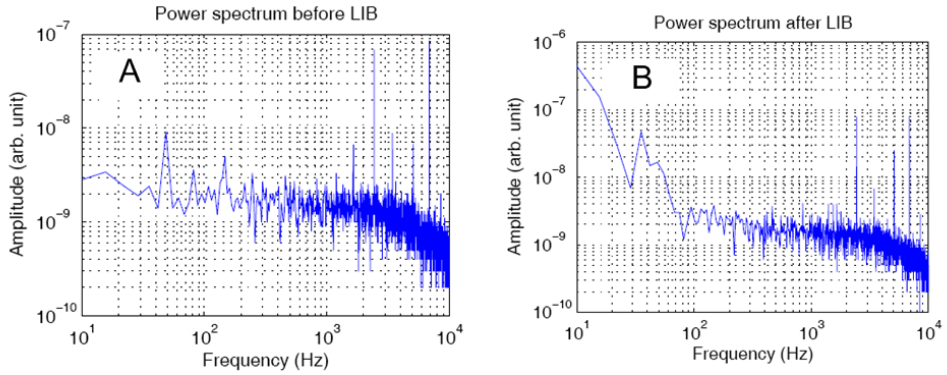

Figure. 9.3 Power spectrum of the position displacement from the probe microsphere (left particle figure 9.1 indicated by the red arrow). Just after the LIB event, there are a range of low frequency signal (f <100Hz). These fluctuations could be due to the expansion/contraction of the bubble formation after the LIB event. The figures are processed with help from Dr Y.Arita.

Although the results from the current data appear to be very promising, there are still some ambiguities that need to be resolve:

1) ***Issue*** - The bubble formation itself can affect the BFP interferometry measurement. This is because of the changes in the refractive index of the medium.

   Possible solution - Use the probe beam, without any trapped probe particle, can be used to measure the background fluctuation signal during and after the LIB event. This can help indicate the background signal and remove any undesirable effects during a single measurement event.

2) ***Issue*** - The repeatability of the blasting event seems to be dependent on the particle size and axial trapping height, available on the particle to create a breakdown.

   Possible solution – Need to repeat the data over a range of particle sizes and axial trapping height.

Besides this, I have constructed the QPD detection system onto four different optical trapping setups. In addition to the optical design, the list of softwares (stage controls (Prior scientific stages, Marzhauser stages), QPD (Hamamatsu Photonics) and PSD(Pacific silicon sensor) meant to convert the position data from the BFP interference into trap stiffness measurements have been written and designed on each individual platform. Finally, my software is currently used in a commercial optical tweezers system designed by Elliot scientific (UK).

9.3. Novel beam optical tweezers

Conclusion - In chapter 4, I started off by reviewing the higher order LG beam modes and paid close attention to the formation of the azimuthal phase variation and its annular intensity pattern. Next, I performed steps to obtain the calibration graph with the BFP interferometry technique. The calibration graph (V/μm) obtained from the QPD with a LG_0^1 beam was comparable to the Gaussian beam, using 1 μm stuck sphere, in all three dimensions. The interference of the LG_0^1 beam created a spiral intensity pattern which increases the cross talk between the transverse planes. By analyzing the cross-correlation of the LG_0^1 beam for different spheres size, I found that the 3μm diameter sphere contains the highest crosstalk. The cross talk was reduced for smaller sized particles. Measurement of the optical stiffness of the LG_0^1 tweezers reveals that it has ≈ 40% higher axial trap stiffness for 2μm spheres as compared with the Gaussian beam. On the other hand, Gaussian beam performed 50% better than LG_0^1 beam when trapping 1 μm spheres. However, both beams provided poor trap stiffness for 3 μm spheres. This is consistent with the results obtained by Friese *et al* [2] using back scattering geometry and PSD analysis.

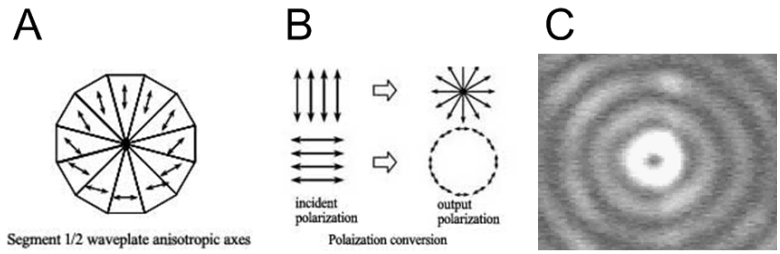

Figure. 9.4 Radial polarisation with 1070 nm laser beam. (A) Radially polarised element, (B) conversion from linear polarised light and (C) final beam profile on the sample.

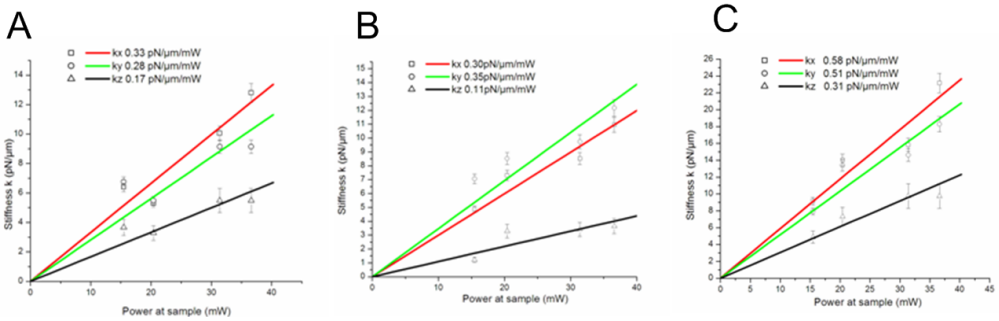

Figure. 9.5 Performance of the radial polarised optical tweezers on microspheres of different diameter (A) 3 μm (B) 2 μm and (C) 1 μm.

Future work – Ideally, it is possible to calibrate optical tweezers that is made up of different beam shapes and geometry. In the current set of work, I have implemented the BFP and QPD system to calibrate radially polarised light field. The generation of the beam is shown in figure 9.4 A and B. Figure 9.4 C shows the beam profile of the final radially polarised light. Using a similar optical setup in figure 4.11 (replacing the spiral waveplate with a segmented waveplate and removing the beam splitters PBS3 and PBS4), I am able to project the radially polarised optical trap onto the sample. Figure 9.5 shows the trapping results for three different polymer sphere of sizes, 3 μm, 2 μm and 1 μm. From the results, it seems to suggest that the trapping performance using the radially polarised beam do not improve the Gaussian optical tweezers substantially. In this particular work, I did not use an annular aperture which will be necessary to spatially remove the central null intensity and allow the linearly polarised light from the annular intensity ring to interfere at the sample plane. This annular aperture is [3, 4] suppose to reduce the central Airy diffraction pattern by a third and form a smaller optical trap. In the future work, it would be possible to generate a much finer optical trap using the annular aperture and to use the BFP and QPD for the assessment of the radially polarised optical trap.

9.4. Phase mapping with multiple trapped spheres

Conclusion – Chapter 5 serves as the last chapter that makes use of an optical trapped particle for interferometry metrology purpose. In this chapter, I have demonstrated the use of a pair of microparticles as a form of diffraction apertures to measure the optical phase and coherence of a sample beam lying in the sample chamber. By scaling the particle size and separation to the beam dimensions, it is possible to directly measure and possibly reconstruct the optical phase of any beam directly.

Future work – One lingering issue with the proposed micro-aperture technique is the differentiation of the phase transition from 2 π to above. This issue can potentially be solved by using a multiple trapping system with an AOD (Appendix D). The system can create different arrangements of microspheres on the probe field. Using the optically trapped microspheres array (much like a Shack-Hartmann microlens array [5]), I can directly map out the wavefront of any beam and potentially higher order phase changes. Other future studies will also include the study of spectra shift on polychromatic light fields using the optically controlled apertures of other materials, e.g. metallic nanoparticles, to probe the coherence of light field with the surface plasmon resonances[6].

9.5. Trapping of nanoparticles

Conclusion – In chapter 6, I start to apply the optical trap onto the trapping of nanometre-sized particles (nanophotonics). In this chapter, I use the optical tweezers system (chapter 2) to demonstrate the stable trapping of semiconductor nanosheets and nanotubes. Using both the BFP interferometry (chapter.3) and conventional brightfield video microscopy, I monitor the trapping of these semiconductor nanoparticles in an aqueous environment. The first experiment demonstrates the optical trapping of CdSe nanosheets (100-150 nm in length/width and 8-10 nm in thickness) that are silica coated. From the current result, the silica coated nanoparticles was shown to be well-confined within the optical tweezers: axial stiffness of 11.9 pN/μm with 150mW. In the second part of the chapter, I qualitatively demonstrated a simple but powerful microsphere tagging technique to manipulate absorptive VOx-NTs. In this optical manipulation process, the microsphere serves as dielectric handles tagged onto the nanotubes. The optical trap exert a force onto these dielectric handles in order to manipulate the nanotubes.

Future works – As mentioned in chapter 6, the back focal plane interferometry system is capable of capturing position fluctuations from nanoparticles. In the same fashion, I attempt to measure the dynamics of trapping single quantum dots (QD) (QDot, Invitrogen) [7]. From the data shown in figure 9.6, it is possible to measure trapping quantum dots with a trapping power of around 500mW at the sample. The photobleaching effect due to two photon absportion is remarkably less than the nanosheets. One possible is due to the different in composition (nanosheets – CdSe + silica coat and quantum dots – CdSe+ ZnS+ polymer coat). The size of the quantum dot from manufacturer's specification is around 20 nm or so (which is five fold less than the nanosheets). Based on nonlinear fitting, I measure a roll off frequency is around 199 Hz. This is close to a recent published result [7]. Additional TEM image of the current QD is required to measure the actual size of the quantum dots and their polydispersy to ensure single quantum dots are suspended in the solution. The quantum efficiency of these QDs are much higher the Cd-Se nanosheet There are instances where the QD is trapped and strong blinking of the fluorescent signal is observed. The trapping efficiency and fluorescence behaviour of the nanosheets and the quantum dots are quite different. More studies need to be made to address the difference between the two as they defers in size and composition.

In addition to the study of direct trapping of semiconductor nanoparticles, I have used an indirect approach to the manipulation of absorptive nanotubes. A future work on the indirect

trapping process will be the measurement of the affinity strength (adhesion force) between the functionalised microsphere and vanadium oxide nanotubes using a dual beam optical tweezers.

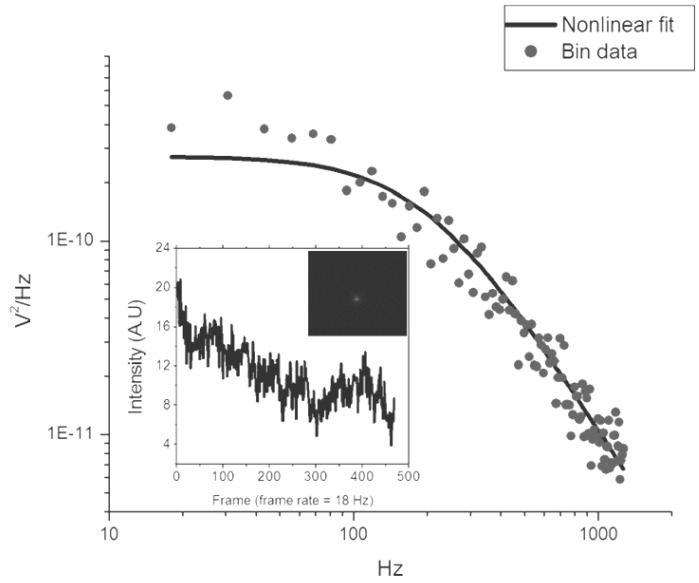

Figure. 9.6 – shows the power spectrum density and fluorescence signal from the trapped quantum dots (inset). From the nonlinear curve fitting on the bin data set, the roll off frequency is around 199.4 Hz. Inset shows the two photon fluorescence signal and the variation over time. There is a slight indication of drop in the fluorescence signal but is less significant (or less severe photobleaching) that the nanosheets.

9.6. Nanoscale heating

Conclusion: In chapter 7, I have explored the use of a trapping gold nanoparticle as a single heating source. By changing the optical power of the trap, it is possible to alter the temperature on the trapping gold nanoparticle. From the fluorescent signal analysis of the cell using a nuclei acid fluorescent staining molecule, I can observe the membrane permeability of a cell over a given period of time during and after laser exposure. When the cell is initially exposure to lower trapping powers, a small cell bleb is formed but does not grow after the initial exposure. However, at higher optical power during the initial exposure can trigger a sudden surge in the growth of the bleb. This effect brings about the question of how the cell can regulate the sudden rise of temperature. More experiments will be needed answer the regulatory process in cell when exposed to a given temperature gradient.

Future works: Using other forms of fluorescence dye to track the membrane changes. Hence, I propose the use of a different (GFP) fluorescence dye [8, 9]. This can possibly elucidate the dynamics of the membrane of the cell during the heating process. One of the issues with the

experiments is that the low frame acquisition rate of the confocal scanning system. It can reach a frame a maximum frame rate of 4 frames/s. In addition, the sensitivity of the PMT contains a large noise level. To improve the imaging system, I propose the use of EMCCD camera. The sensitivity of the fluorescence detection with an EMCCD camera is be increased and the acquisition rate will also be higher (100 frame/s). Another future experiment will be to measure the effect at even lower optical power <35.6mW. Using lower optical power, it might be possible to find the heating threshold when the cell membrane is not compromised at all.

9.7. Optical measurement of nonlinear medium

Conclusion – In this chapter, I have achieved reliable experimental results which compared well with an improved theoretical model which treats nanosuspension as non-ideals gases [10]. The successful inclusion on the level of particle compressibility with experimental parameters marked an important step towards resolving which theoretical model best described the nanosuspension as it address particle-particle interactions.

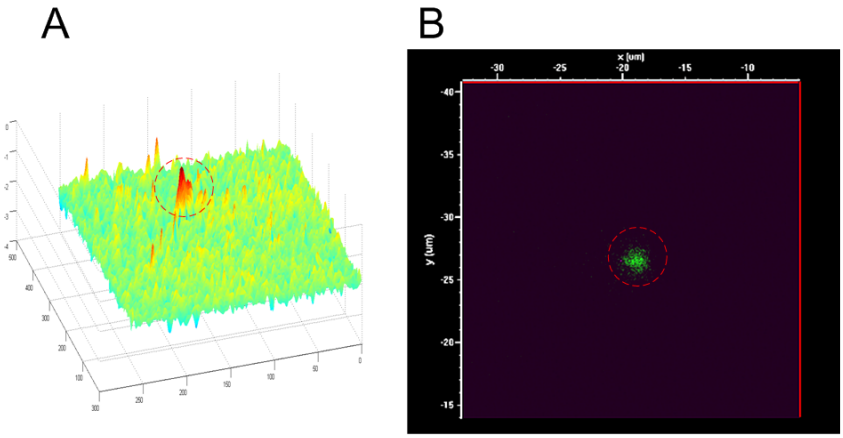

Figure. 9.7 – Optical refractive index measurement with optically trapped nanoparticles. A shows the phase map of aggregating nanoparticles (400 nm in diameter) using an optical tweezers. B shows the corresponding fluorescence imaging captured with a confocal laser scanning microscope.

Future works – Based on the experience of these findings, it is possible to extend the approach in the future to more accurately measure the nonlinear optical response, and also probe the value of the higher virial coefficients B_3. A theoretical issue that deserves more attention is how the granularity of the colloidal suspension enters the nonlinear optical response. In particular, for the concentration used in our experiment the mean distance between colloids is $\ell \approx \rho_0^{-1/3} \approx 0.4\,\mu m$, and I expect physically that the nonlinear refractive-index change will saturate in value for an optical

beam whose size approaches this value. This is perhaps where a non-local nonlinear model could enter the theoretical treatment and lead to a further softening of the nonlinear optical response in comparison to the exponential model. In addition to the modelling aspect of the work, there is also a need to develop an alternative detection system to measure the phase change of the nonlinear medium during its formation. In figure 9.7, I show the application of digital holographic microscopy (Appendix G) to measure the optical phase of the optically trapping nanoparticles. This result marks an important step in direct quantification of the refractive index change due to the imposing optical forces. Other future experimental works includes measurement of the granularity (discrete refractive index change) in the nanosuspension and the characterisation of other types of nanosuspensions i.e. semiconductor nanoparticles (chapter.6), metallic nanospheres (chapter.4) and nanowires.

9.8. References

1. A. Vogel, and W. Lauterborn, "Acoustic transient generation by laser-produced cavitation bubbles near solid boundaries," The Journal of the Acoustical Society of America **84**, 719-731 (1988).
2. M. E. J. Friese, H. RubinszteinDunlop, N. R. Heckenberg, and E. W. Dearden, "Determination of the force constant of a single-beam gradient trap by measurement of backscattered light," Applied Optics **35**, 7112-7116 (1996).
3. Q. W. Zhan, "Trapping metallic Rayleigh particles with radial polarization," Optics Express **12**, 3377-3382 (2004).
4. R. Dorn, S. Quabis, and G. Leuchs, "Sharper Focus for a Radially Polarized Light Beam," Physical Review Letters **91**, 233901 (2003).
5. F. A. Starikov, G. G. Kochemasov, S. M. Kulikov, A. N. Manachinsky, N. V. Maslov, A. V. Ogorodnikov, S. A. Sukharev, V. P. Aksenov, I. V. Izmailov, F. Y. Kanev, V. V. Atuchin, and I. S. Soldatenkov, "Wavefront reconstruction of an optical vortex by a Hartmann-Shack sensor," Opt. Lett. **32**, 2291-2293 (2007).
6. A. Bouhelier, F. Ignatovich, A. Bruyant, C. Huang, G. Colas des Francs, J. C. Weeber, A. Dereux, G. P. Wiederrecht, and L. Novotny, "Surface plasmon interference excited by tightly focused laser beams," Opt. Lett. **32**, 2535-2537 (2007).
7. L. Jauffred, A. C. Richardson, and L. B. Oddershede, "Three-Dimensional Optical Control of Individual Quantum Dots," Nano Letters **8**, 3376-3380 (2008).
8. J. A. Theriot, and T. J. Mitchison, "Comparison of actin and cell surface dynamics in motile fibroblasts," J Cell Biol **119**, 367 - 377 (1992).
9. S. Felder, and E. L. Elson, "Mechanics of fibroblast locomotion: quantitative analysis of forces and motions at the leading lamellas of fibroblasts," J Cell Biol **111**, 2513 - 2526 (1990).
10. R. El-Ganainy, D. N. Christodoulides, E. M. Wright, W. M. Lee, and K. Dholakia, "Nonlinear optical dynamics in nonideal gases of interacting colloidal nanoparticles," Physical Review A **80**, 053805 (2009).

Appendix A

Beam measurements

i. Measuring beam parameters at the focal plane
ii. Dual objective power measurement
iii. Vibration of optical table using geophone

Appendix B

Imaging nanoparticles

i. Differential interference contrast
ii. Fluorescence illumination
iii. Single plane illumination microscopy

Appendix C

Beam propagation method

Appendix D

Time shared optical trapping

Appendix E

Additional position and trap stiffness measurements

i. Mechanical vibration from EMCCD
ii. Position measurement in an LG beam
iii. Trapping 48nm nanospheres
iv. Trapping of CdSe nanosheets without silica coat

Appendix F

Additional interference from multiple trapped spheres.

Appendix G

Digital holography microscopy

A. Beam and power measurement

i. Measuring beam parameters at the focal plane

There are a variety of techniques to measure the focal volume of a lens i.e. scanning knife-edge methods [1]. The key idea of the beam profiling technique is to allow a small amount of light (from the edge of a knife) to pass onto a photo-sensitive detector at incremental steps. With knowledge of the steps and amount of light (intensity) that pass, I can measure the total irradiance. The total irradiance is essentially the integrated intensity over the scan area. By differentiating the intensity, I can subsequently infer upon the beam profile. Most of available techniques for direct beam profiling are limited by the sensitivity of the detector and the resolution of each sampling steps. When measuring the focal volume generated by a high numerical aperture objective (NA > 1), the steps required to achieve an in-situ measurement are more difficult.

Here, I use the two photon excitation signal arising from the fluorescent microspheres with the continuous wave trapping beam ($\lambda_{2\text{-photon}}=\lambda_{trapping}/2$ ≈535nm) that matches same excitation wavelength [2] to measure the profile of the tweezing beam. Using a highly sensitive photo-detection unit (i.e. photon multiplier tube PMT or Electron Multiplying Charge-coupled device, EMCCD), it is possible to record the strong fluorescent signal with red fluorescent spheres (Bangs Labs). In order to satisfy the requirements of the knife edge methods (with the two photon excitation), I chose to use 0.79μm (diameter) fluorescence spheres (Duke scientific). The total diameter of sphere should sufficiently cover the entire beam which leads to the highest two photon-signal. The spheres are dried onto the surface of a coverslip and adhere to the surface due to surface forces. For the nanometric sampling steps, I use a piezo stage (Physikinstrumente, PI733.3D, accuracy of ≈ 1 nm). To obtain a diffraction limited spot, I filled the back aperture with a diameter by 10-15% (excess overfilling leads to unnecessary loss in power). Once the back aperture of the microscope objective is filled, the beam focussing through the microscope objective would reach the required numerical aperture (N.A) of the objective (under filling the back aperture lead to a reduction of NA). The microscope objective used for focussing the tweezing beam has a numerical aperture (NA) of 1.25, a magnification of 100 and a back aperture of 8 mm. The power at the sample that is required to observed the two photon signal was measured to be around 50-100mW, using the dual objective method which is described in the next section, with minimum period of photobleaching >3000s .

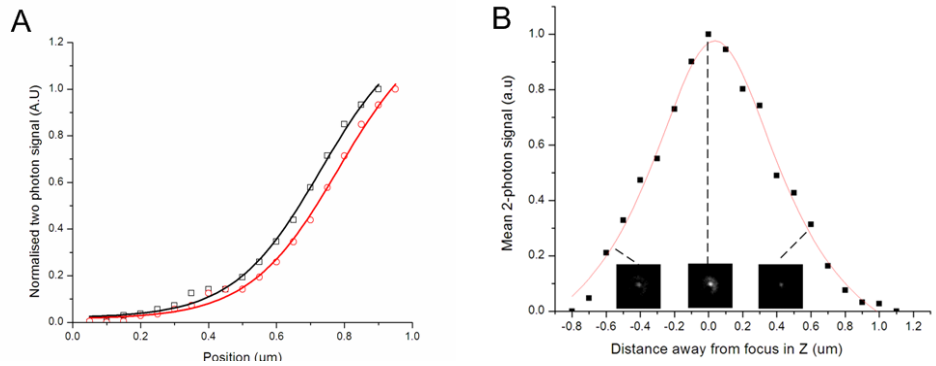

Figure.A.1 Experimentally obtained two photon signal (normalised). A - transverse and axial intensity (633nm) versus position of microsphere (overall integrated intensity). B is the axial intensity versus distance away from focus. Dot lines- experimental signal, solid – nonlinear fit

After scanning the fluorescent sphere along the transverse plane of the beam at a given step size, the two photon signal is collected and plotted over a range of positions. Here I scan the sphere at a step size of 50nm. In figure.A.1A, a graph of the normalised two photon signal (mean intensity) from the stuck fluorescent sphere across a series of transverse positions (X (black) and Y(red)) is shown. By taking the derivative of the graph, I obtain a Lorentzian plot. The full width half maximum (FWHM) of the differentiated signal from figure.A.1A is about $W_{X\text{-}EX}$ = 0.39 +/-0.01 µm, $W_{Y\text{-}EX}$ = 0.28+/-0.01 µm obtained from the Lorentzian fit. Comparing this experimentally obtained results of the beam waist w_{X-EX}, w_{Y-EX} with the theoretical values, the deviation is around $w_Y\% = 10.3\%, w_X\% = 6\%$ (theoretical values are given as

$$w_{X-theory} = 0.55(\lambda / N.A)/1.33 \quad w_{Y-theory} = 0.47(\lambda / N.A)/1.33)\,[3]$$

For the axial measurement, the beam is scanned along the propagation axis of the focused beam. In figure.A1B, a graph of the mean two photon signal (intensity) from the stuck fluorescent sphere across a series of axial positions (scan range of 2µm at a size step of 100nm) is shown. The full width half maximum (FWHM) of the signal is about 0.9849 +/-0.06 µm obtained from the Lorentzian fit. Comparing the experimentally obtained results w_{z-ex} with the theoretically $w_{z-th} = 0.44\left(\lambda/(1.51\sin^2(\alpha/2))\right)/1.33\,[3]$, I obtain a deviation of around 6.2%. The second tweezing beam driven by the AOD is given to be approximately 0.38 +/-0.01 µm in both directions due to the slightly random polarisation arising from the diffractive grating of the AOD.

ii. Dual objective power measurement

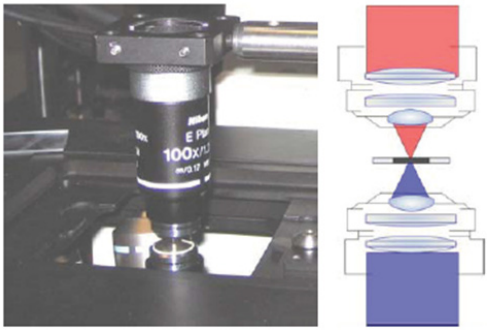

Figure.A.2 shows the dual objective power measurement schem

Microscope manufactures do not usually provide the appropriate optical transmission of the microscope objectives for a specific wavelength. Hence, it is required for one to measure the transmission of the objective by perform a dual objective transmission power measurement, so as to obtain an accurate transmission efficiency of the microscope objective for the chosen laser wavelength. The second objective, figure.A.2 (red rays), essentially collimates focussed light from the first objective figure.A.2 left (blue rays) on to a power meter or a calibrated photodiode. This is to ensure that the amount of light going onto the detector is within the angular tolerance of the photodetector of the power meter. By preparing similar sample geometry (using sample spacer slotted in between two coverslips), the back-reflection from the coverslip are accounted for. The power measured after recollimation divided by the power before entering into the objective is equal to the square of the optical transmission of each microscope objectives, this is given in equation 3.1,

$$\text{Transmission efficiency} = \sqrt{\frac{P_{output}}{P_{input}}} \qquad \text{(A.1)}$$

where P_{output} is power measured at the back aperture of the 2nd microscope objective and P_{input} power is measured at back aperture of 1st microscope objective. The power at the input is measured after a clear aperture that matches the size of the back aperture of microscope objective. It is also important to assess the overall power loss in the optical train, i.e. lenses and mirrors, with a suitable power meter. In table 3.1, I have listed the transmission efficiency for three different types of microscope objectives (brightfield, phase contrast and differential interference contrast) based on the same transmission measurement technique.

Type design	Manu	Mag	NA/Immersion	Contrast	WD	Coverslip correction	Trans % (1070nm)
E Plan (infinity)	Nikon	100	1.25/oil	Brightfield	0.23 mm	0.17 mm	**65%**
E Plan(infinity)	Nikon	100	1.25/oil	Phase contrast/Ph3	0.2 mm	0.17 mm	**42%**
Plan Apo(infinity)	Nikon	100	1.4/oil	DIC	0.13 mm	0.17 mm	**31% (DIC prism - 3%)**

Table.A.1 – show the transmission efficiency table for the different types of imaging contrast objectives.

Reference

1. L. Nugent-Glandorf, and T. T. Perkins, "Measuring 0.1-nm motion in 1 ms in an optical microscope with differential back-focal-plane detection," Opt. Lett. **29**, 2611-2613 (2004).
2. E.-L. Florin, J. K. H. Horber, and E. H. K. Stelzer, "High-resolution axial and lateral position sensing using two-photon excitation of fluorophores by a continuous-wave Nd:YAG laser," Applied Physics Letters **69**, 446-448 (1996).
3. J. B. Pawley, "Fundamental and Practical limtis in Confocal Light-Microscopy," Scanning **13**, 184-198 (1991).

iii. Vibration measurement of optical table using geophone

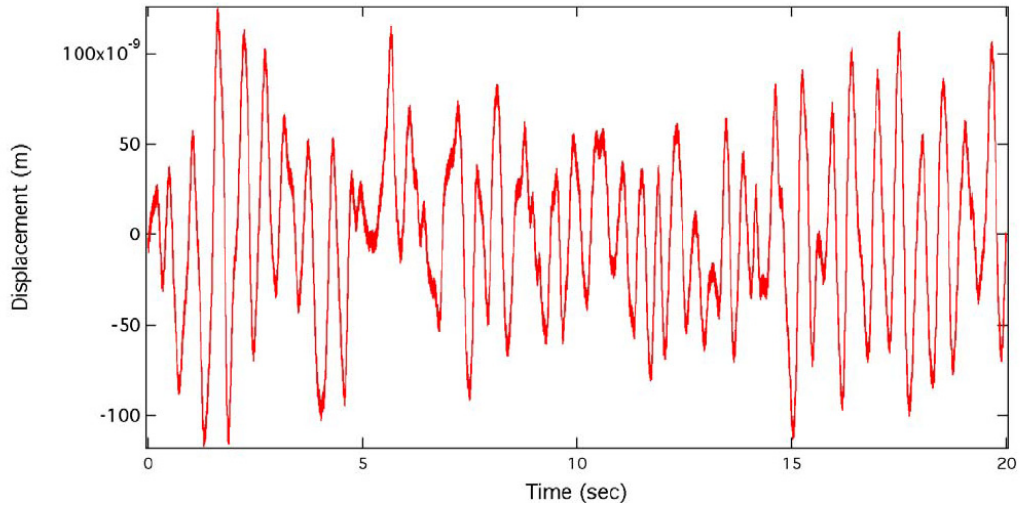

Attached is the displacement graph of the vibration on the laser table as a function of time. The root mean square value is about 50nm and the natural freq of the table is about 2 Hz. The measurement is performed by Dr Worawat Meevasana, University of St Andrews.

B. Imaging nanoparticles

Nanoparticles refer to particles at the size scale of 1 to 100nm. Nanoparticles are often referred to as the bridge between bulk material and atomic or molecular structures. At such a size scale, I can start to observe localized optical phenomenon such as quantum confinement and surface plasmon resonance. However, many of these nanoparticles are in the size scales that are below the imaging resolution (Abbe's law) in brightfield microscopy. The manipulation of these nanoparticles is only complete with the imaging these particles using current imaging techniques. In this section, I shall carry out a number of microscopy imaging modality aimed at optically resolving these nanoparticles with high NA microscope objective.

i. Differential interference contrast

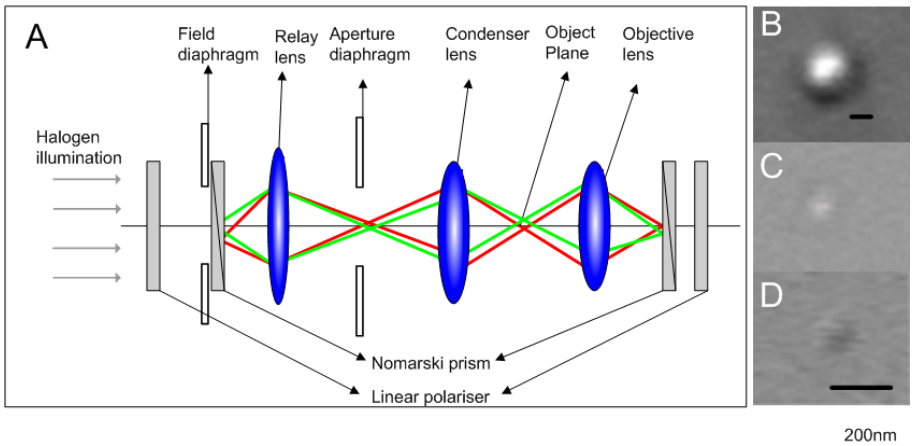

Figure. B.1.A shows a typical DIC setup. B-D shows the DIC image of 500nm, 100nm polymer sphere and 100nm gold respectively. Green and blue lines indicate the S and P polarisation of the linearly polarised light

Differential interference contrast (DIC) microscopy is a technique that is commonly used in the imaging of birefringent particles (crystals) and cells. DIC is a form of interferometry where two beams of orthogonal polarization, from the same source, are led through an object where each beam acquires a different phase change. When the two beams are recombined/ interfered, the phase differences between the two beams create a constructive and destructive interference. Using a partially coherent broadband light source for illumination, the final image appears to contain a distinctive slanted shadow. This technique has been reported by Hansen *et al* [1] for the direct imaging of stuck gold nanoparticle with diameter of 30 nm to 154 nm.

Figure B1A shows a typical DIC imaging setup for a Nikon inverted optical microscope. A Normaski or Wollaston prism splits a linearly polarized light into two orthogonal beams, which are

focused onto the object of interest with the condenser lens. The diffracted light is then collected through the objective lens and recombined with a second Normaski or Wollaston prism. A second linear polarizer (crossed with the first) removes the undiffracted light (parts of the beam that acquired zero phase shifts). A CCD is placed at the image plane of the objective lens. Both the microscope objective and condenser objective are designed so as to accommodate the polarizing prisms at the back focal plane. In order to test the imaging resolution, both dielectric (0.5 μm, 0.1 μm) and metallic (0.1 μm) spheres are left to dry on the sample surface to be imaged by DIC. In figure.B1 (B-D), I show the DIC images of a 500nm (diameter) polymer sphere, 100nm (diameter) polymer sphere and a 100nm (diameter) gold nanoparticle respectively. The microscopic images show a slanted shadow effect due to the phase difference between the two polarisation that is distinctive of DIC images [2]. From figure B1 C-D, the signal to noise ratio (SNR) of the polymer and metallic nanoparticles (100 nm) is only ≈1.1. The weak SNR is primarily due to the small phase change imposed by the nanoparticles. On the other hand, another imaging technique called dark-field imaging has readily shown to be able to image particles down to 40 nm. However, this requires a substantial alternation to the condenser assembly that less suitable for optical tweezing with QPD integration.

ii. Fluorescence illumination

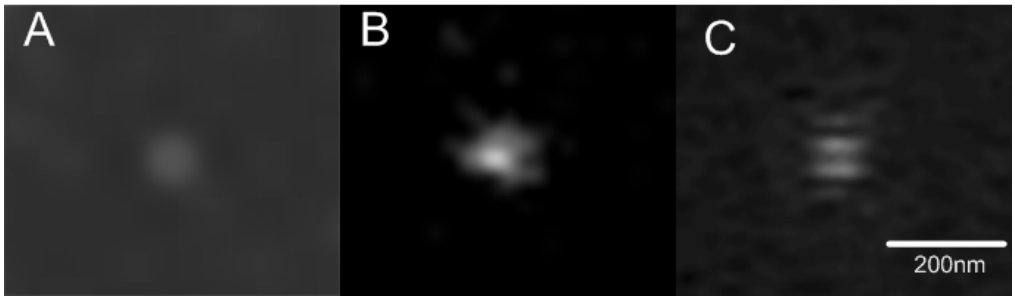

Figure. B.2. Fluorescence images obtained on different nanoparticles, (A) confocal 50nm red fluorescent sphere, (B) 50nm (diameter) two photon fluorescence with EMCCD (C) 100nm (diameter) gold nanoparticle with mercury lamp illumination (530-550nm dichroic mirror).

Alternative to the brightfield imaging technique, a nanoparticle can be made "self-illuminating" using a fluorescence molecule (fluorophore), which in turn can enhance its visual signal. Fluorescence imaging requires the active labelling of the nanoparticles with a specific fluorophore. Fluorescent labelling is the process of covalently attaching a fluorophore (fluorescein or rhodamine) to another molecule, such as a protein or nucleic acid. When the fluorophore absorbs

light from a specific wavelength (excitation), (higher energy level) it will emit a photon at a longer wavelength (lower energy level) (emission). This technique can dramatically enhance the particle visibility at high spatial differentiations (up to tens of nanometres). The excitation of the fluorescent dye can achieve with lasers or mercury lamps with the appropriate bandpass filters. Using the appropriate fluorophores and fluorescent excitation, I can observe their macromolecule dynamics using a high numerical aperture microscope objective [3]. Hence in the same way I can label our nanoparticles (polymer) with a given fluorescent dye and track the emitted light with a digital camera. Commercially purchase nanoparticles with diameter of 10 nm-200 nm come with different fluorescing intensities at a range of excitation wavelength within the visible band (350 – 700nm) of the light spectrum. On the other hand, a gold nanoparticle would exhibit a high scattering intensity when illuminated with a pseudo monochromatic light source (i.e. halogen lamp) near to its resonance wavelength (≈ 500 nm). The enhanced intensity signal (fluorescent and scattering) from the nanoparticles would greatly increase its SNR.

Figure B.2 show the fluorescence imaging of fluorescent spheres and backscattering signal gold nanoparticle. Figure B.2 A shows the image of a red fluorescence 100nm (diameter) stuck onto the surface of coverslip obtained from confocal laser scanning microscopy (Nikon C1-Si). Figure B.2 B shows the two photon excitation of 50nm red fluorescence polymer spheres (optically trapped) with a 1070nm laser beam taken with a cooled (-87^{o}C) EMCCD (Andor, DU886 Ixon). Figure.B.2C shows the back scattering intensity of 100nm gold nanoparticle under fluorescence illumination at wavelength of 543nm captured with an EMCCD [4]. **The SNR of the fluorescent illumination technique is approximately 20 which is much higher than the DIC imaging.**

iii. Single plane illumination microscopy

Recent development in single plane illumination microscopy (SPIM) has shown the possibility of obtaining high resolution images over a wide field of view [5]. In SPIM, the scattered light (figure.B.3A blue ray) from an object is collected by a high NA microscope objective. The main advantage of this imaging modality is that a single plane of illuminating light enters into the sample at an orthogonal path, with respect the imaging objective. This form of illumination is able to cover a wider field of view than confocal fluorescence microscopy (akin to wide field confocal illumination). The resolution of the SPIM is tuned by changing the width of the illuminating plane. Figure B.3 A illustrated the creation of a sheet of light on a single plane with a cylindrical lens that is focused into a glass capillary tube. In our experiment, an illuminating of light is achieved by

elliptically focusing a Gaussian beam with a cylindrical lens. Here, a He-Ne (λ=633 nm) laser beam is used as the input beam and the approximate illumination dimensions stands at 5µm in width and approximately 20µm in length. It is important to choose the illumination laser so as to provide a strong scattering signal (scattering coefficient) for a given particle size or the fluorescent excitation wavelength in the case of fluorescent particles. Figure.B.3B shows the simultaneous imaging of three 100nm polymer spheres (non-fluorescent) spheres using the single plane illumination technique. . A microscope objective (NA of 1.25, X100) collects the scattered light and projects it onto a CCD camera on the orthogonal direction (blue ray in figure. B.3A). During our experiments, we realised that the technique fails to work at position close to the walls of the capillary. This is because of the multiple interference effects between the interface of water and glass that greatly distorts the imaging quality. This technique can be compared with dark-field microscopy [6]. The dark field microscopy imaging technique would require high numerical Cardioid condensers (oblique illumination) which can impede the use of forward scattering QPD detection system. **The SNR of the SPIM technique is approximately 4, which is much higher than the DIC imaging but lower than the fluorescent illumination for the same particle size of 100 nm.**

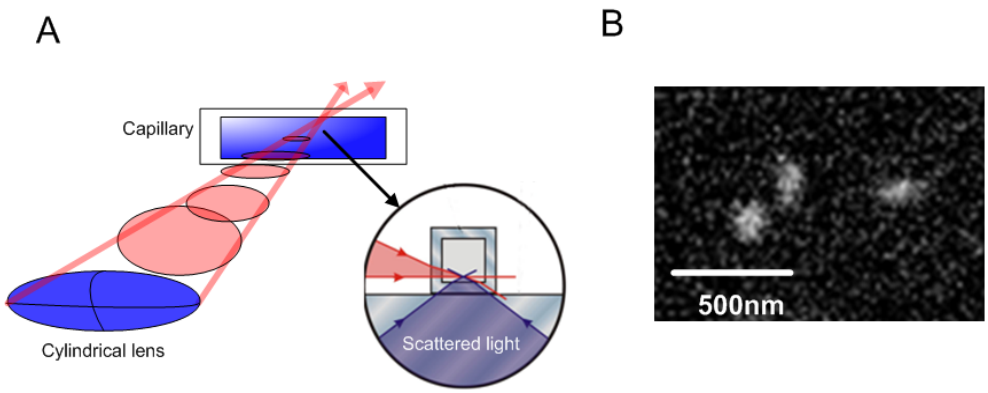

Figure.B.3 (A) shows the light sheet (red) illumination system built as an auxiliary imaging system upon an inverted optical microscope. The beam is introduced onto the size of a capillary tube of 100µm inner diameter. (B) Imaging of three 100nm polymer spheres simultaneously.

The DIC and fluorescent imaging techniques are well-established in the optical microscopy. However, they each require the nanoparticles to have some form of polarisability (polymer or metallic) or be dyed with a fluorphore. On the other hand, SPIM can work with both fluorescence and non-fluorescing particles over a wide field of view but are limited to large sample cell i.e. cuvette or capillary due to the need to couple in the light sheet. A thick sample wall (≥200µm) would impose aberrations on both the tweezing and QPD detection objective, this is not desired.

From the SNR of illumination technique, it is clear that the fluorescent illumination technique is most suited to visualise the tweezed single nanoparticles. On the other hand, in chapter.7, the DIC imaging technique is used to observe the accumulation of large ensemble of nanoparticles within a single beam. This is because the SNR of SPIM technique reduces with increase particle concentration (multiple coherent scattering), whereas the DIC technique can remove the multiple random scatterings.

References

1. P. M. Hansen, V. K. Bhatia, N. Harrit, and L. Oddershede, "Expanding the optical trapping range of gold nanoparticles," Nano Lett. **5**, 1937-1942 (2005).
2. A. Robert Day, A. Nina Strömgren, and L. T. Jeffrey, "Video-enhanced contrast, differential interference contrast (AVEC-DIC) microscopy: A new method capable of analyzing microtubule-related motility in the reticulopodial network of allogromia laticollaris," Cell Motility and the Cytoskeleton **1**, 291-302 (1981).
3. S. Weiss, "Fluorescence spectroscopy of single biomolecules," Science **283**, 1676-1683 (1999).
4. E. Fu, S. A. Ramsey, and P. Yager, "Dependence of the signal amplification potential of colloidal gold nanoparticles on resonance wavelength in surface plasmon resonance-based detection," Anal. Chim. Acta **599**, 118-123 (2007).
5. C. J. Engelbrecht, and E. H. K. Stelzer, "Resolution enhancement in a light-sheet-based microscope (SPIM)," Optics Letters **31**, 1477-1479 (2006).
6. T. Horio, and H. Hotani, "Visualization of the dynamic instability of individual microtubules of dark-field microscopy," Nature **321**, 605-607 (1986).

C. Numerical calculations of free-space propagating beams

In this section, I shall briefly elucidate the numerical method employed in the modelling of beam propagation in free-space propagation. This method is heavily used in the following chapters especially in the investigation of light beam propagation through apertures and spheres. The numerical analysis method is based upon Fourier optics. Here the complex amplitude of the beam of interest is led into its Fourier decomposition and into its respective plane waves in x, y and z. The plane wave of each vector space is being propagated toward a certain distance z_1 and then superposition to form the far-field intensity pattern. This technique has been acknowledged as a useful and important tool for detail analysis of wave propagation. There are basically three steps in the numerical simulation, the transverse electric field distribution E(x, y, 0) of the field is assumed is propagating from the plane z = 0, where z is the propagation direction, to the plane $z = z_1$ and calculate the resulting electric field distribution $E(x, y, z_1)$ at that plane. Firstly, by performing a two-dimensional Fourier transformation of the light field

$$\begin{aligned} E_0(x_1, y_1, z_1) &= \frac{1}{2\pi}\iint \tilde{E}(k_x, k_y, 0).\exp\left(ik_x + ik_y\right).\exp\left(ik_z z_1\right)dk_x dk_y \\ &= \frac{1}{2\pi}\iint \tilde{E}(k_x, k_y, 0)\exp(ik_x + ik_y)\exp\left(i\left(\Delta z\sqrt{2\pi/\lambda - k_x^2 - k_y^2}\right)\right)dk_x dk_y \end{aligned} \tag{C1}$$

where $k_x = 2\pi/\lambda x$, k_x, k_y are the transverse wave vectors, the longitudinal wave vector $k_z = \sqrt{(2\pi/\lambda)^2 - k_x^2 - k_y^2}$ where λ is the wavelength of the monochromatic optical field and $\tilde{E}(k_x, k_y, 0)$ is the representation of $E(x_0, y_0, 0)$ in the frequency spectrum (fourier transform). The propagation factor is the phase shift ϕ experience by the optical field $\phi = -k_z\left(z_1 - z\right)$. An inverse Fourier transformation is performed on equation 1to described the electric field distribution at $z = z_1$.

D. Time shared optical trapping

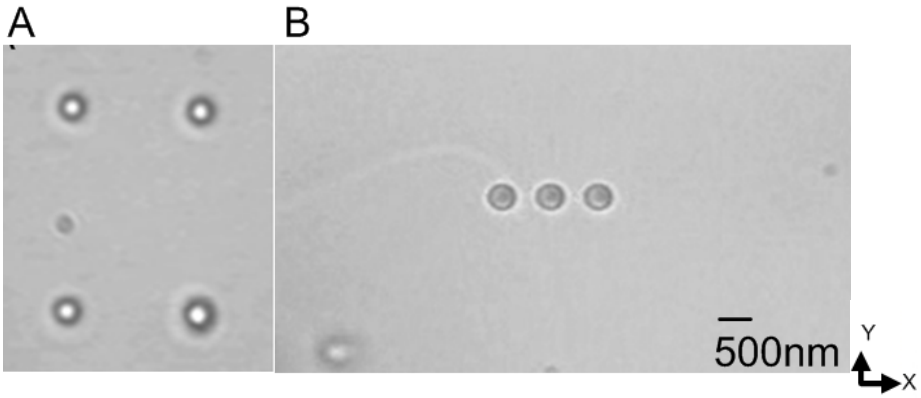

Figure.D1 – multiple 0.5μm diameter spheres trapped with AOD. 2 by 2 grid (A) and a line (B)

An AOD can easily accomplish a repetitive scan rate of the order of tens of kHz due to the fast travelling speed of the acoustic waves. At such high speed scanning, a single beam can be "shared" between different positions at milliseconds.

A particle trapped in an optical tweezers in liquid (medium of high viscosity) is equivalent to an overdamped oscillator. The concept of time shared optical traps is that one may remove the tweezing beam for a very short period of time to tweeze another object and return to this original tweezed particle some time later. Of course, once the optical field is moved away from particle's current position, the particle is left free to diffuse due to Brownian motion. If the tweezing beam returns to its original position within a relatively short time scale (less than a 0.1 millisecond or so) before a micron-sized particle diffuses away due to Brownian motion, the mean position of the particle essentially remains unchanged (it would only have diffused the order of a few nanometres). The distance *d* which the particle would diffuse away from its original trapping position is given by $d = \sqrt{2t\left(k_B T / 6\pi\eta r\right)}$ where k_B is the Boltzmann constant, *T* is the temperature, η is the viscosity, r is the radius of the particle and *t* is the time of absence of the optical tweezing beam. Hence, the smaller the particle the further the diffusion distance will be whilst the trap is absent. This characteristic of the time-shared multiple optical traps is also it's Achilles' heel and needs careful consideration in design of all such systems. This form of automated tweezing technique has greatly improve the precision and repeatability of single molecule experiments (28, 29). In essence, these beam steering systems provide a reasonably accurate and reproducible two dimensional (x-y) intensity pattern by deflecting the input beam. By scanning acousto optic deflector (AOD) at few kHz (≈μs) at specific points in the sample plane, the beam would be effectively the beam can be

effectively “shared” at the positions. Hence it is possible to create multiple trapping sites with the AOD steered optical trap. In figure.D1 (A), I have shown four particles (0.5μm) that are simultaneously trapped within four optical trap created by time-sharing. By distributing the optical trap into a line, one effectively organised particles in to a single file as shown in figure.D1 (B).

E. Additional position and trap stiffness measurements

i. Mechanical vibration from EMCCD

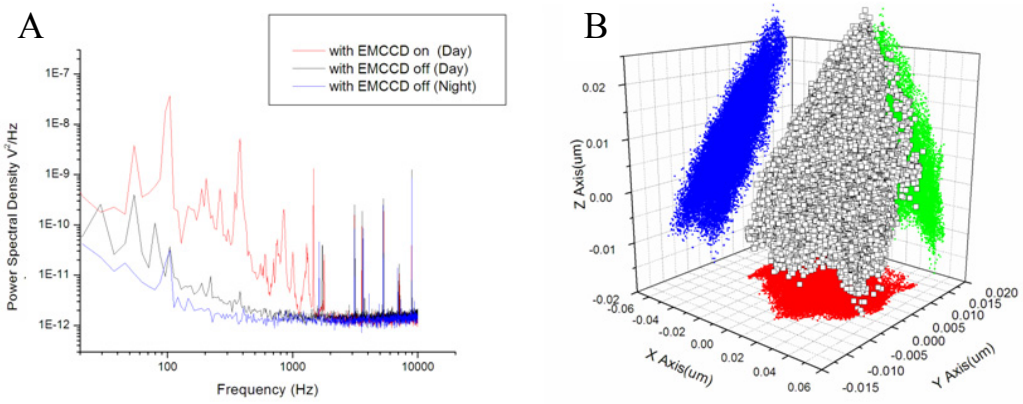

Figure E1 (A) Background power spectrum density (PSD) over frequency. (B) Background position fluctuations (XYZ) in µm with EMCCD over a 6s time interval.

The addition of an EMCCD onto the optical trap allows us to measure low photon signal for fluorescence studies. However, the noise from the cooling fan would impose a relatively strong mechanical fluctuation on the surface of the sample as shown in figure.E1 (A) and figure. E1 (B). Figure E1(A) shows the power spectrum density of the same stuck bead when the EMCCD is on and off during the day and night. I can see the high amplitude of fluctuation from the 100-800Hz from the EMCCD camera (cooling fan) that is left on during the day. On the other hand, even when the EMCCD off, the noise from the activities around the lab still produce some weak ambient noise In the night, there is virtually no background noise in the environment as seen in figure. E1 (A). By plotting the position of the stuck bead when the EMCCD is on during the day, an asymmetrical amplitude fluctuation due to the EMCCD is observed in the figure. E1 (B).

ii. Position measurement in a LG beam optical tweezers

Figure.E2 (A) shows the position time trace of an optically tweezed 1µm sphere using a focussed Gaussian (A) and LG (B) beam. From the position plots, figure E2, the particle is better confined in the Y than X direction in a Gaussian beam. This is due to the polarisation of the input beam Gaussian beam [1]. However, the LG beam of the same polarisation seems to confine the same microsphere in X better than Y, as shown in figure E2 (B). This change in the trapping asymmetry in the LG beam can be accounted for by the asymmetrical beam distribution when LG beam are highly focussed [2].

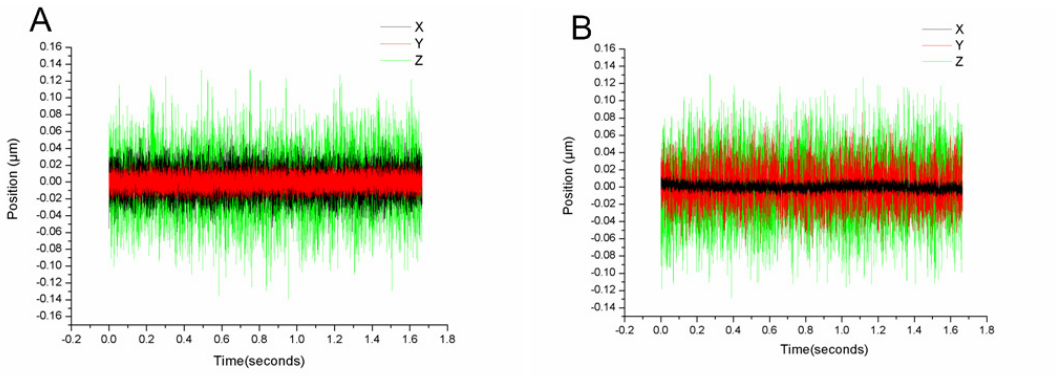

Figure E2 Position trace of an optically tweezed 1 µm sphere using an optical tweezers generated from Gaussian (A) and LG beam (B)

iii. Trapping of 48nm dielectric nanospheres

Next I move onto the tweezing of 48nm polymer sphere as shown in figure.E3, I show the power spectrum of an optically tweezed 48nm (diameter) red fluorescent polymer spheres. The power used to tweeze is 202mW of power at the sample at a depth of 3µm away from the bottom coverslip. From the power spectrum data, the roll off frequency from the Lorentzian fit is about 535 Hz which accounts for a trap stiffness of around 1.58 pN/µm which is comparable with the data obtained by Svoboda and Block [3] .

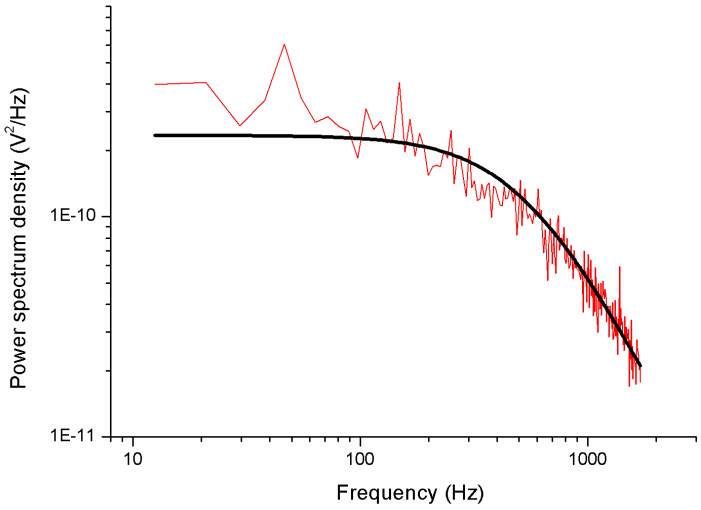

Figure.E3 Power spectrum of a trapped 48nm polymer sphere with an optical power 202mW.

As mentioned before in the previous chapter, the variance of the position fluctuations can be very useful in detecting single and multiple trapped particles. When more than a single particle is trapped, the position fluctuations measured by the QPD would be much larger. Hence, this would lead to a larger variance and histogram of the trap. Figure.E4 shows the variance and histogram (inset) over a period of 110 seconds. From the variance and histogram plot, I can see two discrete jumps of the variance (low pass filter) and the broadening of the position histogram respectively. Each step accounts for a particle jumping into the trap. The variations of the variance step height are most probably due to particle heterogeneity (10% size variations).

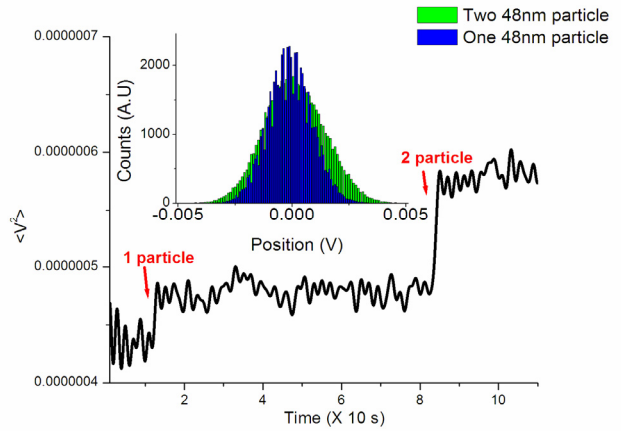

Figure E4 Variance of the trapped 48nm polymer sphere.(inset show the broadening of the histogram).

iv. Trapping of CdSe nanosheets without silica coat

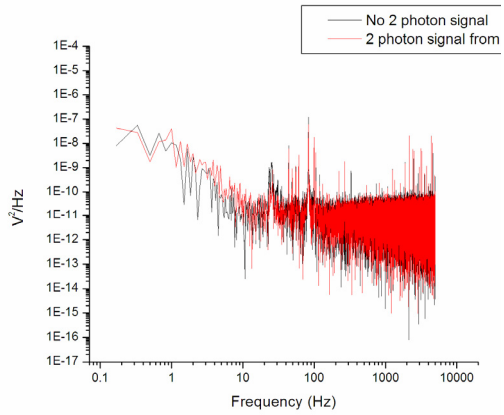

Figure E5 Axial power spectrum density from the CdSe nanosheets. Red shows the two photon signal and black shown without two photon signals. Two photon signals indicate the presence of QD in the trap but here there is virtually not difference in the PSD graphs. This could mean that the nanosheets are not being confined in the trap well enough to be measured by the QPD.

References

1. A. Rohrbach, "Stiffness of optical traps: Quantitative agreement between experiment and electromagnetic theory," Physical Review Letters **95**, 168102 (2005).
2. D. Ganic, X. Gan, and M. Gu, "Focusing of doughnut laser beams by a high numerical-aperture objective in free space," Opt. Express **11**, 2747-2752 (2003).
3. K. Svoboda, and S. M. Block, "Optical Trapping of Metallic Rayleigh Particles," Optics Letters **19**, 930-932 (1994).

F. Additional interference from multiple trapped spheres.

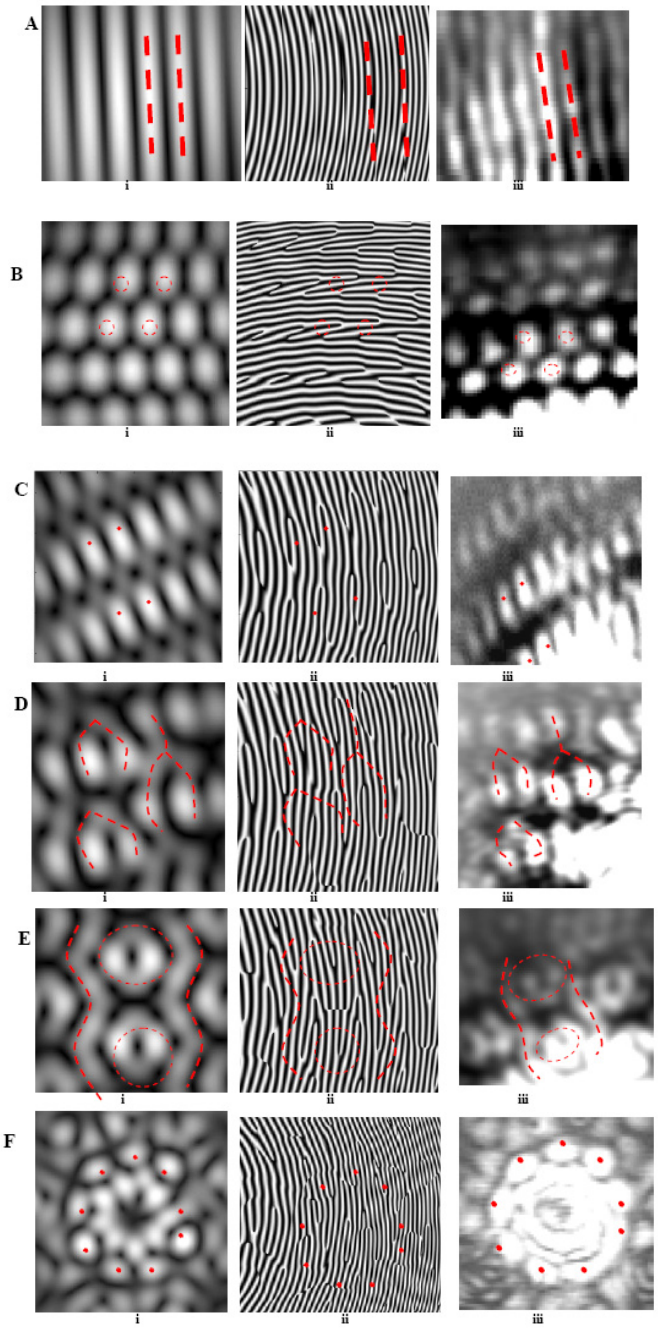

Figure F1 A, B,C, D, E shows the (i) simulation of the intensity , (ii) simulation of the phase map and (iii) experiment of the far-field diffraction pattern of two, three, four, five, six microspheres filling up the annular intensity ring respectively. Fig 4.8F shows the full circular colloidal crystals formed in the annular intensity ring, fully filled with nine spheres. The **red spot & dotted lines** denote the high intensity regions in the far-field pattern on the simulation and experimental results. On the other hand, the **low intensity regions (around the high intensity regions) contain several unity charged vortices.**

Figure F1(A) to (F) show that the far-field intensity patterns consist of a large array of patterns with regions of high and low intensity, ranging from simple interference fringes to complex intensity landscapes. The sequence in which the images are shown is as follows from numerical simulation (intensity (i), phase (ii)) and experimental (intensity, (iii)) data side by side. Figures F1(A)-(F) (i) & (iii), show comparison of the intensity pattern of the experimental data with the simulation result and good agreement is observed. Notably in figure.F1(A), I see that when two colloids are trapped on opposing sides of the LG beam, the far-field diffraction exhibit linear intensity fringes rather akin to a Young's slits experiment at the microscopic scale. When three colloids are trapped at about 60^0 to one another around the circumference, they form a triangular crystal structure (see figure F1(B)). The far-field diffraction forms a two-dimensional optical vortex lattice, when matched to the phase plot as shown in figure.F1 (B). For figure. F1 (C), I trapped two sets of colloids (each containing two microspheres) 180^0 from each other (on each side of the beam), (see figure F1 (C)) and a tilted two dimensional optical vortex lattice forms in the far-field. In figure. F1 (D), I show the formation of fork-like intensity formed in the far-field when two sets of colloids (one containing two microspheres and the other contain three microspheres) are being trapped on opposing sides of the intensity profile (see Fig figure F1 (D)). Likewise, when two set of colloids (each comprising of three microspheres) are being trapped on opposing sides of the intensity profile (see figure F1 (E)), intensity rings coupled with snake-like intensity patterns at its side are formed in the far-field as seen in figure F E. In figure F1 (F), I show that when a circular colloidal structure is being formed within the annular intensity profile of the LG beam, the diffraction patterns shows circularly arranged intensity spots around an annular intensity profile.

Optical vortices are formed by the superposition of three or more plane waves [1]. Using a spatial light modulator [1], it would be possible to generate controlled multiple beam interference which in turn can generate two or three-dimensional landscape of propagating vortex lattices. Hence, in a similar way, the light scattering off each microspheres are much like an individual beam that interferes with its neighbor. The low intensity region could signify a formation of an optical vortex. Through the phase plot from the numerical simulation, I further noticed that when 3 or more spheres are loaded symmetrically around the ring of the LG_0^3 beam, the intensity pattern in the far-field displays periodic areas of minimum intensity points. From the simulation of the phase plot, I can trace the intensity minimum point to the location of the "fork" within the interference pattern (the tilted phase profile of the far-field interference field), which is the location of an optical vortex.

Hence in short, the far-field intensity of a LG_0^3 beam diffracted by 3 or more colloidal particles trapped within annular intensity pattern contains a large amount of unity and opposite charge vortex pairs. This is seen in figure. F1 (B) (ii) to (F) (ii). Therefore, from the simulation and experimental results, I show that the diffracting light fields from the microspheres are very much like numerous individual spherical beams that interfere as plane waves in the far-field. Thus by simply controlling the trapped position of the colloids in a LG beam, a series of complex two dimensional optical vortex landscapes can be generated, without the need to employ any complex mathematical algorithm or any complex multiple beam interferometer setups.

Reference

1. K. O'Holleran, M. J. Padgett, and M. R. Dennis, "Topology of optical vortex lines formed by the interference of three, four, and five plane waves," Opt. Express **14**, 3039-3044 (2006).

G. Digital holography microscopy

One can numerically superimpose the complex amplitude of a "desired" (output) light pattern and a reference (input) beam to form a computer generated hologram from which the desired light pattern can be reconstructed. As such, one can effectively transform an input Gaussian light field into a more elaborate form at will using a computer designed hologram. In this section, I use the holographic technique as an imaging tool in conjunction with optical tweezers. Instead of generating arbitrary optical tweezers with computer generated holograms, I record the interferogram of an optically trapped object and a reference using Mach-Zehnder type interferometer that is built into the instrument, illustrated in figure G.1, digitally on a CCD. This form of imaging modality is often referred to as digital holographic microscopy (DHM) [1, 2]. With this imaging modality, I can accurately measure the effective phase structure of an object.

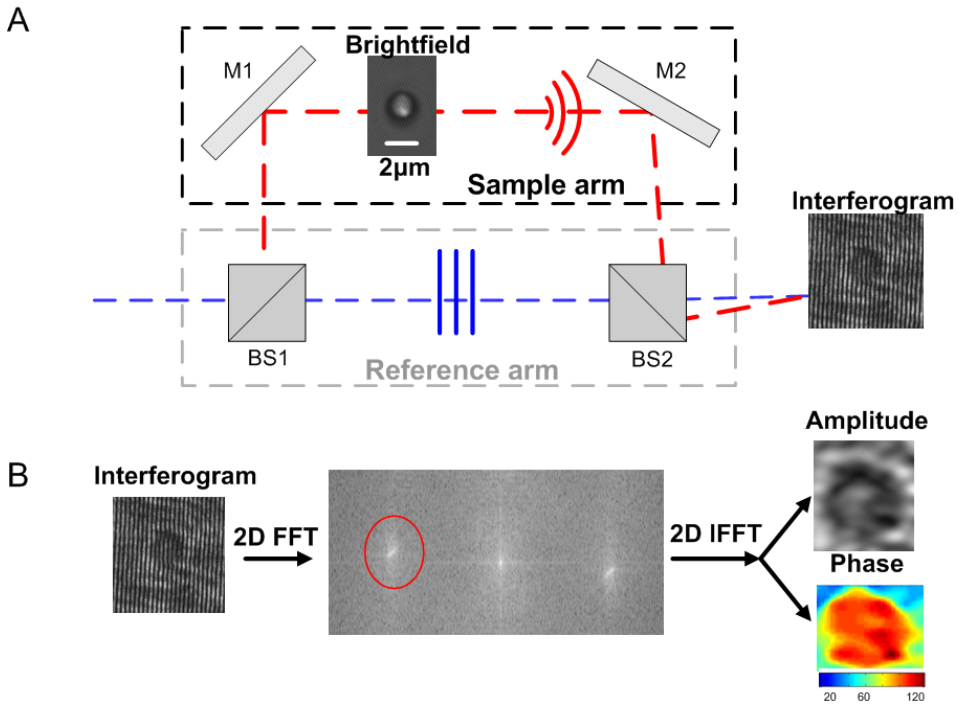

Figure G1 Illustration of digital holography microscopy technique (A) A Mach Zender interferometer to create a hologram of an optically trapped 2um sphere. M1, M2 are mirrors and BS1, BS2 non-polarising beam splitters (B) Fourier transformation (FFT) of the interferogram and select the spatial frequency to reconstruct with inverse Fourier transform and obtaining the amplitude and phase of the 2um sphere.

Traditional recorded holograms, are made with light sensitive films [3], display the interference patterns formed between the light scattered of the object and a reference light field. The light sensitive medium records either the amplitude or phase of an interference pattern. In

amplitude holograms, the transparency of the material is due to the light absportion (photographic emulsion). In phase holograms, the thickness of the material varies with the absorbed intensity. By simply illuminating the hologram with the reference beam, the virtual image of the object appears thereafter. In digital holographic microscopy (DHM) imaging, the light sensitive medium is a replaced by modern digital cameras that records the interferogram. The reconstruction is done mathematical using computer programs. For adapting the interferometer upon a microscopy system, there are certain amount of care needed to make sure the matching of the optical path length (to within coherence length) and wavefront curvature between the reference arm (planar wave) and the sample arm (scattered wave). Once the path length and wavefronts of the two arms are matched, the interference between the beams at an angle would result in a smooth linear fringe patterns as shown in the interferogram, figure G1 (A). A transparent object with a given thickness is placed at the sample arm would shift the phase of the wavefront at the sample (see figure. G1 (A)). This phase shift is recorded as a shift in the interference fringe pattern. The digital processing of the holograms (interferogram) would provide both the phase and amplitude component (complex amplitude) of the object, as shown figure. G1 (B). First, we perform a two dimensional Fourier transforms on the interferogram that will give the corresponding spatial frequencies. After which, I select the spatial frequency from the first diffraction order (see red circle) in figure. G1 (B). A two dimensional inverse Fourier transform based on the chosen spatial frequency (see red circle) is carried out. This would allow us to remove the block unwanted spectral terms in the hologram [4]. The output of the inverse Fourier transform contains both the amplitude and phase of the trapped object. The DHM technique can be applied for fluorescent marker-free cell analysis. With these features, the DHM imaging technique can provide a high resolution imaging of engineered surfaces (nanostructures), microparticles and living cells.

The combination of the two imaging modalities (DHM, confocal laser scanning microscopy), QPD detection and optical micromanipulation form an advanced Biophotonics workstation. In figure. G2., I show the confocal optical tweezers setup combined with DHM. To match the wavefront emerging from the sample, we used a set of compensating optics (same microscope objective and detection objective) placed in parallel in the reference arm. A He-Ne (633nm) laser is used as the DHM light source which is split into the sample and reference arm by BS1. A second CCD2 is place after the second BS2 (beam splitter) to record the holograms. M7-M10 are sliver mirrors used to redirect the beams onto the sample and reference paths. In figure.G2., I show a two optically trapped red fluorescent microspheres (diameter 1μm). With the combination

of DHM with confocal imaging, I can collect both fluorescent signal figure.G2(A) and reconstruct the phase of these optically trapped particles figure.G2(B). In figure.G3 A-C, I show the fluorescence, interferogram and reconstructed phase of a red fluorescent dyed Chinese hamster ovary (CHO) cell respectively. The average phase difference of the microsphere (figure.G2(A)) and the medium (≈0.2) seems to be around 20% off the ideal value. Here, I show that the operation of the advanced biophotonics workstation for both optical manipulation and imaging.

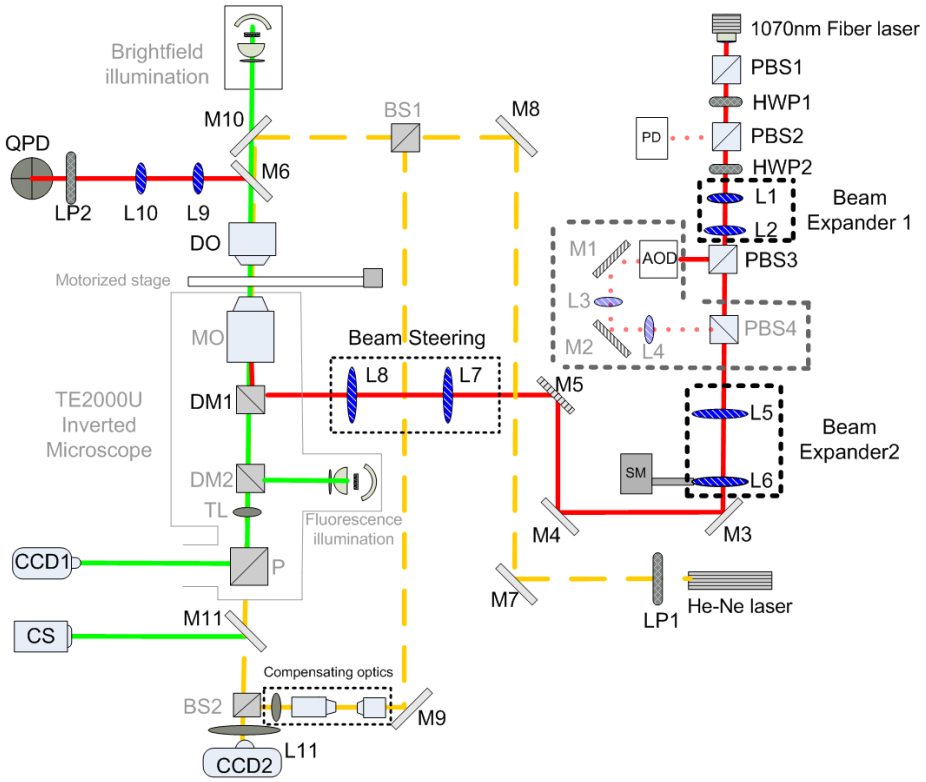

Figure G1 - Confocal optical tweezers with DHM

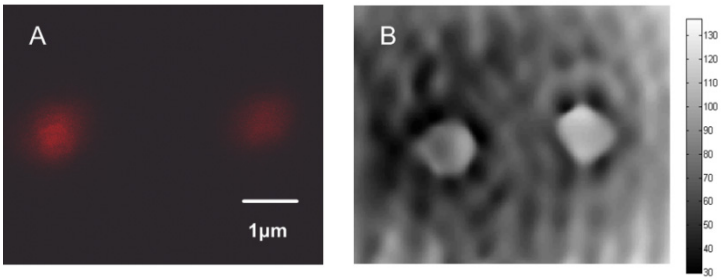

FigureG2– Trapping two 1µm red fluorescent spheres (A) confocal fluorescence image (B) phase

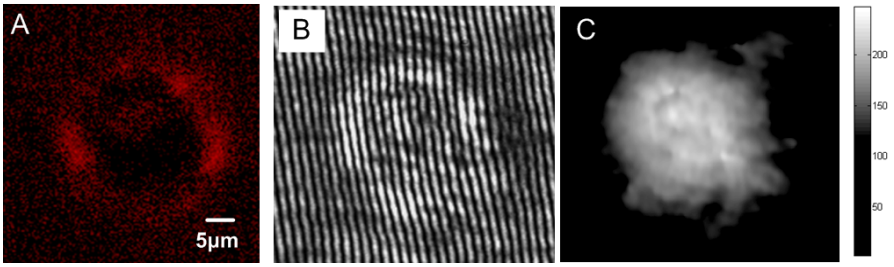

Figure G3. Fluorescence stained CHO cells (A) The membrane and nucleus are expressing fluorescent (≈600nm) signal when Propidium iodide (PI) stains the DNA on the nucleus (B) the recorded hologram of the same cell and (C) phase reconstruction of the cell (additional processing performed by Dr Maciej Antkowiak).

A current issue with the integrated system is that the PI dye emit at the red band of the light spectrum (614 -632nm) which is in direct conflict with the DHM laser (He-Ne, 633nm). Hence it is not possible to use both confocal fluorescence imaging and DHM at the same time. An improvement would be to use a different fluorescent dye that is non-membrane permeable (eg. Sytox® Green) which will allow the confocal to operate at the same time as the DHM. The digital holographic microscopy system (software processing and experimental setup.) was completed with the help and advice from Dr Maciej Antkowiak.

References

1. P. Marquet, B. Rappaz, P. J. Magistretti, E. Cuche, Y. Emery, T. Colomb, and C. Depeursinge, "Digital holographic microscopy: a noninvasive contrastimaging technique allowing quantitative visualization ofliving cells with subwavelength axial accuracy," Opt. Lett. **30**, 468-470 (2005).
2. T. Zhang, and I. Yamaguchi, "Three-dimensional microscopy with phase-shifting digital holography," Opt. Lett. **23**, 1221-1223 (1998).
3. D. Gabor, "Microscopy by Reconstructed Wave Fronts: II," Proceedings of the Physical Society. Section B **64**, 449-469 (1951).
4. C. J. Mann, L. F. Yu, and M. K. Kim, "Movies of cellular and sub-cellular motion by digital holographic microscopy," Biomedical Engineering Online **5**, 10 (2006).

" the method is important for practical procedures, it may form the basis of technological procedures, it contains sufficient novelty to warrant a publication. The work is carried out with expertise; it is well and clearly presented. "

REVIEWER FOR APPLIED PHYISCS LETTER

"The revised manuscript is substantially different from the original submission. It describes a step-by-step process for designing, constructing, and characterizing optical tweezers. It includes references to some of the more recent and highly cited examples of optical tweezer construction guides. The trouble-shooting guides are likely to be useful to neophytes. As the authors point out, optical tweezers are important tools for research across a variety of disciplines, and increasingly many researchers are interested in developing optical trapping capabilities for their laboratories. This guide is timely, therefore, and appropriate…"

REVIEWER FOR NATURE PROTOCOLS

" There is an insistence to write everything in Cartesian coordinate… where radial coordinates would be so much more readable."

REVIEWER FOR NEW JOURNAL OF PHYSICS

October 2009